



HAL
open science

Terahertz Spectroscopy of Topological Phase Transitions in HgCdTe-based systems

Michal Marcinkiewicz

► **To cite this version:**

Michal Marcinkiewicz. Terahertz Spectroscopy of Topological Phase Transitions in HgCdTe-based systems. Physics [physics]. Université Montpellier, 2017. English. NNT : 2017MONT068 . tel-01945240

HAL Id: tel-01945240

<https://theses.hal.science/tel-01945240>

Submitted on 5 Dec 2018

HAL is a multi-disciplinary open access archive for the deposit and dissemination of scientific research documents, whether they are published or not. The documents may come from teaching and research institutions in France or abroad, or from public or private research centers.

L'archive ouverte pluridisciplinaire **HAL**, est destinée au dépôt et à la diffusion de documents scientifiques de niveau recherche, publiés ou non, émanant des établissements d'enseignement et de recherche français ou étrangers, des laboratoires publics ou privés.



THÈSE

Pour obtenir le grade de
Docteur

Délivré par l'**Université de Montpellier**

Préparée au sein de l'école doctorale I2S
Et de l'unité de recherche L2C

Spécialité : **Physique**

Présentée par **Michal MARCINKIEWICZ**

**Terahertz Spectroscopy of Topological
Phase Transitions in HgCdTe-based
systems**

Soutenue le 10 juillet 2017 devant le jury composé de

M. Philippe BALLEET, Ingénieur, CEA, Grenoble	Examineur
M. David CARPENTIER, Professeur, Lab. de Physique, ENS, Lyon	Rapporteur
M. Yves GULDNER, Professeur, LPA, ENS, Paris	Rapporteur
M. Wojciech KNAP, Directeur de Recherche, L2C, Montpellier	Examineur
M. Milan ORLITA, Chargé de Recherche, LNCMI, Grenoble	Examineur
M. Frédéric TEPPE, Chargé de Recherche, L2C, Montpellier	Directeur
M. Eric TOURNIE, Professeur, IES, Montpellier	Examineur
Mme Sandra RUFFENACH, IR CNRS, L2C, Montpellier	Invitée

Abstract

This thesis presents an investigation of different topological phases in mercury-cadmium-telluride (HgCdTe or MCT) based heterostructures. These solid state systems are indeed a perfect playground to study topological states, as their band structure can be easily varied from inverted to non-inverted, by changing internal or external parameters.

If a system has an inverted band ordering, its electronic structure has a non-trivial topology. One cannot change its topological order without closing the band gap, which is inevitably accompanied with the appearance of massless particles in the bulk. A system, that has an inverted band structure and a finite gap in which the Fermi level is positioned, is called a topological insulator. These novel materials are insulators in the bulk, but host gapless metallic states with linear dispersion relation at boundaries, protected against disorder and backscattering on non-magnetic impurities. These states arise at the interfaces between materials characterized by a different topological order. A 2D topological insulator is thus characterized by a set of 1D spin-polarized channels of conductance at the edges, while a 3D topological insulator supports spin-polarized 2D Dirac fermions on its surfaces.

The 2D and 3D massless fermions have already been demonstrated experimentally in HgCdTe-based heterostructures. However, the topological phase transitions during which the massless particles appear remain barely explored. The HgCdTe band structure can be tuned from inverted to non-inverted using chemical composition, pressure, temperature, or quantum confinement. These parameters therefore allow to probe the system in the vicinity of different topological phase transitions. In this thesis, the use of temperature as continuous band gap tuning parameter allows to study the appearance and the parameters of semi-relativistic 2D Dirac and 3D Kane fermions emerging at the points of phase transitions.

The systems investigated were $\text{Hg}_{1-x}\text{Cd}_x\text{Te}$ bulk systems and HgTe/CdTe quantum wells characterized by an inverted and regular band order, and strained HgTe films which can be considered as 3D topological insulators with a residual quantum confinement. All these systems exhibit topological properties, and the experimental results are interpreted according to theoretical predictions based on the Kane model. This thesis is complemented by an overview and the preliminary results obtained on a different compound – a InAs/GaSb broken-gap quantum well, which was also identified as a topological insulator. The structures were studied by means of terahertz and mid-infrared magneto-transmission spectroscopy in a specifically designed experimental system, in which temperature could be tuned in a broad range.

Résumé

Cette thèse porte sur l'exploration de différentes phases topologiques présentes dans des hétérostructures à base de mercure, cadmium et tellure (HgCdTe). Ces systèmes sont de parfaits cas d'études des états topologiques dans la matière condensée. En effet, leur structure de bande peut aisément être modifiée d'inversée à non-inversée par le biais de paramètres internes ou externes.

Lorsqu'un système présente une structure de bande inversée, il a une topologie non triviale. Il est impossible de modifier cet ordre topologique sans fermer son gap, ce qui inévitablement entraîne l'apparition de particules sans masse dans son volume. Un système présentant une structure de bande inversée et un gap d'énergie finie dans lequel se trouve le niveau de Fermi, est appelé isolant topologique. Ce nouveau type de matériau est isolant dans son volume, mais abrite des états métalliques sans gap sur ses bords. Ces derniers ont une relation de dispersion linéaire et sont protégés des effets liés au désordre et de la rétrodiffusion par des impuretés non magnétiques. Ces états particuliers apparaissent à l'interface de matériaux présentant des ordres topologiques différents. Ainsi, un isolant topologique 2D se caractérise par des canaux 1D de conductance polarisés en spin à ses bords, alors qu'un isolant topologique 3D accueille des fermions de Dirac 2D, polarisés en spin, aux surfaces.

L'existence de fermions sans masse 2D et 3D a déjà été démontrée expérimentalement. Cependant, la transition de phase topologique durant laquelle apparaissent les particules sans masse n'a que très peu été explorée. Il est possible de modifier la structure de bande de HgCdTe d'inversée à non inversée par le biais de la composition chimique, la pression, la température ou le confinement quantique. Ces paramètres permettent ainsi de sonder le système au voisinage de différentes transitions de phase topologiques. Dans ce travail, l'utilisation de la température comme paramètre d'ajustement continu du gap permet d'étudier au point de transition de phase l'apparition de fermions semi-relativistes de Dirac (2D) et de Kane (3D) ainsi que leurs propriétés.

Les systèmes étudiés au cours de ces travaux de recherche sont des cristaux massifs de $\text{Hg}_{1-x}\text{Cd}_x\text{Te}$ et des puits quantiques HgTe/CdTe présentant des structures de bandes inversées et non inversées, ainsi que des couches minces de HgTe contraintes pouvant être considérées comme des isolants topologiques 3D ayant un confinement quantique résiduel. Tous ces systèmes possèdent des propriétés topologiques. L'interprétation des résultats s'appuie sur les prédictions théoriques basées sur le modèle de Kane. En annexe, une vue d'ensemble des puits quantiques composites InAs/GaSb, structures également identifiées comme isolants topologiques, est présentée, comportant les résultats préliminaires obtenus sur ces dernières.

Toutes les structures ont été étudiées par magnétospectroscopie en transmission dans les domaines de fréquence terahertz et infra-rouge moyen à l'aide d'un dispositif expérimental spécifiquement conçu pour permettre des mesures sur une large plage de températures.

Contents

1	Introduction	1
1.1	Topological States of Matter	1
1.1.1	Quantum Hall Effect	2
1.1.2	Topological Invariant	2
1.1.3	Topology in Condensed Matter	3
1.1.4	Properties of Topological States	4
1.2	This Work	6
1.2.1	State of the Art	6
1.2.2	Scope of this Thesis	11
2	Optical Properties of Matter	13
2.1	Review of Fundamental Relations for Optical Phenomena	13
2.1.1	The Dielectric Function and Optical Conductivity	13
2.1.2	Probability of Absorption	14
2.2	Density of States and Optical Transitions	15
2.2.1	Density of States in Parabolic Bands	16
2.2.2	Density of States in Linear Bands	17
2.2.3	Optical Transitions	17
2.2.4	Density of States in Magnetic Field	18
2.2.5	Fermi Level	21
2.2.5.1	Temperature Effects	21
2.3	Experimental Methods	22
2.3.1	FIR Spectroscopy	22
2.3.2	Experimental Set-up	22
3	HgCdTe Bulk Systems	27
3.1	Introduction to HgCdTe Systems	27
3.2	Overview of HgCdTe Bulk Crystals	28
3.2.1	Band Structure and Temperature	30
3.2.2	The Simplified Kane Model	33
3.2.3	Bulk HgCdTe at Magnetic Field	33
3.3	Experiment	35
3.3.1	Samples	35
3.3.2	Results	38
3.3.2.1	Sample A	40

3.3.2.2	Sample B	49
3.3.3	Summary	58
4	HgTe Quantum Wells	61
4.1	Overview of HgTe Quantum Wells	61
4.1.1	Band Structure of a HgTe/CdTe Quantum Well	61
4.1.1.1	The Influence of Magnetic Field on the Band Structure	63
4.1.1.2	The Influence of Temperature on the Band Structure	66
4.1.2	Experiment	67
4.1.2.1	Samples	67
4.1.2.2	Results	68
4.1.2.3	Sample A	70
4.1.2.4	Sample B	74
4.1.3	Summary	82
4.2	Strained HgTe Films	85
4.2.1	Band Structure	85
4.2.1.1	Strain	85
4.2.1.2	Surface States	85
4.2.1.3	Magnetic Field	91
4.2.2	Experiment	92
4.2.2.1	Samples	92
4.2.2.2	Results	93
4.2.3	Summary	98
5	Conclusions and Outlook	99
A	InAs/GaSb Quantum Wells	103
A.1	General Properties	103
A.1.1	Carrier Concentration	104
A.1.2	Carrier Mobility	105
A.2	Band Structure	106
A.2.1	Magnetic Field Tunability	108
A.2.2	Electric Field Tunability	108
A.3	Trilayer Quantum Well	109
A.4	Experiment	111
A.4.1	Samples	111
A.4.2	Experimental Details	112
A.4.3	Results	112
A.5	Summary	116
B	HgCdTe Bulk	117
B.1	Magneto-transport Measurements	117
B.1.1	Sample A	117
B.1.2	Sample B	118
B.2	Magneto-spectroscopy Measurements	119
B.2.1	Sample A	120

B.2.2	Sample B	122
C	HgTe Quantum Wells	125
C.1	Hamiltonians	125
C.2	Experimental Results	126
C.2.1	Sample A	126
C.2.2	Sample B	128

Chapter 1

Introduction

Since the dawn of science, people always wanted to encounter new frontiers and cross them, expanding the boundaries of the universal knowledge. Even in the modern times, it is still our duty to explore the matter around us and the laws governing it. Although throughout the XIX and XX century, chemistry succeed in finding and classifying most of the elements – building blocks of matter, there is still plenty of work to do in discovery and classification of the distinct states of matter, called phases. Matter in the quantum approach can form different phases, such as crystalline solids, magnets and superconductors.

Nowadays, the interest of a part of condensed matter physics is focused on a discovery and characterization of novel phases and particles, which appear at the point of phase transitions in solid state materials. These particles appear generally when matter undergoes a specific transition between different quantum phases. The particles often behave in the most uncanny manner – like the Dirac fermions, which behavior mimics the behavior of relativistic particles, or the exotic Majorana fermions, which are their own antiparticles. These kind of excitations and more can be realized in various condensed matter systems.

1.1 Topological States of Matter

One of the most remarkable achievements of condensed matter physics in the recent times is the classification of quantum states of matter by the principle of spontaneous symmetry breaking [1]. The pattern of symmetry breaking led to a unique concept of order parameter, which can be understood in terms of the famous work of Landau-Ginzburg [2], where the notion of the effective field theory is described. The effective field theory is determined by the general properties like the dimensionality and symmetry of the order parameter, and can be used to give a universal description of quantum states of matter.

The following examples can be given to better understand the concept of states of matter and symmetry breaking: a crystalline solid breaks translation symmetry, despite the fact that the interaction between its atomic cells is translationally invariant. A rotational symmetry in magnetic systems is spontaneously broken, even though the fundamental interactions are isotropic. A superconductor breaks the more subtle gauge symmetry, which leads to phenomena such as flux quantization and cooper pair formation [3].

The concept of symmetry breaking and local order parameter used to describe the phase transition is well accepted. However, it fails to explain some interesting phenomena such as the integer Quantum

Hall Effect (QHE) [4] and many body phases of the fractional QHE [5]. The study of these effects ultimately led to a new paradigm in the classification of condensed matter systems – the concept of topological order [6] [7].

1.1.1 Quantum Hall Effect

An electronic band structure of a given system at high magnetic field forms a set of distinct Landau levels. The way how levels are occupied determines whether a current can flow through the system or not. According to the standard band theory, which successfully explains most of the electrical properties of solids, there should be no current flowing through the sample if the chemical potential of the system lies between Landau levels. On the other hand, if the chemical potential crosses a Landau level, the current can flow.

Yet, a system in the quantum Hall state behaves in a different manner. Even if its bulk is insulating (there is an energy gap between the highest occupied band and the lowest empty band), the electrical conductivity is nonzero. The electric current is still carried along the edges of the system, forming discrete channels of conductance. Those edge states are chiral – the direction of current propagation depends on the direction of magnetic field. The current in the channels avoids dissipation and has a very precise value of resistance, giving rise to QHE.

The quantum Hall state turned out to be the very first example of a quantum state being topologically different from all other states of matter known before. The state in which the quantum Hall occurs defines a specific topological phase, meaning that some particular fundamental properties are insensitive to smooth changes in general parameters of the system. The very fundamental reason for such a quantization is the existence of topological invariants – in the case of the QHE such an invariant is the electrical conductance, which takes values only of integer units of e^2/h , and is independent on the type of material investigated. Moreover, it does not change (is *invariant*) with smooth variations of material parameters – it can be considered as a non-local order parameter of the system.

1.1.2 Topological Invariant

Topological invariant, also called *Chern number*, was connected for the first time with the quantized value of Hall resistance by Thouless *et al.* [7]. The idea is related to a specific phase that is acquired by the Bloch wave functions of bulk electrons as the wave-vector \mathbf{k} varies over the boundary of the Brillouin zone. This phase was named Berry phase, after Sir Berry, who described it in 1984 [8]. The Chern number is defined as a sum of the Berry phases over all occupied **bulk** bands, and is strongly related to the number of conducting **edge** modes defining the Hall conductivity in the quantum Hall regime. This means that the topological properties of the edge channels are directly related to the bulk. This relation is called the **bulk-boundary** correspondence and is necessary for understanding of the topological insulators.

The topological invariant was introduced as a mathematical concept used to classify different geometrical objects into broad classes. An example of such invariant might be a number of holes on a geometrical surface. The most famous illustration of this geometrical analogy is a coffee mug and a torus. Both of them are classified to the same topological class because both of them possess exactly one hole. Moreover, one can be deformed, via a smooth transformation, into the other, and vice-versa; a sphere can be smoothly deformed into an ellipsoid, because they share the same number of holes (zero), etc. Topology tends to disregard the small differences of objects and focus on their general

properties. In this context the quantized conductance of quantum Hall state, which can be found in a variety of materials of different shape, remains unchanged – is invariant.

1.1.3 Topology in Condensed Matter

The connection between geometrical classes of objects and condensed matter physics is indirect – topology in the solid state physics has very little to do with a shape of considered material, and definitely the subject is much broader than just the QHE. Those two disciplines were probably first linked for study of topological insulators by the works of Berezinski [9][10], and Kosterlitz and Thouless [11]. It is worth highlighting that a Nobel Prize in Physics in the year 2016 was divided – one half was awarded to David J. Thouless, the other half jointly to F. Duncan, M. Haldane, and J. M. Kosterlitz *for theoretical discoveries of topological phase transitions and topological phases of matter*.

In topological geometry there are surfaces, holes, and smooth transformations of surfaces, which do not require tearing the surface or making holes in it. In condensed matter Hamiltonians are used to describe any system, providing information about its band structure and energy gaps (which may play a role of holes in geometry). There are always ways to transform a given Hamiltonian into a different one, by changing some parameters that the Hamiltonian depends on. If the transformation is smooth in a sense that it does not require a closing of a gap (an equivalent of creating a hole in geometry) at any point, then the transformation preserves the topology of the system. For example – it is impossible to transform a sphere into a torus without tearing its surface. In the same way it is impossible to transform a band structure of a system from a topological insulator phase into a trivial insulator phase without closing the bulk gap.

The name and the idea of topological insulators can be traced back to the works of Kane and Mele, where an universal concept of identifying another topological index (invariant) was described [12]. They proposed a realization of such a system in graphene [13], where the spin-orbit coupling (SOC) opens a band gap, rendering the bulk of the sample insulating. In a similar way magnetic field suppresses bulk conductivity in QHE. However, SOC does not require an application of external magnetic field. Nevertheless, at a boundary of this system a set of topologically protected edge states should emerge, being analogous to the states of the QHE. The difference is that these states are protected by a time-reversal symmetry, thus they are not chiral, as chirality is forbidden, but helical (spin-polarized). That is why the effect of emergence of spin-polarized quantum Hall edge states without magnetic field was called the quantum spin Hall effect (QSHE), and a 2D topological insulator, in which the QSHE occurs – a quantum spin Hall (QSH) insulator.

However, the proposed realisation of the QSHE in graphene turned out to be unrealistic, because the energy gap opened by SOC is extremely small, of the order of 1 μeV [15][16]. Finally, in 2006, QSHE was predicted to exist by Bernevig *et al.* [17][18] in a HgTe/CdTe quantum well (QW) system. One year after the theoretical proposal of Bernevig, the Molenkamp's group at the University of Würzburg fabricated devices and performed the first transport experiments showing a signature of the QSH insulator phase [14]. Their work showed that for thin quantum wells with well width $d < 6.3$ nm, the insulating regime exhibits a conventional behavior of neglectable conductance at low temperature. However, for thicker quantum wells ($d > 6.3$ nm), a nominally insulating regime exhibits a plateau of residual conductance of value close to $2e^2/h$. The residual conductance was independent on the sample dimensions, indicating that it is caused by the edge states [14].

Low temperature ballistic transport via edge states can be understood within a basic Landauer-Büttiker [19] framework, in which the edge states are populated adequately to the chemical potential.

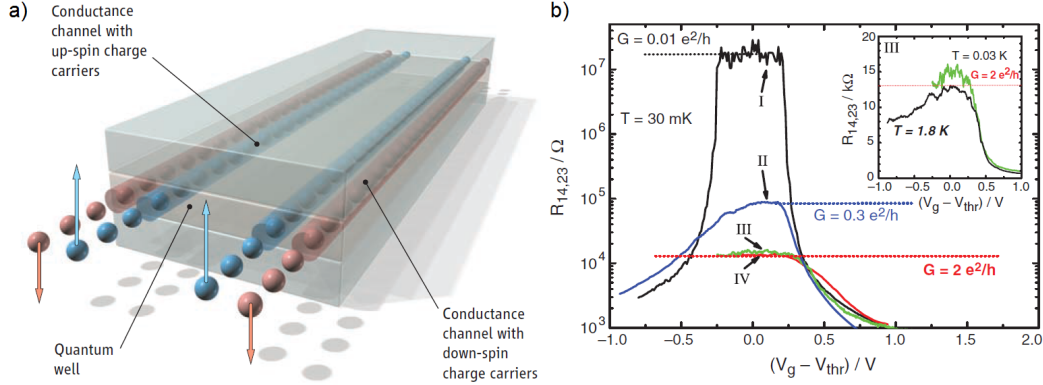


Figure 1.1: **Panel a)** Schematic of the spin-polarized edge channels in a quantum spin Hall insulator. **Panel b)** The longitudinal resistance of various normal (I) and inverted (II, III, and IV) quantum well structures as a function of gate voltage, measured for $B = 0$ T at $T = 30$ mK. The image comes from the work of König *et al.* [14].

As a consequence, conductance is quantized and equal to e^2/h for each set of edge states. Furthermore, the residual conductance is destroyed by an application of small external magnetic field. A quantum phase transition at the critical thickness, $d_c = 6.3$ nm, was also determined independently from the insulator-to-semimetal phase transition induced by magnetic field. After the prediction of topological insulating phase in HgTe/CdTe quantum well, a similar phase was predicted by Liu *et al.* [20] in an InAs/GaSb, and strained GaAs [18].

The initial findings of 2D topological insulators were followed by a prediction of the 3D topological insulating phase in the $\text{Bi}_{1-x}\text{Sb}_x$ alloys for a specific compositions x [22], and shortly after the topologically nontrivial surface states were observed by the angle-resolved photoemission spectroscopy (ARPES) by Hsieh *et al.* [23]. Similarly, the topological insulators in 3D were predicted in Bi_2Te_3 , Sb_2Te_3 [24] and Bi_2Se_3 [24][21] alloys. These compounds exhibit a large bulk band gap and gapless surface states consisting of a single Dirac cone. Xia *et al.* [21] and Chen *et al.* [25] observed a linear dispersion relation of this states using ARPES (Figure 1.2). However, Bi-based compounds often suffer from low mobility, caused by high unintentional doping [26], which makes the observation of surface states difficult due to a high bulk conductivity [27].

On the other hand, a semimetallic HgTe crystal is characterized by a very high crystal quality. Under applied strained it is predicted to belong to 3D TIs [28]. In 2011, Brüne *et al.* proved that strained films of HgTe indeed exhibit a TI phase [27], by performing magneto-transport and ARPES measurements.

1.1.4 Properties of Topological States

Interesting phenomena take place at a boundary of two materials characterized by a different topological number, such as Chern number. The best description can be found in [29], which explains that the presence of the edge states is a fundamental aspect of many topological insulators. The argument revolves around a direct observable manifestation of a Chern number – Hall conductance.

Given a set of two insulators (each with a different value of the Chern number) put in a close proximity (so they have a common boundary), and the two insulators extend to infinity (away from the boundary). The Chern number is always integer, defined separately on both sides of the interface between the two insulators. It cannot be changed unless the bulk gap closes and reopens again with

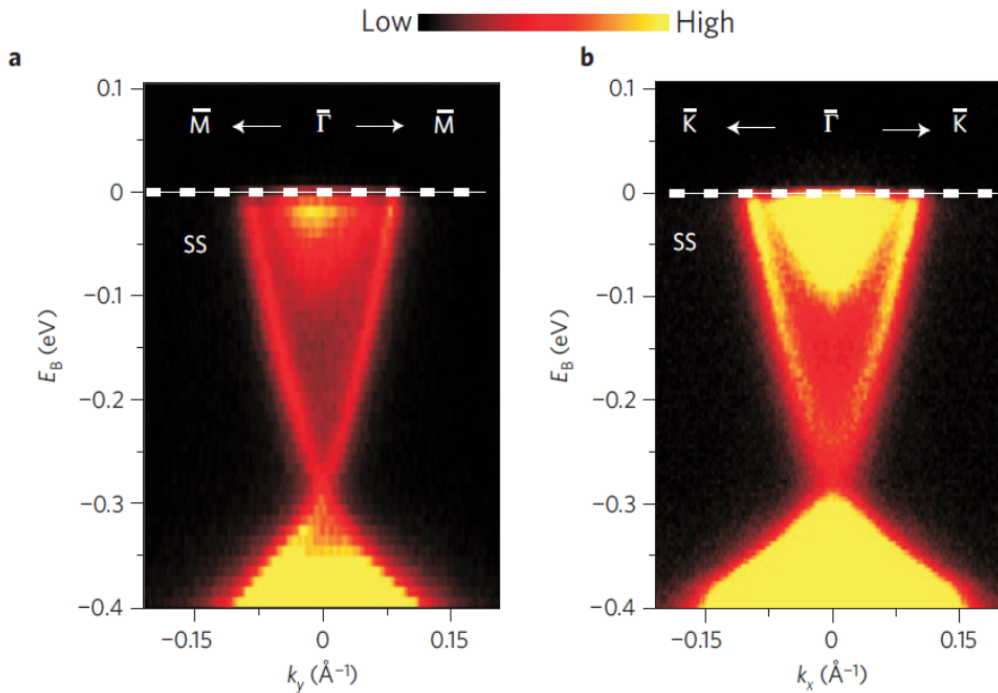


Figure 1.2: ARPES measurements of Bi_2Se_3 (111) evidencing the surface states with a linear energy dispersion, forming a unique Dirac cone in the bulk near the Γ point. The image comes from the work of Xia et al. [21].

a different Chern number on the other side. This means that the boundary region connecting two insulators with different values of Chern number must possess a gap-closing and gap-reopening point somewhere on it – which forms precisely an edge mode. Otherwise, the whole space would be gapped, which by definition means that the Chern number in the whole space would be the same, which does not fulfill the assumptions. This kind of considerations can be applied to any boundary region between two topologically different insulators, as long as the boundary holds the symmetry that protects the bulk-insulating states.

These gapless states, existing at the boundary (edge in 2D, surface in 3D) of a topological insulator, lead to the existence of conducting states with predicted properties unlike any other electronic systems, like a vanishing effective mass and a relativistic (linear) dispersion relation. The effective mass in electronic band in the inverted regime is negative. This is a consequence of the shape of a band, but can also be understood in a relativistic approach. Einstein, in his famous equation, stated that energy is proportional to mass, thus in a system with a negative energy gap the mass should be negative. When the bands tend to join continuously with a positive gap insulator at the boundary, the energy gap and the effective mass switches to positive. The transition has to be smooth, therefore going from negative to positive value at some point the system has to have a gap closure, when the effective mass collapses as well. At this point the particles have to be described by the relativistic equation with a linear dispersion relation [30].

1.2 This Work

At the beginning of this section a history of studies and discoveries related to selected areas of topological insulators will be presented, starting where the previous section finished – at the first discoveries of 2D and 3D topological insulators. The covered areas will deal with the most prominent features of topological insulators and the development of related technology and experimental techniques.

The first paragraph will describe the experiments confirming the properties of the edge channels – like quantized conductance, helicity, lack of dissipation, and spin polarization. The second paragraph will focus on efforts concerning the amplification of the bulk band gap in order to lower its conductivity and to highlight the influence of the edge channels on the total transport properties of a given system. This is related but not limited to the strain engineering, which allows to open the bulk band gap.

Finally, a brief description of phase transitions will be given, which is directly related to the subject of this thesis.

1.2.1 State of the Art

Edge Channels

The discovery of the QHE [4], in which the conductance is quantized, was a surprise to the physical community. This effect occurs in layered metallic structures at high magnetic fields. As a result, conducting one-dimensional channels develop at the edges of the sample. In each of the channels the current flows only in one direction and its conductance is quantized, which is a sign of one-dimensional transport [31]. Moreover, the current flowing through these edge states is resistant to scattering. The value of the quantum Hall conductance is strictly connected to the number of edge channels in the sample. Before the discovery of QSH insulators, the existence of a state exhibiting the quantum Hall conductance was limited to low temperatures and high magnetic field, which was a formidable obstacle to overcome in terms of possible applications.

In the QSH phase the conductance of the edge channels is quantized. The time reversal symmetry requires the edge channels to be helical, which means that electrons with spin up and spin down propagate in opposite directions along the edge of the sample with conserved helicity. As a consequence, carriers on time-reversed paths around a non-magnetic impurity in the helical edge interfere destructively, which results in a zero probability of backscattering. This property was predicted by Murakami *et al.* [32], Kane and Mele [13], and Bernevig *et al.* [18].

A detection of the edge states is an experimentally difficult task. In an ideal QSH phase the current is carried only via the edge states while the bulk is fully resistant. In practice however, the band gap is small, usually a few meV (≈ 4 meV for InAs/GaSb QW [33][34], ≈ 15 meV for HgTe QW [14]). Because of that, assuring the low temperature of measurements is essential in order to prevent thermal excitations of electrons. Moreover, a processing of samples is required – only gated structures have the possibility to tune the chemical potential with enough accuracy into the band gap. Growing the structures where the chemical potential intrinsically lies inside the band gap is a virtually impossible task.

König *et al.* [14] observed for the first time quantized conductance in a HgTe QW in a nontrivial regime, which was the first indication of the existence of the edge channels. Later, in 2009, helicity and dissipationless of the channels was confirmed by studies of a nonlocal transport on multiterminal devices carried out by Roth *et al.* [35] and Büttiker *et al.* [36] (focus paper). However, a direct

evidence of the spin polarization of helical states was still missing.

The existence of the spin polarization of the edge states was confirmed for the first time by Brüne *et al.* [37]. By using specially-designed "H-shaped" HgTe QW-based structures, it was possible to detect the spin polarization of the QSH edge states via the inverse spin Hall effect [38][39]. The investigated structures were in a two-gate configuration, and could be tuned locally from a metallic state into a QSH state, as the carrier concentration in two legs could be adjusted separately. This configuration allowed the metallic state to act as a source of spin-polarized carriers and the QSH state as a detector, and vice-versa.

In the case of InAs/GaSb QWs the situation is more complicated. Except of the quantized channel conductance, there are evidences of a residual bulk conductivity, even at very low (20 mK) temperatures. Knez *et al.*, having studied a set of InAs/GaSb samples with various dimensions and length/width ratios, was able to identify a contribution of the edge channel transport, characterized by a conductance comparable with the expected value. However, the the highest observed resistance was 2-3 times smaller than $\hbar/2e^2$, which can be attributed to the conductivity of the bulk of the order of $10e^2/\hbar$ [40]. Theoretical investigations of Naveh and Laikhtman [41] concluded, that even a finite-level broadening due to the carrier scattering could result in non-zero conductivity, even at $T = 0$.

Later, in 2011, Knez *et al.* remarked that edge modes persist alongside the conductive bulk and show only a weak magnetic field dependence. This decoupling of the edge from the bulk is a direct result of the gap opening, which takes place away from a center of the Brillouin zone and, as a consequence, there is a large disparity in Fermi vectors between bulk and edge states. This leads to a qualitatively different QSHI phase than in the case of a HgTe/CdTe QW, in which the gap opens at the center of the zone [42]. By performing magnetotransport measurements, Knez concluded that despite the fact that conductive bulk allows edge electrons to tunnel from one side to another, the probability of this effect to occur is reduced by a large Fermi wave vector mismatch. The probability of scattering of electrons between the edges is increased if a weak disorder or scattering interactions are taken into account. In a theoretical work Zhou *et al.* [43] found that the edge states on the two sides can couple together to produce a gap in the spectrum. As a result, the single electron elastic backscattering of the edge states is no longer forbidden, and the edge states are not protected completely by the time-reversal symmetry.

Up to that moment, because of the strong bulk influence in electron transport, all the evidences of the quantized edge channels were indirect and unclear. A proposed solution to this problem was to change the transport properties of the bulk, while preserving the conductance of the edge states. There have been several methods applied so far. Suzuki *et al.* [44] performed a systematic study on a set of specially designed six-terminal small Hall devices with a doping layer of beryllium in the QW barrier. The doping allowed to lower the carrier concentration and place the Fermi level closer to the energy gap. As a result, it was possible to tailor the structure to exhibit conducting edge channels while maintaining the gap in the bulk region. Du *et al.* [45] implemented a Si doping directly in the QW, at the interface of InAs and GaSb layer. Silicon acts as a donor in InAs and acceptor in GaSb, inducing a disorder in the structure. Generally, a disorder reduces transport properties of a structure. However, the edge states are topologically protected in nature, therefore the disorder has a small impact on their existence and transport properties. As a result, the carrier mobility in the bulk is greatly reduced. This idea was followed by Knez *et al.* [46], who studied InAs/GaSb QWs in a disordered regime. A similar concept to suppress the bulk conductivity was implemented by Charpentier *et al.* [47]. However, his idea was to use a gallium source with impurities, which has a

direct influence on the transport properties of a structure. He compared two sources of gallium and obtained drastically different results in terms of mobility. The sample grown using "low mobility" gallium had more than one order of magnitude lower mobility than the sample grown using "high mobility" gallium.

A remarkable evidence of the edge channels was provided in 2013 at Stanford by a use of a micrometer SQUID (Superconducting Quantum Interference Device) loop [48] to directly image the current density in a HgTe QW [49] and in 2014 InAs/GaSb BGQW [50]. It was shown that the current in the sample flows via the edge states only if the structure is in an inverted regime, which is presented in Figure 1.3 for the case of an InAs/GaSb system. The edge conductivity persisted despite the fact that the sample was much bigger than the ballistic limit (around $2 \mu\text{m}$ [42]), even at higher temperatures (up to 30 K).

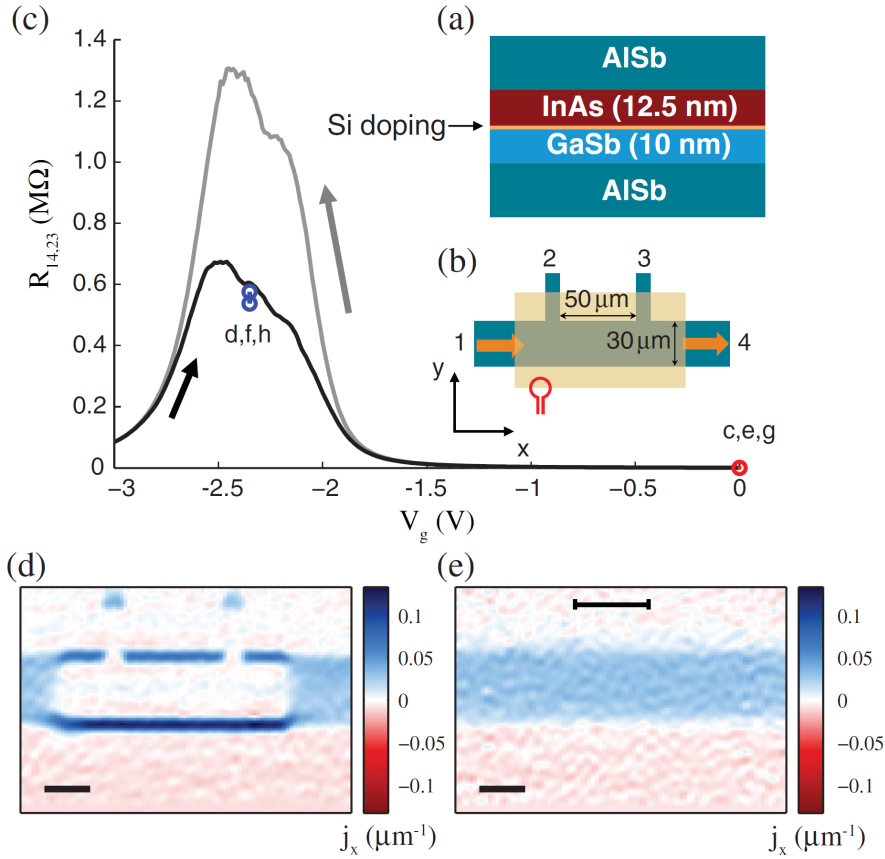


Figure 1.3: Flux and current maps in a four-terminal device made from a Si-doped InAs/GaSb quantum well. **Panel (a)**: Schematic of the device. Si doping (shown in orange) suppresses the residual bulk conductance in the gap. **Panel (b)**: Schematic of the measurement. Alternating current (orange arrows) flows from the left to the right on the positive part of the cycle. A voltage (V_g) applied to the front gate (yellow box) tunes the Fermi level. The SQUID's pickup loop (red circle) scans across the sample surface, with a lock-in detection of the flux through the pickup loop from the out of plane magnetic field produced by the applied current. **Panel (c)**: Four-terminal resistance $R_{14,23} = V_{23}/I_{14}$ as a function of V_g , showing both the upwards (black) and downwards (gray) gate sweeps. $R_{14,23}$ is maximized when the chemical potential is tuned into the gap. **Panel (c, d)**: Flux images for the sample tuned into (d) the bulk gap, $V_g = -2.35 \text{ V}$, and (e) the n-type regime, $V_g = 0 \text{ V}$. The image comes from the work of Spanton et al. [50].

Strain Engineering

Despite the numerous efforts in increasing of the bulk resistivity, the residual conductivity persists even at low temperatures. This limits a possibility to observe the special properties of the edge channels only to cryogenic temperatures for both HgTe/CdTe and InAs/GaSb QW systems. The energy gap in the case of HgTe/CdTe is around three times larger than in InAs/GaSb, which puts it in a privileged position, as the influence of the bulk on the sample conductance can be neglected at low temperatures [14].

In order to decrease the bulk conductivity (by enlarging the band gap) an implementation of a strain engineering was proposed. A band gap in InAs/GaSb originates from a hybridization of electron and hole levels. However, a strength of this effect strongly depends on an overlapping of electron and hole wave functions. Electrons and holes exist in separate layers, thus a spatial separation reduces the overlapping and the hybridization gap as a consequence. The overlapping can be improved by making the layers thinner, however it can be done only up to a point where the structure has an inverted band ordering. Further decrease of thickness of the layers results in a normal band ordering.

One of the possible solutions to this issue was proposed [51] by Smith and Maihot in 1987. They studied inverted InAs/GaSb superlattices for infrared detectors. They implemented a strain in the structure by alloying GaSb with InSb (which has lattice constant around 6.4 Å). The strain in a growth plane shifts an energy of the conduction band in InAs downwards, while an energy of the valence band in InGaSb splits into a heavy hole level and a light hole level. The energy of heavy hole level is higher than the original top of the valence band in pure GaSb. As a consequence, the InAs/InGaSb structures can be grown thinner to achieve the stronger overlapping of the bands, while maintaining the same (inverted) energy structure.

This idea was implemented and further developed by Du *et al.* [52]. An investigation of samples based on InAs/In_xGa_{1-x}Sb with $x = 0.25$ allowed to induce an enhanced interaction of wave functions of electrons and holes, which resulted in an increase of the hybridization gap from around 4 meV up to even 12 meV. The crystalline structure remained coherent across the heterostructure interfaces despite the 1.2 % in-plane strain. As a consequence, transport measurements revealed for the first time an existence of a truly insulating hybridization gap at low temperature [52]. A similar investigation was carried out by Akiho *et al.* [53], who used structure with $x = 0.25$ indium content as well but different thicknesses of the layers, and obtained a similar increase of a hybridization gap, estimated to be equal to 10.8 meV. Akiho also presented calculations for different indium contents, and claimed that it is possible to increase the hybridization gap even more, up to 25 meV, for $x = 0.25$ [53], by inducing a 2.45 % strain.

Strained HgCdTe layers

The studies conducted in 1985 by Volkov and Pankratov [54] on strained HgTe/CdTe quantum wells revealed an increase of energy gap and an emergence of the interface states which lie within the gap. Bernevig, Hughes, and Zhang [17], as well as Fu and Kane [28] identified the strained HgTe films as a 3D topological insulators. Shortly after, Dai *et al.* [55] published results of numerical calculations supporting the existence of boundary states in a strained HgTe film. These findings were followed by ARPES measurements [37] [56], reporting an observation of the surface states and an opening of the gap between the light-hole and the heavy-hole bands.

A standard approach to the strain engineering of HgTe involves a use of MBE grown substrates based on pure CdTe and Cd_{0.96}Zn_{0.04}Te. Both of those materials have the lattice constants larger than HgTe, which results in a tensile strain in the epilayers. Under such conditions, the largest gap

achieved are $E_g = 17$ meV and 25 meV for QWs grown on CdTe and $\text{Cd}_{0.96}\text{Zn}_{0.04}\text{Te}$, respectively [57]. In order to obtain a larger gap, a stronger strain is required. However, highly strained structures often suffer from a low crystal quality.

The idea to deal with this problem, implemented by Leubner [58] *et al.*, was to use strained-layer superlattices based on CdTe- $\text{Cd}_{0.5}\text{Zn}_{0.5}\text{Te}$. These superlattices, grown on GaAs substrate, provided a straightforward control of the strain in the following HgTe layers. This allowed to apply a tensile or compressive strain at will. Out of three samples studied by Leubner, two had almost the same thickness (≈ 15 nm, which is well within the inverted regime), but due to the strain their properties differ significantly. The third one was grown thinner (≈ 7.5 nm) and with a different composition of barriers. The comparison of the samples characterized by a similar thickness revealed that the strain in the layers primarily affects a shape of the valence band. The tensile strain induced an overlap of the valence band and the conduction band, which resulted in a phase transition from a topological insulator to a topological semimetal. At the same time the sample with compressive strain remained a topological insulator with an enlarged band gap up to 17 meV. The band gap in the third sample, characterized by even stronger compressive strain, was enlarged up to 55 meV, which is well above the thermal energy at the room temperature (≈ 26 meV at 300 K) [58].

Topological phase transitions

Phase transitions give a special possibility to study the topological states of matter, as they grant a direct access to the physics occurring in both phases and give a clear evidence of the differences between them. The study of phase transitions in topological insulators began with a theoretical work of Bernevig [17] *et al.*, as he proposed that HgTe/CdTe QW can be tuned via a topological transition from a nontrivial phase to a trivial one, just by varying the QW width. The idea is presented in Figure 1.4. The edge channels with well defined conductivity appear only if the system is in an inverted band gap regime, which takes place for a specific range of QW widths. At the critical thickness the phase transition occurs, and the system changes its phase to a semiconducting with a positive band gap. This transition causes the edge channels to vanish.

However, long before that, in the early sixties, there were many works devoted to studies of an inverted band structure of bulk HgCdTe systems and its properties. Even back then it was realized that by varying the chemical composition of the structure, mainly the cadmium content, it is possible to change the band order of the system from semimetallic (for low Cd content) to semiconducting (for high Cd content). This subject will be broader discussed in Chapter 3. There are more systems, which can exhibit a phase transition driven by a variation of a chemical composition, like topological crystalline insulators $\text{Pb}_{1-x}\text{Sn}_x\text{Te}$ or $(\text{Pb}_{1-x}\text{Sn}_x\text{Se})$, which were studied by ARPES measurements by Xu *et al.* [59], and by magnetooptics by Assaf *et al.* [60] and Phuphachong *et al.* [61] from Guldner's group.

Phase transitions can be induced not only by a strain and a change of a layer thickness and/or chemical composition. There are far more factors like electric and magnetic field, temperature, pressure, etc. Some of them will be described in this thesis. Recently, there have been multiple ideas to induce and investigate topological phase transitions. One of the most important is to use temperature as an external parameter driving the HgTe/CdTe QW from a topological insulator phase to a semiconductor phase by studying electrical properties in both phases [62].

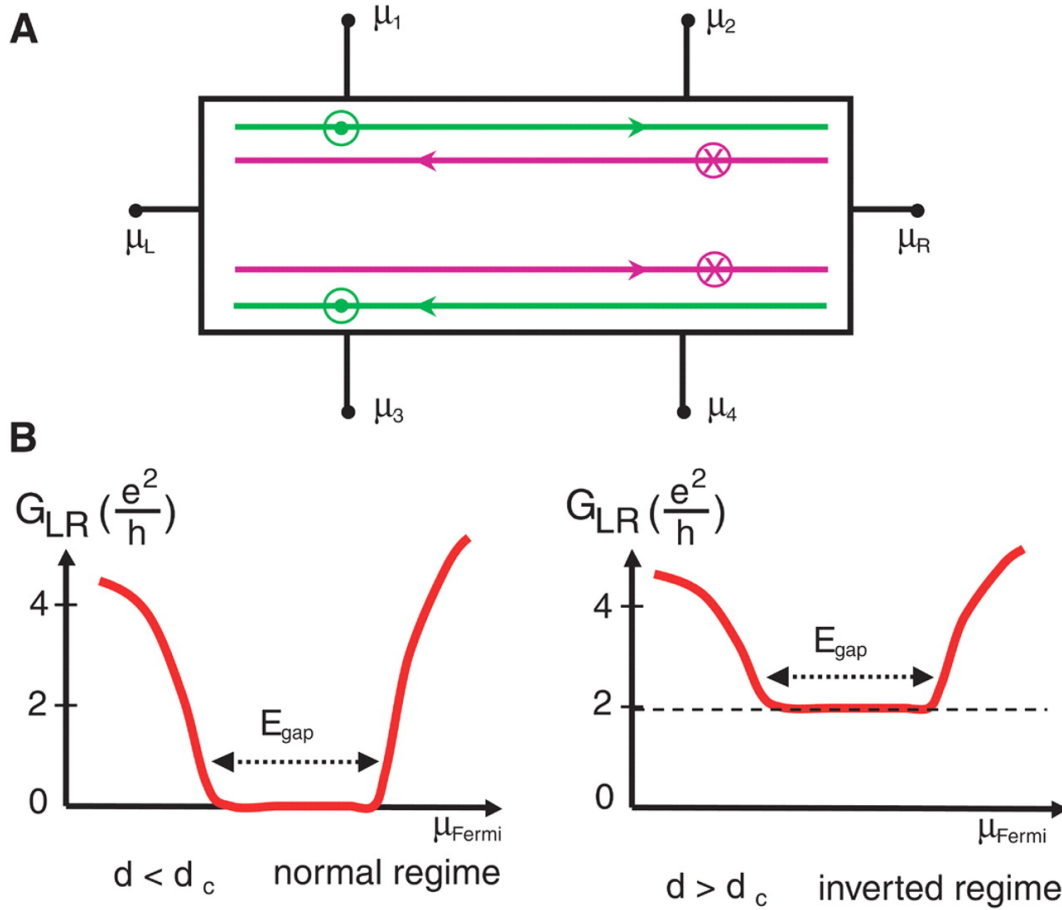


Figure 1.4: **Panel A)** Experimental setup of a six-terminal Hall bar showing pairs of edge states, with spin-up states in green and spin-down states in purple. **Panel B)** A two-terminal measurement on a Hall bar would give G_{LR} close to $2e^2/h$ contact conductance on the QSH side of the transition and zero on the insulating side. In a six-terminal measurement, the longitudinal voltage drops $\mu_2 - \mu_1$ and $\mu_4 - \mu_3$ vanishes on the QSH side with a power law as the zero temperature limit is approached. The spin Hall conductance has a plateau with the value close to $2e^2/h$. The image comes from the work of Bernevig, Hughes, and Zhang [17].

1.2.2 Scope of this Thesis

The principle idea behind this thesis is to demonstrate the possibility to investigate the topological insulators and other narrow-gap semiconductors/semimetals by the means of THz spectroscopy. The systems under the scope of this work are composed of three kinds of mercury-cadmium-telluride heterostructures, which were chosen accordingly to expose some of the topological properties described before.

Chapter 2 is divided into two parts. The first part introduces the actual methods of investigation. It starts with an overview of the interactions of matter with light through the absorption coefficient. It is explained that the Fermi Golden Rule and optical joint density of states are crucial for understanding of the mechanism of absorption. The density of states for systems with parabolic and linear dispersion relation is calculated, as well as its dependence on magnetic field. The second part is where the experimental set-up is described and the general principles of the Fourier spectroscopy are briefly explained with an insight how to read and interpret the results.

Chapter 3 presents the first investigated system – a set of two genuine HgCdTe bulk samples

with thickness of few microns. One of the samples is a positive gap, thus is a regular semiconductor. The other is semimetallic at low temperatures and undergoes a temperature induced semimetal-to-semiconductor phase transition. In this chapter an evolution of the band structures of the both samples is presented, and a special attention is put on the point of phase transition, in which the quasi-relativistic Kane fermions arise.

Chapter 4 is divided into two parts. The first part (4.1) gives the details about the second investigated systems – a set of two HgTe/CdTe QWs with thickness close to the critical, and are referred to as narrow QWs (or simply QWs). These QWs were grown having a well-chosen set of parameters in order to investigate the possibility to observe a temperature induced topological insulator-to-semiconductor phase transition. Again one of the samples is used as a reference and has a positive band gap at the whole temperature range, while the other undergoes a topological phase transition at the critical temperature, characterized by an appearance of the Dirac fermions.

The second part (4.2) overviews the third of investigated systems – a set of three HgTe thick QWs (or films) with different thicknesses above the critical. The films were grown with a strain, which opened the bulk band gap. In this way a semimetallic structure becomes a topological insulator. The thicknesses of the samples are between 15 nm and 50 nm, which means that these systems are in the intermediate state between QW and bulk – are referred to as 3D systems by the literature, however a quantum confinement is still present. These systems give a special opportunity to investigate the physics of HgTe/CdTe interface states, and their possible coupling with bulk states.

At the end, a brief summary with a conclusion and some perspectives and ideas for future work are presented. Some of which are related to another solid state system, which was identified as a 2D topological insulator – an InAs/GaSb QW. An overview and the first experimental results obtained on this system are presented in Appendix A.

Chapter 2

Optical Properties of Matter

In this chapter the principal properties of matter, related to optical phenomena, are presented. From the point of view of spectroscopy, an interaction between light and solid state systems is crucial. This chapter explains the mechanism of an absorption of light inside a solid state system via optical transitions, which is based on two pieces. The first piece depends on a probability of transition, while the second is based on an optical joint density of states, and its dependence on external conditions like temperature and magnetic field.

The chapter starts with an introduction of an absorption coefficient via the electromagnetic wave equation. Later, a probability (also called rate or strength) of an optical transition is explained via a perturbation Hamiltonian. This probability, related to the Fermi Golden rule, is based on an interaction of quantum states taking part in transitions.

Further, the density of states for all-dimensional systems is presented for linear and parabolic electronic dispersion relations, and is explained how does it change while magnetic field is applied. All the concepts in this chapter are presented in a rather qualitative way, under two assumptions. The first assumption is that all the transitions are direct – they take place at $\mathbf{k} = 0$, which is valid since the momentum of a photon is negligible in comparison to the momentum of an electron. The second assumption is that the fields of an electromagnetic wave are small, therefore the calculations require only terms linear with \vec{E} and \vec{B} . This assumption is valid, because the only sources of light intense enough to be considered in terms of the nonlinear optics are the strongest lasers, usually working in a pulse mode, which are not in the scope of this work.

2.1 Review of Fundamental Relations for Optical Phenomena

The absorption spectroscopy allows to investigate an energy band structure, impurity levels, lattice vibrations, excitons, localized defects and many more. The studies are based on measuring certain quantities, which manifest themselves via an interaction of light with matter. The most important quantities are the dielectric function $\varepsilon(\omega)$ and the optical conductivity $\sigma(\omega)$, which are directly related to the energy structure of solids.

2.1.1 The Dielectric Function and Optical Conductivity

The wave equation for electromagnetic waves can be derived from the basic equations of electromagnetism – the Maxwell's equations. The equations are characterized by two very basic constants,

representing electrical permittivity ε and magnetic permeability μ . The wave equation for electric field resembles:

$$\nabla^2 \vec{E} = \frac{\varepsilon\mu}{c^2} \frac{\partial^2 \vec{E}}{\partial t^2} + \frac{4\pi\sigma\mu}{c^2} \frac{\partial \vec{E}}{\partial t}, \quad (2.1)$$

where σ represents the electrical conductivity of space.

In the vacuum, where $\mu = 1$, $\varepsilon = 1$, and $\sigma = 0$, the electromagnetic wave propagates freely and infinitely. However, if the electrical conductivity of the medium is finite, the behavior of the wave is governed by the coefficient of refraction in form:

$$N = \sqrt{\mu\varepsilon_c} = \sqrt{\mu\varepsilon \left(1 + \frac{4\pi i\sigma}{\varepsilon\omega}\right)} = \tilde{n}(\omega) + i\tilde{k}(\omega), \quad (2.2)$$

where \tilde{n} and \tilde{k} are real and imaginary parts of the coefficient of refraction. The coefficient \tilde{k} is responsible for an exponential decay of an amplitude of the wave, thus it is often called the extinction coefficient. It can be related with the absorption coefficient via a relation

$$\alpha(\omega) = \frac{2\omega}{c} \tilde{k}(\omega). \quad (2.3)$$

The absorption coefficient depends on a frequency of the light. It is responsible for energy dissipation of the wave inside a solid. The rate of decay is strongly related to the properties of medium μ , ε , and σ , which is reflected in the band structure, carrier density, etc.

The absorption coefficient takes different values for different optical processes. The full description of dispersion of absorption coefficient in solids can be found in the book of Dresselhaus [63]. The dominant processes described in this thesis are direct optical transitions. In this case the absorption coefficient can be written as

$$\alpha(\omega) = \frac{\hbar\omega \times \text{numer of transitions/unit volume/unit time}}{\text{incident electromagnetic flux}}. \quad (2.4)$$

The denominator in Equation 2.4 (incident electromagnetic flux) can be calculated from the Poynting vector and is proportional to ω^2 . The numerator of the Equation is related with the probability of transition, which is governed by the quantum-mechanical transition rate and the joint density of states. This means that the effective absorption coefficient for optical transitions can be expressed as:

$$\alpha(\omega) \propto \frac{1}{\omega} \times \text{DOS}(\omega), \quad (2.5)$$

where DOS is the density of states.

2.1.2 Probability of Absorption

The absorption of light in a semiconductor can be described classically in the terms of the Beer-Lambert's law. It states that if a beam of light of given intensity I_0 penetrates a surface of a solid, then an intensity of the light decreases with the penetration depth z as

$$I(z) = I_0 e^{-\alpha(\omega)z}, \quad (2.6)$$

where α is an absorption coefficient of a solid. The absorption coefficient is closely related to a quantum-mechanical transition rate W_{if} given by the Fermi Golden Rule. The Fermi Golden Rule expresses the probability per unit time that a photon of energy $\hbar\omega$ excites an electron from an initial state $|\psi_i\rangle$ to a final state $|\psi_f\rangle$:

$$W_{if} = \frac{2\pi}{\hbar} |\langle \psi_f | \mathcal{H}'_{if} | \psi_i \rangle|^2 \rho(\hbar\omega). \quad (2.7)$$

In this expression, the matrix element \mathcal{H}'_{if} corresponds to an external optical perturbation, and $\rho(\hbar\omega)$ expresses the joint density of states (DOS) function describing a density of states associated with an energy of the excitation photon ($E = \hbar\omega$).

The derivation of perturbation Hamiltonian \mathcal{H}'_{if} starts with a standard one-electron Hamiltonian without magnetic field, which takes form of:

$$\mathcal{H}_0 = \frac{p^2}{2m} + V(\vec{r}), \quad (2.8)$$

where $V(\vec{r})$ is a scalar periodic potential. The momentum is replaced by a term $i\vec{\nabla}$, and in the effective mass approximation the periodic potential is replaced by the effective mass m^* .

The single electron Hamiltonian in the presence of magnetic field changes via a substitution $\vec{p} \rightarrow \vec{p} - (e/c)\vec{A}$, thus the full form of Hamiltonian is the following

$$\mathcal{H}_B = \frac{1}{2m} \left(\vec{p} - \frac{e}{c}\vec{A} \right)^2 + V(\vec{r}) = \underbrace{\frac{p^2}{2m} + V(\vec{r})}_{\mathcal{H}_0} - \underbrace{\frac{e}{mc}\vec{A} \cdot \vec{p} + \frac{e^2 A^2}{2mc^2}}_{\text{perturbation}}, \quad (2.9)$$

where the first part resembles the Hamiltonian \mathcal{H}_0 from Equation 2.8, and the second is a perturbation. The optical fields are usually very weak in comparison with fields inside a crystal, thus in a good approximation only the term linear with \vec{A} remains. The expression for the perturbation Hamiltonian is

$$\mathcal{H}' = -\frac{e}{mc}\vec{A} \cdot \vec{p} + \frac{e^2 A^2}{2mc^2} \approx -\frac{e}{mc}\vec{A} \cdot \vec{p}. \quad (2.10)$$

The matrix element, $\langle \psi_f | \mathcal{H}' | \psi_i \rangle$ expressing the coupling of the initial and final states through the optical fields, determines the strength of optical transitions, which depends on the electromagnetic field perturbation \mathcal{H}' .

2.2 Density of States and Optical Transitions

The standard density of states can be quickly derived assuming Born-Karman's periodic boundary conditions for the Bloch functions describing electronic states of a finite periodic crystal lattice. Assuming that the states in the reciprocal space are evenly distributed, and considering the electron spin degeneracy, the \mathbf{k} -space density of states takes form of

$$\rho_{3D}(k) = \frac{2}{(2\pi)^3}, \quad \rho_{2D}(k) = \frac{2}{(2\pi)^2}, \quad \rho_{1D}(k) = \frac{2}{2\pi}, \quad (2.11)$$

for three, two, and one dimensions, respectively. This function describes the momentum-dependent density of states per volume (surface) unit of the reciprocal space of a finite crystal. Knowing that the DOS function is related to the amount of energy states per unit of energy $\rho(E) = dN/dE$, a relation to the reciprocal space can be found by

$$\rho(E) = \frac{dN}{dE} = \frac{dN}{dk} \frac{dk}{dE}, \quad (2.12)$$

where $dN = \rho_D(k)dV_k$. The DOS function $\rho_D(k)$ and an element of volume in \mathbf{k} -space dV_k have to take forms of a proper dimension. Now only a dispersion relation $E(k)$ is needed to calculate the energy-dependent DOS function. Two cases of an energy dispersion relation will be described – parabolic and linear.

2.2.1 Density of States in Parabolic Bands

In the case of parabolic bands and in the effective mass approximation the dispersion relation takes form of:

$$E(k) = \frac{\hbar^2 k^2}{2m^*}, \quad (2.13)$$

thus

$$\frac{dk}{dE} = \frac{m^*}{\hbar^2} \frac{1}{k}. \quad (2.14)$$

If the element of volume dV_k is equal to the difference of volumes of two balls (in 3D) or two discs (in 2D) with radii $k + dk$ and k , then the amount of states in the element of volume can be expressed as:

$$\begin{aligned} dN_{3D} &= \rho_{3D}(k)dV_k = \frac{2}{(2\pi)^3} \cdot 4\pi k^2 dk, \\ dN_{2D} &= \rho_{2D}(k)dV_k = \frac{2}{(2\pi)^2} \cdot 2\pi k dk, \\ dN_{1D} &= \rho_{1D}(k)dV_k = \frac{2}{2\pi} \cdot dk. \end{aligned} \quad (2.15)$$

Substituting Equations 2.14 and 2.15 into Equation 2.13 gives the DOS function per unit energy for parabolic bands for 3, 2, and 1 dimensions:

$$\rho_{3D}(E) = \frac{1}{2\pi^2} \left(\frac{2m^*}{\hbar^2} \right)^{\frac{3}{2}} E^{\frac{1}{2}}, \quad (2.16)$$

$$\rho_{2D}(E) = \frac{m^*}{\pi\hbar^2} \sum_i \Theta(E - E_i), \quad (2.17)$$

$$\rho_{1D}(E) = \frac{1}{\pi} \left(\frac{m^*}{\hbar^2} \right)^{\frac{1}{2}} \sum_i \frac{\Theta(E - E_i)}{\sqrt{(E - E_i)}}, \quad (2.18)$$

where $\Theta(E - E_i)$ is the Heaviside function, equals 1 if $E > E_i$, and the summation is over the electronic energy states i . The plot of DOS as a function of energy is shown in Figure 2.1.

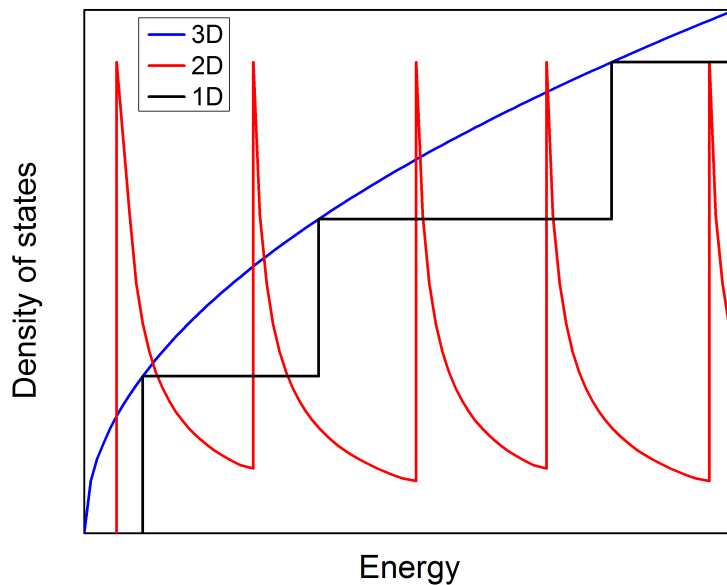


Figure 2.1: *Density of states function of 3D (blue curve), 2D (black curve), and 1D (red curve) systems.*

2.2.2 Density of States in Linear Bands

In the case of linear band the dispersion relation takes form of:

$$E(\vec{k}) = \hbar v_f \vec{k}, \quad (2.19)$$

thus

$$\frac{dk}{dE} = \frac{1}{\hbar v_f}. \quad (2.20)$$

The dispersion relation does not influence the element of volume dV_k , therefore the DOS function per unit energy for linear bands for 3, 2, and 1 dimensions:

$$\rho_{3D}(E) = \frac{E^2}{\hbar^3 v_f^3 \pi^2}, \quad (2.21)$$

$$\rho_{2D}(E) = \frac{E}{\hbar^2 v_f^2 \pi}, \quad (2.22)$$

$$\rho_{1D}(E) = \frac{2}{\hbar v_f \pi}, \quad (2.23)$$

Optical Joint Density of States

Not all states take part in an optical transition. The conservation of energy requires that a difference of energies of available states has to be equal to the energy of an exciting photon $\hbar\omega$. This requires a modification of the calculated DOS functions 2.16 by substituting E by a term $\hbar\omega - \Delta E$, where ΔE is a difference of energy between the final and the initial states. Because of that, the function $\rho_j(E)$ was named *optical joint density of states*, and for the case of the 3D parabolic band it takes form of:

$$\rho_j(\omega) = \frac{1}{2\pi^2} \left(\frac{2m^*}{\hbar^2} \right)^{(3/2)} (\hbar\omega - \Delta E)^{\frac{1}{2}}. \quad (2.24)$$

The only energy range, where the physical solutions of Equation 2.24 exist, requires that $\hbar\omega \geq \Delta E$.

2.2.3 Optical Transitions

The process called interband optical transition is based on an absorption of a photon by an electron, which results in an excitation of an electron into a different energy band. There are also intraband transitions, which take place between levels of a single band. This however requires splitting of the band into subbands, which can be stimulated, for example, by magnetic field or a quantum confinement.

There are few rules, which optical transitions have to obey:

- There is a threshold energy, related to the difference of energies of the initial and final states. Obviously, photons carrying lower energies than this threshold are not absorbed as there are no final states available for the electrons to be excited to. The photons carrying higher energy may or may not be absorbed, depending on the internal band structure and allowed relaxation processes in the system.
- The transitions are either direct or indirect. The conservation of momentum yields that $\vec{k}_v = \vec{k}_c \pm \vec{k}_{\hbar\omega}$. The momentum of a photon $\vec{k}_{\hbar\omega}$ is few orders of magnitude smaller than the dimensions of the Brillouin zone, thus $\vec{k}_{\hbar\omega}$ can be neglected, rendering $\vec{k}_v \approx \vec{k}_c$. However, the transition can still be indirect if a phonon is involved. Nevertheless this is a three-body process thus its probability is much lower than the probability of a direct transition.

- A transition occurs of course from an occupied initial state into an empty final state. If the final state is occupied, due to the Pauli Exclusion Principle, the process cannot take place. Similarly, if the initial state is empty, there is no electron to absorb a photon and the transition does not occur.

2.2.4 Density of States in Magnetic Field

The presence of magnetic field causes changes in the movement of electrons in a solid, forcing the energy bands to split into a set of levels. Without the magnetic field all the states in k -space are distributed evenly. If the magnetic field is applied in the z -direction, only the states in the x, y plane are affected, as they lie in a perpendicular plane to B . An application of magnetic field acts as a form of quantum confinement, creating an additional quantization of energy and momentum states. This limits the available states in k -space to concentric rings (in 2D) or tubes (in 3D) with $\mathbf{k} = 0$ in the center.

To calculate the available energy states for electrons with a parabolic dispersion in magnetic field the two-dimensional Hamiltonian can be used:

$$\mathcal{H} = \frac{\hat{\mathbf{P}}^2}{2m}. \quad (2.25)$$

The canonical momentum $\hat{\mathbf{P}}$ is

$$\hat{\mathbf{P}} = \frac{\hbar}{i}\nabla + \frac{e}{c}\mathbf{A}. \quad (2.26)$$

The magnetic potential is, assuming the Landau gauge, expressed as $\mathbf{A} = (0, Bx, 0)$. The Schrödinger equation takes form:

$$\mathcal{H}\psi(\vec{r}) = \frac{\hbar^2}{2m} \left[-\nabla_x^2 + \left(\frac{1}{i}\nabla_y - \frac{eB}{\hbar c}x \right)^2 \right] \psi(\vec{r}) = E\psi(\vec{r}). \quad (2.27)$$

The choice of gauge grants that the Hamiltonian is independent of y , thus x, y wave functions can be separated:

$$\psi(x, y) = e^{iky}\phi(x). \quad (2.28)$$

Moreover, by separating the wave functions, the result is a one-dimensional Schrödinger equation $\mathcal{H}_x\phi(x) = E\phi(x)$, with the effective Hamiltonian:

$$\mathcal{H}_x = \frac{\hbar^2}{2m} [-\nabla_x^2 + (x - x_k)^2]. \quad (2.29)$$

This Hamiltonian expresses a one-dimensional harmonic oscillator centered at $x_k = l_B^2 k$, where $l_B = \sqrt{\frac{\hbar c}{eB}}$ is the magnetic length. Its solution is a set of equidistant energy levels, called Landau Levels (LLs), which energy can be described by:

$$E_n = \hbar\omega_c \left(n + \frac{1}{2} \right), \quad (2.30)$$

where $\omega_c = \frac{eB_z}{m_c^*}$ is the cyclotron frequency, and $n = 0, 1, 2, \dots$ is an integer quantum number corresponding to different LLs. The Equation 2.30 is valid for a 2D system. In a 3D case the energy of LLs takes form $E_{n,z} = E_n + E(z) = \hbar\omega_c \left(n + \frac{1}{2} \right) + E(z)$.

The amount of independent states in a system of dimensions $L_x \times L_y$ can be estimated using boundary conditions for the function ψ (Equation 2.28) in the y -direction:

$$k = \frac{2\pi}{L_y}m_y, \quad (2.31)$$

for any integer m_y . This means that the allowed values of x_k are separated by $\Delta x = l_B^2 \Delta k = 2\pi l_B^2 / L_y$. If $L_y \gg l_B$, which is not the case only for 1D systems, then $\Delta x \ll l_B$ so the energy separation of successive states is much smaller than their width. The total number of states is equal to $(L_x L_y) / 2\pi l_B^2$ and each LL has $1 / (2\pi l_B^2)$ states per unit area. It is convenient to introduce a quantity, which is related to the way how electrons occupy the LLs, called filling factor ν . The filling factor takes only integer values and describes the amount of occupied LLs. It is closely related with conductivity in plateau of the QHE $\sigma_{xy} = \nu e^2 / h$, and can be expressed as

$$\nu(B) = \frac{n_e h}{B e}, \quad (2.32)$$

where n_e is the electron concentration. The filling factor expresses the amount of occupied LLs at given magnetic field.

Selection Rules

If the magnetic field is applied to a sample, optical transitions have to follow a selection rules, described separately for the Faraday and the Voigt configurations. In the Faraday configuration the magnetic field vector is parallel to the direction of incident light, which is usually along growth direction and the z -axis. In the Voigt configuration the magnetic field vector is perpendicular to the direction of incident light. Only the Faraday configuration is relevant concerning this work, therefore in all calculations and descriptions involving magnetic field it can be assumed that magnetic field is applied along the z direction.

In the Faraday configuration, in case of an unpolarized light, the optical transitions can be executed only between adjacent ($\Delta n = \pm 1$) LLs, characterized by the same spin orientation. This is a consequence of the law of angular momentum conservation. The photons are characterized by \pm angular momentum, which becomes transferred to electrons, as the absorption occurs.

Density of States in Magnetic Field

Magnetic field influences the 3D allowed states only in a plane perpendicular (k_x, k_y) to the applied magnetic field direction (z). This results in a collapse of DOS function of k -space into a set of concentric tubes parallel to \vec{B} . It transforms the DOS as presented in Figure 2.2.

In 2D case the quantization in z -direction is provided by the quantum well, therefore the allowed energy states are fully quantized. This results in an appearance of a distinct LL ladder of states in form of delta functions. However, in real-life systems those levels are broaden due to the scattering effects. In systems with parabolic dispersion relation the LLs are equidistant in energy, as states Equation 2.30. In systems with linear dispersion of bands, the energy difference of LLs has a \sqrt{B} -like dependence. Figure 2.3 presents the DOS(E) function for a case of graphene at $B = 5$ T. The LLs in forms of broadened delta functions are visible, and the levels are not equidistant.

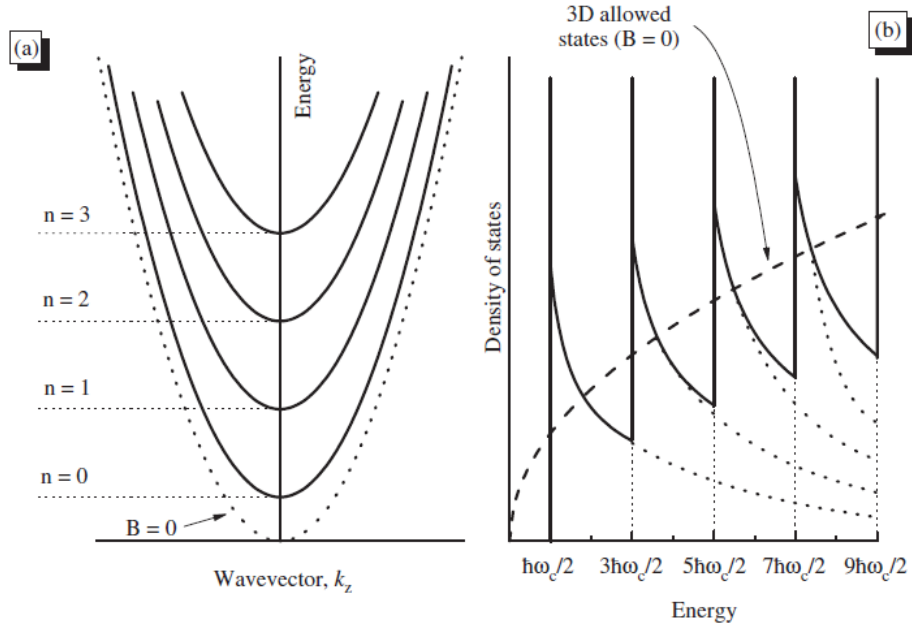


Figure 2.2: **Panel (a)** Electron energy bands for a 3D solid as a function of the z -direction wave vector for different Landau levels ($n = 0, 1, 2, \dots$). **Panel (b)** density of states function for the Landau levels compared with the free electron gas for the case $B = 0$. The image comes from the work of Martinez et al. [64].

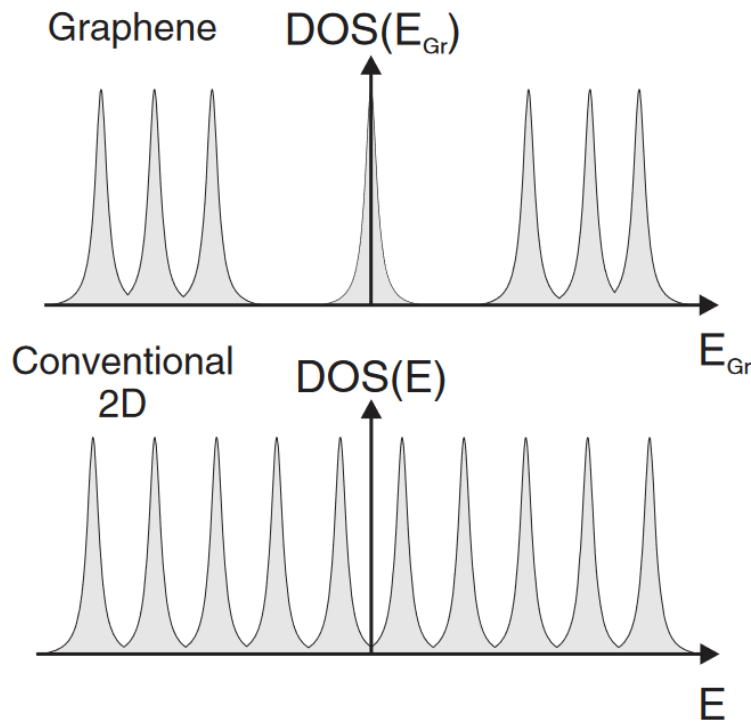


Figure 2.3: Sequence of Landau levels in graphene is unique; the energy spacing depends on the magnetic field as $\Delta E_{LL} \propto \sqrt{B}$, instead of $\Delta E_{LL} \propto B$ as in conventional 2D systems and there exists a LL at $E = 0$, shared equally by electrons and holes. The image comes from the work of Belluci and Onorato [65].

2.2.5 Fermi Level

From the point of view of the optical properties of a solid, the Fermi Golden Rule (Equation 2.7) describes only the strength (or probability) of transitions between two states. However, if a transition is to be executed, the initial state has to be occupied by an electron, which can be excited by a photon. Moreover, the final state has to be unoccupied, as the Pauli exclusion principle forbids two electron to occupy the same quantum state.

The total concentration of electron in a solid has to be distributed on available states. This distribution is governed by two factors – the DOS function (Equation 2.12) and, as the electrons are fermions, the Fermi-Dirac distribution:

$$f(E) = \frac{1}{1 + \exp\left(\frac{E-\mu}{k_B T}\right)}, \quad (2.33)$$

where μ is the chemical potential, and k_B is Boltzmann's constant. The chemical potential is equal to the Fermi energy at $T = 0$ K.

2.2.5.1 Temperature Effects

As stated in Equation 2.33, the Fermi distribution depends on temperature. For $T = 0$ K it resembles a step function – all states below the Fermi level are occupied with probability 1, and all states above are completely empty, as presented in Figure 2.4 (black curve). As the temperature increases, the Fermi distribution gets smoother – the population of electron states of energy above E_f increases at the expense of electron states of energy below E_f . This effect has a profound consequences concerning the optical properties of a solid, as they vary with a change of temperature.

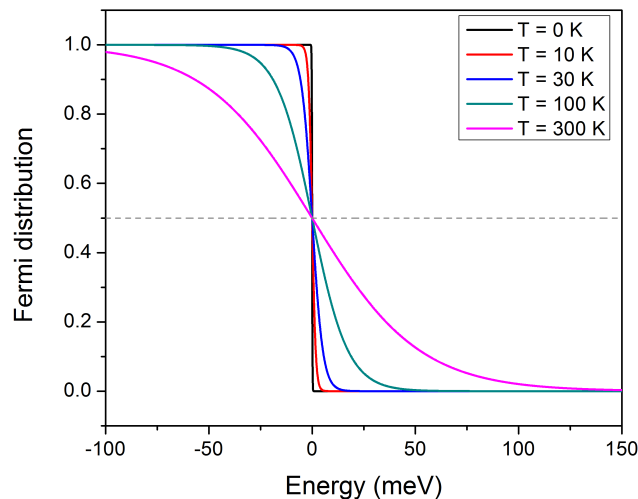


Figure 2.4: *Fermi distribution for various temperatures in range $0K \leq T \leq 300K$. The Fermi level $E_f = 0$ meV. The horizontal grey dashed line marks the probability 0.5.*

At the beginning of this section (2.2.5) a concept of Fermi level and electron distribution was given. The way how the electrons are distributed on the bands is crucial for the shape of an absorption spectra. This means that even if the given transition's strength is high, and there are sufficient electron states

related to the transition (which is governed by the joint density of states), the transition might not occur, unless the initial state is occupied while the final state is empty.

At low temperature an occupation of given level varies very rapidly while crossing the Fermi energy – the bands are either completely filled or empty. With increasing temperature the electron distribution is smoother as a function of energy and some levels with energy close to the Fermi energy are occupied partially, meaning that there are possibilities to execute transitions into and from these partially occupied levels.

2.3 Experimental Methods

2.3.1 FIR Spectroscopy

The whole electromagnetic (EM) spectrum includes all the frequencies – from low-energetic radio waves ($\approx 10^0$ Hz) to high energy gamma rays (up to 10^{22} Hz). There is no single spectroscopic method which allows to study the light and matter at the whole EM spectrum. As the properties of matter differ with the frequency, different spectroscopic techniques have to be used to investigate specific physical phenomena in a given spectral region. For example, in solid state physics the electronic energy levels span over a wide energies in a range from few meV to few eV. This corresponds to energies of photons from far-infrared (FIR), through visible, to ultraviolet range.

The parts of EM spectrum, relevant in the scope of this thesis, are the THz and FIR regions, as they allows to investigate physical phenomena in narrow-gap semiconductors (NGS) and topological insulators (TI). In general, the THz region spans over the frequency domain between 0.3 THz to 30 THz, which translates to 10 - 1000 cm^{-1} , or $\approx 1.25 - 125$ meV. This energy range covers most of the possible inter- and intra-LL transitions in NGSs and TIs, which allows to investigate their band structure in a thorough way.

2.3.2 Experimental Set-up

The experimental work of this thesis is based on the infrared/THz magneto-spectroscopy measurements of TIs and NGSs. The spectroscopy experiments were performed using a specially customized Oxford liquid helium cryostat coupled to a Bruker Fourier spectrometer IFS 66v/S. The schematics of the system is presented on Figure 2.5. At the bottom of the cryostat an additional chamber was placed (white space), separated from the rest of the system by a diamond window, which is well transparent in the infrared range and isolates thermally the chamber itself. A composite germanium bolometer QGEB/X was placed inside the chamber, being cooled by a liquid helium. A helium bath assures that the bolometer is kept at low temperature at all times. Sensitivity of a bolometer is strongly related to an operational temperature, and decreases drastically with increasing temperature.

A thermal separation provided by the diamond window assures the optimal environment for the bolometer while the temperature can be varied in the vicinity of the sample in a broad range. A temperature sensor and a heater are placed near the sample. A combination of these two devices is used to set the temperature in the vicinity of the sample space on demand up to around 140 K. Higher temperatures are difficult to obtain due to the thermal radiation emitted by the sample and its surroundings, which heats up the bolometer, decreasing its sensitivity. The temperature in the cryostat can be decreased to around 1.6 K, by lowering the liquid helium pressure. At the ambient pressure the

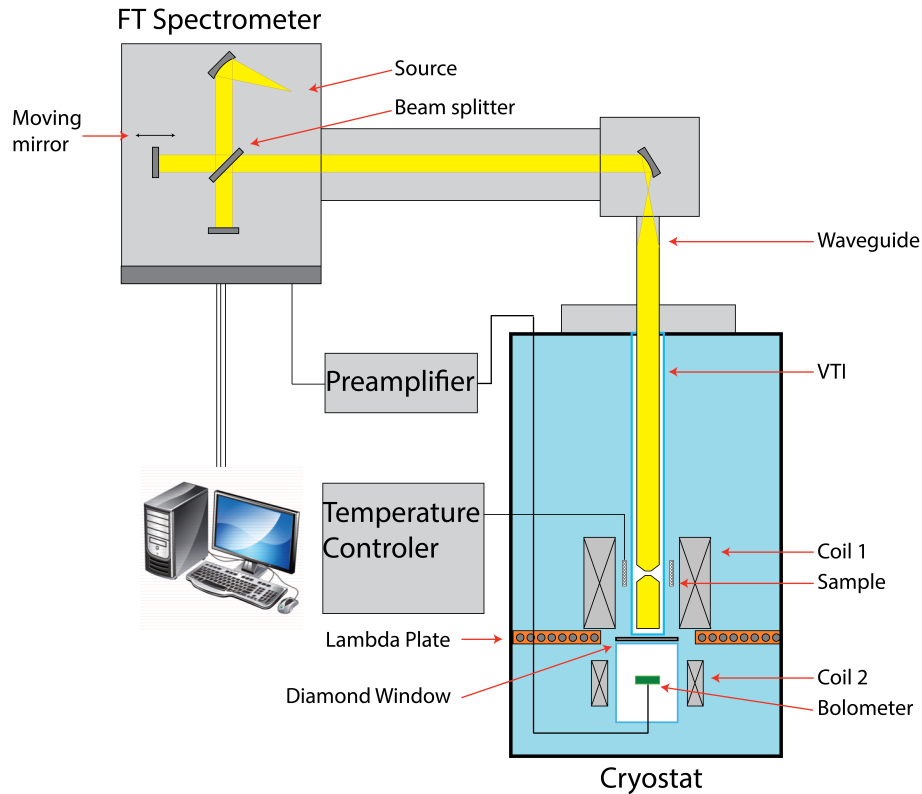


Figure 2.5: *Sketch of the experimental set-up. The first part is composed of a Fourier (FT Spectrometer) spectrometer with a Gobar lamp (Source), which works using the Michelson interferometer principle. The radiation is guided (by a Waveguide) into the cryostat. The liquid-helium cryostat is supplied with a liquid nitrogen coating. The sample is placed inside the cryostat in a variable temperature insert (VTI). The superconducting coil (Coil 1) can provide magnetic field with inductance up to 16 T, while the compensating coil (Coil 2) keeps the overall magnetic field at zero in the vicinity of the bolometer. Near the sample there is a temperature controller, allowing to vary and stabilize the temperature. The bolometer is separated (by a Diamond Window) from the sample space.*

boiling temperature of helium is equal to 4.2 K. At the λ point helium becomes superfluid – at around 22 mbar the temperature reaches around 1.8 K, which is the lowest possible in this experimental set-up.

A system of two superconductive coils was embedded into the cryostat (Figure 2.5). The main coil (Coil 1) is capable of creating a constant and homogeneous magnetic field of inductance up to 16 T in the vicinity of the sample. At the same time, the second coil (Coil 2) compensates the magnetic field created by the Coil 1 in the vicinity of the bolometer. This procedure is required to maintain zero magnetic field at the position of the bolometer. This system allows to perform measurements in a broad range of temperatures and magnetic fields, while preserving optimal environment for the bolometer.

In the experiment a global lamp integrated with the spectrometer was used as a radiation source. Globar is a broadband thermal emitter, which is typically used for infrared spectroscopy. It is formed by a silicon carbide rod heated electrically up to a couple of hundreds degrees Celsius. Its radiation is suitable for spectroscopy as it is continuous and resembles the blackbody radiation. The radiation is delivered to the cryostat via a waveguide, which ends with a light-focusing cone. The focused light passes through and interacts with the sample. The transmitted light is detected by the bolometer. An

electrical response of the bolometer is passed back to the spectrometer, where the Fourier transform occurs and the final spectra are calculated.

Fourier spectrometer

A Fourier transform spectrometer has a Michelson interferometer in its core. The Michelson interferometer consists of two mirrors, one in a fixed position and one is moveable, and a beamsplitter. The light from the source is split into two paths and gets reflected by the mirrors. By moving the movable mirror over some distance, the relative optical path of two beams is varied, and an interference pattern is created that encodes the spectrum of the source. The interference pattern is a Fourier transform signal of the original spectrum. The Fourier spectrometer has some advantages over the regular spectrometers:

- it can scan multiple wavelengths simultaneously, greatly increasing the operational speed,
- high speed allows to increase the number of measurements, increasing the signal-to-noise ratio,
- it does not require prism/grating to split the beam in order to analyze it.

A coupling of a Fourier spectrometer as a source of light and a bolometer as a detector can be used to perform spectroscopy of solid state systems quickly and effectively.

Bolometer

A bolometer is a device used to measure the power of incident electromagnetic radiation through heating of an absorptive element. Any radiation illuminating the absorptive element raises its temperature – the higher the absorbed power, the higher the increase of temperature. The temperature change can be measured directly with an attached resistive thermometer, or the resistance of the absorptive element itself can be used as a thermometer. Nowadays, most of the bolometers are based on semiconductor or superconductor absorptive elements, which allows them to operate at cryogenic temperatures, significantly increasing the sensitivity.

Analysis of spectroscopic data

Transmission spectra are used to characterize samples and give an insight to their energetic structure. The peak positions in an FIR spectrum correlate with an optical transitions between distinct energy levels within the sample. The standard way to obtain a transmission spectrum is to acquire a spectrum with respect to some reference. A use of a reference spectrum allows to remove features, which are related to the experimental set-up itself, and do not provide any useful information about the sample. For example, in magneto-spectroscopy, a spectrum taken at zero magnetic field ($T_{B=0T}$) can serve as the reference to a different spectrum, taken at nonzero magnetic field ($T_{B\neq 0T}$). Both of the obtained spectra are influenced by all of the optical parts of the set-up, therefore a formula for the measured reference spectrum can be expressed as

$$f_{B=0T}(\hbar\omega) = E_{src}(\hbar\omega) \cdot T_{setup}(\hbar\omega) \cdot T_{sample,B=0T}(\hbar\omega) \cdot S_{det}(\hbar\omega), \quad (2.34)$$

where E_{src} is the emission spectrum of the source, T_{setup} is the transmission of the elements of the experimental set-up, T_{sample} is the actual transmission through the sample, and S_{det} is the sensitivity of the detector. All of those parameters depend on the frequency of light (ω). A similar formula can be written for a spectrum at nonzero magnetic field

$$f_{B\neq 0T}(\omega) = E_{src}(\omega) \cdot T_{setup}(\omega) \cdot T_{sample,B\neq 0T}(\omega) \cdot S_{det}(\omega), \quad (2.35)$$

where all but one (T_{sample}) elements are the same. This is obvious since magnetic field influences only the sample. The final transmission is obtained by dividing the spectrum at nonzero magnetic field (Equation 2.35) by the reference spectrum (Equation 2.34):

$$T(\omega) = \frac{f_{B \neq 0T}(\omega)}{f_{B=0T}(\omega)} = \frac{E_{src}(\omega) \cdot T_{setup}(\omega) \cdot T_{sample, B \neq 0T}(\omega) \cdot S_{det}(\omega)}{E_{src}(\omega) \cdot T_{setup}(\omega) \cdot T_{sample, B=0T}(\omega) \cdot S_{det}(\omega)}. \quad (2.36)$$

this division allows to explicitly remove parts depending on E_{src} , T_{setup} , and S_{det} . Only the parts of the transmission related to the sample remain

$$T(\omega) = \frac{T_{sample, B \neq 0T}(\omega)}{T_{sample, B=0T}(\omega)}. \quad (2.37)$$

To obtain a complete evolution of optical transition as a function of magnetic field, this procedure has to be repeated at different values of magnetic field, with a proper resolution. There exists experimental set-ups, where the detector is situated close to the sample, where magnetic field can have an influence on the detector as well. In these systems, the parameter S_{det} does not reduce itself in Equation 2.36, thus additional reference spectra have to be obtained to eliminate the magnetic field dependence of the detector on the signal.

$$T(\omega) = \frac{T_{sample, B \neq 0T}(\omega)}{T_{sample, B=0T}(\omega)} \cdot \frac{S_{det, B=0T}(\omega)}{S_{det, B \neq 0T}(\omega)}, \quad (2.38)$$

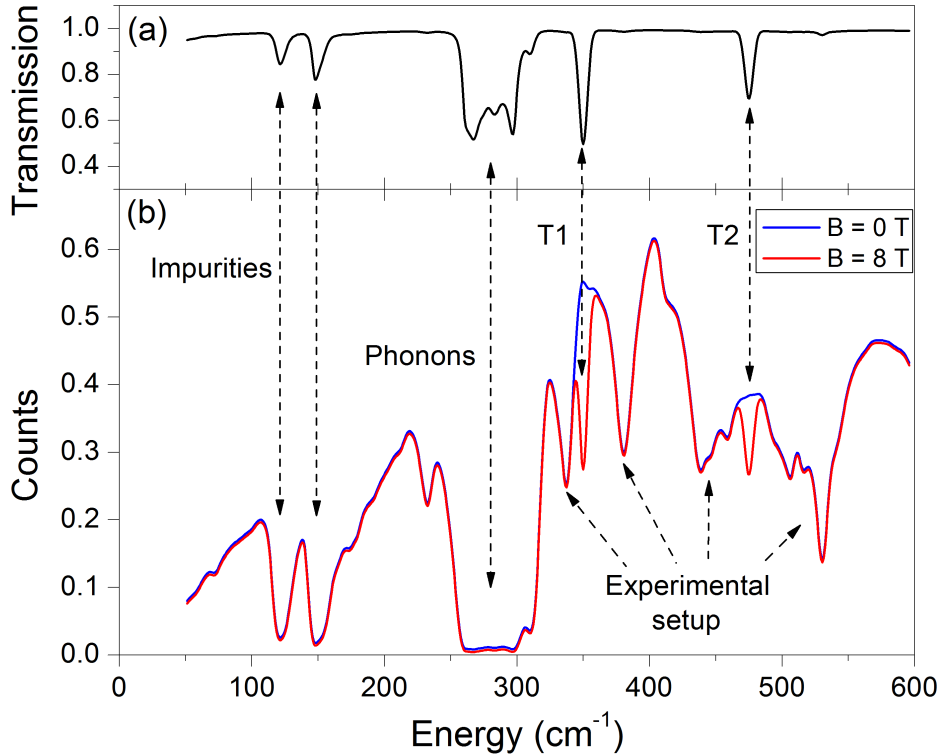


Figure 2.6: **Panel (a)**: Transmission spectra calculated from spectra from panel (b). **Panel (b)**: Example spectra obtained at $B = 0$ T (blue) and $B = 8$ T (red). The minima present in both spectra are explained by the absorption on the parts of experimental set-up, phonons, or impurities. The minima present only in red spectrum correspond to optical transitions marked as T1 and T2. Each minimum on transmission spectra was connected to a corresponding minimum of the raw spectra.

An example of infrared spectra, as well as the transmission obtained via the described procedure, is presented in Figure 2.6. Panel (b) shows two curves, which are an example of raw spectra obtained by a spectrometer. Both spectra are presented as a plot of counts versus energy, where counts correspond to the intensity of light detected at given energy (wavelength) of light. The blue spectrum was taken at zero magnetic field, while the red spectrum at $B = 8$ T. The spectra are similar at the whole energy range, except at the vicinity of two wavenumbers, 340 cm^{-1} and 475 cm^{-1} , where red spectra exhibit a visible minimum, absent in blue spectra. Those minima correspond to optical transitions marked as $T1$ and $T2$.

Those minima are linked with corresponding minima of a transmission spectra presented on Panel (a). The transmission spectrum was obtained by a division of the red spectrum ($T_{B=8T}$) by the blue spectrum ($T_{B=0T}$), and it presents five absorption peaks (with one broad around $260\text{-}320\text{ cm}^{-1}$).

The minima on red and blue spectra, which are related to the sample itself have their corresponding minima on the transmission spectra:

- Two minima around 120 and 150 cm^{-1} correspond to an absorption on impurities and defects of the sample. As they are present at both magnetic fields, they potentially could be removed from transmission spectrum by division. It is not the case because the absorption is almost 100%, which means that the intensity detected is very small (therefore the signal-to-noise ratio is high), and it results in such artifacts in division of two very small numbers.
- The broad absorption, visible around $260\text{-}320\text{ cm}^{-1}$, corresponds to the absorption by the phonon bands. It remains visible in the transmission spectra because of the same reason – the absorption is almost 100% leading to division artifacts.
- The actual optical transitions $T1$ and $T2$, which resulted from an evolution of energy levels in magnetic field and transitions between them.

The rest of minima are absent in transmission spectra, which means that they are related to the absorption by the experimental set-up, rather than by the investigated sample.

Chapter 3

HgCdTe Bulk Systems

In this work a significant attention will be paid to 3D bulk systems, 2D quantum well heterostructures, and strained HgTe layers with intermediate thickness. This variety of systems gives a unique opportunity to study different physical effects taking place in the structures.

At the beginning of the chapter a general introduction to HgCdTe-based materials will be given. Later, the bulk system will be described. A $\text{Hg}_{1-x}\text{Cd}_x\text{Te}$ system is very versatile in terms of band structure. In a HgCdTe crystal in an inverted band order phase the conduction and valence bands overlap, which means that the bulk is conductive. However, if a bulk band gap is opened by strain or a different mechanism, the system could exhibit a TI phase. In a regular band order phase, a band gap is present, which means that HgCdTe can be either a semiconductor or a semimetal, depending on its both internal and external parameters. It will be shown that it is possible to demonstrate a phase transition from inverted to regular band order, which makes these systems particularly interesting. In the bulk systems in a gapless state a new class of relativistic excitations arises, called Kane fermions, which can be studied using THz spectroscopy.

The description and experimental results on HgTe/CdTe QWs will be presented in the Chapter 4.1. The band structure of a QW might exhibit a topologically insulating phase, as there is a way to obtain a band inversion with a bulk energy gap, which is provided by the quantum confinement within the QWs structure. Finally, in Chapter 4.2, an overview and preliminary experimental results obtained on strained HgTe films will be presented. HgTe films can be considered as thick QWs, because the quantum confinement is still present in these systems. However, it is too small to open an energy gap. A different mechanism of gap opening is used – a strain.

3.1 Introduction to HgCdTe Systems

HgCdTe alloy crystal is formed by II-VI compounds which crystallize in a zincblende structure, which consists of two face-centered cubic sublattices. In the zincblende structure each of Te-ions has four nearest neighbors, which can be either Hg or Cd. The presence of a different atom on each lattice site breaks the inversion symmetry, which results in reducing the point group symmetry from cubic to tetrahedral.

Both compounds, HgTe and CdTe, are well lattice-matched, having the lattice constant parameter equal to 6.45 Å and 6.48 Å, respectively. $\text{Hg}_{1-x}\text{Cd}_x\text{Te}$ mixed crystals have a direct band gap, which value varies from 1.6 eV for pure CdTe, a relatively large gap semiconductor, to -0.3 eV for pure HgTe, a semimetal. A negative band gap is a consequence of an unusual band alignment in the crystal, where

p -type (Γ_8) bands lie around 0.3 eV above the s -type (Γ_6) bands. This is caused by an extraordinary large SOC in HgTe (due to the presence of a heavy element Hg), which leads to an inverted band structure. The light-hole Γ_8 band forms the conduction band, the heavy-hole band forms the first valence band, and the electron s -type Γ_6 band is pulled below the Fermi level and lies between the heavy-hole band and the spin-orbit split-off band Γ_7 . The band order of both CdTe and HgTe is presented in Figure 3.1.

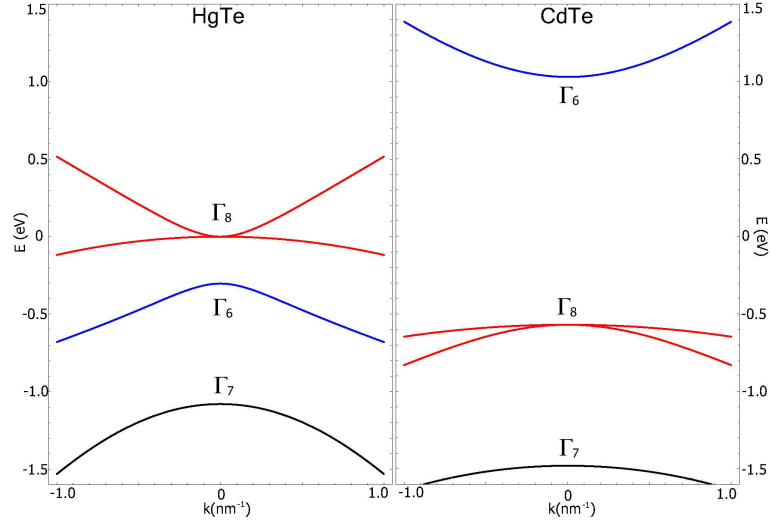


Figure 3.1: *Inverted band order of HgTe and normal band order of CdTe. Figure comes from work [17].*

3.2 Overview of HgCdTe Bulk Crystals

The earliest studies of $\text{Hg}_{1-x}\text{Cd}_x\text{Te}$ crystals were aimed at a development of infrared detectors, especially for radar applications. In 1958, Lawson *et al.* synthesized for the first time a mixed crystal of HgCdTe at the Royal Radar Establishment in England. Their work was published [66] a year later. Because of its extraordinary properties, HgCdTe was recognized early as the most versatile material for detection over the whole infrared range, with a special attention put on the wavelength of around 10 μm . This is the range of the second wide atmospheric window, which made it of a great interest for communication applications. Moreover, it covers the range of the maximum of thermal radiation at the room temperature, which opened a way for possible applications for everyday life.

The following studies were focused on a determination of the band gap of mixed compounds with composition ranging from $x \approx 0.2$ to $x \approx 0.6$ by optical methods [67][68] (based on a detection of the absorption edge), which provided the band structure parameters for a wide range of temperatures and empirical formulae for the value of the band gap as a function of Cd content and temperature. Moreover, an indication of a semimetal-to-semiconductor phase transition was observed. The studies of samples with band gaps close to zero were performed by Groves *et al.* [69] and Saur [70]. Further magneto-optical studies performed on samples with small energy gap by Kim *et al.* [71] explored the properties of the band structure in a semimetallic regime. The first extensive magneto-spectroscopic studies of HgCdTe in a semiconducting [72] and a semimetallic [73] phase were performed by Guldner *et al.* and Rigaux [74]. The investigations allowed to explore the phenomena such as the band structure evolution at the point of phase transitions or polaron anomalies.

Recently, as the growth techniques have gradually advanced over the years, the quality of HgCdTe-based structures improved significantly. Especially, a Molecular Beam Epitaxy (MBE) method gives a possibility to grow structures of immense quality. Despite this, the growth of Hg-based structures is still a challenging task and requires a lot of experience and know-how to be done properly. That is why there are only few laboratories in the world (like CEA-LETI, Würzburg or Novosibirsk) where the growth process was mastered.

MBE method is an epitaxial method of growing crystalline films on top of a monocrystal substrate. MBE takes place in an ultra-high vacuum environment (around 10^{-10} mbar). The vacuum prevents a deposition of unwanted molecules, reducing the amount of non-intentional impurities. In a solid source MBE, pure elements are heated separately in effusion cells or electron beam evaporators until they start to slowly sublimate. The gaseous elements are delivered to a wafer, where they condensate, forming a crystal. They may also react with each other, creating mixed crystals. The quality of the growth can be controlled in-situ by a reflection high energy electron diffraction, which provides information about a growth rate. There are also other methods of epitaxial crystal growth, which will not be described in this work. The most popular and widely used are: liquid phase epitaxy, vapor phase epitaxy, and metalorganic chemical vapor deposition.

Nowadays, because of the possibilities given by the high quality growing methods, the applications of HgCdTe compounds is no longer limited to the infrared detection. There has been a renewal of interest of physical community in this topic as a HgTe/CdTe QW was demonstrated to be a 2D TI, which was followed by the discoveries of 2D Dirac Fermions and 3D TIs. The attention of the part of physics community is now centered at the phenomena relative to the fundamental science of narrow-gap semiconductors and TIs. These phenomena are, including but not limited to, the variations of effective mass of electrons, appearance of new quasi-particles in semiconductor systems and new exotic phases of matter that they are related to.

The electrical and optical properties of $\text{Hg}_{1-x}\text{Cd}_x\text{Te}$ crystals are determined by its dielectric function and conductivity, which are closely related to the band structure. The shape of both electron and hole bands can be described using the Kane model [75]. The band gap varies from negative to positive monotonically and almost linearly with the cadmium content x – the crystal composition. It means that at some point there must be a special composition, where the band gap vanishes, which, according to [30], implies that the effective mass collapses as well, and quasi-relativistic particles appear. HgCdTe bulk crystals give a special opportunity to realize and investigate a condensed matter system with particles exhibiting relativistic Dirac-like properties in all three dimensions. Three dimensional topological insulators also exhibit states with a relativistic dispersion relation, but their presence is limited to the 2D surfaces of a sample.

Recent experimental [76] and theoretical [77] works on $\text{Hg}_{1-x}\text{Cd}_x\text{Te}$ crystals characterized by a cadmium concentration close to the critical led to a discovery of another massless Dirac-like quasi-particles called Kane fermions [76]. These three dimensional particles are not equivalent to any other known relativistic particles. Kane fermions show a resemblance to the pseudospin-1 Dirac-Weyl system [77] – the band gap vanishes [78] and their energy dispersion relation forms a Dirac cone with an additional band crossing the vertex. These conical bands may have several spectacular properties similar to those in Dirac and Weyl semimetals (such as Klein tunnelling and suppressed backscattering) [76].

3.2.1 Band Structure and Temperature

The band structure and electronic dispersion relation of a $\text{Hg}_{1-x}\text{Cd}_x\text{Te}$ crystal can be varied both intrinsically and externally. Intrinsically – by changing the chemical composition. Externally – by varying external parameters, like temperature [79] or pressure [80].

However, the method of variation of chemical composition of band structure engineering has its limitations. First of all, it can be done only once – during the crystal growth. Secondly, it is technologically difficult as even small fluctuations of composition may disable the ability to perform fine tuning of the band gap in the vicinity of the critical value, where the band gap vanishes and a topological semimetal-to-semiconductor phase transition takes place.

To deal with these issues, there is a need to find an easy-controllable external parameter, which allows to fine tune the band structure, and is generally available even in a simple experimental set-up. It turns out that a temperature regulation allows to precisely control the band structure and provides a well-set environment to investigate the relativistic properties of Kane fermions, which arise while the system is tuned across the gapless state at the point of a phase transition [81]. The only major drawback of the usage of temperature as a tuning parameter is its range. There are two general factors limiting the range of available temperatures.

The first limit is related to the properties of the material itself. Mercury is a very volatile element, which tends to diffuse and alter the sample structure even at relatively low temperature in comparison to other compounds, which reduces the quality of the structure. This limitation is the reason, why processing of mercury-based compounds is a very challenging task. In general, it is assumed that the highest safe temperature for a HgCdTe system should be around 80°C [82].

The second limit is related to the energy range that one wants to investigate. If a desired phenomenon, like an optical transition, is in energy range comparable with the thermal energy kT , it will not be observed. Moreover, an increase of temperature usually follows an increase of disorder within the sample, reducing the signal-to-noise ratio of measurements. This renders the available temperature range narrower than possibly anticipated. That is why, the cadmium content allows to tune the band gap in a broad range, while the temperature acts as a fine tuning parameter. Depending on the phenomena that one wants to observe, it is required to choose the specific cadmium content, which makes the band gap close to the desired value. In case of this work, the desired value of the band gap was negative, preferably close to zero, which would allow the temperature to tune it from a negative to a positive regime.

At low temperatures a $\text{Hg}_{1-x}\text{Cd}_x\text{Te}$ crystal is a regular semiconductor for cadmium content higher than the critical value $x > x_c \approx 0.17$. On the other hand, if the cadmium content is lower than the critical value $x < x_c$, the band structure is inverted, as schematically shown in Figure 3.2, and the structure exhibits a semimetallic behavior. The two phases are not topologically equivalent, as characterized by the Z_2 topological invariant [17].

As was mentioned before, the band structure depends on more parameters than only the cadmium content. Considering temperature as a second parameter, the point of closing the band gap becomes a curve on a two dimensional (x, T) parameter space. This clarifies that the critical concentration $x_c \approx 0.17$ is valid only for temperatures close to the absolute zero. However, samples with a little lower cadmium content have the critical temperature elevated. Our team for the first time used the temperature as an external parameter to induce a topological phase transition and investigate the Kane fermions arising in the gapless state [81]. The two samples (A and B) used in that experiment had the cadmium content of $x_A = 0.175$ and $x_B = 0.155$. This allowed to study the physics of Kane

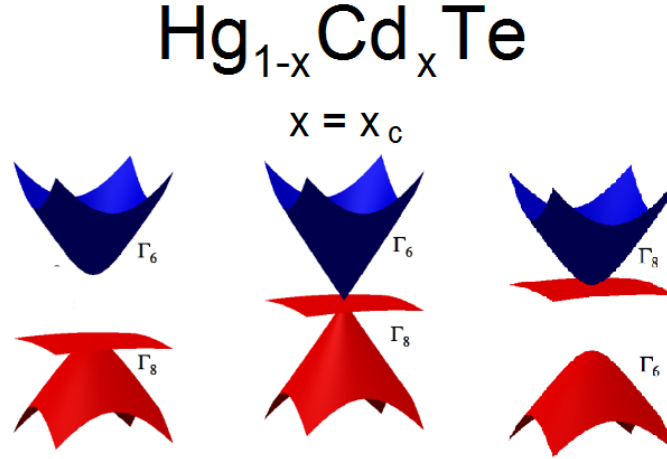


Figure 3.2: A dispersion relation of a $\text{Hg}_{1-x}\text{Cd}_x\text{Te}$ system for different cadmium contents x . A blue surface represents an electron band, while red surfaces represent light- and heavy-hole bands. The heavy-hole band is almost dispersionless, as the effective mass of a heavy-hole is large in comparison to the mass of a light-hole and an electron. On the left side a band structure in a semiconducting phase is shown, where the band gap is positive and the conduction band is formed by a Γ_6 band. On the right side the band structure is inverted. The band gap is negative and the conduction band is formed by a Γ_8 band. For both regular and inverted band orders the bands are parabolic. For a critical concentration x_c the band gap vanishes and the system exhibits a Dirac-like dispersion relation with additional flat band (heavy-hole). The image comes from the work of Orlita *et al.* [76].

fermions at higher temperatures, as the temperature of phase transition of the Sample B was around 77 K.

The temperature is an important factor considering the physical phenomena occurring in solid state materials, especially in NGSs like HgCdTe. Temperature also influences the energy structure via a lattice thermal expansion. This modifies the Hamiltonian and the band structure in the consequence, by elevating the hole band energy. In the case of NGSs, especially if the dependence on temperature is significant, it can lead to a gap closure, as in the case of HgCdTe. The energy gap depends on cadmium content x and temperature T , and that dependence can be expressed (following Laurenti *et al.* [83]) as:

$$E_g(x, T)[\text{eV}] = -0.303(1-x) + 1.606x - 0.132x(1-x) + \frac{6.3(1-x) - 3.25x - 5.92(1-x)}{11(1-x) + 78.7x + T} 10^{-4} T^2, \quad (3.1)$$

which is a function on two parameter space. If the left side of Equation 3.1 is equal to zero, it obviously limits the space to a case of the gapless state. A dependence $x_c(T, E_g = 0)$ can be derived from Equation 3.1, which gives a quantitative information about the band structure in a form of a phase diagram with both samples marked is presented in Figure 3.3. Sample A is in a normal semiconducting regime at the whole relevant temperature range. Sample B, on the other hand, at low temperature is in an inverted band order regime, and as the temperature rises it enters the normal regime.

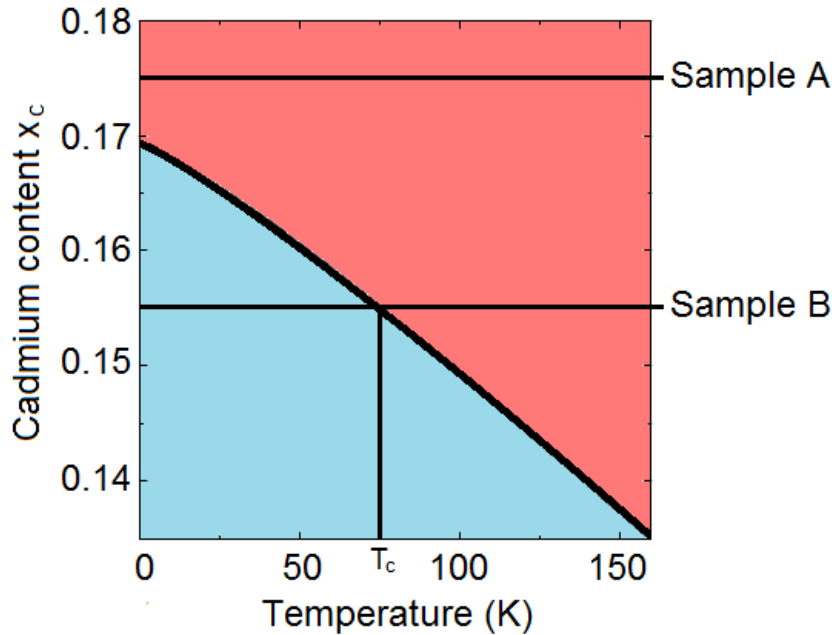


Figure 3.3: Phase diagram of a bulk $Hg_{1-x}Cd_xTe$ crystal as a function of temperature T and cadmium content x_c . The red (blue) area represents a parameter range, where the system is in a semiconducting (semimetallic) state. The two horizontal lines mark the Cd concentration of Sample A (0.175) and Sample B (0.155). For Sample B, which undergoes a phase transition, the critical temperature T_c is marked as well.

The appearance of Kane fermions is not restricted only to the gapless state, where they are truly massless. Even if a system has a gap, the behavior of (massive) carriers can be regarded as relativistic as long as the considered energy range is small in terms of the energies of nearby bands, mainly the spin-split Γ_7 band, which lies $\Delta_{SO} \approx 1$ eV [84] lower in energy. Moreover, HgCdTe systems are not the only ones, where Kane fermions can be found. Recent studies of another extraordinary material, namely cadmium arsenide, revealed that Kane fermions are indeed potentially present in that system [85] as well.

Cd_3As_2 has been identified as a 3D topological Dirac semimetal in which a topological phase is stable under ambient conditions [86]. This system brought again a considerable interest in the electronic properties of the scientific community, upon which investigations started in the late sixties [87][88]. This compound was at first expected to contain the Dirac-like particles. ARPES measurements confirmed those expectations, claiming that the electronic bands of Cd_3As_2 consist of a single pair of symmetry-protected 3D Dirac nodes, located close to the Γ point of the Brillouin zone, which span over a few hundred meV [89][90], or even eV [86]. However, a recent optical reflectivity experiments performed by Akrap *et al.* [85] shed some light on that matter. As it turns out, the electronic bands of Cd_3As_2 are quite different if considered in high and low energy scales. In high energy scales, in the order of few hundreds of meV, the band structure resembles a set of two conical bands, which originate from the Kane model applied to a narrow gap semiconductor. The bands are not symmetry protected and they host a genuine Kane fermions. However, at low energy scales, of the order of few meV, the band structure may be formed by two sets of twin Dirac cones, which are protected by the symmetry. This means that the excitations of the higher energy behave accordingly to the Kane particles, while the excitations of the lower energy, if present, are Dirac-like.

3.2.2 The Simplified Kane Model

The simplified Kane model [91][75] can be used to describe an electronic structure of a HgCdTe crystal near the Γ point of the Brillouin zone, where all the interesting physics takes place. This model accounts for the $k \cdot p$ interaction between the Γ_6 and Γ_8 bands, while neglects the influence of the remote spin-split Γ_7 band. The final Hamiltonian (3.2), neglecting the small quadratic in momentum terms, takes form of:

$$\hat{H} = \tilde{\beta}\tilde{m}\tilde{c}^2 + \tilde{c}\tilde{\alpha}_x p_x + \tilde{c}\tilde{\alpha}_y p_y + \tilde{c}\tilde{\alpha}_z p_z, \quad (3.2)$$

where \tilde{c} is the Fermi velocity, \tilde{m} is the effective mass, and p_i is the momentum. This Hamiltonian resembles the one for the true 3D Dirac fermions, presented in the Dirac equation (3.3),

$$i\hbar \frac{\partial \Psi}{\partial t} = (\beta m c^2 + c\alpha_x p_x + c\alpha_y p_y + c\alpha_z p_z) \Psi. \quad (3.3)$$

However, the matrices $\tilde{\alpha}_i$ are different from α_i [81]. There are multiple bulk condensed matter systems, which can be described well by the Dirac equation 3.3. Nevertheless, the Hamiltonian 3.2 does not reduce itself to the Dirac Hamiltonian nor to any other known Hamiltonian describing relativistic particles. The 6×6 matrix version of Equation 3.2 is:

$$\hat{H}_{p_x, p_y, p_z} = \begin{pmatrix} \tilde{m}\tilde{c}^2 & \frac{\sqrt{3}}{2}\tilde{c}p_+ & -\frac{1}{2}\tilde{c}p_- & 0 & 0 & -\tilde{c}p_z \\ \frac{\sqrt{3}}{2}\tilde{c}p_+ & -\tilde{m}\tilde{c}^2 & 0 & 0 & 0 & 0 \\ -\frac{1}{2}\tilde{c}p_- & 0 & -\tilde{m}\tilde{c}^2 & -\tilde{c}p_z & 0 & 0 \\ 0 & 0 & -\tilde{c}p_z & \tilde{m}\tilde{c}^2 & -\frac{\sqrt{3}}{2}\tilde{c}p_- & \frac{1}{2}\tilde{c}p_+ \\ 0 & 0 & 0 & -\frac{\sqrt{3}}{2}\tilde{c}p_- & -\tilde{m}\tilde{c}^2 & 0 \\ -\tilde{c}p_z & 0 & 0 & \frac{1}{2}\tilde{c}p_+ & 0 & -\tilde{m}\tilde{c}^2 \end{pmatrix} \equiv \tilde{c}\mathbf{p} \cdot \mathbf{J}, \quad (3.4)$$

where $p_{\pm} = p_x \pm ip_y$, $E_g = \tilde{m}\tilde{c}^2$ is the energy gap, and $\tilde{c} = \sqrt{2P^2/3\hbar^2}$ is the universal velocity. The material properties are included within the model by E_g and the Kane element P . There are three eigenvalues of Equation 3.4, representing the energetic structure of the system. Each one is doubly degenerated due to the Kramers theorem. The eigenvalues can be presented as:

$$E_{\xi}(p) = \xi^2 \tilde{m}\tilde{c}^2 + (-1)^{1-\theta(\tilde{m})} \xi \sqrt{\tilde{m}^2 \tilde{c}^4 + p^2 \tilde{c}^2}, \quad (3.5)$$

where the ξ parameter takes values of $\xi = -1$ for the light-hole band, $\xi = 0$ for the heavy-hole band, and $\xi = 1$ for the electron band. $\theta(\tilde{m})$ is the Heaviside step function, equals to 1 for $\tilde{m} \geq 0$, and 0 if $\tilde{m} < 0$. An eigenvalue for $\xi = 0$ means that the heavy-hole band is energetically completely flat (dispersionless), which is a consequence of an assumption that the heavy-hole mass is infinite. The assumption is valid as long as the effective electron mass is significantly smaller than the effective heavy-hole mass of about $m_{hh} \approx 0.5 m_0$ [78], which is the case for narrow gap regime [76].

3.2.3 Bulk HgCdTe at Magnetic Field

The energy structure becomes quantized in a presence of magnetic field. The 3D dispersion relation takes form of a set of unequally spaced Landau levels (LLs), or more precisely, a form of 1D Landau bands which disperse with the momentum component along the field direction (usually z axis). Moreover, these LLs are characterized by a distinct $E \sim \sqrt{B}$ behavior, as is stated in Equation 3.6. The similar behavior is found for example in a gapless graphene, where the LL structure can

be expressed by $E_n = \text{sgn}(n)\sqrt{2e\hbar\tilde{c}^2B|n|}$, where $\text{sgn}(n)$ takes value $+1$ for electronic LLs, and -1 for hole-like LLs [92]. This is a direct consequence of the linear dispersion relation $E(p) \propto p$, as states the Equation 3.5. In a case of a parabolic dispersion relation $E(p) \propto p^2$, found in the most semiconductors, the LL structure takes form of $E = \hbar\omega_c(n + 1/2) = \hbar\frac{eB}{m^*}(n + 1/2)$. In this case, the energy of a LL is proportional to applied magnetic field, and each consecutive LL is separated from the adjacent one by a constant factor of $\hbar\omega_c$.

Magnetic field forces modification of the Hamiltonian by an inclusion of components related to a magnetic vector potential \mathbf{A} , through the standard Peierls substitution $\hbar\mathbf{k} \rightarrow \hbar\mathbf{k} - e\mathbf{A}$. In the case of a 3D material like HgCdTe, the LL spectrum of massless and massive fermions takes a more complex form:

$$E_{\xi,n,\sigma}(p_z) = \xi^2\tilde{m}\tilde{c}^2 + (-1)^{1-\theta(\tilde{m})}\xi\sqrt{\tilde{m}^2\tilde{c}^4 + \frac{1}{2}e\hbar\tilde{c}^2B(4n - 2 + \sigma) + p_z^2\tilde{c}^2}, \quad (3.6)$$

where n is a Landau level index, σ accounts for the Kramers degeneracy lifted by the magnetic field, and can be considered as the Zeeman (spin) splitting of LLs [81]. The index n takes only integer values, with respect to the parameter ξ . For $\xi = \pm 1$, n takes values of nonzero positive integers $n = 1, 2, \dots$. For $\xi = 0$, n takes values of zero or all positive integers except one $n = 0, 2, 3, \dots$. The parameters \tilde{c} , n , and p_z fully determine the spin splitting. Moreover, when the effective mass \tilde{m} vanishes, and at $p_z = 0$, the spin splitting of LLs is exactly proportional to \sqrt{B} . This means that the g -factor, defined in the standard way as $g_{\xi,n} = (E_{\xi,n,\uparrow} - E_{\xi,n,\downarrow})/(\mu_B B)$ diverges at $B \rightarrow 0$. This is an extraordinary situation in a solid state system, and in particular, it does not exist in the case of graphene [76], as the SOC is very weak [16]. An uncommon case of \sqrt{B} spin splitting takes place in HgCdTe because the g -factor becomes effectively infinite as the band gap vanishes.

At magnetic field, the energy spectrum becomes quantized into a set of LLs, and the Fermi energy separates filled LLs from the empty ones. An example of a LL structure created following Equation 3.6 is presented in Figure 3.4. The possible transitions between LLs have to follow the basic rules presented in Chapter 2. Moreover, the spin in a transition has to be conserved. It means that a transition can take place between two LLs only if they are characterized by the same spin orientation. The allowed transitions for this system, both inter- and intraband, are presented as arrows in Figure 3.4.

In the case of bulk HgCdTe the energy of the heavy-hole level does not depend on the k vector nor magnetic field. According to the Equation 3.6 it has zero energy for all nonzero integer values of n (except $n = 1$), and both values of $\sigma = \pm 1$. As a consequence, it is not formed by a single level but contains many levels, which are $2n$ times degenerate in energy. This is why transitions from a heavy-hole band into electron LLs with indices $n = 1$ or $n = 3$ are possible. However, the transitions into an electron LL with index $n = 2$ are forbidden, as it would require an existence of a heavy-hole LL with $n = 1$, which is not the case.

Interband transitions give a valuable information, because at zero magnetic field the energies of the transitions are equal to the energy gap itself. Intraband transitions, on the other hand, tend to have zero energy at zero magnetic field, as the Landau quantization disappears. It is worth to mention, that despite the fact that a transition is allowed, it might not be possible to observe it by the means of spectroscopy, as it was explained in Chapter 2.

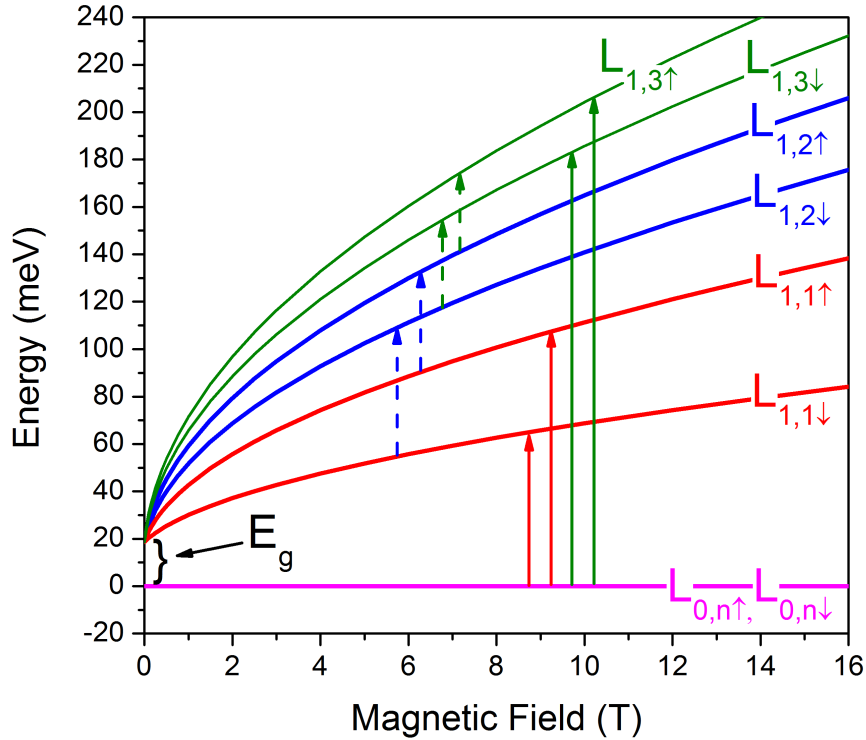


Figure 3.4: Landau level graph of a bulk HgCdTe system as a function of magnetic field. Colored lines represent Landau levels, characterized by a different value of ε , n , and σ , as described in indices of L on the right side of the graph. The electron band Landau levels (with $\varepsilon = 1$) have a near- \sqrt{B} behavior. The heavy-hole Landau level, plotted in purple, is fully degenerated. The vertical arrows represent a possible transitions between Landau levels in this system. Dashed arrows are intraband transitions, while solid arrows are interband. Energy gap was also marked on the figure by E_g .

3.3 Experiment

3.3.1 Samples

The high-quality HgCdTe bulk samples were grown using an MBE method on a (013)-oriented semi-insulating GaAs substrate in Novosibirsk by Dvoret'skii and Mikhailov. The substrate was followed by a ZnTe nucleation layer and a thick CdTe buffer layer to decrease the defect density arising from the lattice mismatch between the GaAs substrate and the HgCdTe layer. An actual $\text{Hg}_{1-x}\text{Cd}_x\text{Te}$ layer was approximately 3.2 micron thick to assure three-dimensionality of an active region of the sample, which was further confirmed by absorption coefficient measurements (Figure 3.7). The whole structure was capped by a CdTe layer to prevent environmental degradation processes like oxidation. The structure scheme of the samples is presented in Figure 3.5.

Sample characterization

To estimate the properties of the samples, like carrier concentration, the transport measurements were performed at magnetic field as a function of temperature. Samples were contacted with indium balls in a Van der Pauw configuration and placed in perpendicular quantized magnetic field (the Faraday configuration). The carrier concentrations of the structures for temperatures in a range of 2 K – 140 K were established based on a low-field part of the Hall measurements. The magneto-transport results are presented in Appendix B. The summary is presented in Figure 3.6. The electron



Figure 3.5: Layer structure of $Hg_{1-x}Cd_xTe$ bulk samples. The cadmium content was equal to $x_A = 0.175$ and $x_B = 0.155$ for samples A and B, respectively. The active region of the system is composed of an approximately $3.2 \mu\text{m}$ thick $Hg_{1-x}Cd_xTe$ layer, marked on blue on the sketch.

concentrations in both samples are comparable (one order of magnitude difference) and ranges from $n_A \approx 3 \cdot 10^{14} \text{ cm}^{-3}$ for Sample A and $n_B \approx 2 \cdot 10^{15} \text{ cm}^{-3}$ Sample B at $T = 2 \text{ K}$ up to $n_A \approx 8 \cdot 10^{15} \text{ cm}^{-3}$ and $n_B \approx 9 \cdot 10^{16} \text{ cm}^{-3}$ at $T = 140 \text{ K}$ for Sample A and Sample B, respectively. Relatively low concentration allowed to perform the transmission measurements as the absorption was moderate.

The dependence of absorption coefficient on incident photon frequency $\lambda(\omega)$ in 3D systems with a conical dispersion relation is linear, which resembles a behavior of 3D Weyl systems [77]. This is a direct consequence of the joint density of states of electrons with the linear dispersion, being proportional to ω^2 in 3D, and ω in a 2D case, as presented in Chapter 2. An explicit formula for the absorption coefficient as a function of energy can be written (following Chang *et al.* [93]) as:

$$\alpha(\hbar\omega) = \frac{B}{\hbar\omega} \left[(\Delta + b)\sqrt{(\Delta + b)^2 - b^2} + \frac{1}{8}(\Delta + 2b)\sqrt{(\Delta - 2b)^2 - 4b^2} \right], \quad (3.7)$$

where $\Delta = \hbar\omega - E_g$, and parameters b and B depend on cadmium content and can be determined by fitting. The first term in bracket represents the absorption coefficient involving the heavy-hole band, while the second term represents the contribution of the light-hole band. The situation is qualitatively different from 2D Dirac systems like graphene, where the absorption coefficient is independent on frequency [94].

The analysis of the absorption coefficient, presented in Figure 3.7, provided two pieces of information. The first one – the dependence of the absorption coefficient is indeed linear as a function of photon energy (and its frequency), even up to 300 meV, which is a sign that the system is three-dimensional. Moreover, the fits of Equation 3.7 to the experimental data, excluding the influence of phonon absorption, indicate that the samples differ from each other, as was expected because the cadmium content is different.

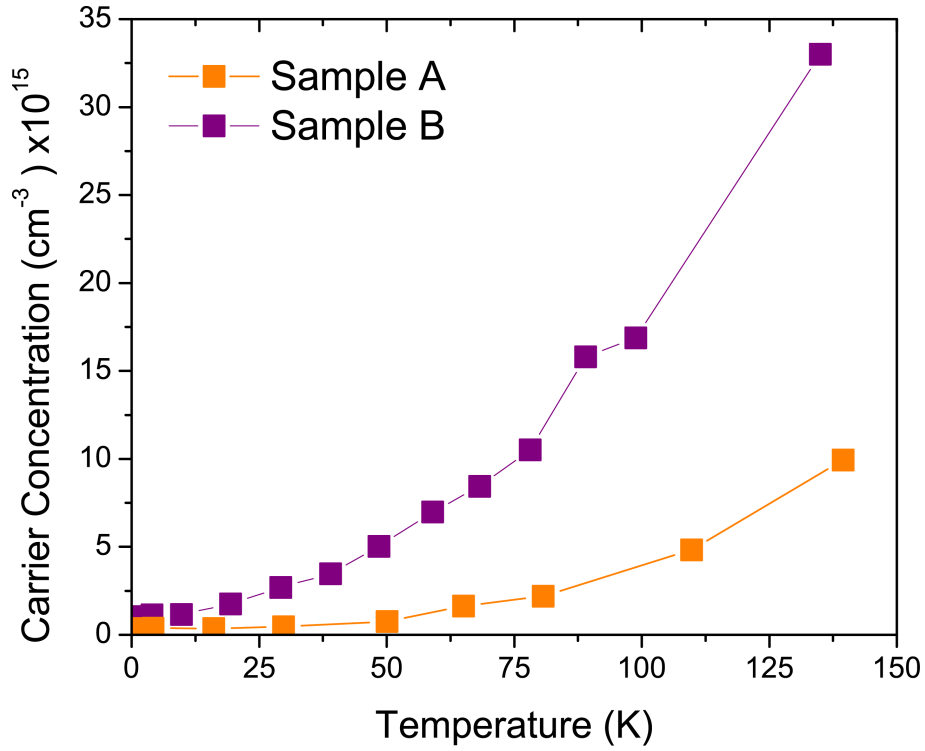


Figure 3.6: *Electron concentration as a function of temperature of Sample A (orange squares) and Sample B (purple squares).*

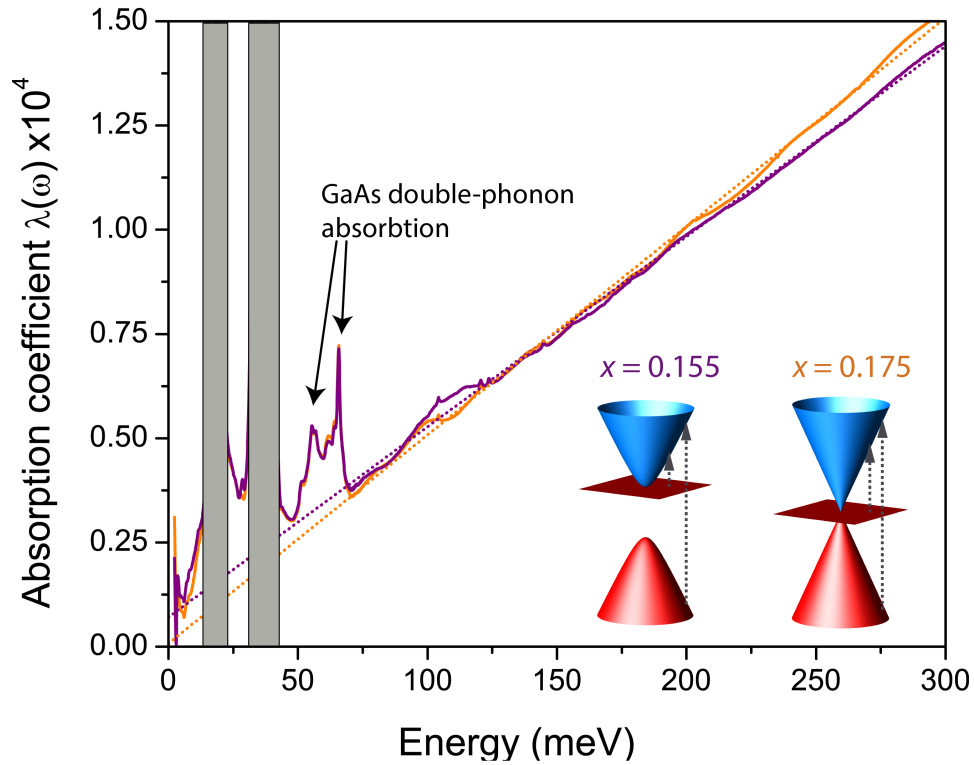


Figure 3.7: *Optical absorption of pseudo-relativistic Kane fermions in $Hg_{1-x}Cd_xTe$ at $T = 4.2$ K. Zero field absorption coefficients exhibit a linear behavior reflecting the relativistic character of the 3D carriers. The band gap values of 4 ± 2 meV and -20 ± 4 meV for Sample A and B, respectively, are extracted from fits (dashed lines). The inset depicts inter-band transitions that contribute to the linear optical absorption.*

3.3.2 Results

In this section magneto-spectroscopy results of two HgCdTe bulk samples are presented and their band structure evolution as a function of temperature is compared. One of the samples (Sample A) is a positive-gap semiconductor, and its band gap increases monotonically with temperature. The second sample (B) is in a semimetallic state at low temperature and undergoes a semimetal-to-semiconductor phase transition as the temperature increases. A theoretical analysis of the results based on a simplified Kane model is presented and the implications are discussed.

In order to fully describe the Kane fermions in MCT, arising in the vicinity of a semimetal-to-semiconductor phase transition, there is a need to carry the system through the transition and make measurements along the way. The two investigated bulk samples provided an opportunity to directly see the difference between the two different phases, characterized by an inverted and non-inverted band ordering, and the evolution of their properties as a function of temperature.

The theoretical model of the LL structure of the samples, based on Equation 3.6, allowed to predict observable optical transitions. However, the parameters \tilde{m} and \tilde{c} had to be extracted directly from the experiment by fitting. In theory, the parameter \tilde{c} , describing the carrier velocity, should be temperature independent, as it depends only on the Kane element P and physical constants, as described by Equation 3.4. On the other hand, the rest mass \tilde{m} , depending on both E_g and \tilde{c} , is expected to change as the energy gap changes.

Related experimental works

This chapter presents experimental results which can be considered as a direct extension and continuation of the work done by Orlita *et al.* on bulk HgCdTe [76], in which bulk sample, close to the point of a semiconductor-to-semimetal topological transition, was studied by an infrared magneto-spectroscopy. However, this investigation was limited to a constant and low temperature only. The authors demonstrated for the first time the relativistic 3D Kane fermions, as they manifest themselves through, among other effects, an $E \propto \sqrt{B}$ dependence on inter- and intra- Landau level transitions (Figure 3.8).

Experimental details

The transmission measurements were performed using the transform Fourier spectrometer. A data acquisition range was 10-700 cm^{-1} (1.25-87.5 meV) with spectral resolution of 4 cm^{-1} . A transmission spectrum was calculated by dividing a spectrum at given magnetic field by a reference spectrum, taken at zero magnetic field. This allowed to detect changes in relative transmission as an effect of magnetic field. Multiple spectra were gathered at a constant and stable magnetic field to increase the signal-to-noise ratio, and after measurements the field was changed. A usual magnetic field resolution was 0.25 T, and results obtained with such a resolution are presented in this chapter. Few more measurements at different temperatures were carried out with lower magnetic field resolution (0.5 T - 1.0 T). Those results are presented in the Appendix B.

The data is presented in a form of three figures for each temperature. The first figure presents a LL structure of a sample. Each level $L_{\xi,n,\sigma}$ is described by a set of three parameters ξ, n, σ , according to Equation 3.6. LLs with a different number n were plotted with different colors, without any distinction for the spin (\uparrow, \downarrow). A flat, black line represents the heavy-hole band with $\xi = 0$ ($L_{0,\{0,2,3,\dots\}\{\uparrow,\downarrow\}}$), red curves represent electron ($\xi = 1$) LLs with $n = 1$, namely $L_{1,1\{\uparrow,\downarrow\}}$. Consequently, blue curves represent LLs with $n = 2$ ($L_{1,2\{\uparrow,\downarrow\}}$), and green curves represent LLs with $n = 3$ ($L_{1,3\{\uparrow,\downarrow\}}$). Moreover,

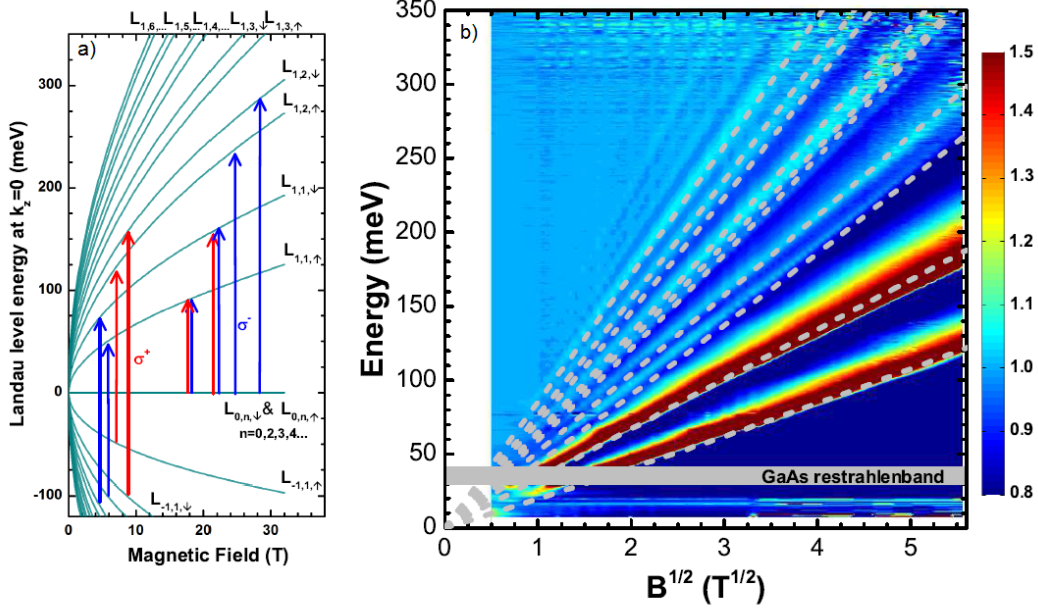


Figure 3.8: **Panel a)** Landau levels in gapless MCT, $L_{\xi,n,\sigma}$, as a function of the magnetic field, calculated using the eight-band model. Arrows of different colors show the optically allowed transitions in undoped gapless MCT in the two circular polarizations σ^+ and σ^- . **Panel b)** Relative change of absorbance $A_B/A_{B=0}$ plotted as a false color-map. All of the observed resonances clearly follow a \sqrt{B} -dependence. The dashed lines are calculated positions of inter-LL resonances at $k_z = 0$ using parameters $v_F = 1.06 \cdot 10^6$ m/s and $\Delta = 1$ eV. The presence of the spin-orbit split band, expressed by parameter Δ , does not qualitatively change the LL spectrum, but introduces a weak electron-hole asymmetry. These images come from the work [76].

visible transitions at given temperature are marked with arrows with a unique color and an assigned capital letter. There are two types of arrows – solid ones and dashed ones. Solid arrows indicate interband transitions while dashed arrows indicate intraband transitions.

The second figure is a colormap. It represents a plot of spectra in a form of a surface plot, where blue color represent a value of 1, and reddish colors represent lower values, usually around 0.5. The scale is adjusted to every colormap to make fainter transitions visible, while avoiding to saturate the scale. Colormaps for Sample B are plotted with x -axis in a \sqrt{B} scale to highlight the $E \propto \sqrt{B}$ behavior, which should appear as a straight line in a \sqrt{B} scale. This is not the case for Sample A, where the linear scale is preserved. The transitions are highlighted by white lines (representing the fits to the data) and an explicit description of the origin and final level of the transition. The same pattern of style (solid, dashed) of lines is applied to distinguish the interband from the intraband transitions, as in the LL plot.

Due to the phonon absorption, there are two regions of energy where the data acquisition was not possible, as the samples are completely opaque. Those regions are called reststrahlen bands. Phonon excitations can absorb up to 100% of incoming radiation, therefore the transmission is almost zero, and the signal-to-noise ratio is high. This means that the standard method of calculating the transmission spectra may give useless results. There are two reststrahlen bands in presented transmission results. One originates from the phonons of GaAs substrate (between 30 and 40 meV), the other from the phonons of HgCdTe itself (between 15 and 20 meV). This is why transmission results presented in this

Chapter have two grey stripes, covering relevant energy ranges.

The magnetic field resolution on a colormap seems to be higher than 0.25 T. This is due to the way the data is processed. In order to present data in a smooth and visibly clear way, the data was enhanced numerically by performing a linear extrapolation between consecutive spectra. This resulted in an artificial increase of magnetic field resolution and an appearance of unwanted artifacts in a form of oscillations of linewidth, visible near deep transitions. This effect is not physical, but numerical, and should be disregarded.

The third figure, composed of two panels, shows the way how data was fitted to transitions (left panels) and the raw transition spectra (right panels). The points on the left panels represent the position of minima of a given transition, and the color of a set of points is consistent with the color of the arrow from the LL plot. The spectra on a waterfall plot (right side) are plotted every 1 T and each consecutive spectrum is shifted vertically by an appropriate value for clarity. A symbol is added over every visible minimum to mark its position. The shape and color of symbols correspond to the symbols used on the left panel of the figure.

The curves obtained via fitting, are plotted on the colormaps as well. Each fit provided two parameters – the effective rest mass of carriers \tilde{m} and the carrier velocity \tilde{c} .

3.3.2.1 Sample A

Temperature 1.8 K

The temperature of 1.8 K is the lowest achievable in the experimental setup. The experimental conditions are similar to the ones of work [76] (Figure 3.8), as the sample is the same and the temperature is 1.8 K instead of 4 K. The band gap of the sample is positive and equal to 5 meV. There are no intraband transitions visible, most likely due to the limits of a sensitivity of the experimental set-up. The band structure is presented in Figure 3.9. Only the transitions A, B, E, and F are observable.

The colormap (Figure 3.10) shows that the transitions follow an almost $E \approx \sqrt{B}$ dependence. The band structure can be compared with a band structure of Sample B at 87 K, which is above the critical temperature. The transitions marked as A and B are the most intense ones. This is a consequence of an enormous density of states of the heavy-hole band in comparison to the density of states of the electron band, which is directly related to a probability of a transition and its strength. The high-energetic transitions E and F are barely visible.

Filled and open squares shown in Figure 3.11 represent interband and intraband transitions, respectively. The difference in intensity between interband and intraband transition is explicitly noticeable. The effective rest mass obtained from the fits, presented on Figure 3.11, turned out to be equal to $\tilde{m} = 0.61 \pm 0.34 \cdot 10^{-3} m_0$. The carrier velocity was estimated to be equal to $\tilde{c} = 1.062 \pm 0.089 \cdot 10^6$ m/s. The uncertainty of measurements, here and for all later fits, is based on a standard deviation of values obtained from all fitted transitions. At $T = 2$ K there were only four fits (to each transition), that is why the uncertainty of the effective mass is around 50%.

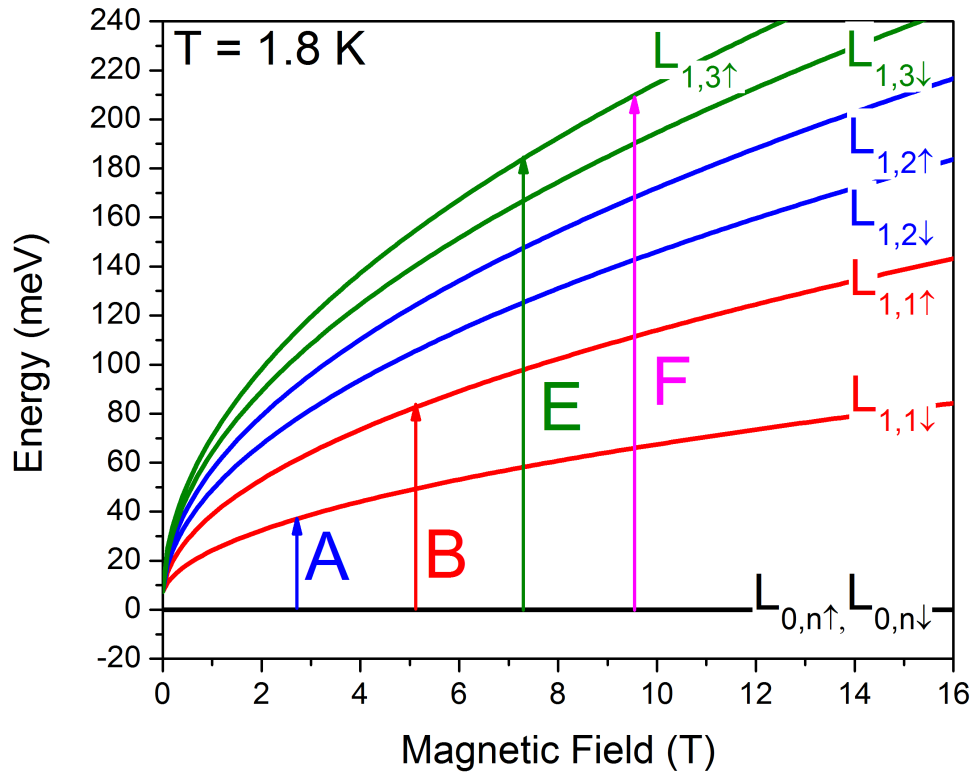


Figure 3.9: Landau level graph of Sample A as a function of magnetic field at $T = 1.8$ K. Colored lines represent Landau levels, characterized by different values of ϵ , n , and σ , as described as indices of L on the right side of the graph. The electron band Landau levels (with $\epsilon = 1$) have a near- \sqrt{B} behavior. The heavy-hole Landau level, plotted in black, is fully degenerated. The vertical arrows with corresponding capital letters represent observed transitions between Landau levels in this system. Solid arrows (A, B, E, and F) mark interband transitions.

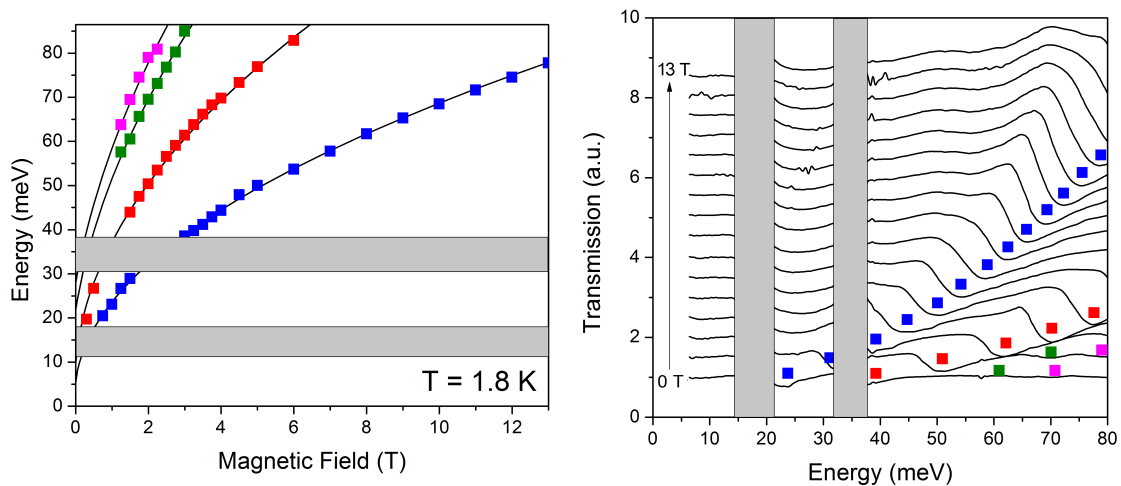


Figure 3.11: **Left panel:** Points corresponding to the minima of the transmission of Sample A at $T = 2$ K with fits showing the expected evolution of transitions as a function of magnetic field. **Right panel:** Transmission spectra plotted at magnetic fields in range from 0 to 13 T, with symbols corresponding to the transitions from left panel. Symbols represent interband transitions.

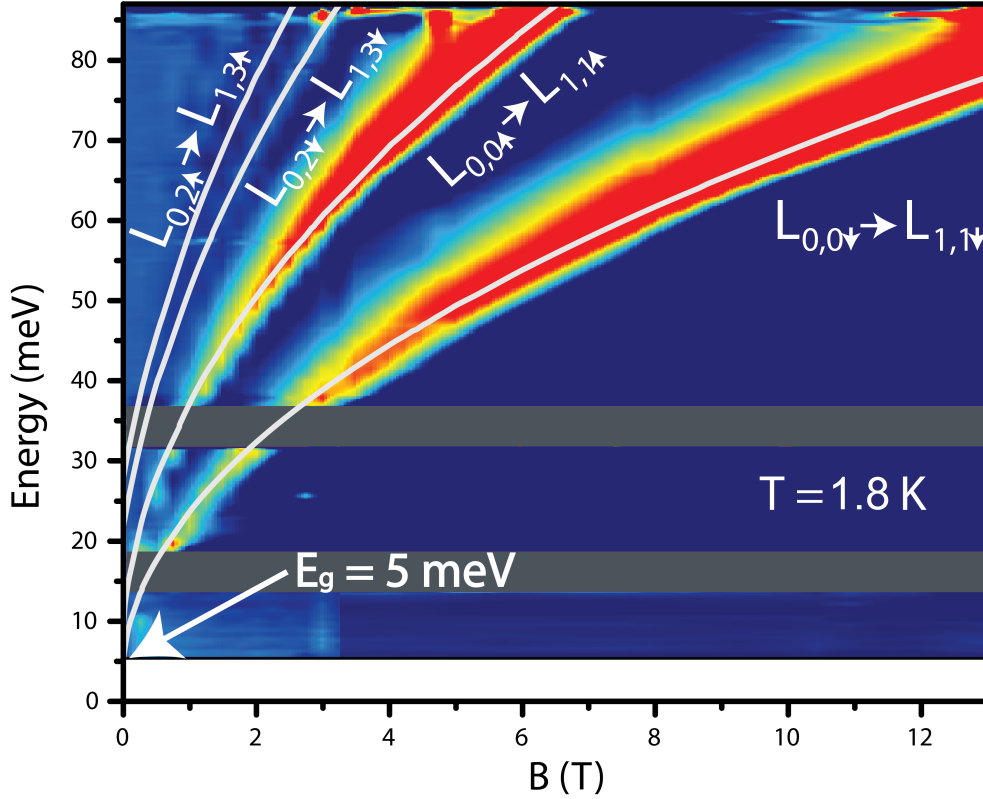


Figure 3.10: False color map of a transmission of Sample A as a function of energy and magnetic field at $T = 2$ K. Blue color represents areas where the transmission is equal to 1, while lightblue/yellow/red colors indicate where the absorption takes place. White curves show fits of the energy difference of Landau levels to the experimental points. White arrow points the value of the band gap.

Temperature 57 K

Temperature of 57 K slightly changed the band structure. The band gap increased to 28 meV. The transitions to LLs with $n = 3$ are not detectable anymore, therefore the LLs with $n = 3$ are not plotted on the LL graph presented in Figure 3.12, as they are irrelevant. At this temperature an intraband transition C became visible, represented by a dashed teal arrow.

The presence of the transition C allows to differentiate the intraband and interband transitions, which was difficult at $T = 2$ K, as all of the transitions converged close to zero energy and zero magnetic field. At $T = 57$ K the band gap is enlarged, thus there is a clear difference between the points of convergence for interband and intraband transitions, as it is presented on the color map in Figure 3.13.

The intensities of the transitions are not constant at the whole range of energies. The most pronounced example is an intensity of the transition C, which decreases at $E \approx 40$ meV, while the intensities of the transitions A and B increase radically. As was explained in Chapter 2, this is a consequence of the density of filled states and a position of the chemical potential, which lies around 40 meV above the heavy-hole band. Majority of the states below the chemical potential are occupied, so a transition from an occupied state into another occupied state is not possible. In this sense the transition A is less probable at magnetic field below ≈ 1 T, as the energy of level $L_{1,1\downarrow}$ lies below the chemical potential. On the other hand, the transition C is possible at low magnetic field, because the level $L_{1,1\downarrow}$ lies below the chemical potential while the level $L_{1,2\downarrow}$ lies above it. The situation changes

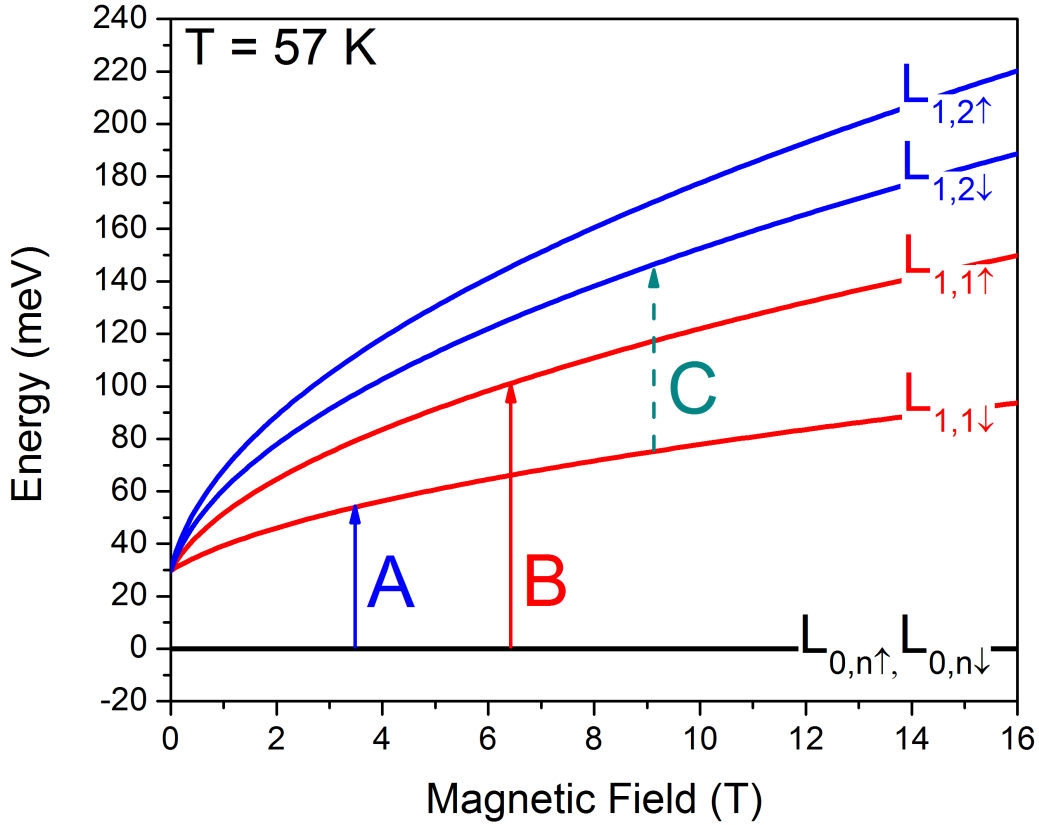


Figure 3.12: Landau level graph of Sample A as a function of magnetic field at $T = 57$ K. Colored lines represent Landau levels, characterized by different values of ε , n , and σ , as described as indices of L on the right side of the graph. The electron band Landau levels (with $\varepsilon = 1$) have a near- \sqrt{B} behavior. The heavy-hole Landau level, plotted in black, is fully degenerated. The vertical arrows with corresponding capital letters represent observed transitions between Landau levels in this system. Solid arrows (A and B) mark interband transitions, while dashed arrow (C) marks an intraband transition.

at around $B = 3$ T, where both levels lie above the chemical potential, thus there are no occupied states to execute a transition.

A new feature appeared on the color map at the energy of around 10 meV. This horizontal feature is attributed to an absorption on defects of the structure. To be more precise on the mercury vacancies, which act as a doubly-ionized acceptor centers [95], which got thermally activated by the elevated temperature. The fits allowed to estimate the effective rest mass to be equal to $\tilde{m} = 2.82 \pm 0.77 \cdot 10^{-3} m_0$, and the carrier velocity to be equal to $\tilde{c} = 1.057 \pm 0.060 \cdot 10^6$ m/s.

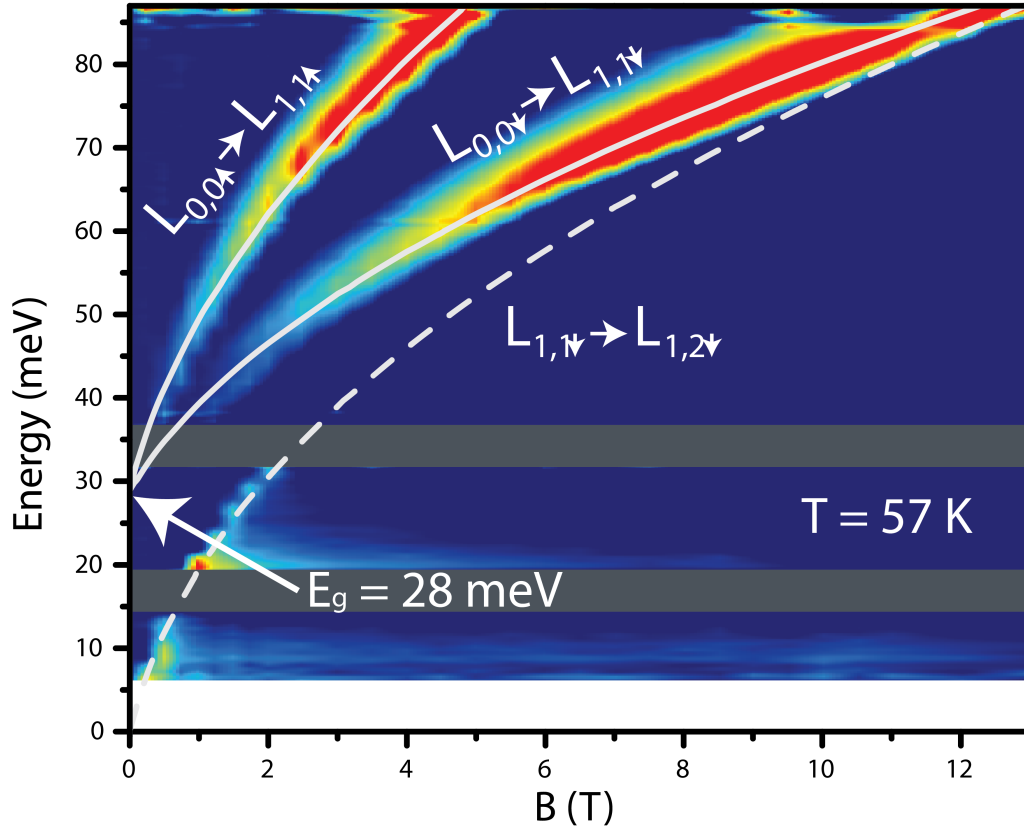


Figure 3.13: *False color map of a transmission of Sample A as a function of energy and magnetic field at $T = 57$ K. Blue color represents areas where the transmission is equal to 1, while lightblue/yellow/red colors indicate where the absorption takes place. White curves show fits of the energy difference of Landau levels to the experimental points. White arrow points the value of the band gap.*

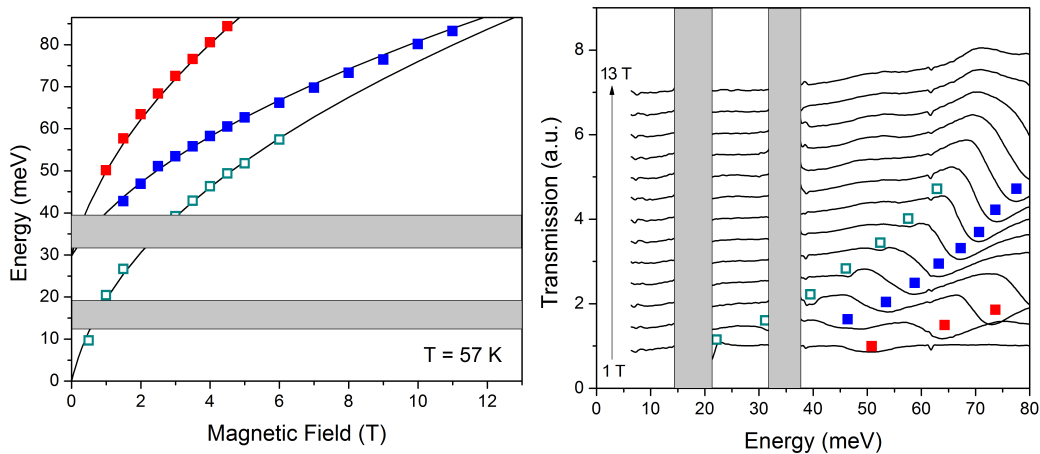


Figure 3.14: **Left panel:** *Points corresponding to the minima of the transmission of Sample A at $T = 57$ K with fits showing the expected evolution of transitions as a function of magnetic field.* **Right panel:** *Transmission spectra plotted at magnetic fields in range from 0 to 13 T, with symbols corresponding to the transitions from left panel. Open (full) symbols represent intraband (interband) transitions.*

Temperature 77 K

At the temperature of 77 K the band gap increases further to 36 meV. The transitions A, B, and C are still visible. A new interband transition D becomes detectable, as it is shown in Figure 3.15 as a dashed orange arrow.

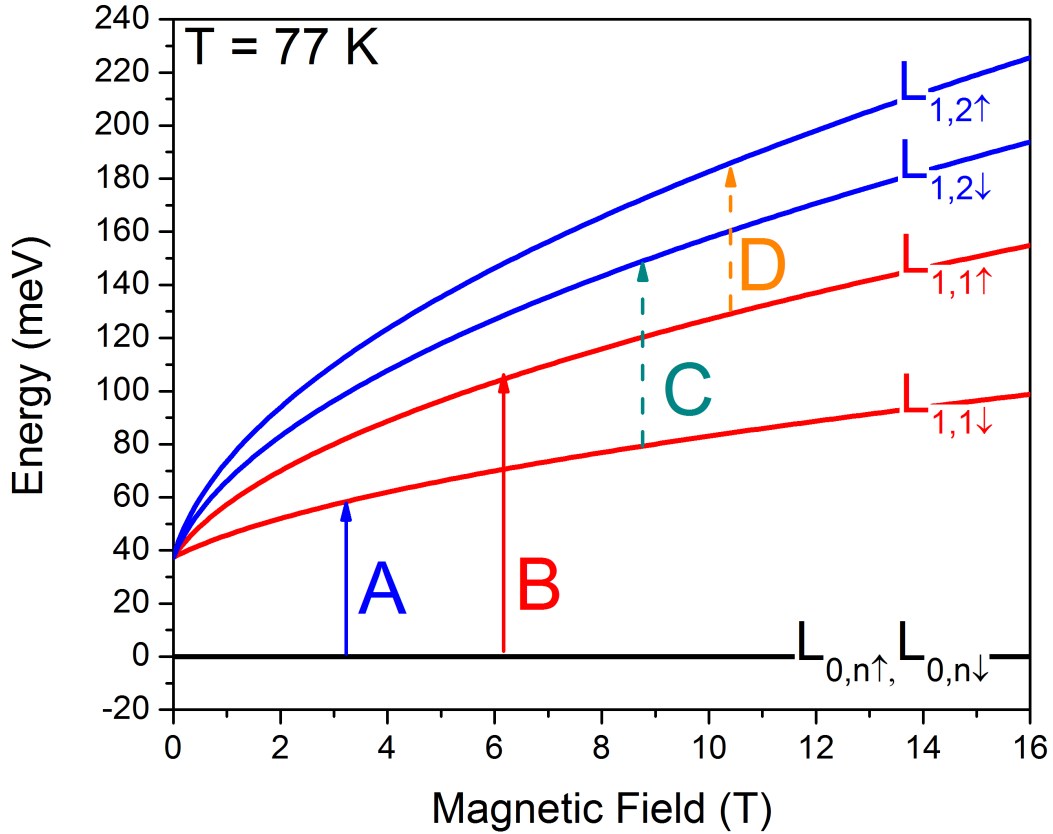


Figure 3.15: Landau level graph of Sample A as a function of magnetic field at $T = 77$ K. Colored lines represent Landau levels, characterized by different values of ε , n , and σ , as described as indices of L on the right side of the graph. The electron band Landau levels (with $\varepsilon = 1$) have a near- \sqrt{B} behavior. The heavy-hole Landau level, plotted in black, is fully degenerated. The vertical arrows with a corresponding capital letter represent observed transitions between Landau levels in this system. Solid arrows (A and B) are interband transitions, while dashed arrows (C and D) are intraband transitions.

The temperature is high enough to lift the chemical potential up to around 45 meV, which causes transitions A and B to gain intensity above this energy, while transitions C and D become fainter. The horizontal feature, related to absorption on Hg vacancies becomes more pronounced. Also, at this temperature it is accompanied by a second feature (visible at energies around 20 meV) just above the reststrahlen band of HgTe. This absorption is related to the energy of TO CdTe-like phonons, arising in a magneto-absorption due to the electron-phonon interactions. The frequency of these phonon modes is independent on temperature [96].

The fits to experimental data allowed to estimate the effective rest mass to be equal to $\tilde{m} = 3.19 \pm 0.41 \cdot 10^{-3} m_0$, and the carrier velocity to be equal to $\tilde{c} = 1.049 \pm 0.052 \cdot 10^6$ m/s.

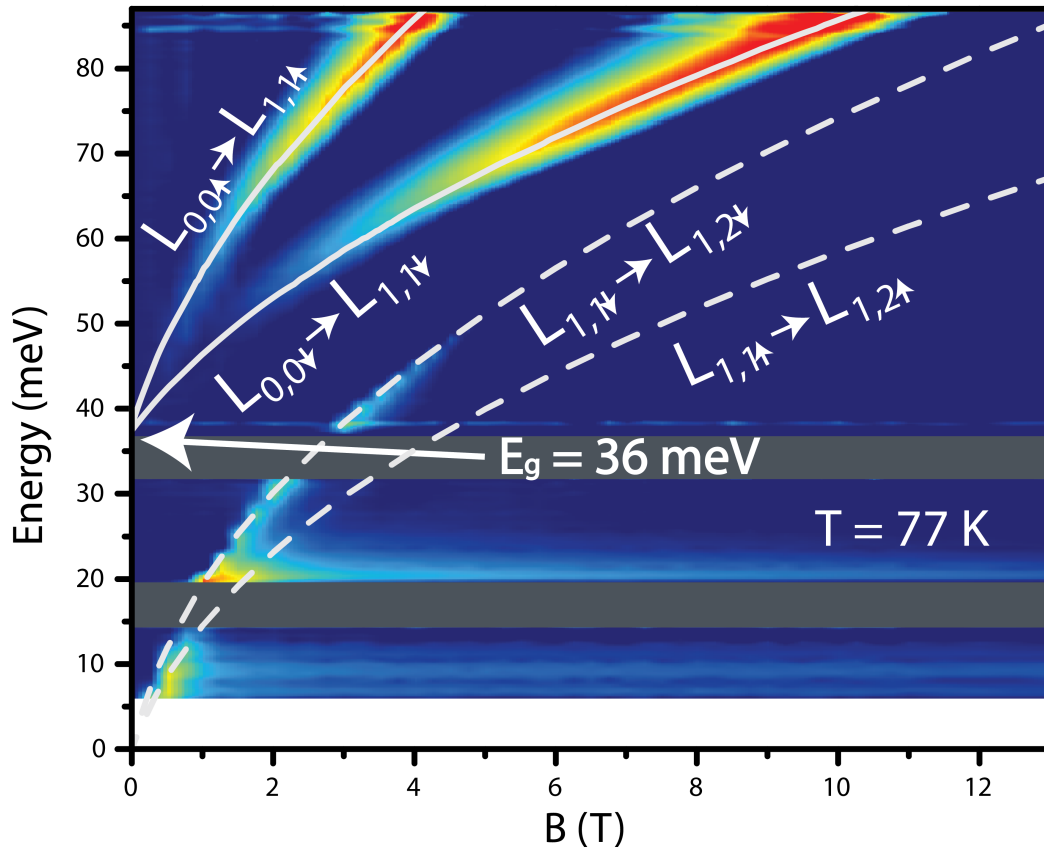


Figure 3.16: *False color map of a transmission of Sample A as a function of energy and magnetic field at $T = 77$ K. Blue color represents areas where the transmission is equal to 1, while lightblue/yellow/red colors indicate where the absorption takes place. White curves show fits of the energy difference of Landau levels to the experimental points. White arrow points the value of the band gap.*

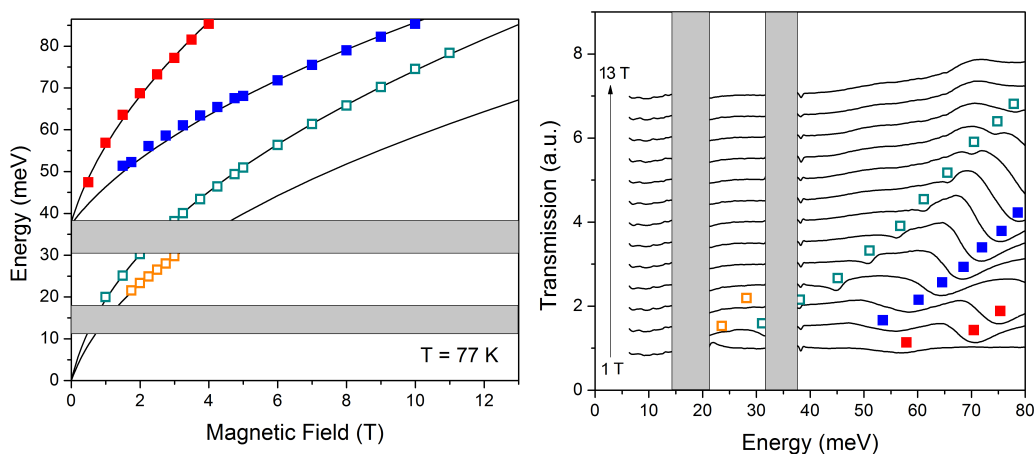


Figure 3.17: **Left panel:** *Points corresponding to the minima of the transmission of Sample A at $T = 77$ K with fits showing the expected evolution of transitions as a function of magnetic field.* **Right panel:** *Transmission spectra plotted at magnetic fields in range from 0 to 13 T, with symbols corresponding to the transitions from left panel. Open (full) symbols represent intraband (interband) transitions.*

Temperature 120 K

At $T = 120$ K the band gap of Sample A reaches as much as 59 meV, as it is shown in Figure 3.30. The number of detectable transitions at that temperature is the same, as in the case of $T = 77$ K – the transitions A, B, C, and D are visible.

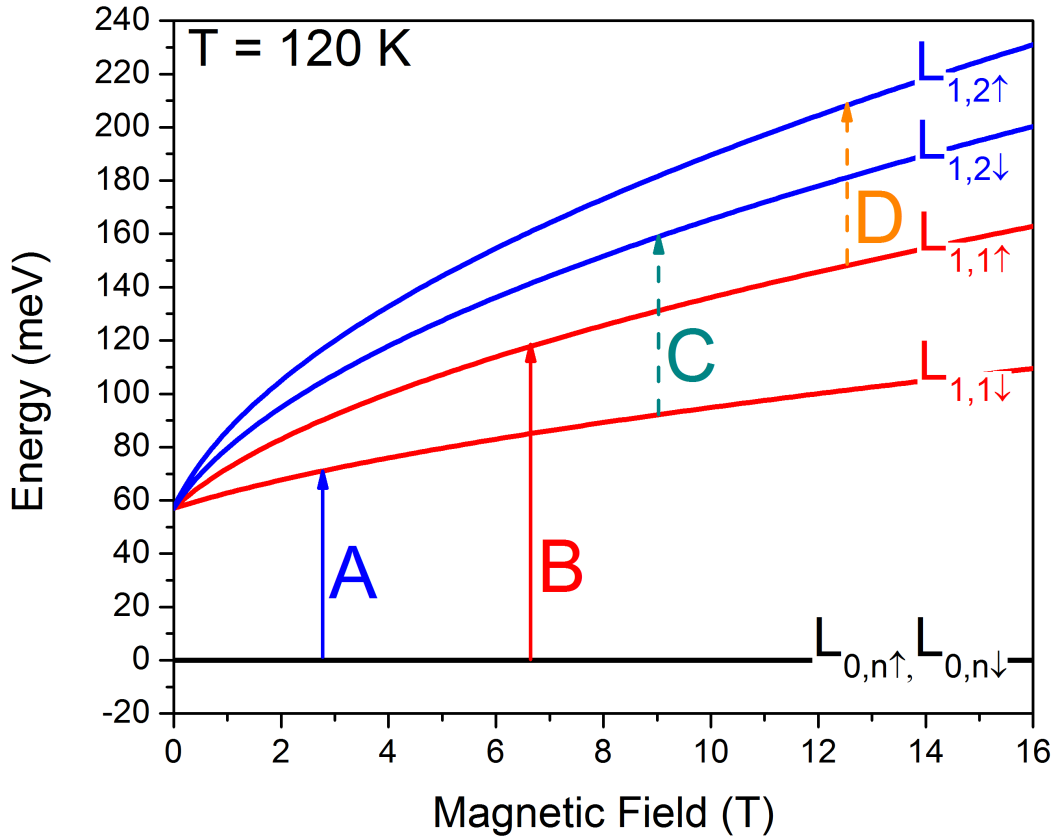


Figure 3.18: Landau level graph of Sample A as a function of magnetic field at $T = 120$ K. Colored lines represent Landau levels, characterized by different values of ε , n , and σ , as described as indices of L on the right side of the graph. The electron band Landau levels (with $\varepsilon = 1$) have a near- \sqrt{B} behavior. The heavy-hole Landau level, plotted in black, is fully degenerated. The vertical arrows with corresponding capital letters represent observed transitions between Landau levels in this system. Solid arrows (A and B) are interband transitions, while dashed arrows (C and D) are intraband transitions.

Due to the position of the chemical potential, which lies more than 80 meV above the heavy-hole band, the transitions A and B are not visible at low magnetic field. Moreover, the transitions C and D vanish at high magnetic fields, as the filling factor changes.

The fits to experimental points are very accurate for available data (Figure 3.32). The temperature related features become even stronger, as the thermal energy at 120 K is slightly more than 10 meV. The fits allowed to estimate the effective rest mass to be equal to $\tilde{m} = 3.38 \pm 0.46 \cdot 10^{-3} m_0$, and the carrier velocity to be equal to $\tilde{c} = 1.037 \pm 0.027 \cdot 10^6$ m/s.

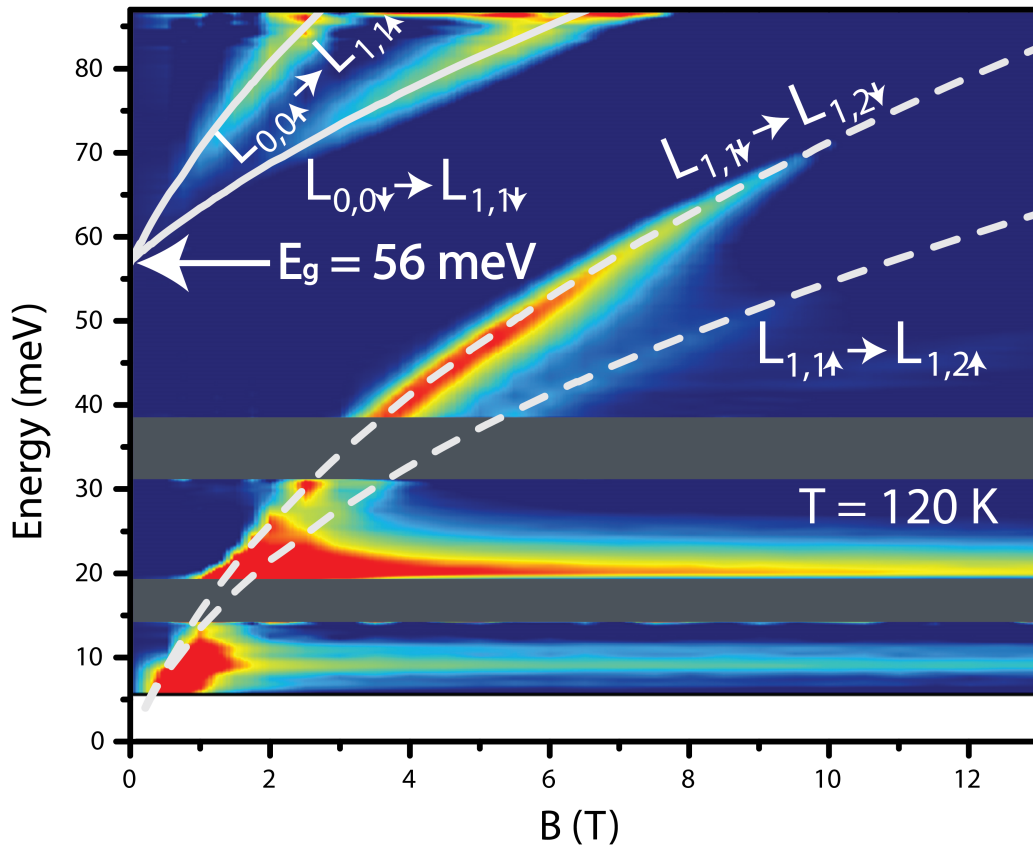


Figure 3.19: False color map of transmission of Sample A as a function of energy and magnetic field at $T = 120$ K. Blue color represents areas where transmission is equal to 1, while lightblue/yellow/red colors indicate where absorption takes place. White curves show fits of the energy difference of Landau levels to the experimental points. White arrow points the value of the band gap.

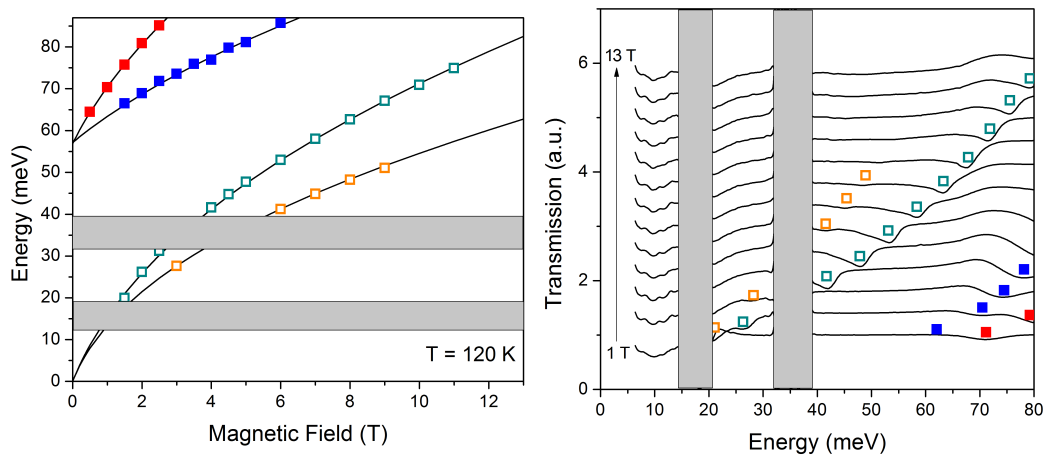


Figure 3.20: **Left panel:** Points corresponding to the minima of the transmission of Sample A at $T = 120$ K with fits showing the expected evolution of transitions as a function of magnetic field. **Right panel:** Transmission spectra plotted at magnetic fields in range from 0 to 13 T, with symbols corresponding to the transitions from left panel. Open (full) symbols represent intraband (interband) transitions.

3.3.2.2 Sample B

Temperature 1.8 K

At the temperature 1.8 K Sample B is in the inverted regime with the largest negative band gap. The LL structure of the Sample B is presented in Figure 3.21. All of the LLs originating from both electron and heavy-hole bands converge as the magnetic field goes to zero, even though the sample has a negative energy gap. This is explained by the model via Equation 3.6. By assuming the energy gap to have a non-positive value and putting $B = 0$, the whole expression equals to zero. There are six observable transitions – four interband, marked with solid lines, and two intraband, marked with dashed lines.

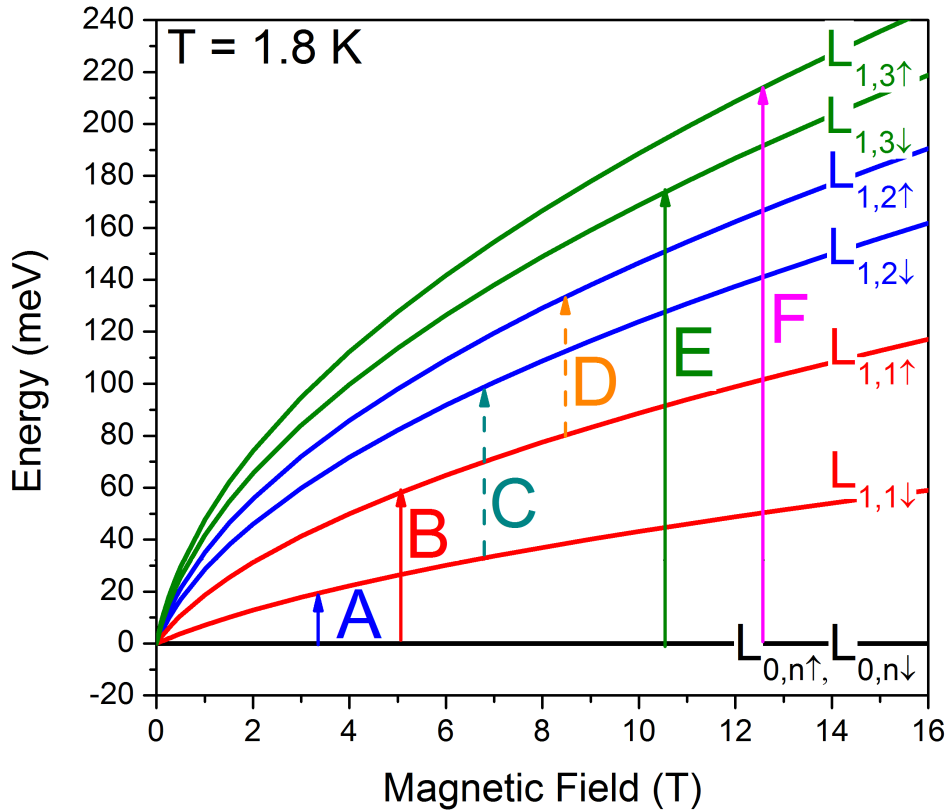


Figure 3.21: Landau level graph of Sample B as a function of magnetic field at $T = 1.8$ K. Colored lines represent Landau levels, characterized by different values of ε , n , and σ , as described as indices of L on the right side of the graph. The electron band Landau levels (with $\varepsilon = 1$) have a near- \sqrt{B} behavior. The heavy-hole Landau level, plotted in black, is fully degenerated. The vertical arrows with corresponding capital letters represent observed transitions between Landau levels in this system. Solid arrows (A, B, E, and F) are interband transitions, while dashed arrows (C, D) are intraband transitions.

All of the observed transitions are presented in Figure 3.22. A green dashed line was plotted on the figure to give an idea about a value of the energy gap. It was drawn as an extrapolation of the transition A at high magnetic fields. One way to understand this is to invoke Equation 3.6. There are two factors under the square root, first depends on the energy gap, and second depends on magnetic field. For high magnetic fields the first factor is negligible, so the whole expression formally resembles an expression in a form of $E(B) = E_g/2 + \sqrt{\alpha B}$, where α is a constant. This equation can be plotted

as a straight line in a \sqrt{B} scale and it intercepts the y -axis exactly where $E(B = 0) = E_g/2$, which gives an indication of the value of the band gap divided by two. In Figure 3.22 this value is marked with a black arrow and equals to -12 meV, which translates to $E_g = -24$ meV.

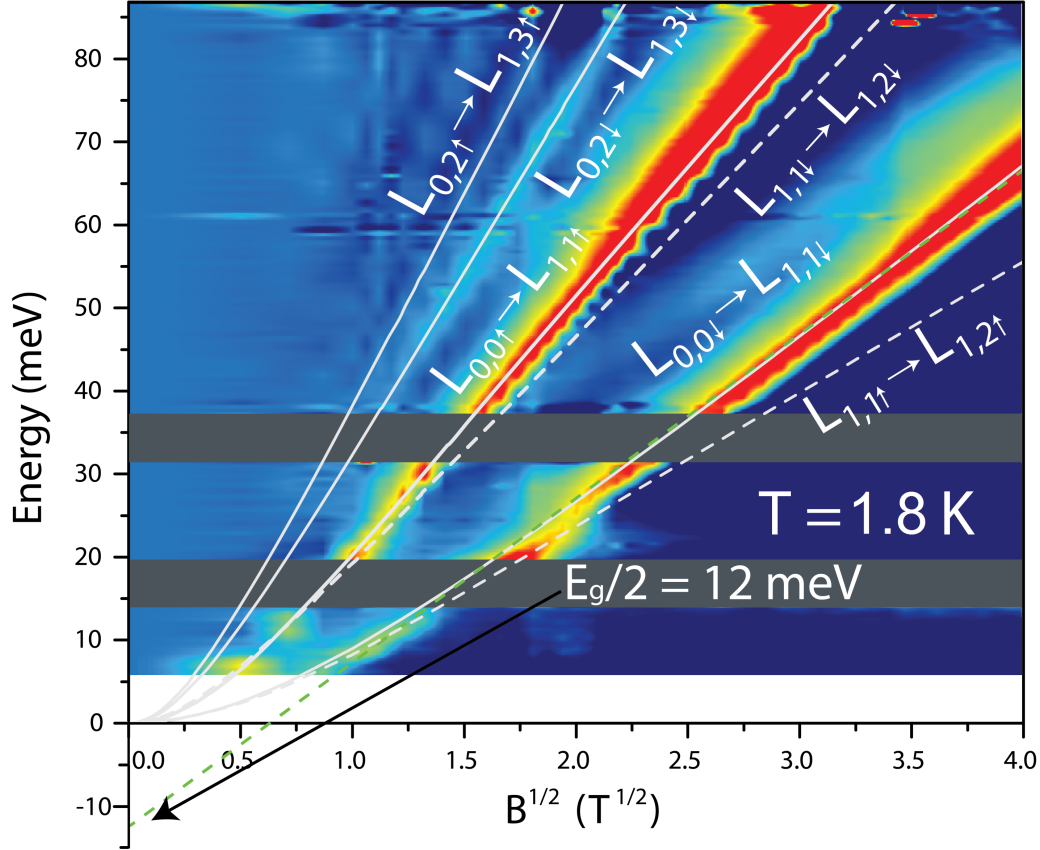


Figure 3.22: False color map of the transmission of Sample B as a function of energy and magnetic field at $T = 2$ K. Magnetic field is presented in a \sqrt{B} scale. Blue color represents areas where the transmission is equal to 1, while lightblue/yellow/red colors indicate where the absorption takes place. White curves show fits of the energy difference of Landau levels to the experimental points. The green dashed line is an extrapolation of the transition $L_{0,0\downarrow} \rightarrow L_{1,1\downarrow}$, which points the value of the (negative) band gap.

The colormap (Figure 3.22) shows that the transitions follow a dependence, which is neither linear nor \sqrt{B} -like, but resembles a mixture of these two. This is expected because the dispersion relation is neither parabolic nor exactly Dirac-like, as there is a finite (negative) band gap.

The fits to experimental points and the waterfall plot of transmission spectra are presented in Figure 3.23. On Panel a) there is an unknown transition, represented by grey points, which is visible as well in Figure 3.22. The fits allowed to estimate the effective rest mass to be equal to $\tilde{m} = -1.91 \pm 0.58 \cdot 10^{-3} m_0$, and the carrier velocity to be equal to $\tilde{c} = 1.091 \pm 0.069 \cdot 10^6$ m/s.

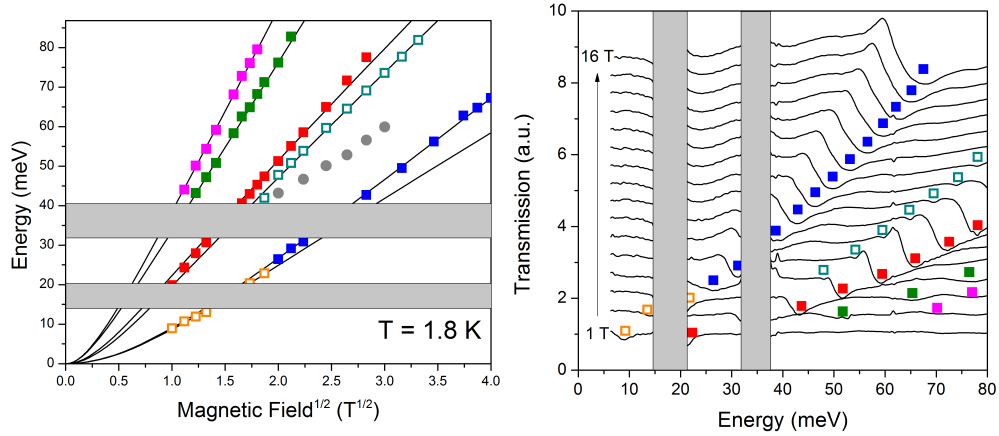


Figure 3.23: **Left panel:** Points corresponding to the minima of transmission of Sample B at $T = 1.8$ K with fits showing the expected evolution of the transitions as a function of magnetic field. **Right panel:** Transmission spectra plotted at magnetic fields in range from 0 to 16 T, with symbols corresponding to the transitions from left panel. Open (full) symbols represent intraband (interband) transitions.

Temperature 37 K

Temperature of 37 K slightly changed the band structure, as shown in Figure 3.24. The negative energy gap got smaller, down to -14 meV. The LLs still converge at zero magnetic field. The most noticeable change is a disappearance of the transition F.

Transitions C, D and E are faint in general, as their probability is relatively low, as is presented on the color map in Figure 3.25. The horizontal feature (at around 10 meV) related to absorption on mercury vacancies, starts to be visible. The position of the Fermi level lies close to 25 meV above the heavy hole band, as the intensity of transitions A i D switch. However, both transitions are further separated in comparison with the situation at $T = 1.8$ K. This can be explained by a change of the Fermi distribution as the temperature is increased. The fits allowed to estimate the effective rest mass to be equal to $\tilde{m} = -1.44 \pm 0.68 \cdot 10^{-3} m_0$, and the carrier velocity to be equal to $\tilde{c} = 1.052 \pm 0.052 \cdot 10^6$ m/s.

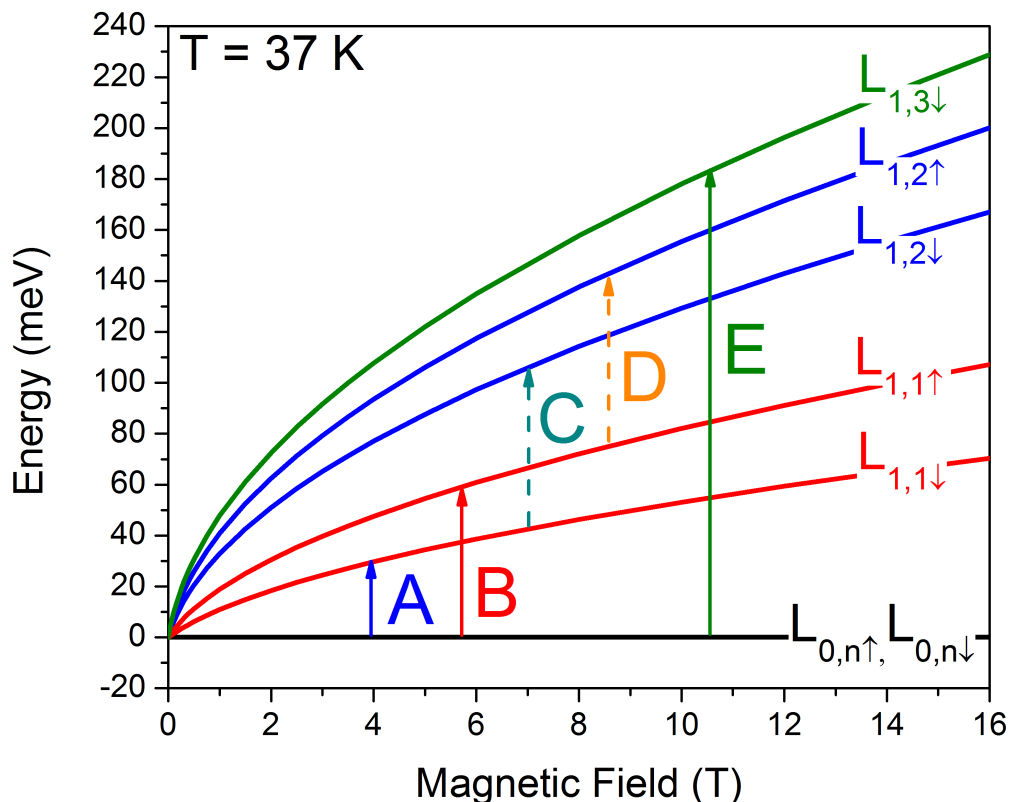


Figure 3.24: Landau level graph of Sample B as a function of magnetic field at $T = 37$ K. Colored lines represent Landau levels, characterized by different values of ε , n , and σ , as described as indices of L on the right side of the graph. The electron band Landau levels (with $\varepsilon = 1$) have a near- \sqrt{B} behavior. The heavy-hole Landau level, plotted in black, is fully degenerated. The vertical arrows with corresponding capital letters represent observed transitions between Landau levels in this system. Solid arrows (A, B, and E) are interband transitions, while dashed arrows (C and D) are intraband transitions.

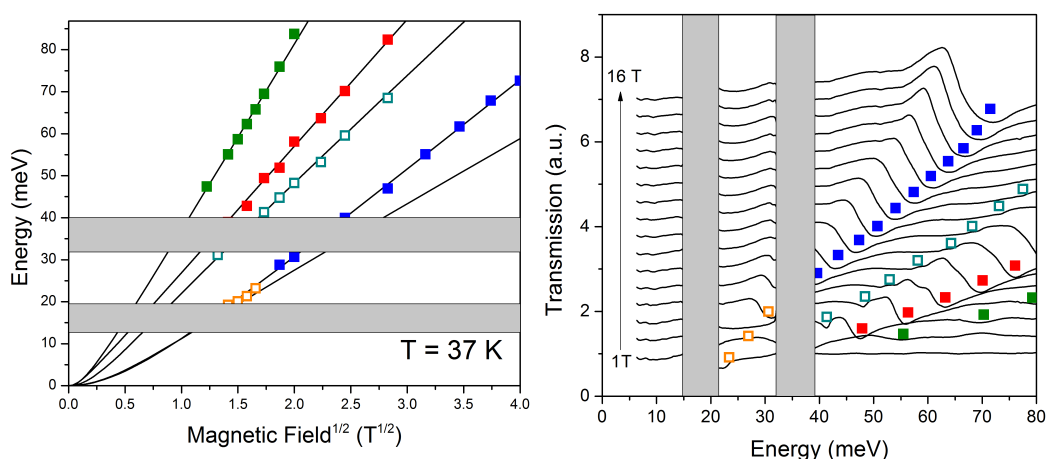


Figure 3.26: **Left panel:** Points corresponding to the minima of the transmission of Sample B at $T = 37$ K with fits showing the expected evolution of transitions as a function of magnetic field. **Right panel:** Transmission spectra plotted at magnetic fields in range from 0 to 16 T, with symbols corresponding to the transitions from left panel. Open (full) symbols represent intraband (interband) transitions.

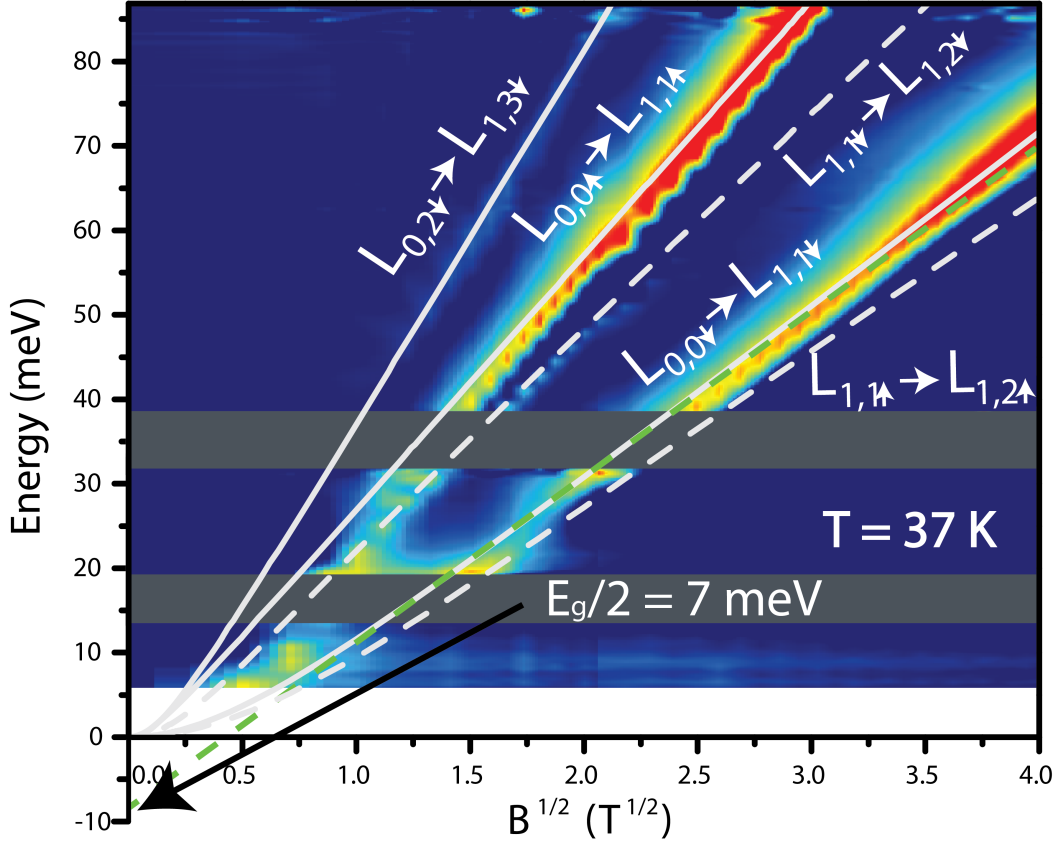


Figure 3.25: False color map of the transmission of Sample B as a function of energy and magnetic field at $T = 37$ K. Magnetic field is presented in a \sqrt{B} scale. Blue color represents areas where the transmission is equal to 1, while lightblue/yellow/red colors indicate where the absorption takes place. White curves show fits of the energy difference of Landau levels to the experimental points. The green dashed line is an extrapolation of transition $L_{0,0\downarrow} \rightarrow L_{1,1\downarrow}$, which points the value of the (negative) band gap.

Temperature 77 K

The temperature of 77 K is the critical temperature for Sample B. This is where the band gap vanishes completely and the dispersion relation is linear and is formed by a Dirac cone. The amount of detectable transitions is the same as at $T = 37$ K, however the transition E becomes even fainter and more difficult to detect.

The Figure 3.27 presents that the band gap is zero and LLs follow precisely a \sqrt{B} dependence on energy. This means that all of the LLs converge at zero magnetic field. As a consequence, all the transitions follow an exact \sqrt{B} dependence on energy as well, as presented on a color map in Figure 3.28.

The temperature is high enough to lift the chemical potential up to around 50 meV, which causes transitions A and B to gain intensity above this energy, while transitions C and D become fainter. The transition E is barely visible. Both horizontal features related to absorption on defects become more pronounced at this temperature.

The fits allowed to estimate the effective rest mass to be equal to $\tilde{m} = -0.49 \pm 0.53 \cdot 10^{-3} m_0$, and the carrier velocity to be equal to $\tilde{c} = 1.056 \pm 0.001 \cdot 10^6$ m/s. The effective rest mass at $T = 77$ K is the lowest observed in this experiment. The value is not equal to zero as, firstly, it resulted from

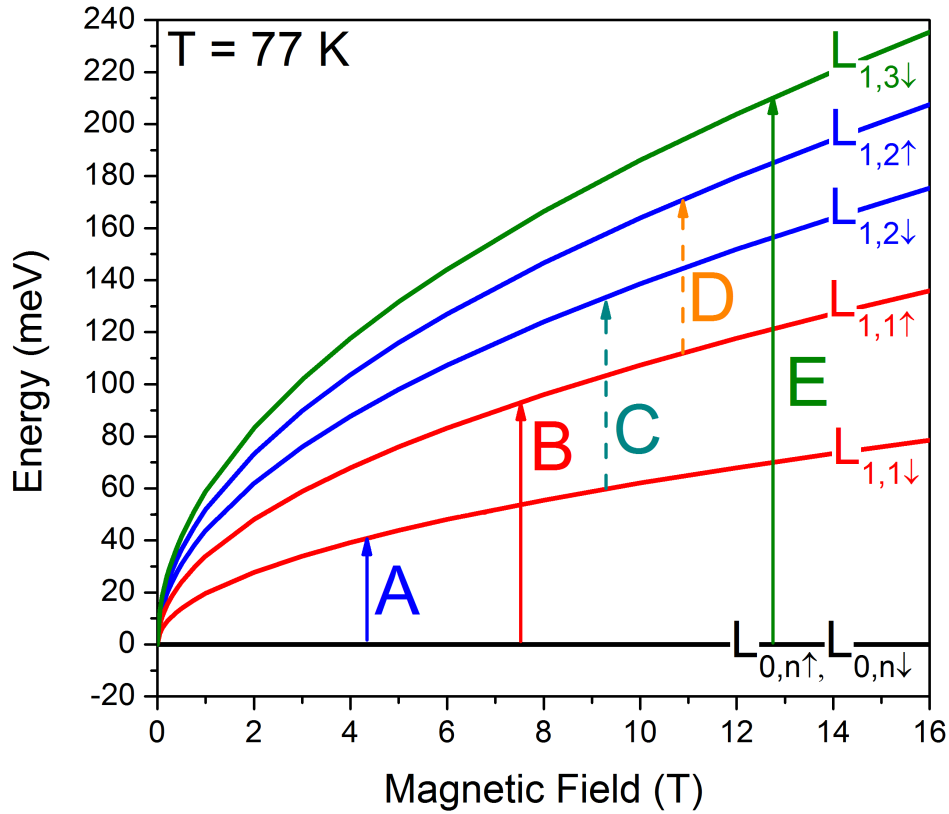


Figure 3.27: Landau level graph of Sample B as a function of magnetic field at $T = 77$ K. Colored lines represent Landau levels, characterized by different values of ε , n , and σ , as described as indices of L on the right side of the graph. The electron band Landau levels (with $\varepsilon = 1$) have a near- \sqrt{B} behavior. The heavy-hole Landau level, plotted in black, is fully degenerated. The vertical arrows with corresponding capital letters represent observed transitions between Landau levels in this system. Solid arrows (A, B, and E) are interband transitions, while dashed arrows (C and D) are intraband transitions.

an approximate theory relating energy gap with effective rest mass, and secondly, it was obtained by performing fits to the experimental data, which are always flawed by an uncertainty.

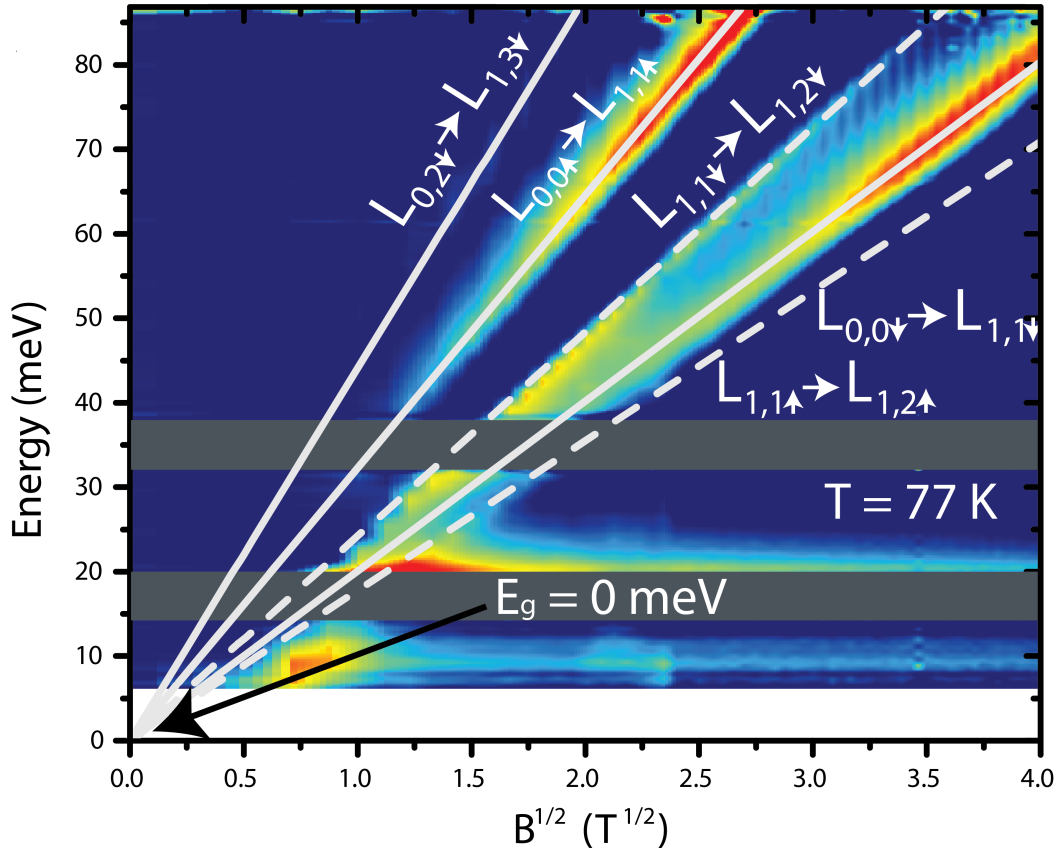


Figure 3.28: *False color map of the transmission of Sample B as a function of energy and magnetic field at $T = 77$ K. Magnetic field is presented in a \sqrt{B} scale. Blue color represents areas where the transmission is equal to 1, while lightblue/yellow/red colors indicate where the absorption takes place. White curves show fits of the energy difference of Landau levels to the experimental points. All of the transitions converge at $B = 0$ T, when the band gap vanishes.*

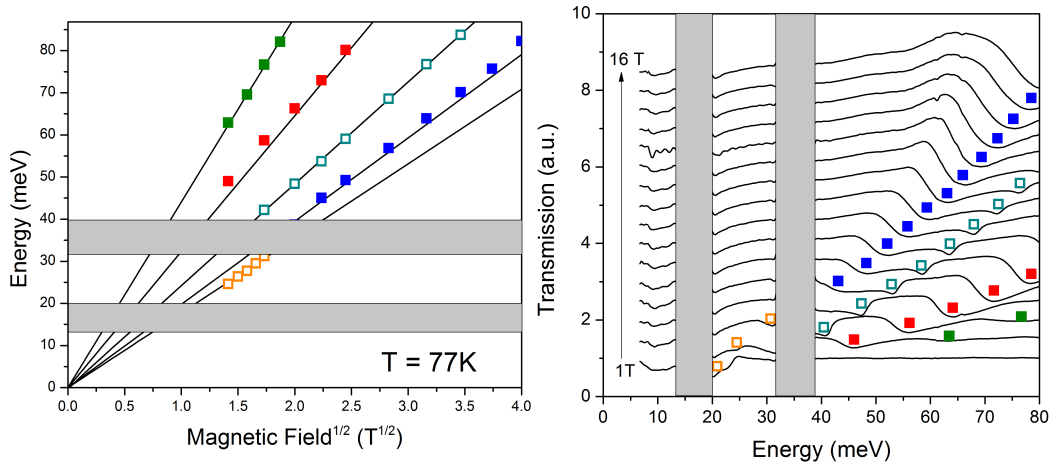


Figure 3.29: **Left panel:** *Points corresponding to the minima of the transmission of Sample B at $T = 77$ K with fits showing the expected evolution of transitions as a function of magnetic field.* **Right panel:** *Transmission spectra plotted at magnetic fields in range from 0 to 16 T, with symbols corresponding to the transitions from left panel. Open (full) symbols represent intraband (interband) transitions.*

Temperature 120 K

Above the critical temperature of 77 K Sample B becomes semiconducting, as the band gap opens. At $T = 120$ K the band gap reaches as much as 18 meV, as is shown in Figure 3.30. The number of detectable transitions diminished, as only transitions A, C, and D are visible.

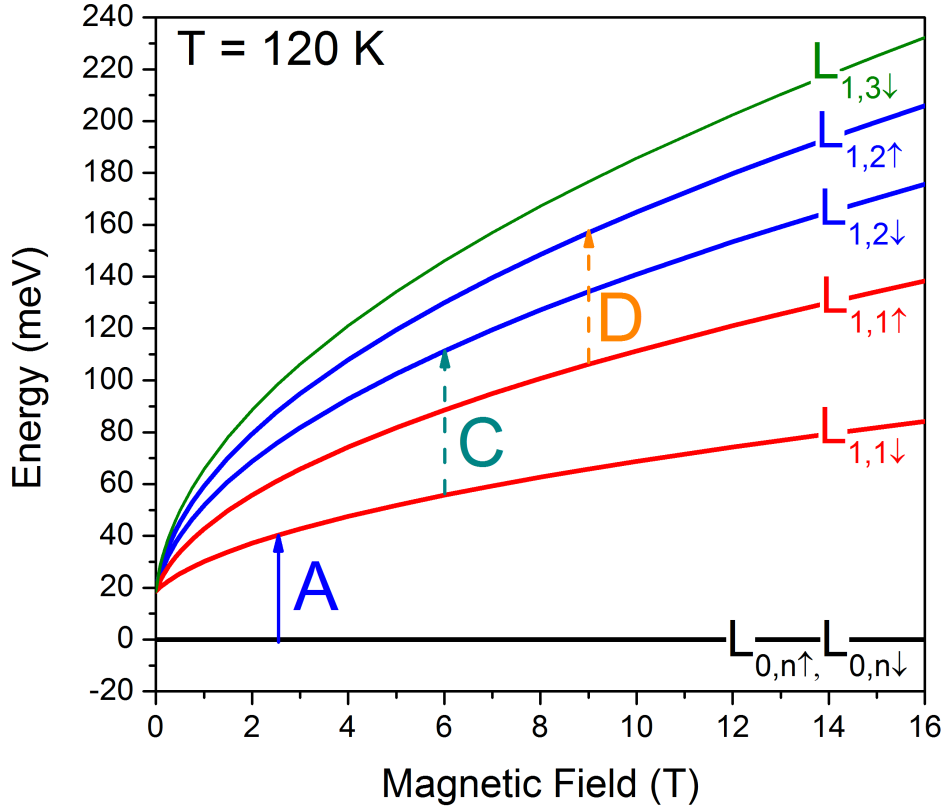


Figure 3.30: Landau level graph of Sample B as a function of magnetic field at $T = 120$ K. Colored lines represent Landau levels, characterized by different values of ε , n , and σ , as described as indices of L on the right side of the graph. The electron band Landau levels (with $\varepsilon = 1$) have a near- \sqrt{B} behavior. The heavy-hole Landau level, plotted in black, is fully degenerated. The vertical arrows with corresponding capital letters represent observed transitions between Landau levels in this system. The solid arrow (A) is an interband transition, while dashed arrows (C and D) are intraband transitions.

An interband transition A, for the first time for Sample B, does not converge at zero energy at zero magnetic field. This is a direct indication that the band gap has opened. When the band gap is positive, at zero magnetic field it points exactly to the value of the band gap, which is presented in Figure 3.31. Due to the position of the chemical potential, being more than 80 meV above the heavy-hole band, the transition A is not visible at small magnetic field. Because of the same reason the transition D vanishes at high magnetic fields. However, the fit to experimental points is very accurate for available data (Figure 3.32).

The temperature related features become even stronger, as the thermal energy at 120 K is higher than 10 meV. The fits allowed to estimate the effective rest mass to be equal to $\tilde{m} = 2.15 \pm 0.46 \cdot 10^{-3} m_0$, and the carrier velocity to be equal to $\tilde{c} = 1.010 \pm 0.007 \cdot 10^6$ m/s.

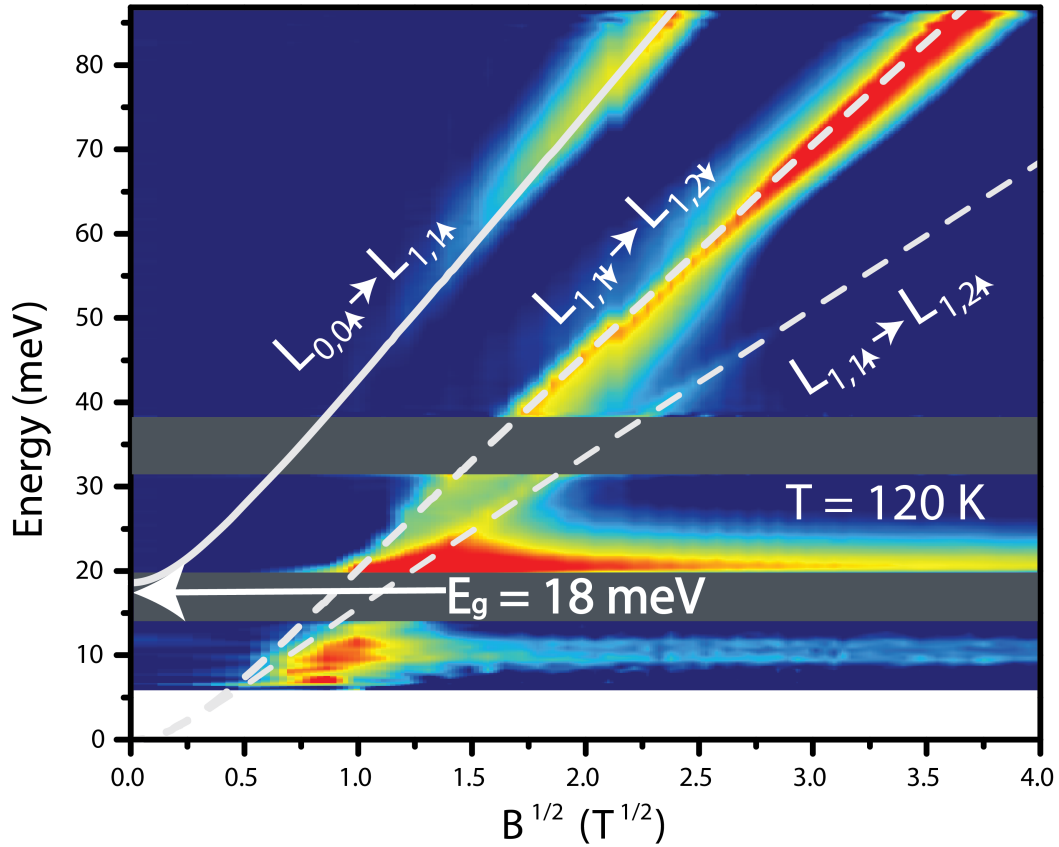


Figure 3.31: False color map of the transmission of Sample B as a function of energy and magnetic field at $T = 120$ K. Magnetic field is presented in a \sqrt{B} scale. Blue color represents areas where the transmission is equal to 1, while lightblue/yellow/red colors indicate where the absorption takes place. White curves show fits of the energy difference of Landau levels to the experimental points. White arrow points the value of the band gap.

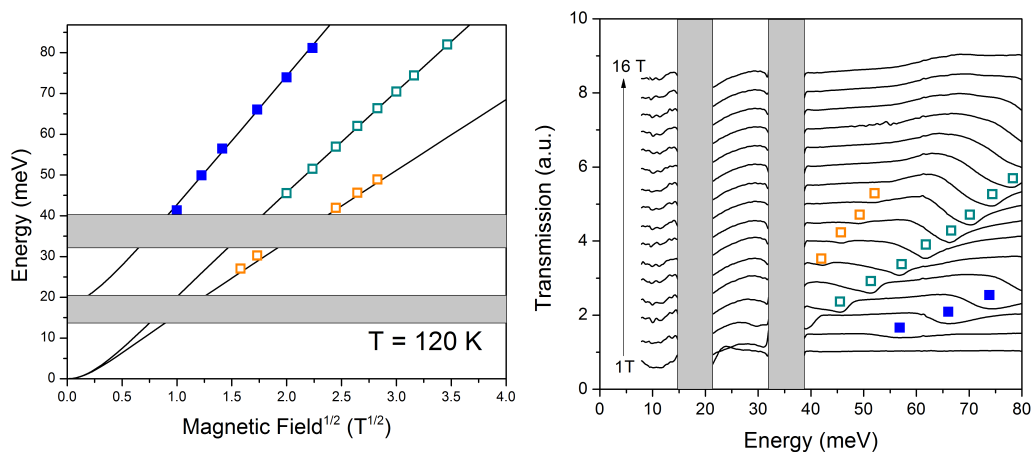


Figure 3.32: **Left panel:** Points corresponding to the minima of the transmission of Sample B at $T = 120$ K with fits showing the expected evolution of transitions as a function of magnetic field. **Right panel:** Transmission spectra plotted at magnetic fields in range from 0 to 16 T, with symbols corresponding to the transitions from left panel. Open (full) symbols represent intraband (interband) transitions.

3.3.3 Summary

The results presented in this chapter present in a direct and straightforward way the evolution of the band structure of bulk $\text{Hg}_{1-x}\text{Cd}_x\text{Te}$ crystals characterized by a cadmium concentration close to the critical. Results based on two samples were shown and compared to easily highlight the differences of the band structure between a regular and an inverted band order systems. The temperature evolution of the band gap and a semiconductor-to-semimetal phase transition was studied by the means of magneto-spectroscopy.

A critical temperature was found by an investigation of LLs evolution as a function of magnetic field – at the critical temperature two conditions must be met:

- All transitions between LLs have to follow an $E \propto \sqrt{B}$ dependence at a broad scale of magnetic fields and energies,
- All transitions between LLs have to converge to zero energy at zero magnetic field, showing that the band gap vanishes.

Those conditions were met by Sample B with cadmium concentration of $x = 0.155$ at the temperature $T_c = 77$ K. Moreover, a positive band gap opening was registered at higher temperature $T > T_c$, as the interband transitions converged at $B = 0$ T at nonzero energy. The value of the band gap increased as the temperature got higher. This process was expected due to the study of Sample A, which band gap was positive at the whole range of temperatures, and its value increased with temperature.

These results are the first evidence of a temperature induced phase transition investigated by the THz magneto-spectroscopy on bulk HgCdTe structures with well-chosen chemical composition. The genuine Kane fermions were observed at the critical temperature of 77 K. In order to describe and analyze the data, the simplified Kane model was used. It allowed to determine the pseudo-relativistic Dirac-like Kane fermions parameters \tilde{m} and \tilde{c} as a function of temperature and cadmium concentration. The nonzero rest mass obtained from fits at the critical temperature corresponds to the limit of precision of the experimental set-up. The results are in agreement with theoretical predictions and are consistent with the data obtained previously by Orlita *et al.* [76].

The magnetic field evolution of the transitions is shown explicitly in Figure 3.33, where the transition $L_{0,0\downarrow} \rightarrow L_{1,1\downarrow}$ is shown for the broad range of temperatures between 2 K and 87 K. For $T = 120$ K the transition $L_{0,0\uparrow} \rightarrow L_{1,1\uparrow}$ was plotted instead, as the transition $L_{0,0\downarrow} \rightarrow L_{1,1\downarrow}$ is not visible. The x -axis is presented in a \sqrt{B} scale for clarity. The band gap is negative for all the temperatures below the critical, and the dispersion relation does not resemble the Dirac cone, as the transitions do not follow a true \sqrt{B} dependence. The band gap opens above the critical temperature, as the transitions for 87 K and 100 K do not converge to zero energy at zero magnetic field. Finally, at the critical temperature, the band gap vanishes completely, and a pure \sqrt{B} dependence is observed, which confirms that the system exhibits a true Dirac cone.

Each transition was fitted according to the model (Equation 3.6). One fit provided a set of values of \tilde{c} and \tilde{m} . All of the obtained values are plotted in Figure 3.34. The top panel (a) presents the rest mass, while the bottom panel (b) presents the velocity. Error bars in Figure 3.34 originate from the standard deviation of the values taken for every transition at given temperature.

Interestingly, the Kane fermion velocity \tilde{c} is nearly constant over the whole range of temperatures for both samples with Cd contents of 0.155 and 0.175. The extracted value of $\tilde{c} = (1.07 \pm 0.05) \cdot 10^6$ m/s is in a very good agreement with the theoretical value defined by $\tilde{c} = \sqrt{2P^2/3\hbar^2}$, which equals

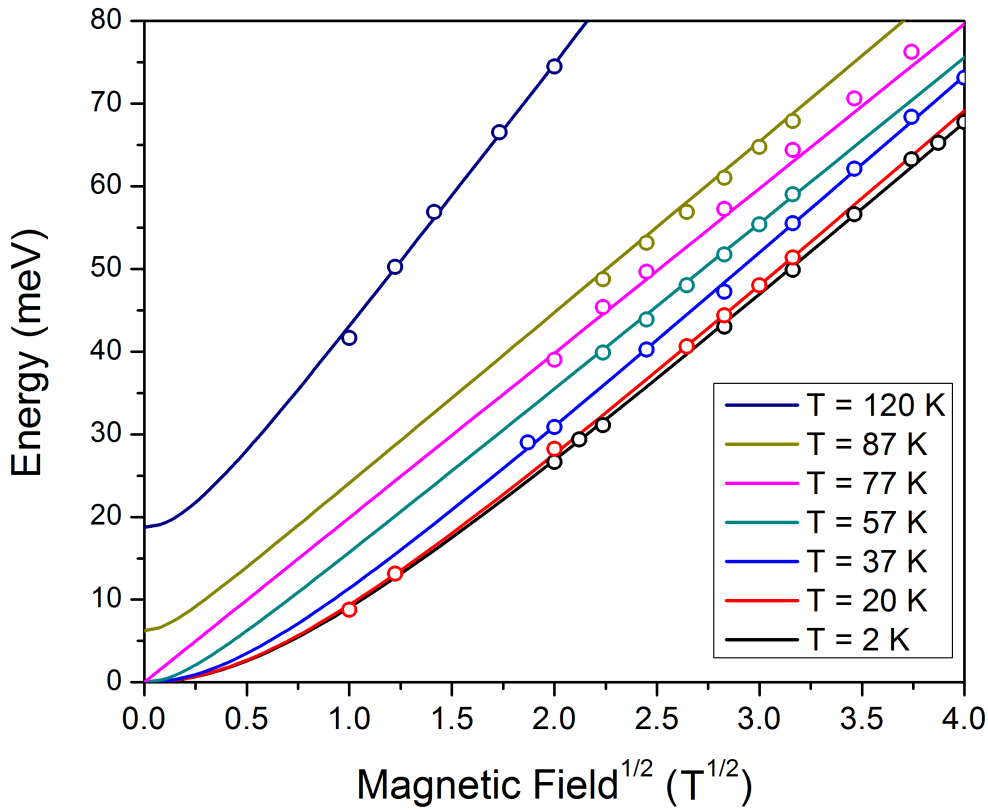


Figure 3.33: Evolution of the transition $L_{0,0\downarrow} \rightarrow L_{1,1\downarrow}$ for different temperatures ($L_{0,0\uparrow} \rightarrow L_{1,1\uparrow}$ for $T = 120$ K). For all temperatures $T < T_c$ the band gap is negative, thus the transition converges at $E = 0$ meV at $B = 0$ T and the shape of transition does not have a pure \sqrt{B} dependence. At $T = T_c$ the band gap vanishes and the transition follows precisely a \sqrt{B} (a straight line on \sqrt{B} scale). At $T > T_c$ the transition does not follow a \sqrt{B} dependence again. Moreover, it converges to a finite value of the band gap at $B = 0$ T, which is a sign of the (positive) band gap opening.

to $1.05 \cdot 10^6$ m/s for the well-accepted value of $E_p = 2m_0P^2/\hbar^2 \approx 18.8$ eV. Therefore, this universal value of \tilde{c} allows to determine the particle rest-mass for band gap values in the vicinity of a semimetal-to-semiconductor phase transition induced by temperature, Cd content, or other external parameter (e.g. pressure).

There are two points limiting the applicability of the simplified Kane model, considering the Γ_6 and Γ_8 band only, for the actual HgCdTe crystals. The first one, already mentioned, is related with the presence of other bands, considered as remote and not included in the model. The energy gap between the second and the lowest conduction bands in CdTe exceeds 4 eV, while the corresponding gap in HgTe is about 3 eV. Therefore, the cut-off energies for conduction bands in the simplified model should be lower than 3 eV. For the valence band, the cut-off energy is defined by the energy difference $\Delta \approx 1$ eV between the split-off Γ_7 band, and the heavy-hole band. The second limitation is attributed to the flat heavy-hole band, characterized by an infinite effective mass in the model. To ignore the parabolic terms in the electron dispersion of the heavy-hole band, one has to consider sufficiently low energies E , such that the relativistic mass of the fermions E/\tilde{c}^2 should be significantly lower than the

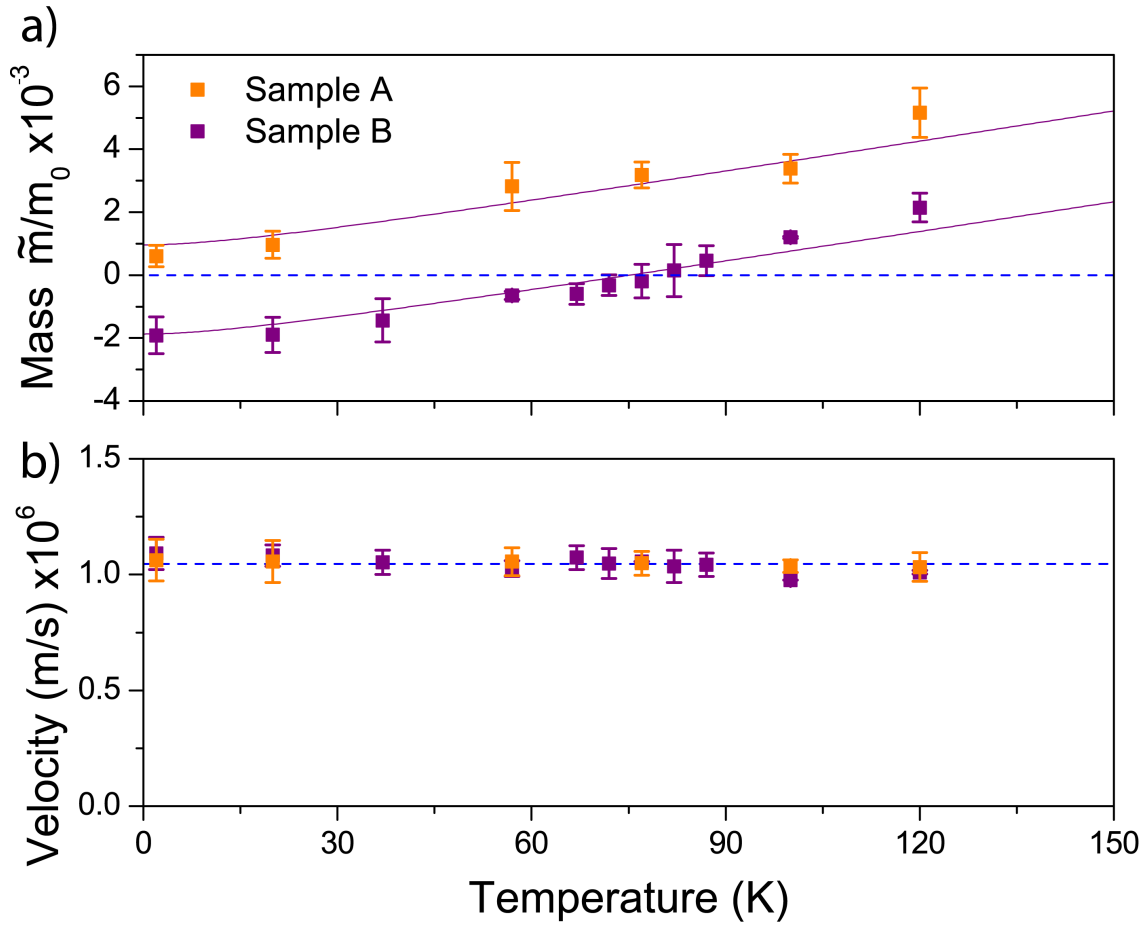


Figure 3.34: Parameters \tilde{m} and \tilde{c} obtained from fits to the experimental data as a function of temperature. **Panel a)**: Rest mass of Kane fermions. For Sample B the mass changes sign at the T_c , while for Sample A the mass is always positive. **Panel b)**: Velocity of Kane fermions. Velocity is constant at all temperatures, for both samples, which is highlighted by a dashed blue line placed at $v = 1.07 \cdot 10^6$ m/s.

heavy-hole mass m_{hh} . Assuming $m_{hh} \approx 0.5 m_0$, where m_0 is the free electron mass, a cut-off energy is estimated to be equal to about 3 eV for the flat band approximation, which exceeds Δ .

Chapter 4

HgTe Quantum Wells

4.1 Overview of HgTe Quantum Wells

A typical HgTe/CdTe QW is formed when a layer of HgTe is sandwiched between two layers of CdTe (or $\text{Hg}_{1-x}\text{Cd}_x\text{Te}$), which form barriers for the HgTe layer. Positions of energy levels, for both electrons and holes, depend on the QW width. As the QW width varies, the relative positions of the first electron-like subband ($E1$) and the first hole-like subband ($H1$) change. For thin quantum wells with QW thickness $d < 6.3$ nm the quantum confinement is strong and the structure exhibits a normal semiconducting phase with a conventional subbands alignment – the level $E1$ lies above the $H1$ level.

In an opposite case, for quantum wells with $d > 6.3$ nm, the situation is reversed – the quantum confinement is weaker and the $H1$ level lies above the $E1$ level, which results in a band inversion. Consequently, for $d_c = 6.3$ nm the band gap vanishes and the system undergoes a topological phase transition from a trivial insulator to a QSH insulator, and the QW hosts single-valley 2D massless Dirac fermions [99].

The other way to understand this is to realize that the structure of a thin QW ($d_{\text{HgTe}} \rightarrow 0$) should behave like CdTe and have a regular band ordering, i.e. bands with Γ_6 symmetry form the conduction subbands and the Γ_8 symmetry bands form the valence subbands. On the other hand, if the d_{HgTe} is large ($d_{\text{HgTe}} \rightarrow \infty$) the structure resembles the properties of HgTe, characterized by an inverted band order. Somewhere in between, as the thickness reaches a critical value $d_c = 6.3$ nm, the Γ_6 and Γ_8 subbands cross and the structure becomes inverted – the Γ_6 bands become valence subbands and the Γ_8 bands become conduction subbands. The QW states derived from the heavy-hole band are named H_n , where $n = 1, 2, 3, \dots$ denotes the states existing in the QW. Similarly, the levels originating from the electron and light-hole bands are named E_n . The band structure and first few energy levels of a HgTe/CdTe QW as a function of QW width are shown in Figure 4.1.

4.1.1 Band Structure of a HgTe/CdTe Quantum Well

An energy dispersion of the $E1$ and $H1$ subbands of a HgTe/CdTe QW near the critical thickness can be calculated using the 8-band Kane model. It turns out that near the Γ point of the Brillouin zone the dispersion depends linearly on momentum \mathbf{k} . Using the states (after BHZ [17]) $|E_1, \frac{1}{2}\rangle$, $|H_1, \frac{3}{2}\rangle$, $|E_1, -\frac{1}{2}\rangle$, $|H_1, -\frac{3}{2}\rangle$ as a basis, an effective Hamiltonian for the $E1$ and $H1$ subbands takes

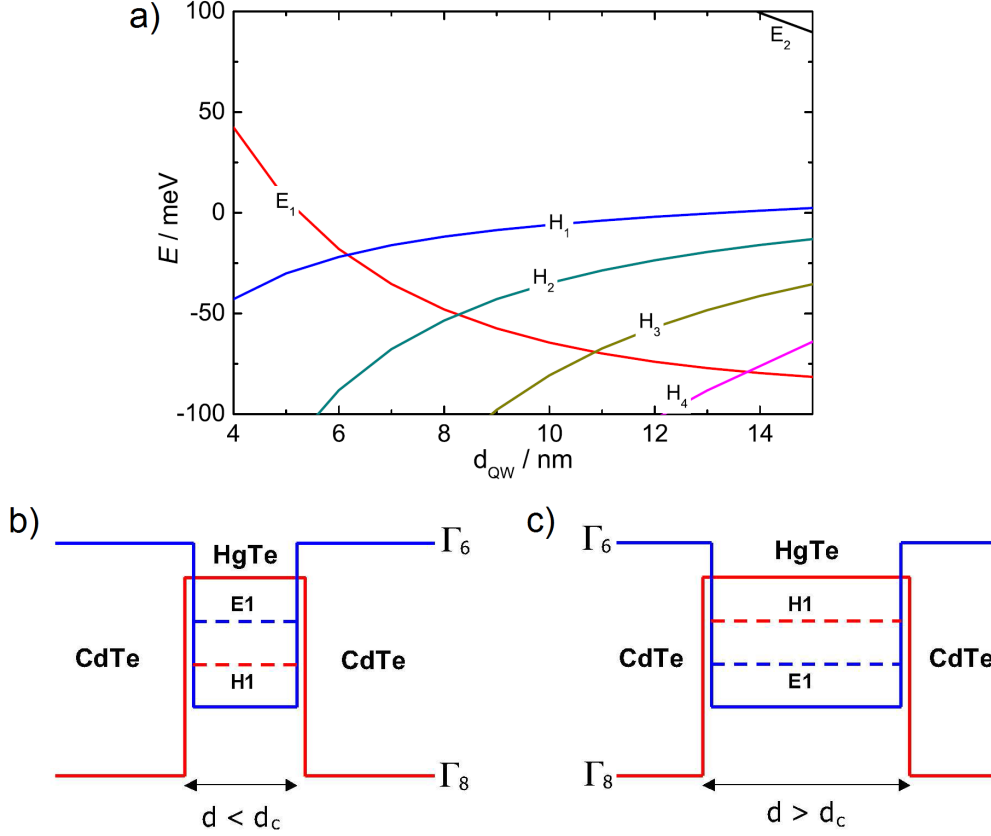


Figure 4.1: **Panel a)** The energy of the states in the quantum well as a function of the width of the HgTe QW layer. E_n represent electron-like states, while H_n represent hole-like states. **Panels b), c)** Schematic of a quantum well geometry and lowest subbands for thicknesses below (b) and above (c) the critical thickness. Images come from the works of König [98] (a), and Bernevig [17] (b,c).

form of:

$$H_{BHZ}(k_x, k_y) = \begin{pmatrix} H(k) & 0 \\ 0 & H^*(-k) \end{pmatrix}, \quad (4.1)$$

$$H = \epsilon(k) + d_i(k)\sigma_i,$$

where σ_i are the Pauli matrices, and

$$\begin{aligned} d_1 + id_2 &= \mathcal{A}(k_x - ik_y) \equiv \mathcal{A}k_-, \\ d_3 &= \mathcal{M} - \mathcal{B}(k_x^2 + k_y^2), \\ \epsilon &= \mathcal{C} - \mathcal{D}(k_x^2 + k_y^2). \end{aligned} \quad (4.2)$$

The two components of the Pauli matrices σ in Equation 4.1 denote the E1 and H1 subbands, while the two diagonal blocks $H(k)$ and $H^*(-k)$ represent spin-up and spin-down states, connected to each other by the time reversal symmetry.

In a gapples state, the relativistic mass \mathcal{M} in Equation 4.2 vanishes. By neglecting the nonlinear terms in each spin, $H(k)$ and $H^*(-k)$ can be approximated by the massless Dirac Hamiltonian describing the genuine Dirac fermions. Since a HgTe QW does not have any valley degeneracy, the Dirac fermions exist only in a single valley configuration. A comparison of an approximate Dirac-like band structure and the results of numerical calculations of the band structure based on the Kane model

(solid curves) are presented in Figure 4.2. As mentioned before, the Dirac approximation (plotted as dotted curves) is valid in the vicinity of $\mathbf{k} = 0$, where higher in momentum terms can be neglected.

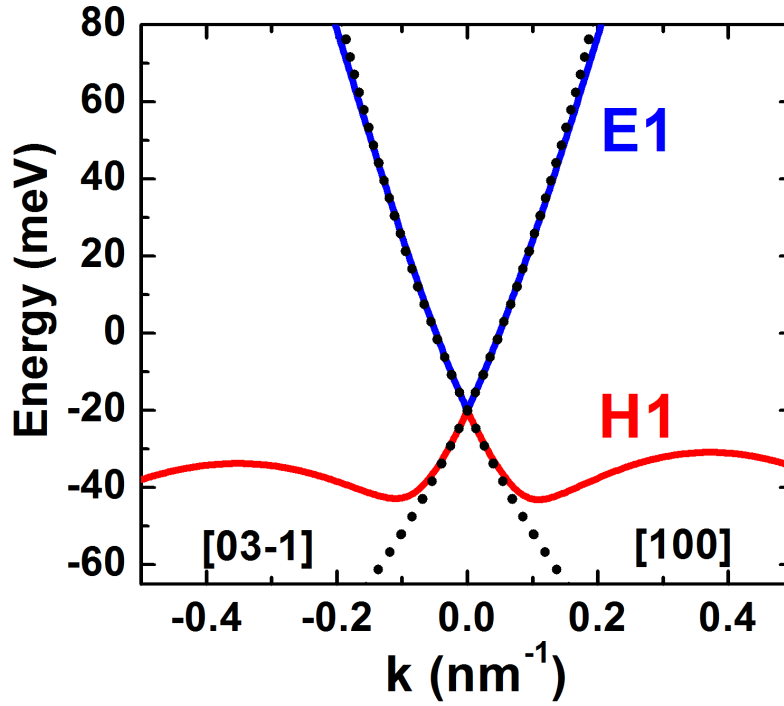


Figure 4.2: Comparison of band structures obtained using the 8-band Kane model (red and blue solid curves) and the Dirac-type 2D Hamiltonian (black dotted curves) for a gapless state. Blue curve represents an electron level $E1$, while red curve represents a hole level $H1$.

4.1.1.1 The Influence of Magnetic Field on the Band Structure

The LL structure of a HgTe QW at applied magnetic field can be described in two ways. The first way is based on an approximation using the Dirac Hamiltonian, which can be solved explicitly to obtain the equations describing the energy of the LLs. The approximation based on the Dirac Hamiltonian holds only for a limited range of parameters. The second (more accurate and versatile) approach is based on the 8-bands Kane Hamiltonian. However, its solutions can be found only via numerical calculations.

The Dirac-like Hamiltonian describing a HgTe QW system in magnetic field takes form of:

$$\hat{H}_{eff} = H_{BHZ} + H_{Zeeman} + H_{SIA} + H_{BIA}, \quad (4.3)$$

where \hat{H}_{eff} is the effective Hamiltonian from equation 4.1 with a Peierls substitution $\mathbf{k} \rightarrow \mathbf{k} + \frac{e}{\hbar} \mathbf{A}$ applied, H_{Zeeman} includes Zeeman effects, H_{SIA} represents the structure inversion asymmetry (SIA), and H_{BIA} bulk inversion asymmetry (BIA). The expressions for H_{Zeeman} , H_{SIA} , and H_{BIA} can be found in Appendix C.1.

Neglecting the SIA and BIA terms, the Landau level spectrum takes form of:

$$\begin{aligned}
E_{\alpha}^{\uparrow}(n) &= -\frac{eB_{\perp}}{\hbar}(2\mathcal{D}n + \mathcal{B}) + \frac{\mu_B B_{\perp}}{4}(g_E + g_H) \\
&+ \alpha \sqrt{2n\mathcal{A}^2 \frac{eB_{\perp}}{\hbar} + \left(\mathcal{M} - B_{\perp} \left(\frac{e}{\hbar}(\mathcal{D} + 2\mathcal{B}n) - \frac{\mu_B}{4}(g_E + g_H)\right)\right)^2} \\
E_{\alpha}^{\downarrow}(n) &= -\frac{eB_{\perp}}{\hbar}(2\mathcal{D}n - \mathcal{B}) - \frac{\mu_B B_{\perp}}{4}(g_E + g_H) \\
&+ \alpha \sqrt{2n\mathcal{A}^2 \frac{eB_{\perp}}{\hbar} + \left(\mathcal{M} - B_{\perp} \left(\frac{e}{\hbar}(-\mathcal{D} + 2\mathcal{B}n) + \frac{\mu_B}{4}(g_E + g_H)\right)\right)^2},
\end{aligned} \tag{4.4}$$

where $n = 1, 2, \dots$, $\alpha = +1$ for conduction band, and $\alpha = -1$ for valence band. The parameter \mathcal{C} is usually set to zero to put the Dirac point at zero energy. For a sample in a gapless state ($\mathcal{M} = 0$) the expression 4.4 (for conduction band $\alpha = +1$) at low magnetic fields reduces to

$$E_0^{\uparrow(\downarrow)} = B_{\perp} \left(-\frac{e}{\hbar}(2\mathcal{D}n + \mathcal{B}) + \frac{\mu_B}{4}(g_E + g_H) \right) + \alpha \sqrt{2n\mathcal{A}^2 \frac{eB_{\perp}}{\hbar}} \tag{4.5}$$

up to linear terms. This is an origin of the square-root magnetic field dependence that became the signature of Dirac fermions in graphene [100], with an additional linear term describing the large g -factor of a HgTe QW. This model holds well for low magnetic field regime, where the approximations are valid. For higher magnetic fields, the 8-band Kane model has to be used and the magnetic field dependence no longer follows a pure square-root function.

Meanwhile, the states for $n = 0$, called *zero-mode* [17] LLs, can be described by equations 4.6. It is worth to mention that these states are labeled with $n = 0$ only in the Dirac-like Hamiltonian approximation. In the Kane-model approach, these states are numbered differently, but still are referred to as zero-mode.

$$\begin{aligned}
E_0^{\uparrow} &= \mathcal{M} - \frac{eB_{\perp}}{\hbar}(\mathcal{D} + \mathcal{B}) + \frac{\mu_B B_{\perp}}{2}g_E \\
E_0^{\downarrow} &= \mathcal{M} + \frac{eB_{\perp}}{\hbar}(-\mathcal{D} + \mathcal{B}) - \frac{\mu_B B_{\perp}}{2}g_H.
\end{aligned} \tag{4.6}$$

The spin splitting of those LLs takes form

$$\Delta E_s = E_0^{\uparrow} - E_0^{\downarrow} = 2\mathcal{M} - \frac{2eB_{\perp}}{\hbar}\mathcal{B} + \frac{\mu_B B_{\perp}}{2}(g_E + g_H). \tag{4.7}$$

The detailed LL spectrum of a HgTe/CdTe QW is derived from the 8-band Kane Hamiltonian and requires solving a set of eight coupled differential equations for a given LL. In general, for LLs with $n \leq 0$, there are only 7, 4, and 1 non-trivial solutions for $n = 0, -1, \text{ and } -2$, respectively. For LLs with higher n indices the results consists of four pairs of spin-split levels. The single LL with $n = -2$ has a pure heavy-hole character and its energy decreases linearly with magnetic field. This level, along with one of the levels labeled as $n = 0$, form a set of zero-mode LLs, already described in Dirac-like Hamiltonian approximation.

Zero-mode Landau levels

A very particular property of zero-mode LLs manifests itself with a variation of an applied magnetic field. For magnetic fields below a critical value B_c , the lower zero-mode LL has an electron-like character and arises from the valence band, while the higher zero-mode LL has a heavy-hole-like character and arises from the conduction band. The edge channels are present as the structure is in inverted band order phase. However, they are no longer protected by the time-reversal symmetry, as the magnetic field is applied.

With increasing magnetic field the zero-mode LLs merge and eventually cross themselves, reversing the order of the bands, and turning the system into the QHE phase. This critical magnetic field, where

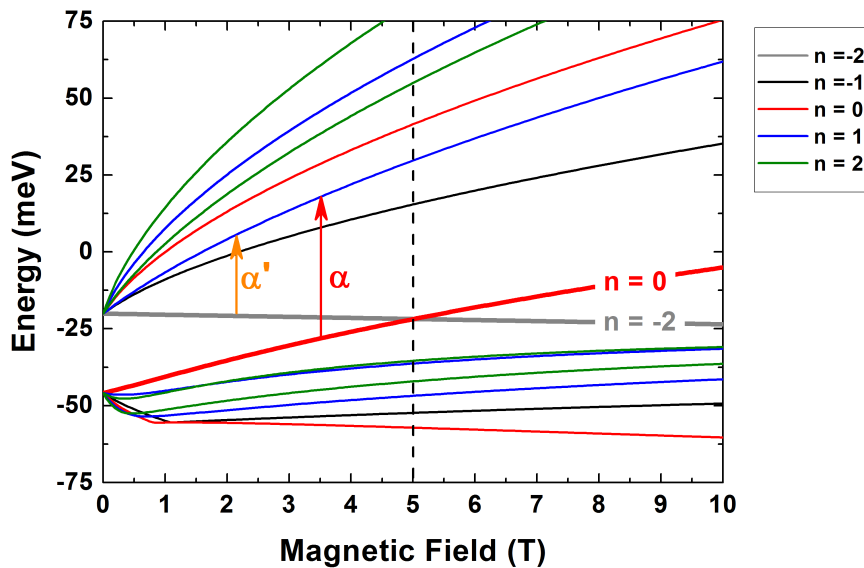


Figure 4.3: Landau level structure obtained using the 8-band Kane model for an inverted state. Thick red ($n = 0$) and grey ($n = -2$) curves represent zero-mode LLs, which exhibit a crossing at $B_c \approx 5$ T, marked with a vertical dashed line. The crossing point separates an inverted band ordering phase ($B < B_c$) from a regular band ordering phase ($B > B_c$). Transitions originating from zero-mode LLs are represented with arrows marked as α and α' .

the crossing occurs, can be derived from Equation 4.7. By substituting $\Delta E_s = 0$ and neglecting small g -factor terms, the expression for the critical magnetic field takes form of $B_{\perp}^c = \frac{\hbar M}{eB}$. In the inverted regime $M/B > 0$, the crossing takes place at a positive magnetic field value, while in the normal regime $M/B < 0$, the crossing extrapolates to a negative value of magnetic field. For a gapless QW, the crossing occurs at zero magnetic field. Therefore, the position of the crossing is a well-defined indication of the phase of the system. The zero-mode LLs (thick red and grey curves) and their crossing point (marked with a vertical dashed line), separating the inverted phase from the QHE phase, is presented in Figure 4.3.

In the case of a HgTe/CdTe QW in a gapped state, the off-diagonal terms of the massless Dirac Hamiltonian have to be completed by the diagonal massive terms. In any case, the zero-mode LLs still appear due to the off-diagonal, linear in \mathbf{k} terms. Moreover, in a gapped state, the zero-mode LLs are split in energy due to the existence of the mass term, and their position changes monotonically as a function of the temperature or the width of the QW. The magnetic field evolution of the zero-mode LLs in HgTe QWs, and their crossing at B_c can be considered as a field-driven insulator-metal-insulator phase transition. The transport data [14] gave an indication that those LLs simply cross themselves, but also a possibility of a weak anticrossing was considered [98].

Indeed, several magneto-spectroscopy studies [101][102] proved that those levels may exhibit an anticrossing in the vicinity of the calculated B_c . This effect can be observed in magneto-spectroscopy as an evolution of two transitions, which are shown as arrows in Figure 4.3. The first of those transitions is a regular transition from LL $n = 0$ to LL $n = 1$, designated as transition α , following the notation of Schultz *et al.* [103]. However, the second transition, designated as α' , is a transition from LL $n = -2$ to LL $n = 1$. This transition does not satisfy the selection rules $\Delta n = \pm 1$ in the Faraday configuration, and is forbidden in the electric dipole approximation, as was explained earlier. The appearance of this transition is related to a coupling between the LLs $n = 0$ and $n = -2$, resulting from BIA. The

band structure calculations of HgTe QWs often neglect BIA, which is inherently present in zinc-blend crystals. A consequence of BIA is a mixing of the states of the zero-mode LLs in the vicinity of B_c . This mixing activates the transition α' , rendering it detectable in magneto-optical studies.

4.1.1.2 The Influence of Temperature on the Band Structure

Apart from the variation of a QW thickness, which is inherently an internal parameter of the structure – once set (at growth) cannot be changed, external parameters like hydrostatic pressure [80] and temperature [62] (as in the case of HgCdTe bulk systems presented in Chapter 3) can be used to induce a phase transition in HgTe QW systems. This is a consequence of a strong temperature dependence of energy of the E1 level. The temperature dependence of the energy gap and a band order evolution is presented in Figure 4.4 for two systems – a 6 nm HgTe QW with a regular band order at all temperatures (Panel a)), and an 8 nm HgTe QW with an inverted band order at low temperature (Panel b)). The second system undergoes a temperature-induced phase transition at a critical temperature T_c , and turns into a regular semiconductor at higher temperatures. The energy of H1 (and H2) bands does not change with temperature at all, while there is a clear dependence of energy on temperature of the E1 band.

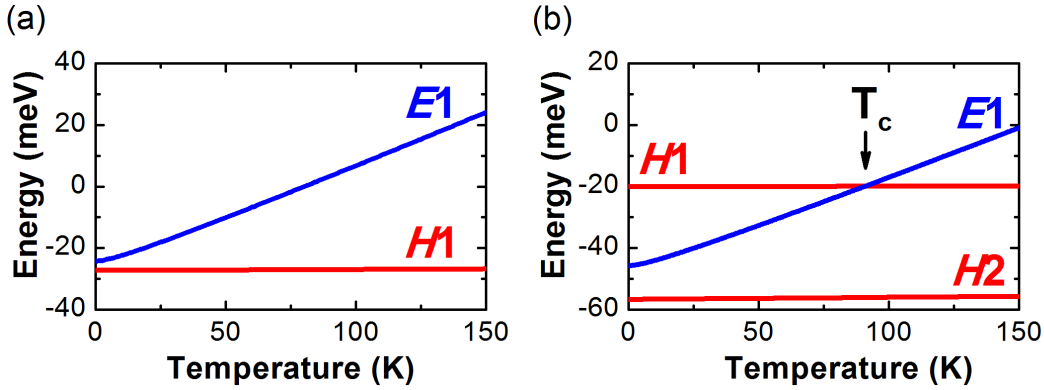


Figure 4.4: *Temperature dependence of the electron-like E1 (blue curve) and hole-like H1, H2 (red curves) subbands at $k = 0$, calculated for Panel (a) a 6 nm HgTe/CdTe quantum well, and Panel (b) an 8 nm HgTe/CdTe quantum well. At $T = T_c$ the 8 nm quantum well undergoes a phase transition characterized by a band inversion.*

The calculations of the band structure and the band nonparabolicity are based on the 8-band Kane model which takes into account the temperature dependence of all relevant parameters, including but not limited to the lattice and elastic constants of $\text{Hg}_{1-x}\text{Cd}_x\text{Te}$. The model takes into account also the interactions between Γ_6 , Γ_8 , and Γ_7 bands. Despite the fact that the electronic states of HgTe QWs can be described qualitatively by the 6-band model, only the inclusion of the Γ_7 band in the calculations allows to obtain the quantitative values of hydrostatic pressure or temperature of the phase transition [80]. For other HgCdTe-based materials, like bulk systems, this is not the case – the influence of the Γ_7 band can be neglected in the calculations [77].

The calculations of the band structure of the 8 nm thick QW revealed that at high temperatures the band order is regular and the energy gap between E1 and H1 bands considerably decreases with decreasing temperature, which is presented in Panel (c) of Figure 4.5. At the critical temperature $T_c = 90$ K the band gap vanishes giving rise to massless Dirac fermions (Panel (b)). Further decrease of temperature induces a phase transition and renders the band structure inverted with an indirect

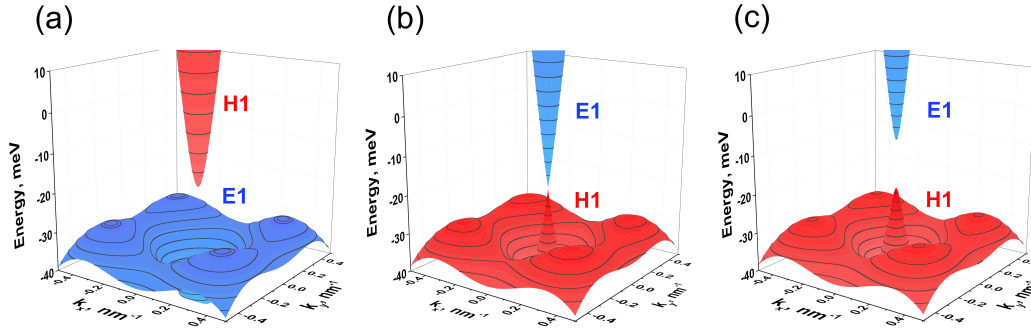


Figure 4.5: Dispersion relation of an 8 nm HgTe/CdTe quantum well in **Panel (a)** the topological insulator phase $T < T_c$, **Panel (b)** the gapless state $T = T_c$, and **Panel (c)** the semiconductor phase $T > T_c$. The electron-like E1 (hole-like H1) subband is represented as a blue surface (red surface). In the inverted phase the indirect band gap is formed by the presence of side maxima of the E1 subband.

band gap, which arises due to the presence of the side maxima of the valence band (Panel (a)).

4.1.2 Experiment

4.1.2.1 Samples

The high-quality HgTe QW samples were grown in Novosibirsk by Dvoretiskii and Mikhailov [104] using an MBE technique on a (013)-oriented semi-insulating GaAs substrate followed by a relaxed CdTe buffer layer. An active part of a QW consists of a (6 nm for Sample A, 8 nm for Sample B) HgTe layer sandwiched between 40 nm thick $\text{Cd}_x\text{Hg}_{1-x}\text{Te}$ barriers. A cap layer of CdTe was deposited on top of the structures to prevent oxidation. Sample A remained undoped, while the barriers of Sample B were doped on each side with a 15 nm layer of indium with the doping concentration of $6.5 \cdot 10^{16} \text{ cm}^{-3}$. This resulted in a formation of a 2D electron gas in the QW of Sample B. The QW width d and cadmium concentration in barriers x of investigated structures is given in Table 4.1.2.1.

Table 4.1: The properties of investigated HgTe/CdTe quantum wells – quantum well thickness, Cd concentration in the barrier, and type (p for holes, n for electrons) and concentration of dominant carriers.

Sample name	QW thickness	Barrier Cd rate x	Type, carrier concentration (2 K)
Sample A	6 nm	0.62	$p = 3 \cdot 10^{10} \text{ cm}^{-2}$
Sample B	8 nm	0.80	$n = 3 \cdot 10^{11} \text{ cm}^{-2}$

The critical thickness corresponding to a phase transition at different temperatures for HgTe/ $\text{Hg}_{1-x}\text{Cd}_x\text{Te}$ samples with $x = 0.62$ (the same as Sample A) and $x = 0.80$ (the same as Sample B) is presented in Figure 4.6. The 6 nm Sample A (represented by a black curve) is in a semiconducting state at the whole temperature range. The 8 nm Sample B (red curve) at low temperature is a topological insulator and is expected to exhibit a phase transition at $T = 90 \text{ K}$ followed by an opening of the band gap.

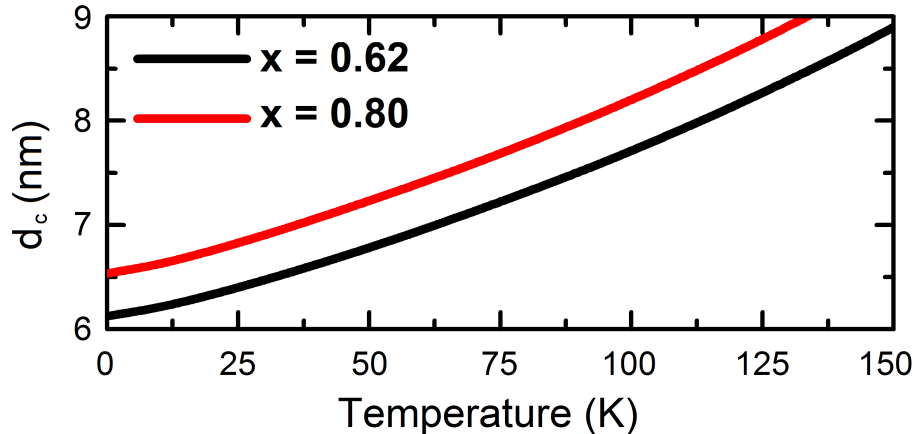


Figure 4.6: The critical thickness at different temperatures for $\text{HgTe}/\text{Hg}_{1-x}\text{Cd}_x\text{Te}$ samples with $x = 0.62$ (black curve) and $x = 0.80$ (red curve).

4.1.2.2 Results

Related experimental works

The first results, concerning the particular behavior of zero-mode LLs were reported in works of König *et al.* [14] and Zhang *et al.* [24]. It was shown that the magnetic field evolution of the zero-mode LLs in HgTe QWs is an origin of a magnetic field-driven insulator-metal-insulator phase transition, which is characteristic for these systems. It is worth to stress that this is not a topological insulator-metal-insulator transition but a topological insulator-metal-insulator transition, as the magnetic field breaks the time-reversal symmetry and, as a consequence, the topological protection. A crossing of these levels at the critical field was confirmed in [14] by magneto-transport data.

Orlita *et al.* [101] demonstrated for the first time by magneto-spectroscopy measurements on two 8 nm wide HgTe QWs an evolution and an anticrossing of transitions originating from the zero-mode LLs. These findings were confirmed by the work of Zholudev *et al.* [105], in which the anticrossing was observed via magneto-spectroscopy as well, and its presence was attributed to BIA. Moreover, it was speculated that some other processes can cause the levels to avoid crossing, e.g. electron-electron interactions [101].

The first systematic magneto-spectroscopy study of HgTe QWs systems with different QW widths close to the critical was performed by Zholudev [102]. In his experiment a set of four samples was used – two of them being in an inverted regime of thickness, while the other two being in a non-inverted regime. This allowed to directly observe the difference between the two separate topological phases and the band structure that they originate from. An anticrossing of zero-mode LLs was also observed.

The first temperature dependent study of phase transition in HgTe QWs were done by Ikonnikov [106]. The study was conducted in pulsed magnetic fields up to 45 T using monochromatic radiation sources. It revealed a temperature-induced merging of the absorption lines, corresponding to the transitions from the zero-mode LLs. The results are presented in Figure 4.7.

All the magnetospectroscopy studies of Dirac fermions in HgTe mentioned above were conducted either at low temperatures and/or using monochromatic THz sources. In 2015, a magneto-transport study conducted by Wiedmann *et al.* [62] showed fingerprints of a temperature-induced transition from the topological insulator at 4.2 K to the semiconductor phase at 300 K. However, the critical

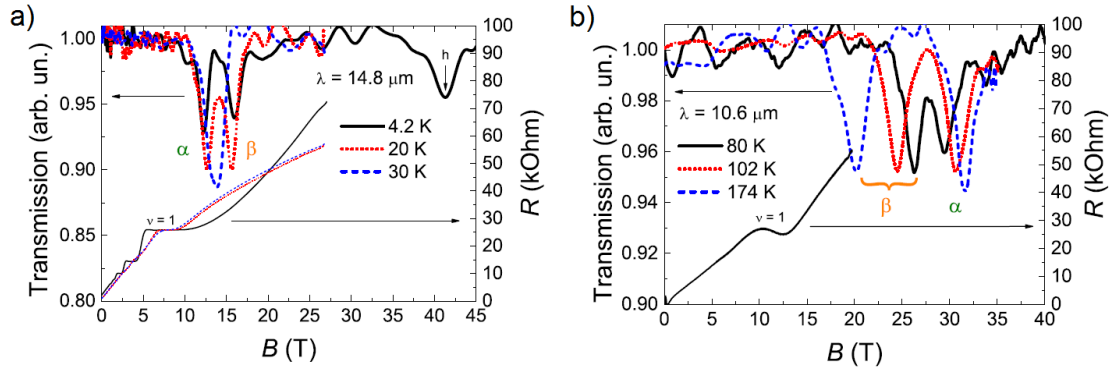


Figure 4.7: *Magneto-resistance and magneto-absorption spectra obtained at different temperatures on an 8 nm HgTe QW. Panel a) Solid lines 4.2 K, dotted lines 20 K, dashed lines 30 K, using a 14.8- μm QCL. Panel b) Solid lines 80 K, dotted lines 102 K, dashed lines 174 K, using a CO_2 laser emitting at 10.6 μm . Images come from the work of Ikonnikov [106].*

temperature for the samples, where the phase transition occurs and the massless Dirac fermions arise, was too high to be determined by this technique. This is caused by a significant degradation of resolution between LLs observed in magneto-transport at high temperatures.

Experimental details

In this work a set of two samples was investigated in order to determine if a temperature induced topological phase transition takes place in HgTe/CdTe QW. Similarly to the bulk systems, the first QW sample exhibits a semiconducting behavior at the whole range of temperatures, while the second one has an inverted band structure at low temperatures, then undergoes a phase transition at the critical temperature, and finally turns into a regular semiconductor at high temperatures. In contrary to bulk systems, a two-dimensional HgTe/CdTe QW in inverted state is not a semimetal but a topological insulator (if no magnetic field is applied).

Magneto-spectroscopy measurements were performed at magnetic fields up to 16 T and in energy range 80 - 800 cm^{-1} ($\approx 10 - 100$ meV) with a 4 cm^{-1} resolution. The relevant temperature range was between 2 K and 130 K. The infrared transmittance spectra were measured by a Fourier spectrometer with a Globar lamp as a source of radiation. The system was coupled to a liquid helium cryostat. The transmission spectra were obtained by dividing the spectra taken at given magnetic field by the spectra obtained at zero magnetic field.

In order to interpret the experimental results, a set of temperature-dependent band structure and LL structure calculations based on the 8-band Kane Hamiltonian were performed. The calculations took into account a tensile strain in the layers resulting from the mismatch of lattice constants of CdTe buffer, $\text{Cd}_x\text{Hg}_{1-x}\text{Te}$ barriers, and HgTe QW. The energies of LLs were obtained using an axial approximation, while the calculations of dispersion relations held also non-axial terms.

On each spectra there is a completely opaque region due to the presence of reststrahlen bands, existing between 16 and 21 meV and 30 and 37 meV corresponding to a phonon absorption of HgTe/HgCdTe layers and a GaAs substrate, respectively. Because of that, the energy regions corresponding to these bands were covered by grey areas on the spectra.

4.1.2.3 Sample A

Temperature 2 K

The results of the LL calculations for $T = 2$ K for Sample A are presented in Figure 4.8. Only two bands (E1 and H1) are present. In the Faraday configuration, optical transitions between LLs are required to follow a $\Delta n = \pm 1$ selection rules, provided by the electric dipole approximation (Chapter 2). By taking into account the previous optical studies of HgTe QWs [103][101][102][106][107][105], the transmission spectra are expected to be dominated by the transitions between LLs with low indices. Those transitions are marked in Figure 4.8 by small Greek letters (α_1 , α_2 , β) and solid arrows, as all visible transitions are interband transitions, which is a consequence of the low concentration of holes as dominant carriers in Sample A. According to a convention applied in HgCdTe bulk systems in Chapter 3, dashed arrows are reserved for intraband transitions.

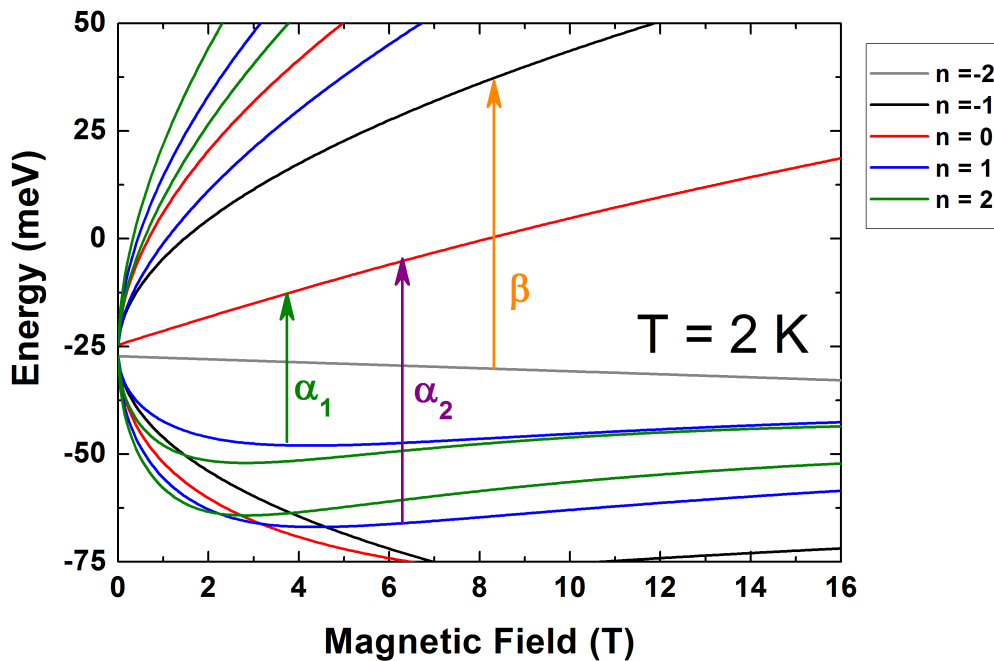


Figure 4.8: Landau level graph of Sample A as a function of magnetic field at $T = 2$ K. Colored lines represent Landau levels, characterized by a different value of n , as described as indices of L on the right side of the graph. The Landau levels with $n = -2$ and $n = 0$ are zero-mode Landau levels. The energy of those levels at zero magnetic field is an indication of the band gap. The vertical arrows with corresponding Greek letters represent observed transitions between Landau levels in this system. Solid arrows α_1 , α_2 , and β indicate interband transitions.

The band gap is equal to 2.7 meV. The electrons from both of the zero-mode LLs, denoted as $n = -2$ and $n = 0$, take part in optical transitions, which allowed to confirm that these LLs do not cross (for a positive value of magnetic field). This is an indication that the sample is in a semiconducting phase.

The expected dependence of energy of transitions on magnetic field can be derived from the difference of the calculated LLs. In the Panel a) of Figure 4.9 these expected transitions are presented along with experimental points corresponding to the minima of transmission of given spectra. There is a strong agreement between the experimental data and the theoretical calculations. The strongest transitions are α_1 and β , which is shown on a waterfall plot in Panel b) of Figure 4.9. The spectra are plotted every 1 T and shifted vertically for clarity.

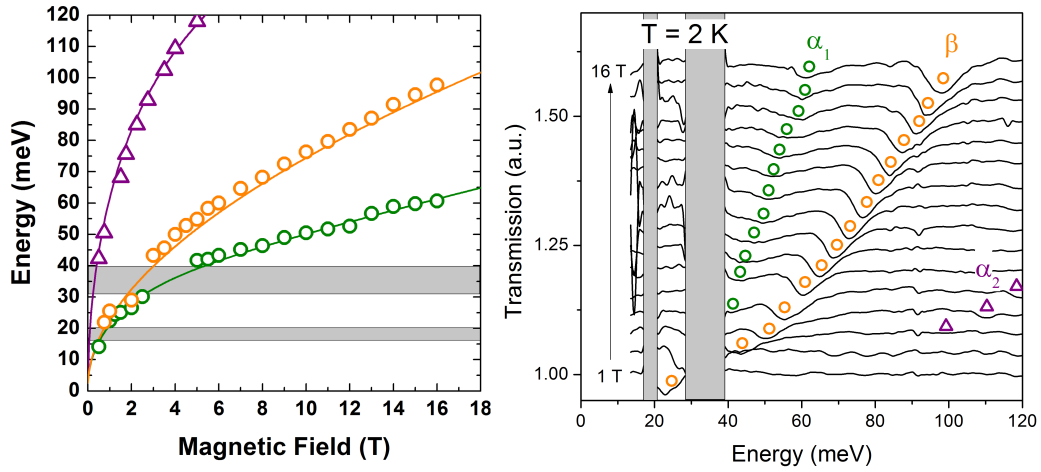


Figure 4.9: **Left Panel:** Points corresponding to the minima of the transmission of Sample A at $T = 2$ K with theoretical predictions of transitions as a function of magnetic field. **Right panel:** Transmission spectra plotted for magnetic fields in range from 1 to 16 T every 1 T, with symbols corresponding to the transitions from left panel.

Temperature 30 K

At $T = 30$ K the band structure of Sample A slightly changed. The energy difference of zero-mode LLs at zero magnetic field got higher – the band gap is equal to 10.2 meV. The LL structure is presented in Figure 4.10.

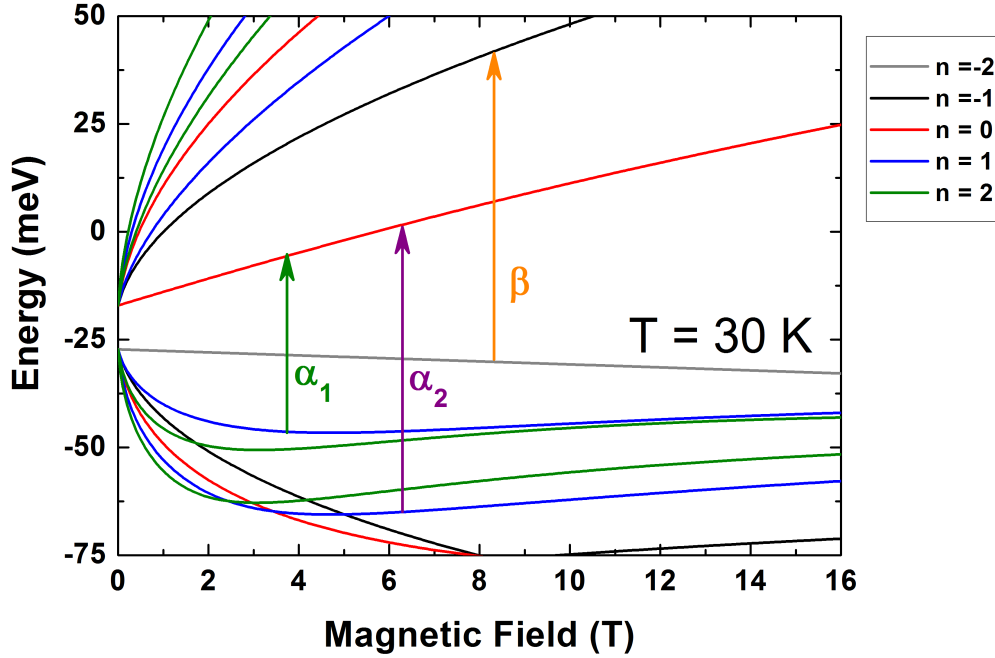


Figure 4.10: Landau level graph of Sample A as a function of magnetic field at $T = 30$ K. Colored lines represent Landau levels, characterized by a different value of n , as described as indices of L on the right side of the graph. The Landau levels with $n = -2$ and $n = 0$ are zero-mode Landau levels. The energy of those levels at zero magnetic field is an indication of the band gap. The vertical arrows with corresponding Greek letters represent observed transitions between Landau levels in this system. Solid arrows α_1 , α_2 , and β indicate interband transitions.

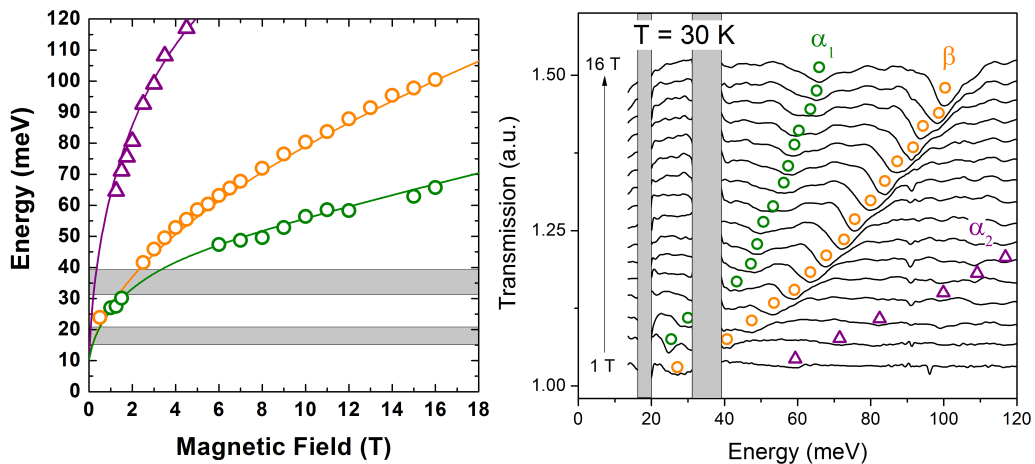


Figure 4.11: **Left Panel:** Points corresponding to the minima of the transmission of Sample A at $T = 30$ K with theoretical predictions of transitions as a function of magnetic field. **Right panel:** Transmission spectra plotted for magnetic fields in range from 1 to 16 T every 1 T, with symbols corresponding to the transitions from left panel.

Temperature 70 K

At $T = 70$ K the band structure of Sample A changed even more. The energy difference of zero-mode LLs at zero magnetic field got a higher – the band gap is equal to 23.2 meV. The LL structure is presented in Figure 4.12.

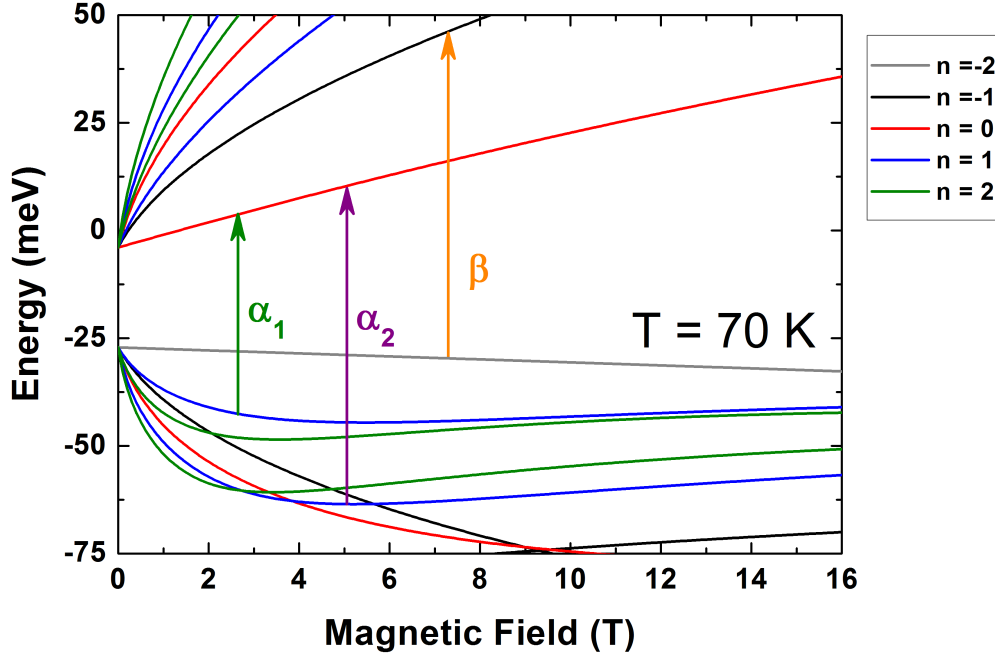


Figure 4.12: Landau level graph of Sample A as a function of magnetic field at $T = 70$ K. Colored lines represent Landau levels, characterized by a different value of n , as described as indices of L on the right side of the graph. The Landau levels with $n = -2$ and $n = 0$ are zero-mode Landau levels. The energy of those levels at zero magnetic field is an indication of the band gap. The vertical arrows with corresponding Greek letters represent observed transitions between Landau levels in this system. Solid arrows α_1 , α_2 , and β indicate interband transitions.

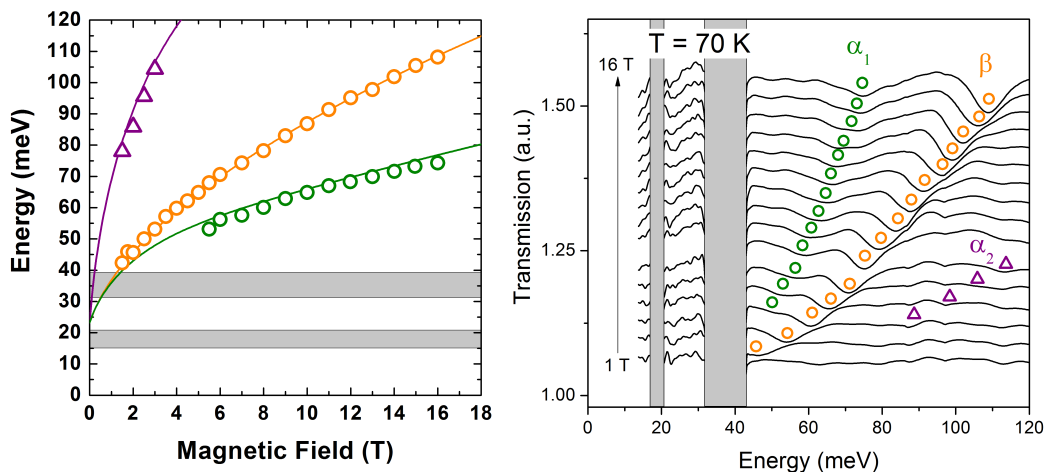


Figure 4.13: **Left Panel:** Points corresponding to the minima of the transmission of Sample A at $T = 70$ K with theoretical predictions of transitions as a function of magnetic field. **Right panel:** Transmission spectra plotted for magnetic fields in range from 1 to 16 T every 1 T, with symbols corresponding to the transitions from left panel.

4.1.2.4 Sample B

Temperature 2 K

At $T = 2$ K Sample B is in a topological insulator phase. The LL structure is presented in Figure 4.14. The value of the direct band gap is estimated to be $E_g \approx 26$ meV. It is important to note that at this temperature the $H1$ band is energetically higher than the $E1$ band, thus the band gap should be considered as negative.

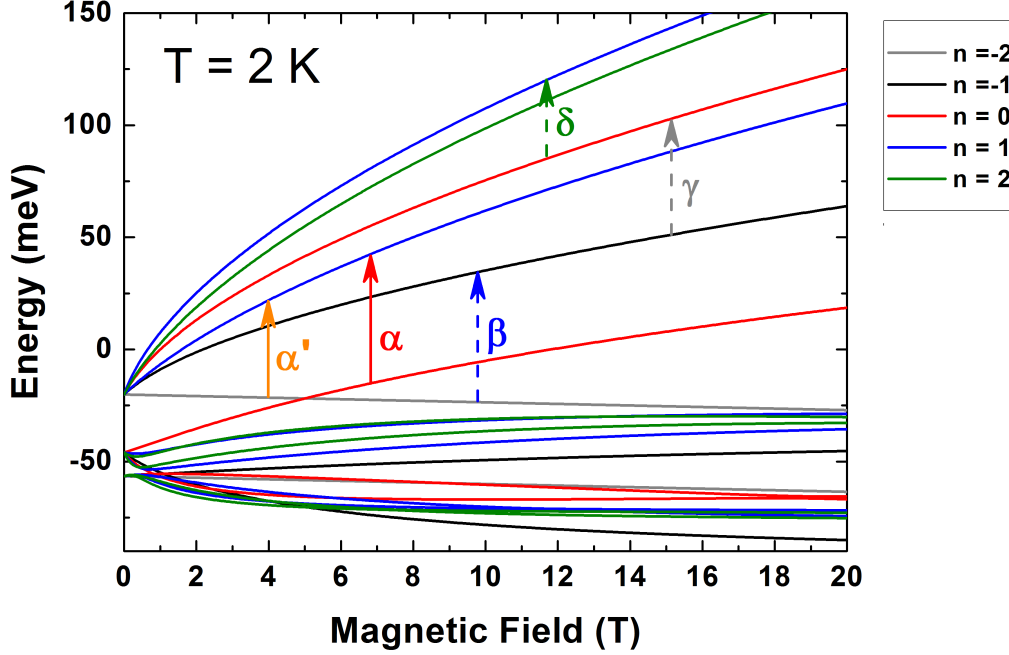


Figure 4.14: Landau level graph of Sample B as a function of magnetic field at $T = 2$ K. Colored lines represent Landau levels, characterized by a different value of n , as described as indices of L on the right side of the graph. The Landau levels with $n = -2$ and $n = 0$ are zero-mode Landau levels. The energy of those levels at zero magnetic field is an indication of the band gap. Their crossing indicates the point of field induced semiconductor-metal-semiconductor phase transition, and indicates that the sample is in the inverted band order phase. The vertical arrows with corresponding Greek letters represent observed transitions between Landau levels in this system. The solid arrows indicate interband transitions α and α' , while dashed arrows indicate intraband transitions β , γ , and δ .

The most interesting feature of the LL structure presented in Figure 4.14 is the crossing of the lower level of the conduction band (with hole-like symmetry) with $n = -2$, and the upper level of the valence band (with electron-like symmetry) with index $n = 0$, which takes place at the magnetic field value of $B_c \approx 5$ T. An application of magnetic field breaks the time-reversal symmetry making the boundary states no longer protected, nevertheless the inverted band order is preserved. The situation changes at $B > B_c$ – the zero mode LLs swap and the structure becomes a conventional quantum Hall insulator.

There are five visible transitions in the spectra, all of them were marked by arrows in Figure 4.14. An anticrossing of transitions α and α' was already observed and reported [101][102][105]. Here, the anticrossing is visible at magnetic fields close to the calculated $B_c \approx 5$ T, as presented in Figure 4.15. However, the anticrossing is visible for magnetic fields from around 4.5 T up to around 8 T. This evident lack of symmetry in regard to B_c is caused by the position of chemical potential in the sample. Below 4.5 T there are no empty states at LL $n = 1$ so the probability of both α and α'

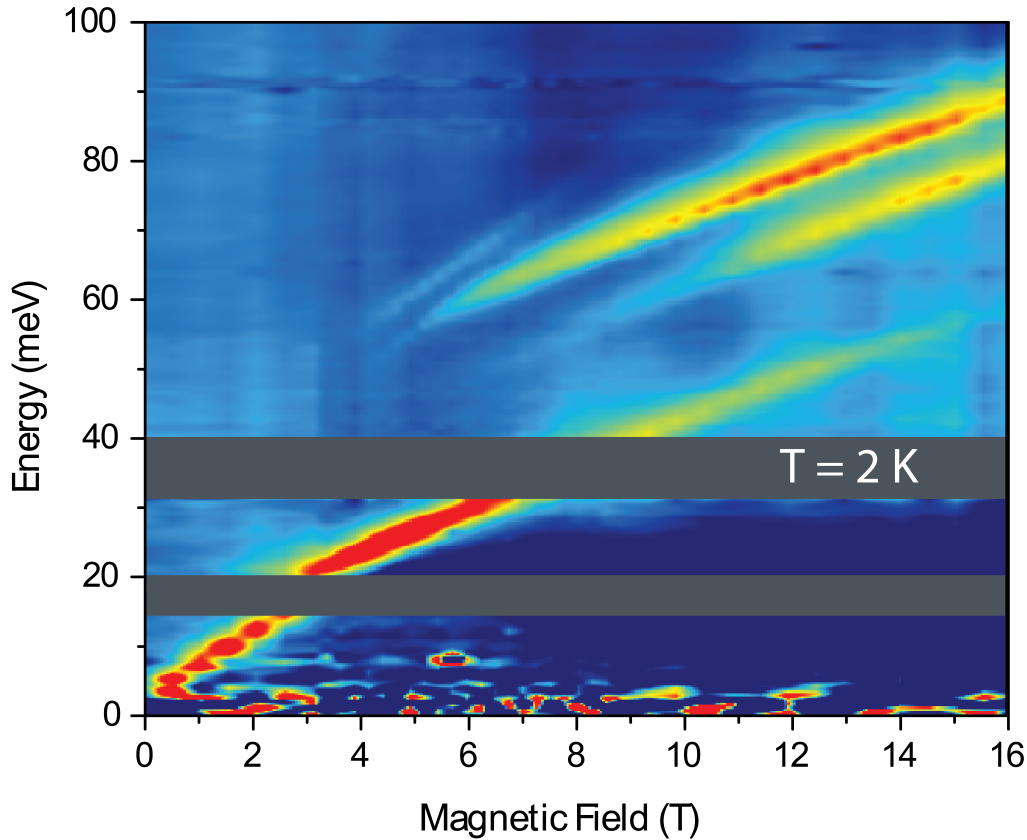


Figure 4.15: False color map of the transmission of Sample B as a function of energy and magnetic field at $T = 2$ K. Blue color represents areas where the transmission is equal to 1, while lightblue/yellow/red colors indicate where the absorption takes place. An anticrossing of transitions originating from the zero-mode Landau levels is visible close to $B_c \approx 5$ T.

transitions is equal to zero. For the same reason the β transition starts to be visible from energies higher than 50 meV, which takes place at magnetic field of around 8 T.

Besides the α' transition there are four other ones. The one with the largest intensity at high magnetic field is denoted as α . It represents an optical transition between LLs $n = 0$ and $n = 1$. This is also the only interband transition visible at 2 K. Its extrapolation to zero magnetic field gives an idea about the value of energy gap in the system. The intraband transition β , occurring between LLs with $n = -2$ and $n = -1$ is energetically close to the transition α , and that relative energy difference will change as the temperature increases. Two remaining transitions are γ and δ . The γ transition occurs between $n = -1$ and $n = 0$. The δ transition, related to the cyclotron resonance, occurs between $n = 0$ and $n = 1$.

The expected dependence of transition on magnetic field can be derived from the difference of the calculated LLs. In the left panel of Figure 4.16 these expected transitions are presented along with experimental points taken from the spectra. Open squares, as well as dashed arrows on LL plot in Figure 4.14, represent intraband transitions, while full points (and solid arrows) represent interband transitions. There are visible discrepancies between experimental data and the theoretical predictions, which will be discussed in the summary of experimental results.

The right panel of Figure 4.16 shows the spectra plotted every 1 T, shifted vertically for clarity. Every minimum was marked with a colored symbol corresponding to the scheme presented on the left panel of the figure. The intensity of α and β transition dominate the spectra for the high values of

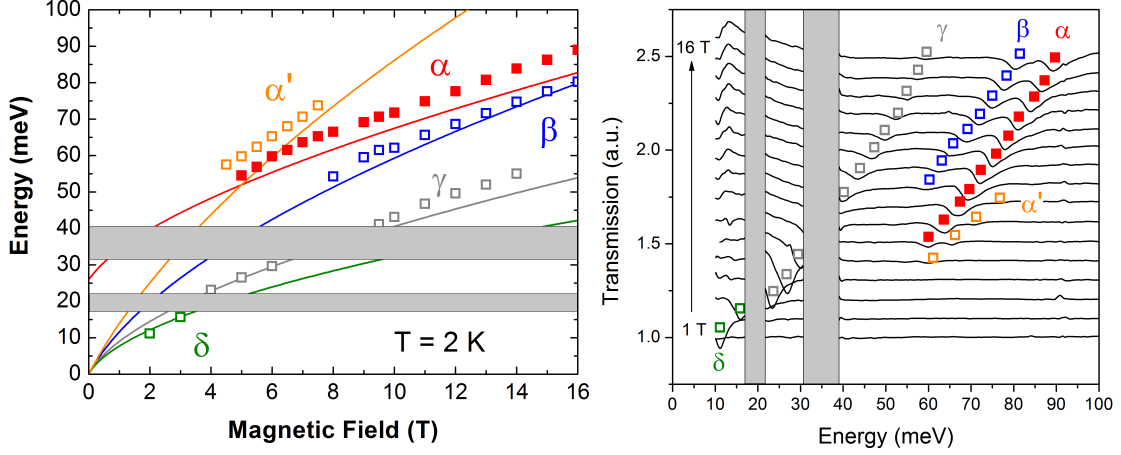


Figure 4.16: **Left Panel:** Points corresponding to the minima of the transmission of Sample B at $T = 2$ K with theoretical predictions of transitions as a function of magnetic field. Full symbols represent interband transitions, while open symbols represent intraband transitions. **Right panel:** Transmission spectra plotted for magnetic fields in range from 1 to 16 T every 1 T, with symbols corresponding to the transitions from left panel.

magnetic field, while γ dominates the low field region.

At low magnetic field the energy of the cyclotron resonance line depends linearly on magnetic field, which is visible in Figure 4.15 below the first reststrahlen band ($E < 17$ meV). At higher magnetic field the cyclotron resonance line evolves into δ transition [101], not visible due to the particular LL filling factor. The effective mass of electrons, obtained from the linear fitting of cyclotron resonance (δ) line, is equal to $m^* = eB/\omega_c = 0.025 \pm 0.011 m_0$.

Temperature 50 K

At temperature 50 K the band structure, presented in Figure 4.17, is visibly different in comparison to the band structure at 2 K. The band gap is smaller and the crossing of LLs with indices $n = -2$ and $n = 0$ takes place at a smaller magnetic field value $B_c \approx 3$ T. This is a reason why the anticrossing is not visible – the chemical potential lies above the LL $n = 1$, thus excitations to this level are forbidden. However, $T = 2$ K is not the only temperature at which the anticrossing is visible. This is the case for higher temperatures as well. Even at $T = 30$ K, a faint sign of an anticrossing can be traced on spectra. This is presented in Appendix C.

There are four transitions visible on the spectra – one interband α and three intraband β , γ , and δ . The energy gap, pointed by the α transition at zero magnetic field, is still negative and equal to 13 meV, which is considerably smaller than the energy gap at $T = 2$ K.

The transitions α and β are relatively close to each other, which makes them difficult to distinguish at some point, as presented on the right panel in Figure 4.18. It can be assumed that transition α starts to be detectable around $B = 5$ T, while transition β around $B = 9$ T. Both of them are visible up to at least 16 T. The two lower in energy transitions, namely γ and δ , are visible in intermediate fields and low fields, respectively.

The effective mass of electrons, obtained from the linear fitting of δ line, is equal to $m^* = eB/\omega_c = 0.021 \pm 0.003 m_0$.

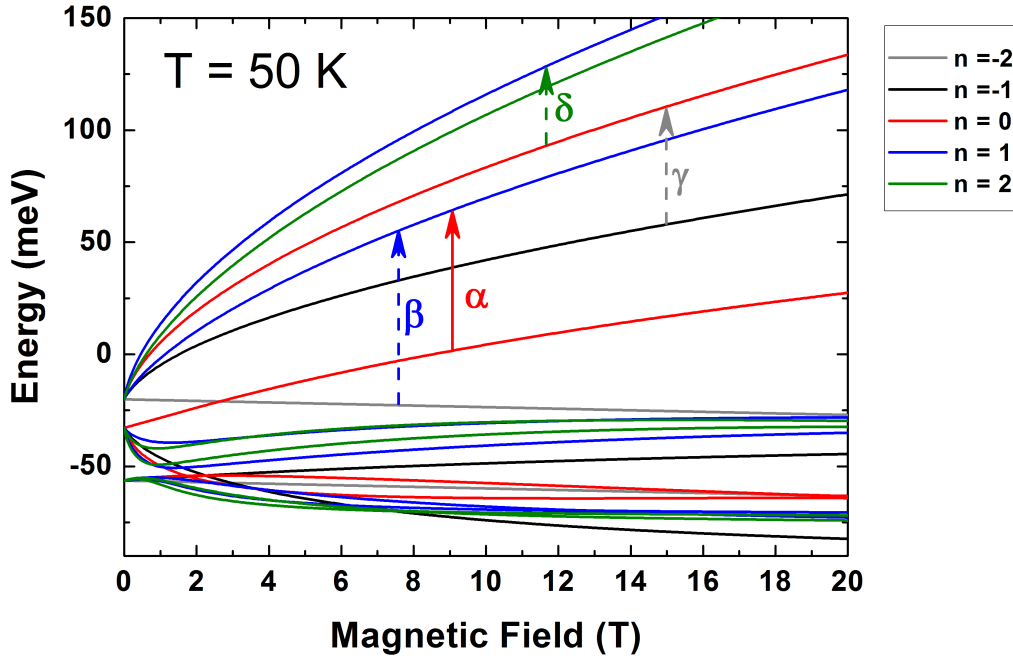


Figure 4.17: Landau level graph of Sample B as a function of magnetic field at $T = 50$ K. Colored lines represent Landau levels, characterized by a different value of n , as described as indices of L on the right side of the graph. The Landau levels with $n = -2$ and $n = 0$ are zero-mode Landau levels. The energy of those levels at zero magnetic field is an indication of the band gap. Their crossing indicates the point of field induced semiconductor-metal-semiconductor phase transition, and indicates that the sample is in the inverted band order phase. The vertical arrows with corresponding Greek letters represent observed transitions between Landau levels in this system. A solid arrow indicates an interband transition α , while dashed arrows indicate intraband transitions β , γ , and δ .

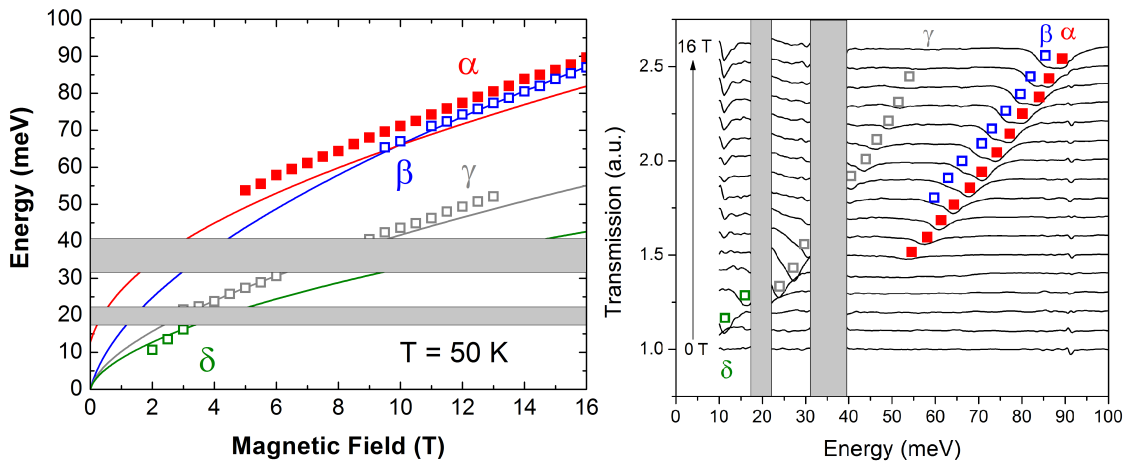


Figure 4.18: **Left Panel:** Points corresponding to the minima of the transmission of Sample B at $T = 50$ K with theoretical predictions of transitions as a function of magnetic field. Full symbols represent interband transitions, while open symbols represent intraband transitions. **Right panel:** Transmission spectra plotted for magnetic fields in range from 1 to 16 T every 1 T, with symbols corresponding to the transitions from left panel.

Temperature 90 K

The temperature 90 K is critical for Sample B. The band gap vanishes as the $HH1$ band merges with the $E1$ band at $B = 0$ T, as presented in Figure 4.19. It can be thought as the anticrossing of LL $n = 0$ and LL $n = 1$ takes place at $B_c = 0$ T. Both transitions α and β converge at zero energy at zero magnetic field. At the critical temperature the LL $n = -2$ is formed by a mixture of both $H1$ and $E1$ bands, thus it is impossible to declare whether transitions α and β are interband or intraband. This was marked in the Figure 4.19 by dotted arrows.

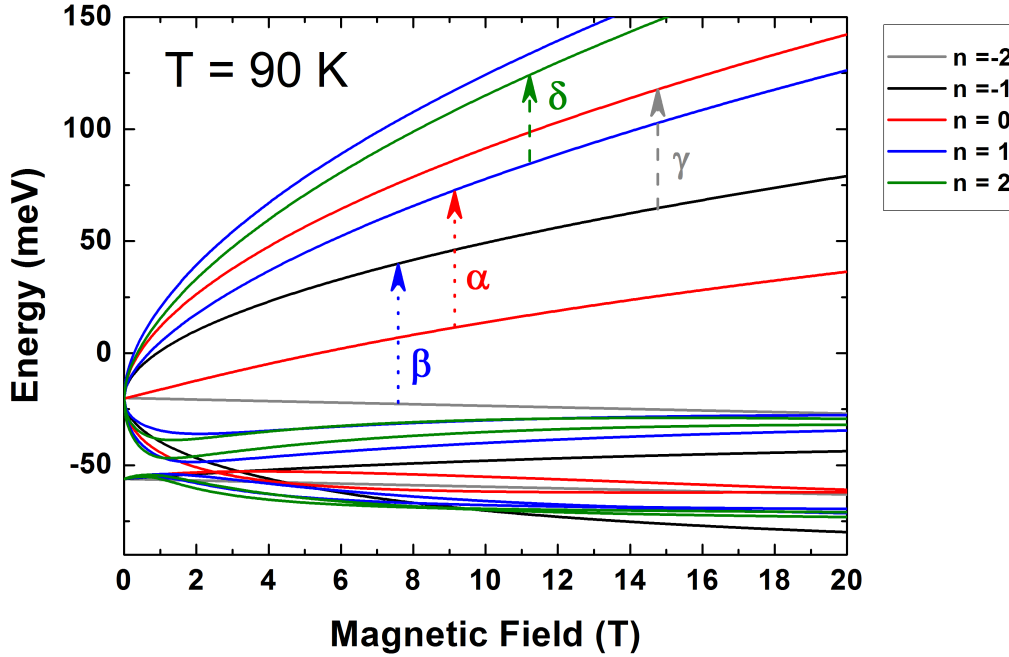


Figure 4.19: Landau level graph of Sample B as a function of magnetic field at $T = 90$ K. Colored lines represent Landau levels, characterized by a different value of n , as described as indices of L on the right side of the graph. The Landau levels with $n = -2$ and $n = 0$ are zero-mode Landau levels. Their crossing takes place at zero magnetic field, which means that the sample is gapless. The vertical arrows with corresponding Greek letters represent observed transitions between Landau levels in this system. It is not possible to determine whether α and β are inter- or intraband transitions, therefore they were marked with a dotted line. Dashed arrows indicate intraband transitions γ and δ .

The transitions α and β are further separated than at $T = 50$ K, and their intensity is comparable, as presented on right panel of Figure 4.20.

The transition α starts to be visible at around $B = 8$ T, while the transition β as low as $B = 4$ T. $T = 90$ K is the first temperature where the transition β starts to be visible at lower magnetic field than the transition α . Also, at this temperature, β has higher energy than α . The transition γ is visible at intermediate fields, and the transition δ at low. The effective mass of electrons, obtained from the linear fitting of δ line, is equal to $m^* = eB/\omega_c = 0.023 \pm 0.012 m_0$.

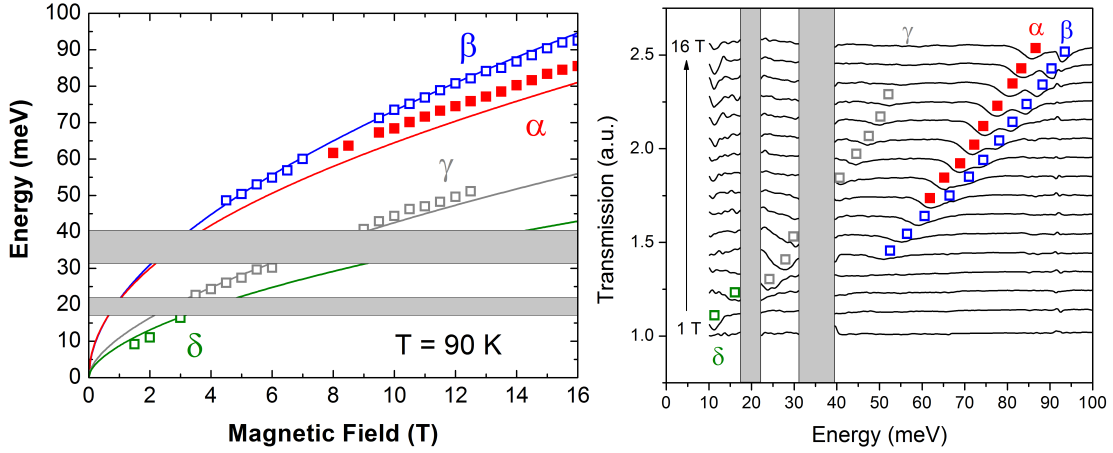


Figure 4.20: **Left Panel:** Points corresponding to the minima of the transmission of Sample B at $T = 90$ K with theoretical predictions of transitions as a function of magnetic field. Full symbols represent interband transitions, while open symbols represent intraband transitions. **Right panel:** Transmission spectra plotted for magnetic fields in range from 1 to 16 T every 1 T, with symbols corresponding to the transitions from left panel.

Temperature 110 K

At temperature 110 K the band order of Sample B is regular and the system is in a semiconductor state. The LL $n = -2$ is the highest energetic level of the H1 level, while the LL $n = -0$ is the lowest energetic level of the E1 level. The LL structure is presented in Figure 4.21. There are four transitions visible – one interband β , and three intraband α , γ , and δ . The zero-mode LLs crossing is not present anymore, which indicates that a phase transition took place and the system is in the regular band order. Because of that, the transition β is interband, while the transition α is intraband, which was not the case in the inverted regime. The band gap is positive and equal to 6 meV.

The transitions α and β are further apart than at lower temperatures. They start to be visible at around 6 T and their intensity is the highest at high magnetic field. The transition γ dominates in the intermediate values of magnetic field, while the transition δ is visible only at low B . The effective mass of electrons, obtained from the linear fitting of δ line, is equal to $m^* = eB/\omega_c = 0.022 \pm 0.010 m_0$.

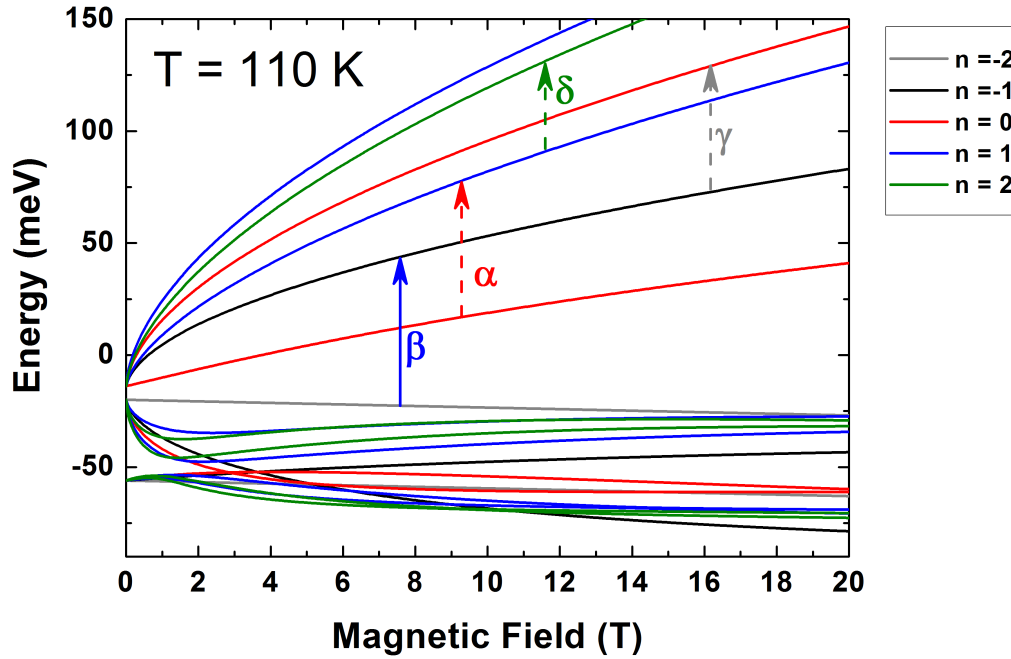


Figure 4.21: Landau level graph of Sample B as a function of magnetic field at $T = 110$ K. Colored lines represent Landau levels, characterized by a different value of n , as described as indices of L on the right side of the graph. The Landau levels with $n = -2$ and $n = 0$ are zero-mode Landau levels. The energy of those levels at zero magnetic field is an indication of the band gap. The vertical arrows with corresponding Greek letters represent observed transitions between Landau levels in this system. A solid arrow indicates an interband transition β , while dashed arrows indicate the intradband transitions α , γ , and δ .

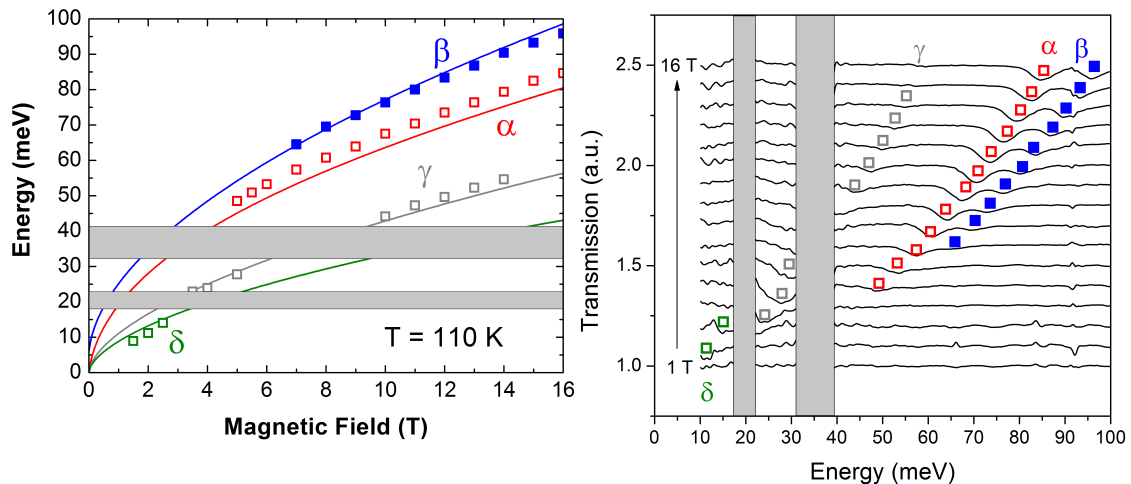


Figure 4.22: **Left Panel:** Points corresponding to the minima of the transmission of Sample B at $T = 110$ K with theoretical predictions of transitions as a function of magnetic field. Full symbols represent interband transitions, while open symbols represent intradband transitions. **Right panel:** Transmission spectra plotted for magnetic fields in range from 1 to 16 T every 1 T, with symbols corresponding to the transitions from left panel.

Temperature 130 K

At temperature 130 K Sample B is in a semiconductor state. The LL structure is presented in Figure 4.21. Similar to $T = 110$ K, there are four transitions visible – one interband β , and three intraband α , γ , and δ . The band gap is positive and equal to 12 meV.

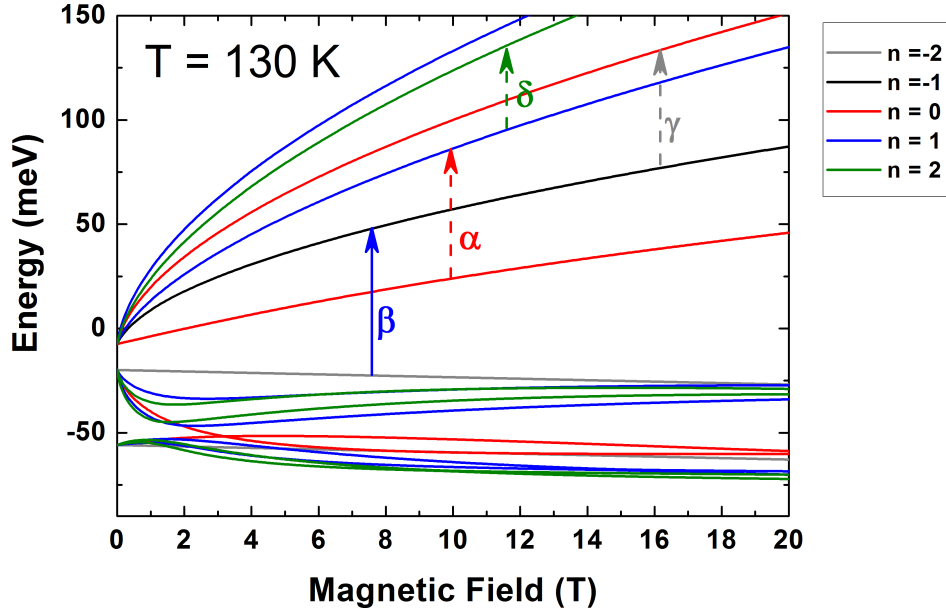


Figure 4.23: Landau level graph of Sample B as a function of magnetic field at $T = 130$ K. Colored lines represent Landau levels, characterized by a different value of n , as described as indices of L on the right side of the graph. The Landau levels with $n = -2$ and $n = 0$ are zero-mode Landau levels. The energy of those levels at zero magnetic field is an indication of the band gap. The vertical arrows with corresponding Greek letters represent observed transitions between Landau levels in this system. A solid arrow indicates an interband transition β , while dashed arrows indicate the intraband transitions α , γ , and δ .

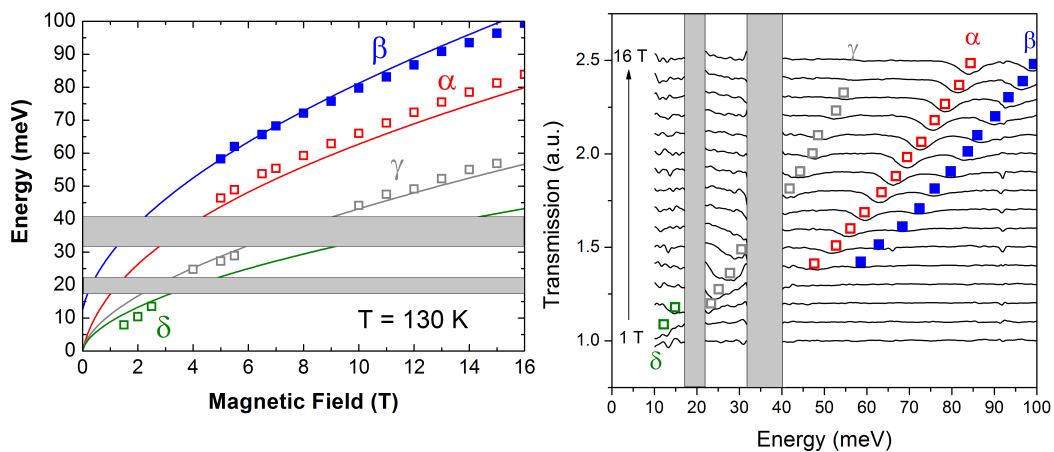


Figure 4.24: **Left Panel:** Points corresponding to the minima of the transmission of Sample B at $T = 130$ K with theoretical predictions of transitions as a function of magnetic field. Solid symbols represent interband transitions, while open symbols represent intraband transitions. **Right panel:** Transmission spectra plotted for magnetic fields in range from 1 to 16 T every 1 T, with symbols corresponding to the transitions from left panel.

The transitions α and β continue to further separate. They start to be visible at around 5 T and their intensity is the highest at high magnetic field. The transition γ dominates in the intermediate values of magnetic field, while the transition δ is visible only at low B . The effective mass of electrons, obtained from the linear fitting of δ line, is equal to $m^* = eB/\omega_c = 0.021 \pm 0.008 m_0$.

4.1.3 Summary

The FIR magneto-optical results presented in this chapter prove that temperature can be used as an adjustable external parameter to control a band structure of HgTe/CdTe QW and, as a consequence, to induce a topological TI-metal-semiconductor phase transition. A set of two samples was investigated – one sample (A) is in semiconducting state at the whole temperature range, while the other (B) is a TI at low temperature and undergoes a phase transition at $T_c = 90$ K, characterized by a band gap closure and a lack of crossing of zero-mode LLs.

The energy gap of Sample A is positive at all temperatures and its value increases with increasing temperature. This behavior is presented in Figure 4.25. The Figure 4.25 presents the energy values of minima of the transmission as a function of magnetic field for Sample A (open symbols), and the results of numerical calculations based on the 8-band Kane model for different temperatures. The

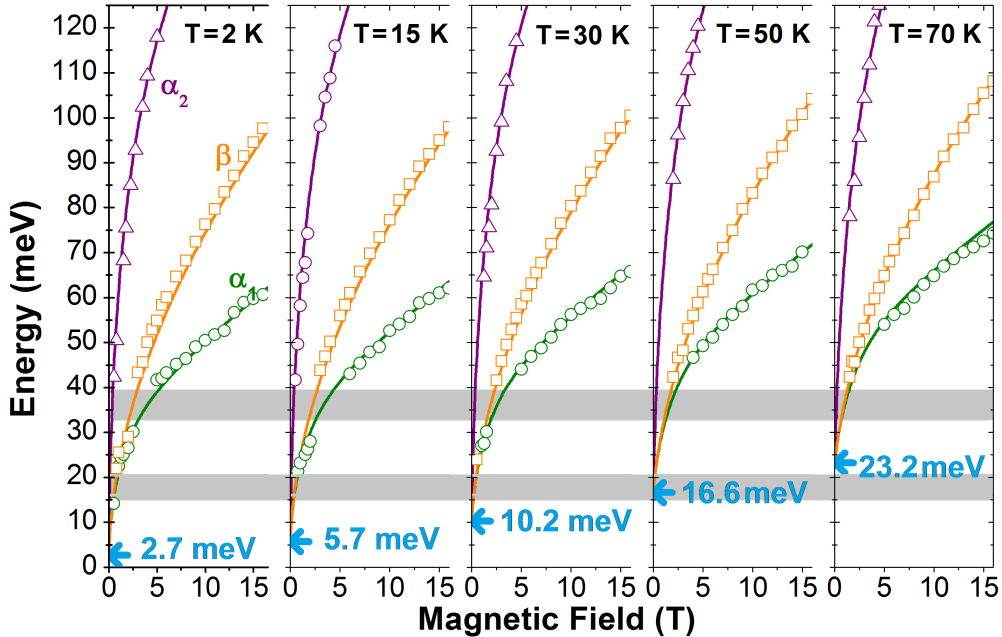


Figure 4.25: Energy of α_1 (green curve), α_2 (purple curve), and β (orange curve) transitions as a function of magnetic field for Sample A at $T = 2$ K, 15 K, 30 K, 50 K and 70 K. The experimental data corresponding to minima of the transmission is represented by open symbols. The value of band gap is indicated with a blue arrow. The reststrahlen bands are covered by grey areas.

blue arrow points to the value of a band gap at given temperature. The experimental results and theoretical predictions are in a good agreement. Sample A is almost gapless at $T = 2$ K, and its band gap value increases up to $E_g = 23.2$ meV at $T = 70$ K.

The evolution of energy gap and inter- and intra-LL transitions for Sample B is presented in Figure 4.26. At $T < T_c = 90$ K the sample has an inverted band structure and negative energy gap, characterized by the relative position of zero-mode LLs.

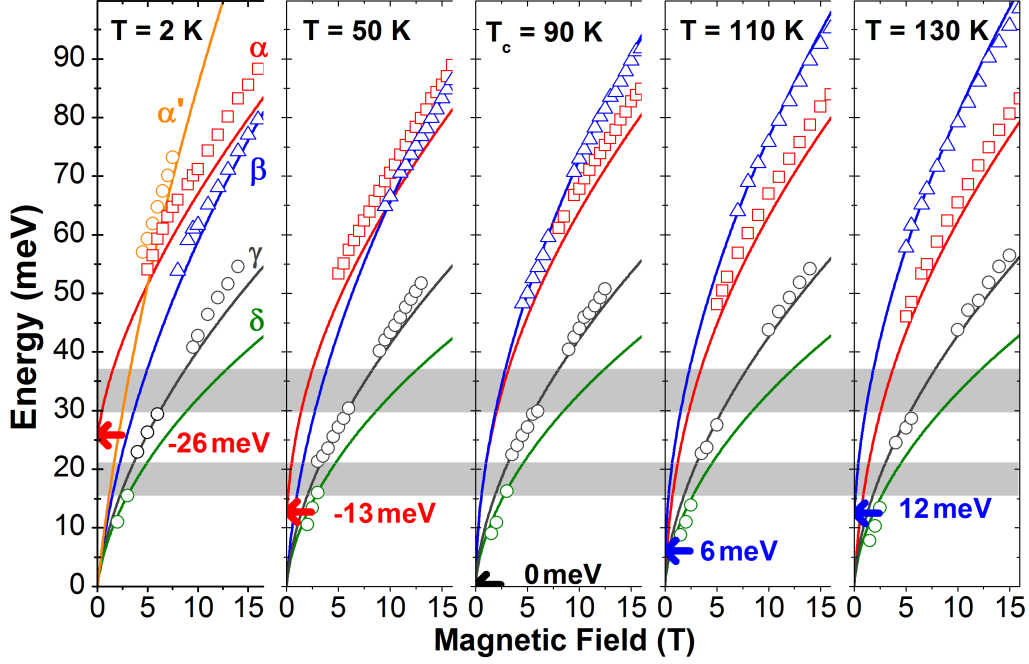


Figure 4.26: Energy of α (orange curve), α' (red curve), β (blue curve), γ (grey curve), and δ (green curve) transitions as a function of magnetic field of Sample B at $T = 2$ K, 50 K, 90 K, 110 K and 130 K. The experimental data corresponding to minima of the transmission is represented by open symbols. The value of negative (positive) band gap is indicated with a red (blue) arrow. The gapless state corresponding to the gap closure (black arrow) takes place at $T_c = 90$ K. The reststrahlen bands are covered by grey areas.

At $T = 2$ K (and $T = 30$ K, as presented in Appendix C) an additional transition α' appears in the spectra in a small magnetic field range, which corresponds to the avoided crossing of zero-mode LLs. This anticrossing is a direct indication of an inverted phase. The α' transition is forbidden by the selection rules. However, because BIA causes a mixing of zero-mode LLs and an activation of the transition α' , its appearance is possible and was previously reported in [101][102][105].

At $T > T_c = 90$ K the Sample B is in a semiconducting phase. The band gap is positive, which is represented by a blue arrow in Figure 4.26, and reaches up to 12 meV at $T = 130$ K.

At the critical value $T = T_c$ the band gap vanishes (black arrow) and the system hosts massless Dirac fermions. The appearance of massless particle is characterized by a square-root dependence of energy of inter- and intra-LL transitions on magnetic field. However, in the case of HgTe QWs, this is valid only in the range of quasimomenta, where the band structure can be approximated by the Dirac Hamiltonian. This reduces the characteristic $E \propto \sqrt{B}$ dependence to the electrons in the vicinity of the Γ point of the Brillouin zone, where $\mathbf{k} \approx 0$. The terms proportional to \mathbf{k}^2 in the Hamiltonian become relevant at higher values of \mathbf{k} . As a consequence, at high magnetic field the dependence of the energy of the transitions on B becomes linear functions.

Figure 4.27 shows a comparison of the evolution of transitions α , β , and γ as a function of \sqrt{B} in the gapless case in the presence of the Dirac cone in the vicinity of the Γ point. The transitions were calculated using an approximate Dirac approach and the numerical 8-band Kane model. The calculated LLs transitions, based on the Kane model (solid curves), β and γ do not follow a square-root magnetic field dependence over the whole magnetic field range, which is not the case for the LLs transitions based on Dirac model (dotted curves). On the other hand the transition α (solid red

curve in Figure 4.27) has a square-root-like dependence (which means that the position of solid curve coincides with the position of dotted curve). However, this behavior is not related to the conical band dispersion, but is a consequence of the mutual compensation of the high order k terms in the 8-band Kane model.

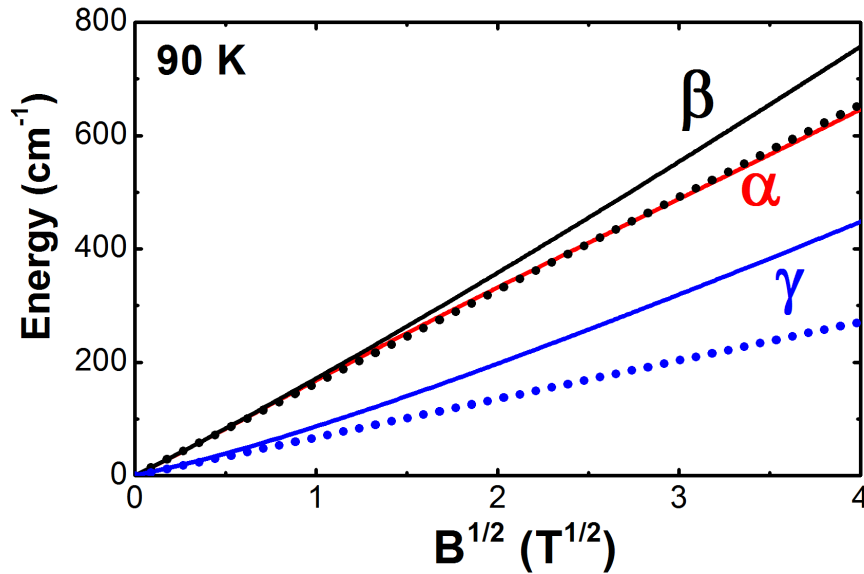


Figure 4.27: Energy evolution of transitions α , β , and γ as a function of \sqrt{B} at $T = 90$ K approximated by Dirac Hamiltonian (dotted curves) and calculated using 8-band Kane Hamiltonian (solid curves).

A characteristic property of NGS with a non-parabolic dispersion is a sub-linear dependence of cyclotron resonance on magnetic field. At low fields, the dependence is linear and allows to extract the effective (cyclotron) mass of electrons. However, at higher fields the linear cyclotron resonance line evolves into a transition denoted as δ [101]. The value obtained from the average of fits of δ transition at low magnetic fields, is equal to $m^* = eB/\omega_c = 0.022 \pm 0.004 m_0$, which exactly matches previous results from works [101][102].

The experimental results for Sample A are in a fair agreement with the theoretical calculations. However, there are unquestionable discrepancies between the theory and experimental results of Sample B, reaching around 10%. The origin of these discrepancies is not totally clear, as there are many factors that could possibly be omitted in considerations. One of these factors is an electron-electron interaction, which can be relevant in the case of Sample B, as there is one order of magnitude difference in carrier concentration, and can perturb the result. In addition, Sample B was doped on both sides in the barriers, and this donor states can influence the results as well. Moreover, as was already highlighted in [102] mercury-based heterostructures, can degrade with time via mercury diffusion. This process is especially critical to structures with sharp interfaces, like QWs, because the QW parameters like the shape of the well, the cadmium content in the barriers can change with time. This has a profound influence on the obtained results as the investigated structure is different than expected (at the time of growth).

4.2 Strained HgTe Films

The systems, in which a HgTe layer sandwiched between CdTe, is wide enough to neglect the interface interactions but not wide enough to cause a merging of the levels into bands, are called films or slabs. These systems can be considered to be in an intermediate state between 2D and 3D. However, these systems are semimetallic, as the quantum confinement is low – a different mechanism is necessary to open an energy gap to render the bulk insulating. The solution to this problem is to apply a strain to the material [55]. If a HgTe film is compressively strained, the bulk becomes fully gapped in a response to a lowered symmetry [27]. This can be achieved by growing a layer of HgTe on a substrate with a different lattice constant, which opens an energy gap. If the chemical potential lies inside the band gap, the only conducting states left are topological surface states.

The existence of Dirac-like surface states in bulk HgTe has been known since the eighties [108][109], however their topological nature has never been investigated in detail. These systems can potentially allow to study already predicted novel properties of 3D TIs, such as topological magneto-electric effect [110], superconducting proximity effects and Majorana fermions [111][112].

4.2.1 Band Structure

In thin HgTe QWs the band gap is formed by a quantum confinement which originates from an interaction between states at interfaces with barriers, and exists as long as the wave functions of these interface states overlap. For the case of wider QWs this interaction is smaller, as well as the resulting energy gap. As the thickness increases, the quantum confinement is still present but becomes too small to open an energy gap, therefore the system becomes semimetallic. If a QW thickness is increased even more, the relative distances between consecutive levels within the well shrink. If the process continues up to a point where the level broadening (for example due to temperature) is higher than the distance between the levels, the levels merge and form a band, and the system is considered as bulk.

4.2.1.1 Strain

The lattice constant of HgTe grown on CdTe is 0.3 % larger than that one of bulk HgTe, which leads to an appearance of a strain. As long as a HgTe layer is not thicker than around 150 nm (150 nm [56], 200 nm [27]), the layer adopts the lattice constant of a substrate and it is strained homogeneously. However, in thicker layers the strain starts to be partially relaxed via the formation of dislocations. In a fully strained system a band gap can be increased to approximately 20 meV [27][56]. Using a different substrate, like $\text{Cd}_{0.96}\text{Zn}_{0.04}\text{Te}$ [58], it is possible to apply a stronger strain which increases the value of the band gap. However, the stronger strain makes the structure more prone to relax via exhibiting dislocations, reducing the maximal possible width.

4.2.1.2 Surface States

One of the most prominent features of narrow HgTe QWs (with thickness close to the critical) is existence of one-dimensional channels of conductance on the edge, as presented in Chapter 1 in Figure 1.1. These states are available for electrons taking part in carrier transport, but do not take active part in the light absorption. It has to be stressed that their presence is not related to an existence of the interfaces between HgTe QW and CdTe barriers, but a one-dimensional interface between HgTe QW and the surrounding vacuum (or air). From the point of view of the edge states, the sole role of

CdTe barriers is to provide the quantum confinement, which opens the bulk gap and suppresses the bulk conduction.

It is often neglected that the 2D interfaces between a HgTe QW and CdTe barriers are still present in the system. The QW and barriers are characterized by a different topology, therefore a set of states with linear dispersion relation should appear at the interface as well. These states are interesting from the point of view of magneto-optics, because only electrons on the surfaces perpendicular to the beam of light can absorb photons. The Figure 4.28 shows the results of the ARPES measurements, which allowed to resolve topological-like features connecting heavy- and light-holes, which proved that the boundary states are still present in the system but they are buried deep in the heavy-hole band.

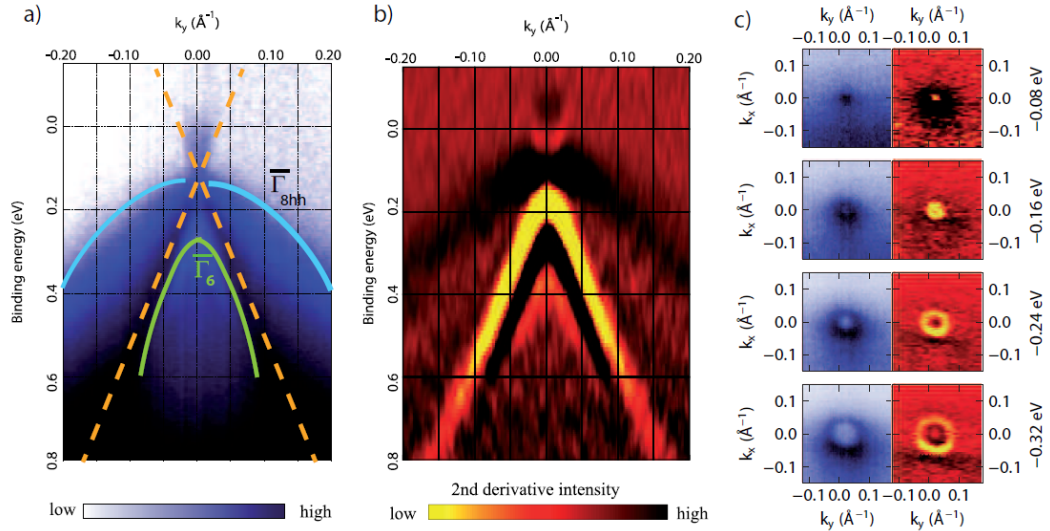


Figure 4.28: *High resolution ARPES spectra for a maximally strained [100] HgTe/vacuum interface in the vicinity of the Γ -point measured at room temperature. **Panel (a):** Energy-momentum intensity spectrum after a background subtraction. **Panel (b):** The second derivative of the intensity data to enhance the contrast. **Panel (c):** Intensity spectrum at different energies. Raw data on the left and its second derivative on the right. The cone structure has a circular section up to ≈ 0.4 eV. Images come from the work of Brüne et al. [27].*

The edge states on the interface between HgTe and vacuum can be considered one dimensional as long as the thickness of HgTe layer is small. If the thickness is increased, the 1D edge transforms into a 2D surface, and an appearance of interface surface states should occur.

Origin of surface states

The band structure of a bulk HgTe is presented in Figure 3.1 in the introduction to HgCdTe-based structures in Chapter 3. In the presence of strain an insulating energy gap opens between the heavy-hole (HH) and light-hole (LH) bands by pushing the HH band downward in energy. To understand better the processes occurring here, it is useful to ignore the HH band and consider the LH and E bands only. According to the Kane model, the coupling of the LH and E bands, which takes place in the vicinity of the Γ point, can be represented by a 3D anisotropic massive Dirac Hamiltonian. The Dirac Hamiltonian conserves the parity symmetry, therefore the bands can be labeled by parity eigenvalues. The coupling is linear, thus there must be one even and one odd band. If the odd parity band lies energetically below the even parity band, there will be a nontrivial \mathbb{Z}_2 topological invariant, which indicates an odd number of pairs of surface states that cross at invariant points [55][28]. The

presence of the HH band changes only the features of the dispersion, it does not change the presence of the surface states, nor their protected crossing, as long as the strain-induced gap is opened, and the chemical potential lies in the gap.

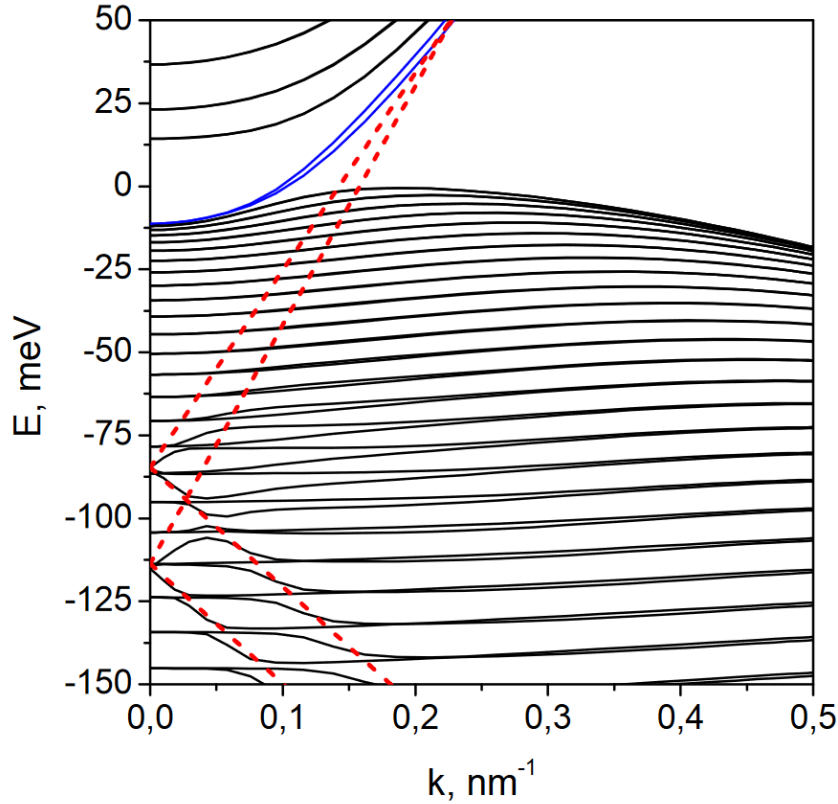


Figure 4.29: *Band structure of a 70 nm thick 0.3% strained HgTe slab. The Dirac-like states in the gap are plotted in blue. The dashed red line schematically shows the dispersion of the Dirac surface states at the two opposite surfaces before their hybridization with the Γ_8 heavy-hole band. The image comes from the work of Brüne et al. [27].*

The energy structure of a 70 nm thick strained HgTe film is presented in Figure 4.29. The surface states are represented in blue. In an absence of the HH band, their dispersion would be linear. A qualitatively similar situation takes place in bulk PbSnTe, where the Dirac-like surface states are near the L point of the Brillouin zone, connecting L_6^\pm bands 4.30. However, in HgTe the HH band mutually interacts with electron band and surface states, effectively changes the dispersion relation of the whole system, as presented in Figure 4.29.

It is worth to mention that the names LH $|\Gamma_{8,\pm 1/2}\rangle$ and E $|\Gamma_{6,\pm 1/2}\rangle$ are used to describe energy bands in bulk system, along with HH $|\Gamma_{8,\pm 3/2}\rangle$. In the language of QWs, the energy levels are named with a letter (E for electron-like band, and H for hole-like band) and an appropriate number. What does it really mean is that both the electron-like and hole-like bands contain a mixture of E and LH bands of the bulk:

$$\begin{aligned} E_n &= \alpha_n(x, L) |\Gamma_{6,\pm 1/2}\rangle + \beta_n(x, L) |\Gamma_{8,\pm 1/2}\rangle, \\ H_n &= \tilde{\alpha}_n(x, L) |\Gamma_{6,\pm 1/2}\rangle + \tilde{\beta}_n(x, L) |\Gamma_{8,\pm 1/2}\rangle, \end{aligned} \quad (4.8)$$

where α_n , β_n , $\tilde{\alpha}_n$, $\tilde{\beta}_n$ are constants, which values depend on Cd content x , and film thickness L . For sufficiently large L , the constants β_n and $\tilde{\alpha}_n$ become small, and the QW levels E and H resemble the bulk bands E and LH, respectively. This superposition of $|\Gamma_{6,\pm 1/2}\rangle$ and $|\Gamma_{8,\pm 1/2}\rangle$ allows to smoothly

switch from the bulk band to the QW band description. Due to the mixing of bands, only at $k = 0$ it is possible to classify which band a given energy level belongs to.

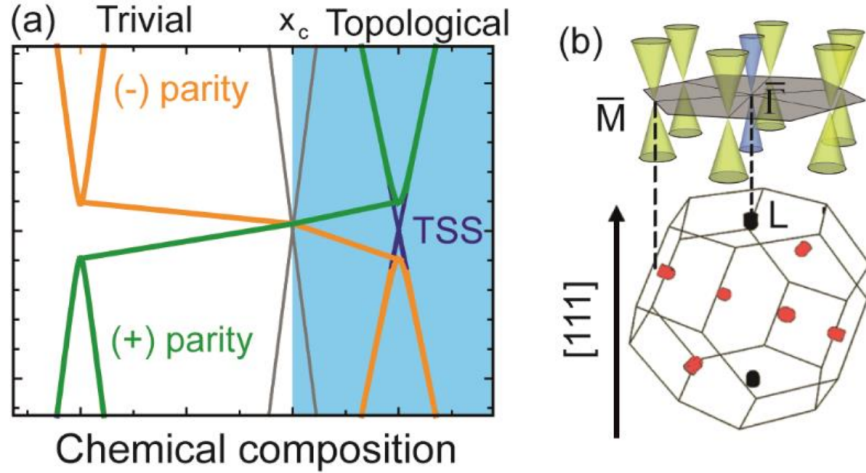


Figure 4.30: *Topological phase transition and the Brillouin zone of $Pb_{1-x}Sn_xSe$ and $Pb_{1-x}Sn_xTe$. Panel (a): Sketch of a topological phase transition that occurs at a critical point x_c as a function of composition in a system having a conduction and valence band of opposite parity (different color). The bulk band gap closes at x_c . Topological surface states emerge in the topological regime $x > x_c$ (shaded blue region). In IV-VI topological crystalline insulators, this occurs at a critical Sn concentration x_c . Panel (b): Bulk Brillouin zone of [111] IV-VI semiconductors, showing the longitudinal (black), and oblique (red) valleys. The topological surface band structure above the bulk Brillouin zone shows the $\bar{\Gamma}$ (blue) and the \bar{M} (yellow) Dirac cones. The image comes from the work of Assaf et al. [60].*

Surface states in inverted and non-inverted systems

The band structure and the dispersion of surface states changes with the cadmium content and the thickness of the film (and other parameters, which are out of the scope of this thesis, like temperature, pressure, etc.). As the cadmium content increases, it shrinks both the strain gap (because of reduced lattice mismatch) and a band gap (the difference between Γ_6 and Γ_8 bands). If this process continues, at some point it reaches a critical value, where the band structure becomes regular, exactly as in the case of relaxed HgCdTe for $x > x_c$. This process is presented in Figure 4.31 for a strained structure of thickness $L = 80$ nm. The QW approach is used to describe the energy levels, therefore levels E_n are composed of the mixture of electron and light-hole bands, and levels H_n are composed of the heavy-hole band (Equations 4.8). The surface states are always composed of a mixture of E_1 and H_1 subbands, and because of that it is only possible to classify which subband is dominant at $k = 0$. As the cadmium content varies along the relative position of the bands, the either E_1 or H_1 part dominates.

For Cd content x lower than $x_c = 0.14$ (Panel (a)), the structure is more HgTe-like – the band order is inverted, and can be qualitatively compared with the one presented in Figure 4.1 for high d_{QW} . The subbands $E_{2,3,\dots}$ are more LH-like, and lie above the HH subbands H_2 , while the subband E_1 lies buried deep in H_n subbands (not shown in the Figure). In this situation the surface states (dotted line) are composed of a mixture of E_n (LH-like) and H_n states (HH-like), and at $k = 0$ the HH part dominates. The Dirac point lies inside the HH band (its position as well as the shape of surface states in the absence of the HH band is plotted in green).

For the critical Cd content $x = x_c$ (Panel (b)) the band structure has similar properties to the

band structure of bulk HgCdTe at $x = x_c$ (Chapter 3, Figure 3.2). The easily visible differences are: the bands are split into subbands due to the quantum confinement, and the shape of the HH band is changed due to the strain and interactions between bands. The dispersion of surface states is linear. This is the exact Cd concentration where band inversion occurs. Because of that the E_n bands are more electron-like than LH-like, therefore the surface states at $k = 0$ are composed dominantly of E_1 band. The Dirac point lies close to the top of HH band.

For Cd content x higher than x_c (Panel (c)), the structure is more CdTe-like. The system is a 3D band insulator. The E_n subbands are composed of the electron-like states. In this situation the surface states are trivial and are composed of a mixture of E_n (electron-like) and H_n subbands, at $k = 0$ are formed predominantly by the E_1 subband. The Dirac point lies inside the H_n subbands.

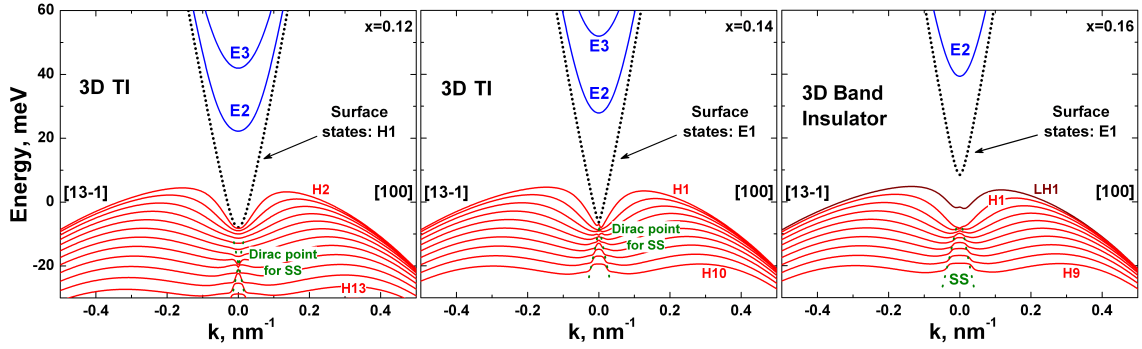


Figure 4.31: Band structure of an 80 nm thick strained $\text{Hg}_{1-x}\text{Cd}_x\text{Te}$ film calculated for $[13-1]$ and $[100]$ crystallographic directions. The band description is according to a QW approach. E_n subbands (blue) represent electron-like states, while H_n subbands (red) represent hole-like states. The dispersion of the surface states is plotted as dashed curves. **Panel (a)**: Cadmium content $x = 0.12$, the system is a topological insulator. The surface states at $k = 0$ are composed predominantly of H_1 subband. **Panel (b)**: Cadmium content $x = 0.14$, the system is at a topological insulator-to-band insulator phase transition. The surface states at $k = 0$ are composed predominantly of E_1 subband. **Panel (c)**: Cadmium content $x = 0.16$, the system is a band insulator. The surface states are trivial, and at $k = 0$ are composed predominantly of E_1 subband.

Figure 4.32 explains in detail what does it mean that the surface states are composed of a mixture of E_n and H_n subbands, and what is a dominant component. The black curve shows the squared sum of modules of the wave functions (probability) as a function of z coordinate. It is clear that the surface states are localized close to both surfaces, and they exponentially decay in the bulk. Moreover, as the Cd content is zero, the dominant component of the surface states should originate from the H_1 subband (Panel (a) of Figure 4.31), which is formed by HH states $|\Psi_{\Gamma_8, \pm 3/2}\rangle$. Indeed, as is presented in Figure 4.32 the $|\Psi_{\Gamma_8, \pm 3/2}\rangle$ wave functions (purple and magenta curves) dominate over E and LH wave functions.

The second parameter which can modify the band structure is a thickness of the film, which changes the effective quantum confinement and the relative position of LH and E bands. The dispersion of surface states can be related to a mutual interaction between them. This interaction gets stronger as the overlapping of the wave functions of the bottom and the top surfaces increases. A typical penetration length is approximately equal to $\delta \approx 20$ nm, as is presented in Figure 4.32, taken from the work of Dantscher *et al.* [113]. It shows the result of six-band $k \cdot p$ calculations for a (013)-oriented 80 nm thick structure. The states, shown as curves representing the probability density functions of electrons belonging to different bands, are localized at the film interfaces, and predominantly formed

by the HH states $|\Psi_{\Gamma_8, \pm 3/2}\rangle$.

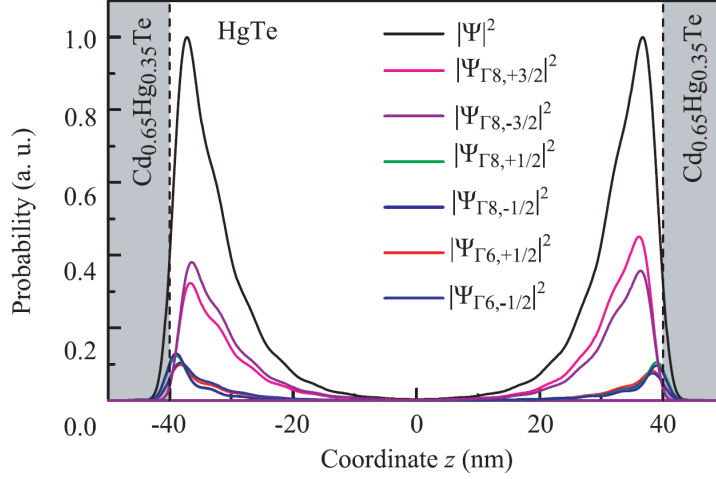


Figure 4.32: Wave functions of surface states in a (013)-grown 80 nm strained HgTe film. Calculations are carried out for the electron energy $E = 11$ meV, the wave vector components $k_x > 0$ and $k_y = 0$, and the built-in electric field $E_z = 2$ kV/cm. The image comes from the work of Dantscher et al. [113].

The results of the calculations of band structure based on the Kane model for 50, 25, and 15 nm thick strained HgTe films are presented in Figure 4.33. The LH and HH bands are represented as blue and red curves, respectively. The bands are split due to the residual quantum confinement. The surface states are represented as black solid curves. If SIA is present in the structure, the degeneracy of states on the bottom and top surfaces is lifted, which leads to a splitting of dispersion of surface states, not shown in the Figure. Black dotted curves represent the dispersion of the surface states in the absence of the HH band.

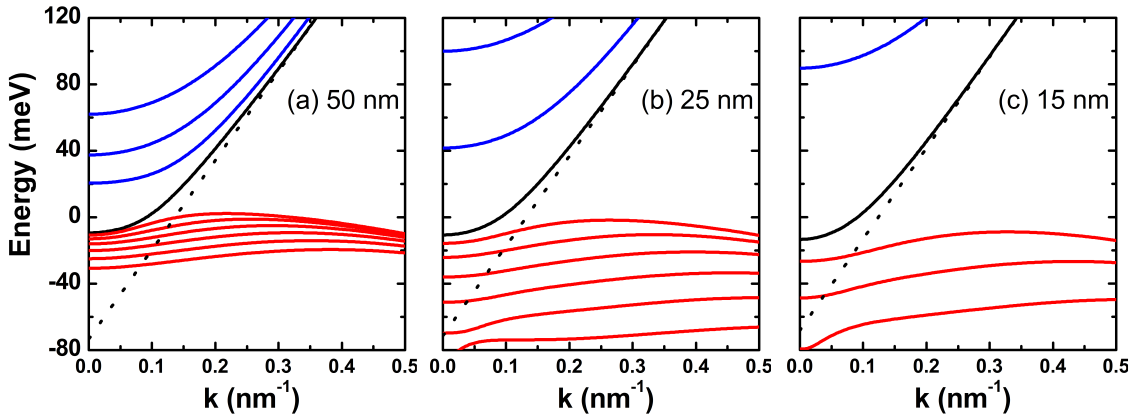


Figure 4.33: Band structure calculations of strained HgTe films with thicknesses **Panel (a)**: 50 nm, **Panel (b)**: 25 nm, and **Panel (c)**: 15 nm. The dispersion relations of the surface states are plotted as solid black curves. Dotted black curves represent the dispersion relations of the surface states in an absence of the HH band. The HH and the LH subbands are plotted as red curves and blue curves, respectively. The system is in an inverted band order, therefore the surface states at $k = 0$ are dominantly formed by the H_1 level.

For films thicker than $L > 2\delta \approx 40$ nm (Panel (a)), the wave functions are well separated – their

interaction is negligible and the band structure does not qualitatively change as the thickness increases [114]. The Dirac points of the surface states lies deep in the HH band, which leads to a level mixing and a deviation of the dispersion relation from the linear [113]. Because of this, the energy of surface states at the Γ point is similar to the energy of the top of the HH band. The dispersion of surfaces states is gapless, therefore they are massless. This situation is conserved even for thicker structures.

However, the interaction of the surface states in films with thickness smaller than 2δ leads to a hybridization and opens an energy gap as a consequence [114], which is visible in Figure 4.33 on Panel (b). The appearance of the energy gap changes the character of the surface states from massless to massive. With decreasing thickness the strength of the quantum confinement increases, which further separates the subbands (Panel (c)). If the process continues and the thickness reaches $d_c = 6.3$ nm, a phase transition occurs and the structure becomes semiconducting (as stated in Chapter 4.1).

4.2.1.3 Magnetic Field

In the presence of magnetic field the energy of surface states becomes quantized. Magnetotransport measurements performed at mK temperatures [27] on a 70 nm HgTe strained film revealed distinct features characteristic for a 2D system – the plateaux of Hall resistance R_{xy} occur when the longitudinal resistance R_{xx} is in its minimum, and the R_{xy} takes expected values. A particular sequence of Hall plateaux for odd filling factors at low magnetic field indicates the presence of zero mode LLs, characteristic for systems with linear dispersion of Dirac fermions, which has been already found in graphene [100] and in thin HgTe QWs close to the critical thickness [102]. These results suggest that the current is carried mostly by bottom and top surface states, which can be populated differently if the SIA is present (for example in gated structures as the top surface effectively screens the gate potential, or if the structure is doped asymmetrically). There are indications that there is some residual conductivity which can originate from the conductivity of side edge channels, which remain metallic [115].

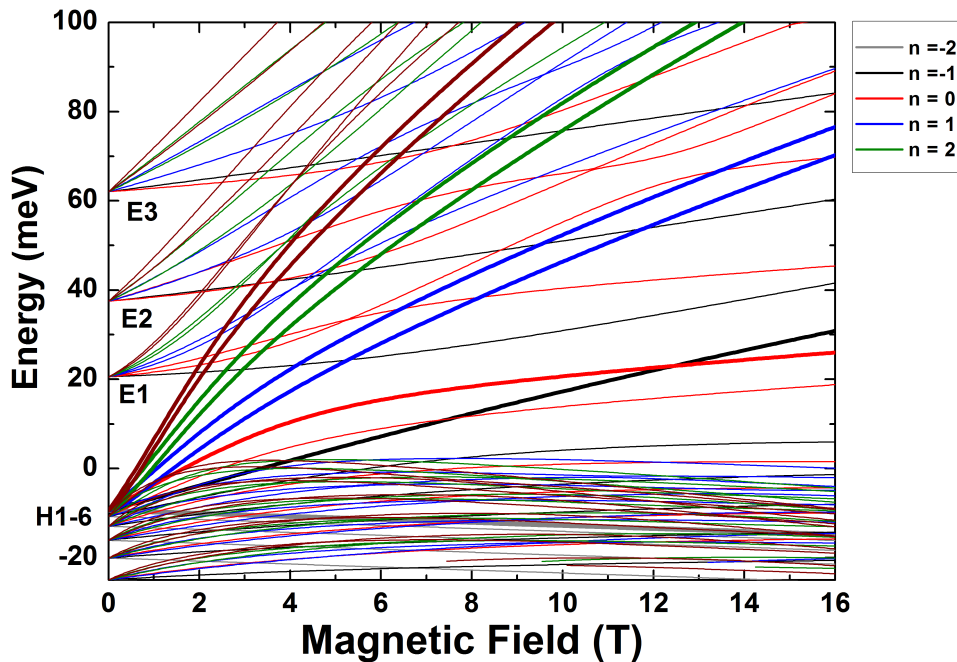


Figure 4.34: Landau level plot of a strained 50 nm HgTe film. Curves designated as E (H) form the conduction (valence) subbands. The surface states are plotted as thick solid lines.

The LL spectrum of a 50 nm film is presented in Figure 4.34. There are multiple subbands present, resulting from double quantization – the LL quantization and the one originating from the quantum confinement. The LH band is split into three subbands (E1 - E3), while the HH band is split into six subbands (H1 - H6). The surface states, highlighted by thick curves, are formed by the H1 subband.

4.2.2 Experiment

The magneto-spectroscopy study of strained HgTe films could potentially provide an insight into the energy structure of the surface states, and how does it change with the parameters of the system. The study can also reveal what those states are in detail, which is important to understand the origin and their relation with the bulk states.

The main experimental part of this Chapter is related to a study of a strained 50 nm-thick HgTe film (Sample A), as it allowed to observe the surface states. The magneto-transmission measurements were performed on Sample B and C as well, but the interpretation of the results is still missing. All the spectra were taken at $T = 2$ K with a bolometer placed directly under an investigated sample. In order to obtain a final transmission spectra, an additional reference spectra without the sample was recorded and Equation 2.38 was used. All measurements were performed at magnetic fields up to 16 T and in energy range 80 - 800 cm^{-1} ($\approx 10 - 100$ meV) with a 4 cm^{-1} resolution. The infrared transmittance spectra were measured by a Fourier spectrometer with a Globar lamp as a source of radiation. The system was coupled to a liquid helium cryostat. The transmission spectra were obtained by dividing the spectra taken at given magnetic field by the spectra obtained at zero magnetic field.

On each spectra there is a completely opaque region due to the presence of reststrahlen bands, existing between 16 and 24 meV corresponding to a phonon absorption of HgTe/HgCdTe layers. Because of that, the energy regions corresponding to these bands were covered by grey areas on the spectra.

4.2.2.1 Samples

The investigated samples were grown using the MBE method (by Philippe Ballet) in CEA-LETI (Grenoble, France). The growth process and samples characterization is thoroughly presented in a Ph.D. thesis of Candice Thomas [116]. They consist of a 0.7 mm (100) CdTe substrate followed by a 200 nm CdTe buffer layer. The active part of the structure is formed by a HgTe layer (of various thicknesses) enclosed within two 30 nm $\text{Hg}_{0.3}\text{Cd}_{0.7}\text{Te}$ barriers. The layer structure of the samples is presented in Figure 4.35. Three samples were investigated, characterized by thicknesses of $d = 15, 25,$ and 50 nm. Table 4.2.2.1 presents the main characteristics of the samples, like the nominal thickness, the measured thickness, and the carrier concentration. The latter was used to estimate the position of the chemical potential, under assumptions that the measured concentration at $T = 55$ mK is the same as at $T = 2$ K, and that the sample processing does not influence the concentration.



Figure 4.35: Layer structure of investigated films. The active region of the system is composed of a strained HgTe layer with thicknesses $d = 50$ nm, 25 nm, and 15 nm for Sample A, B, and C, respectively.

Table 4.2: The properties of investigated strained HgTe films – measured thickness, concentration of electrons. Thickness measurements were based on high resolution x-ray diffraction. Data come from the Ph.D. of Candice Thomas [116].

Sample name	Nominal thickness	Measured thickness	Carrier concentration (55 mK)
Sample A	50 nm	58 nm	$2 \cdot 10^{11} \text{ cm}^{-2}$
Sample B	25 nm	26 nm	$1 \cdot 10^{11} \text{ cm}^{-2}$
Sample C	15 nm	15.5 nm	$2.3 \cdot 10^{11} \text{ cm}^{-2}$

4.2.2.2 Results

Related experimental works

One of the first THz magneto-optical studies of strained and unstrained HgTe films were focused on investigations of the THz magneto-optical Faraday effect conducted by Shuvaev *et al.* [117][118], and Hancock *et al.* [119]. Soon after Shuvaev *et al.* [120] published a work in which the CR line in HgTe was observed.

Recently, a very interesting study has been published by Datscher *et al.* [113]. It presents results of investigations of strained HgTe films by the means of magneto-transport and magneto-optics, which were focused on cyclotron-resonance-induced photocurrents by the THz radiation. Because of the fact that the surface electrons are expected to be spin-locked, an absorption of a polarized light results in a macroscopic surface spin polarization. This effect was investigated for various temperatures and the differences were attributed to the change of carrier concentration.

Sample A

The results of the LL calculations for Sample A are presented in Figure 4.36. The E band is split into three subbands (E1 - E3), while the HH band is split into six subbands (H1 - H6), and the surface states are formed by the H1 subband. The visible transitions are marked in Figure 4.36 by small Greek letters and arrows. Solid arrows represent interband transitions $\alpha_2^{(4)}$, β_2 , and γ_3 , while dashed arrow represents an intraband transition α_1 , α_2 , and β_1 . The transitions α_1 , α_2 , β_1 , β_1 , β_1 , $\alpha_2^{(4)}$ involve the surface states.

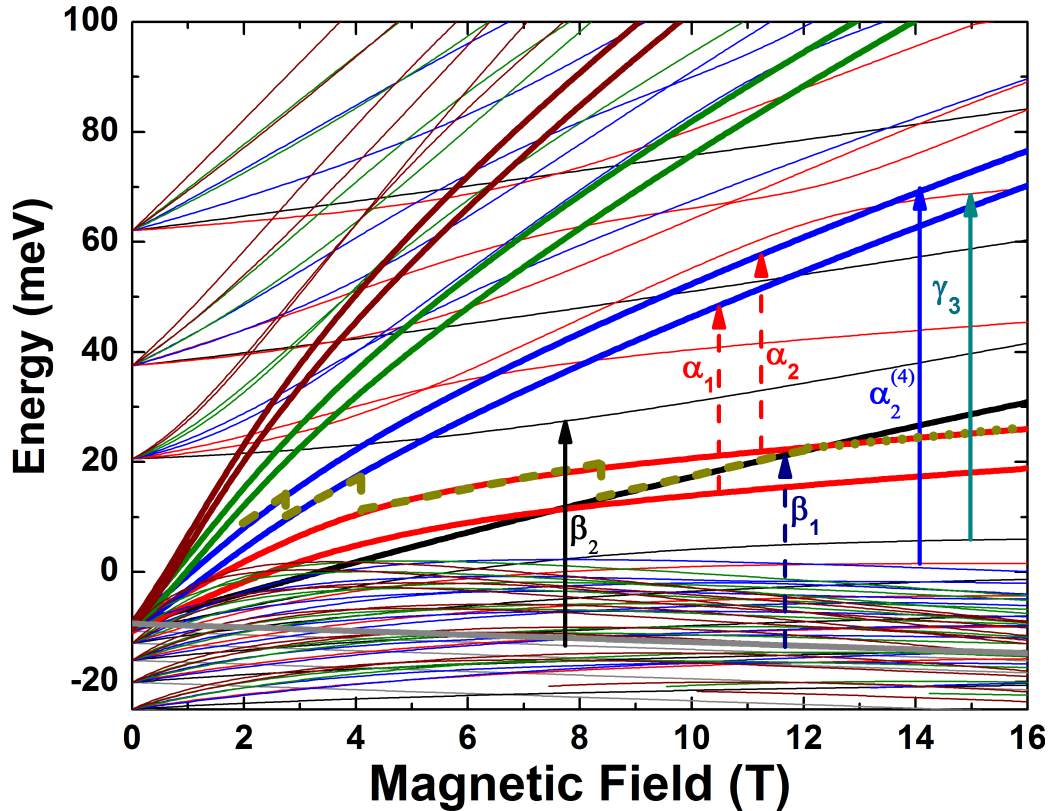


Figure 4.36: Landau level plot of a strained 50 nm HgTe film. There are three LH subbands (E1 - E3) and six HH subbands (H1 - H6), and the surface states are formed by the H1 subband. The surface states are plotted as thick solid lines. Observed transitions are marked with Greek letters and arrows, solid arrows represent interband transitions, while dashed arrows represent intraband transitions. The position of the Fermi energy was plotted as a dotted line.

The transitions α_1 and α_2 have the same energy, therefore most likely both of them are visible in the transmission spectra (marked as α_1). The experimental points corresponding to the minima of transmission for different magnetic fields are presented in Figure 4.37. There are four transitions visible, which have not been yet identified, marked with orange, brown, magenta, and dark yellow points.

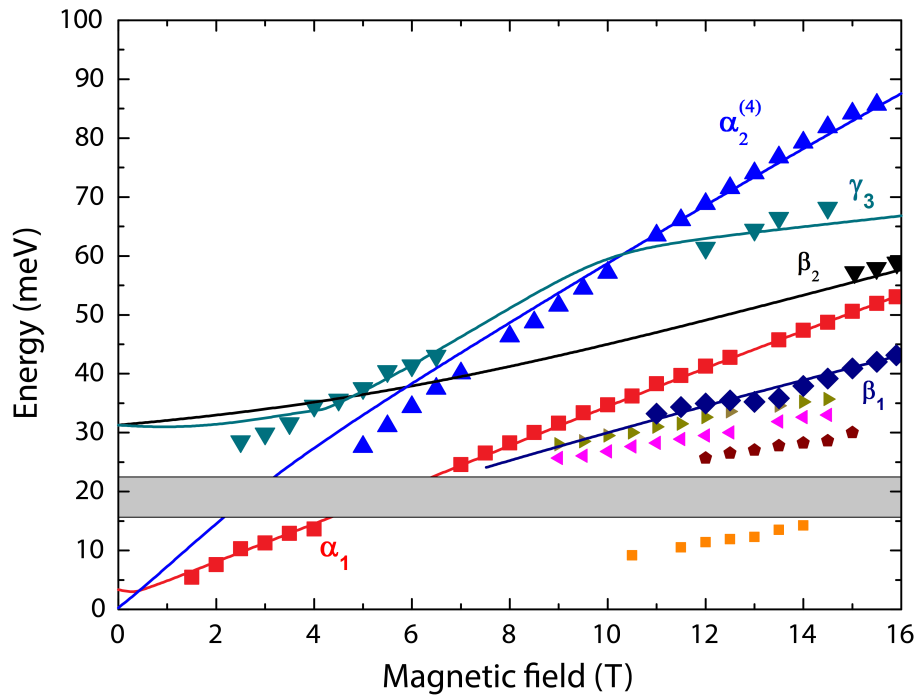


Figure 4.37: Points corresponding to the minima of the transmission of Sample A at $T = 2$ K with theoretical predictions of identified transitions as a function of magnetic field.

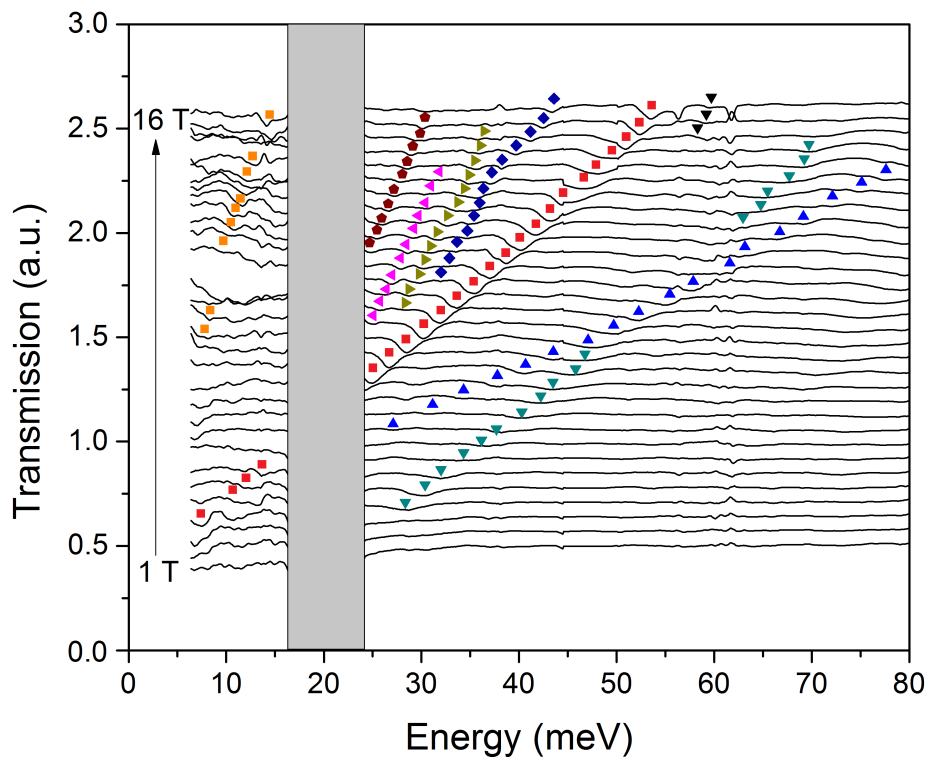


Figure 4.38: Transmission spectra of Sample A measured at $T = 2$ K, plotted every 1 T for magnetic fields in range from 1 to 16 T.

Sample B

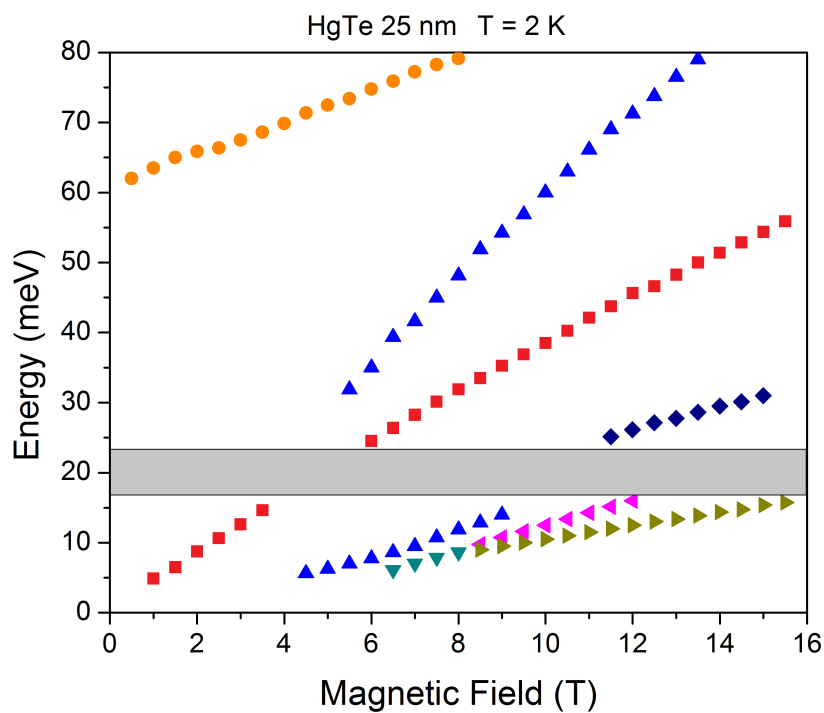


Figure 4.39: Points corresponding to the minima of the transmission of Sample B at $T = 2$ K.

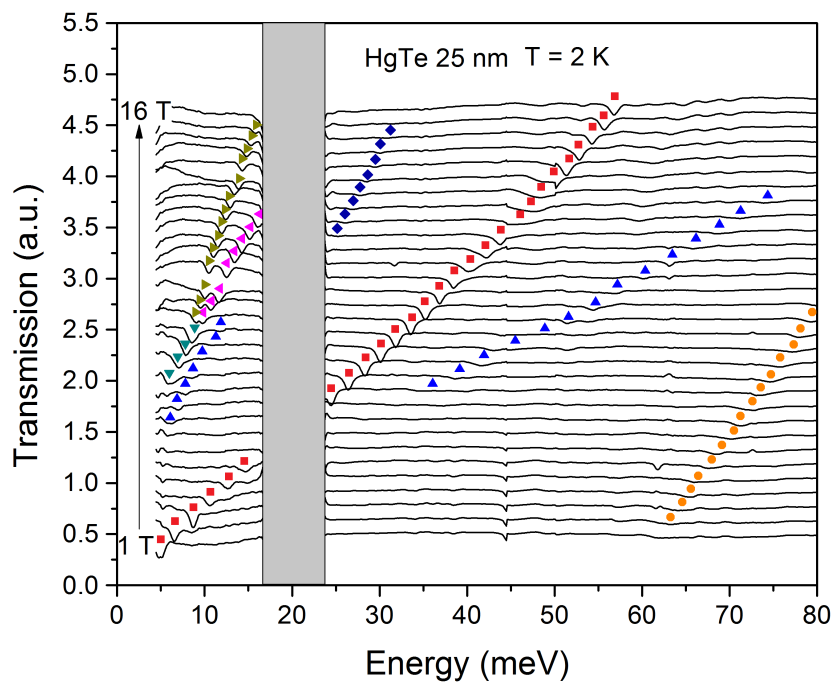


Figure 4.40: Transmission spectra of Sample B measured at $T = 2$ K, plotted for magnetic fields in range from 1 to 16 T every 1 T.

Sample C

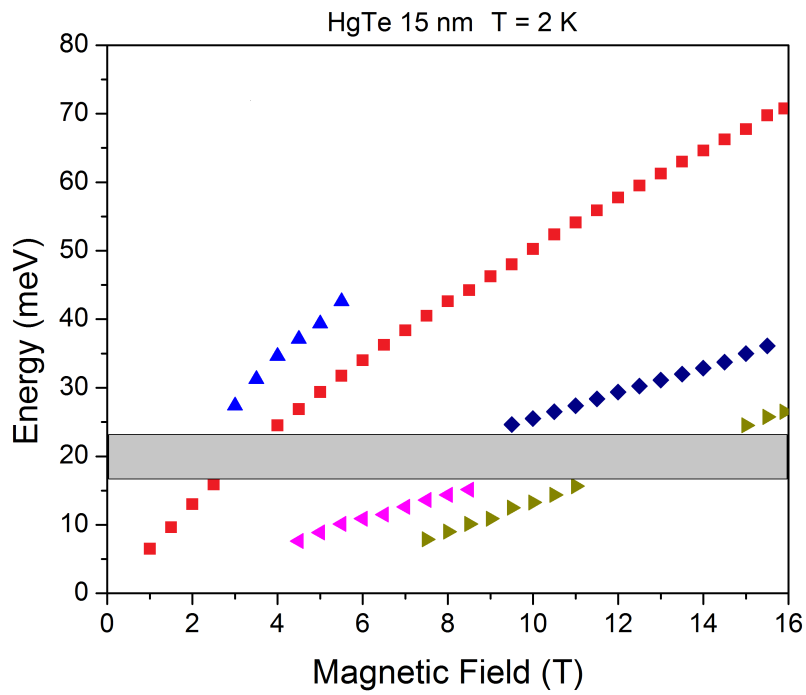


Figure 4.41: Points corresponding to the minima of the transmission of Sample C at $T = 2$ K.

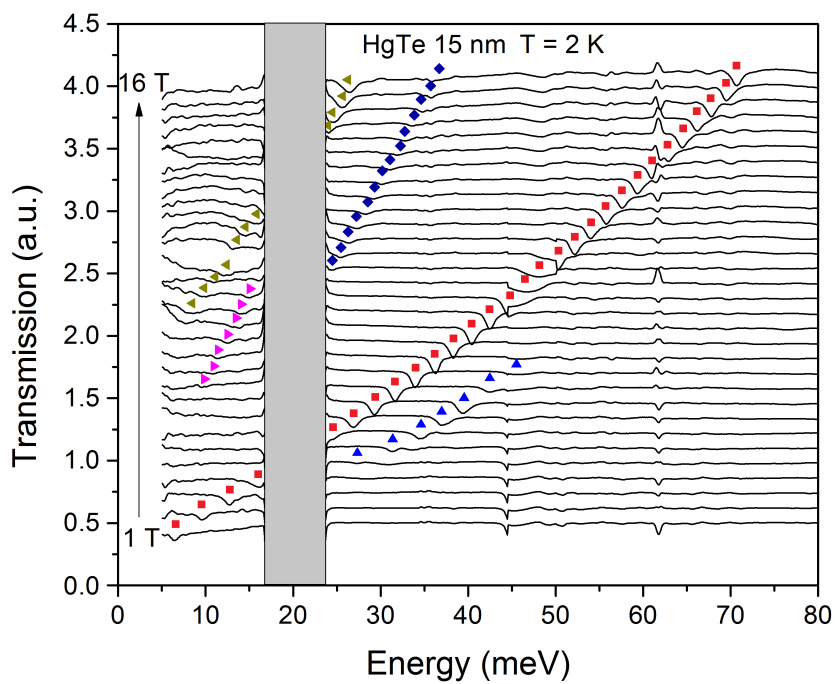


Figure 4.42: Transmission spectra of Sample C measured at $T = 2$ K, plotted for magnetic fields in range from 1 to 16 T every 1 T.

4.2.3 Summary

In this section an overview of strained HgTe films was presented. It was explained that strain opens an energy gap in an otherwise semimetallic HgTe, transforming it into a 3D TI. Numerical calculations of the band structure were presented, along its dependence on the film thickness and Cd content. It was shown that topological phase transitions can be induced by those two parameters:

- by the Cd content – in a similar manner as in the bulk HgCdTe. The system remains a TI, characterized by an inverted band order, as long as the Cd content is low. Increasing Cd concentration renders the structure more CdTe-like, up to a point of critical concentration, when a phase transition occurs,
- by the film thickness – the quantum confinement and the mutual interaction of the surface states can change the band structure as well, especially the energy differences between the subbands. For thick films the quantum confinement is low and the interaction (governed by the overlapping of the wave functions) between the surface states is negligible. With decreasing thickness the subbands start to separate and change positions. At small thickness the structure resembles a thin QW, and finally at the critical thickness, a topological phase transition occurs, accompanied by a band inversion.

It was also stated that those parameters influence also the composition of the surface states, which are always formed by a mixture of E_1 and H_1 bands, and only at $k = 0$ it is possible to determine which one is dominant. This information is necessary to grasp the idea about the origin of the surface states, and understand that they are not separated, but indeed form an integral part of the whole system.

The preliminary experimental results of a Fourier magneto-spectroscopy were shown as well as its interpretation for the 50 nm thick sample (Sample A). This thickness was sufficiently high to avoid a mutual interaction of the surface states. At the same time, the thickness was sufficiently low to avoid strain relaxation via the creation of dislocations, and provide a non-negligible quantum confinement. In this sample the surface states are not supposed to be massive, as the wave functions of the surface states are well-separated, therefore the sample is gapless. The obtained transmission spectra are extraordinarily rich in transitions, reflecting the complicated nature of the LL structure of the system, formed by many subbands originating from the E, HH, and LH bands. Multiple inter- and intraband absorption lines were observed, involving the transitions from and to the surface states. The surface states in the 50 nm sample were labeled as $H1$, as they are composed predominantly of the HH-like states.

Two more samples were investigated but the LL structure calculations and the interpretation of the obtained results are still missing. The results gathered on different samples vary, which proves that the band structure indeed depends on the thickness of the film. The study of a dependence of the band structure on the film thickness in the regime above the critical QW width is particularly interesting, because it might allow to understand the transition between 2D and 3D TI states. The surface states in 3D TIs become massive by decreasing the thickness. On the other hand the edge states (at the HgTe/vacuum interface) of 2D TI become surface states by increasing the QW width. It is clear that despite the fact that a strained HgTe film was identified as a topological insulator in three dimensions, the influence of the quantum confinement on the band structure cannot be neglected. In this sense, the two-dimensional approach (as in the case of QWs) can be successfully used to describe energy levels of a HgTe-based 3D TI.

Chapter 5

Conclusions and Outlook

Selected topological properties of various mercury-cadmium-telluride structures were investigated in this thesis. A particular attention was paid to 3D Kane semimetal systems, as well as to 2D and 3D TIs based on $\text{Hg}_{1-x}\text{Cd}_x\text{Te}$ heterostructures and thick films. These systems are characterized by a small (positive or negative) energy gap, which gave a possibility to study phase transitions between a regular and an inverted band order phase. The experimental part of this thesis was divided into three main parts, according to the investigated systems. All the magneto-spectroscopy experiments were performed using a Fourier spectrometer in a custom-designed experimental set-up, described in Chapter 2. The calculations of the band structure were performed based on the Kane model, which is successfully being used for decades to model HgCdTe-based compounds.

The first experimental part deals with a study of two bulk $\text{Hg}_{1-x}\text{Cd}_x\text{Te}$ samples. The study of bulk systems was motivated by a renewal of interest in this compounds of the physical community, as HgCdTe bulk was studied thoroughly in sixties and seventies of the XX century. However, most of those studies were aimed at a development of tunable infrared detectors. Nowadays, as the progress of crystal manufacturing techniques allowed to grow structures of the highest quality, and the discovery of topological phases of matter and their strong relation to narrow (and negative) gap semiconductors took place, it was quickly realized that HgCdTe structures are perfect candidates to investigate the fundamental quantum and relativistic physics.

Two HgCdTe bulk structures were investigated, both characterized by the cadmium content close to the critical, meaning that the band gap was designed to be close to zero at low temperature. One sample had a positive energy gap and exhibited semiconducting behavior, while the other had a negative gap and exhibited semimetallic behavior. As the temperature increased, the band gap of the second sample got smaller and finally experienced a gap closing and reopening with a positive value, rendering the system semiconducting. The experimental results proved that this behavior is related to the change of topology of the system – a topological phase transition.

The simplified Kane model, which was used to calculate the band structure of these bulk samples, required only two parameters – an effective rest mass of carriers and their velocity. It turned out that the rest mass indeed changes sign at the point of the phase transition, but the carrier velocity is constant for the whole temperature range as well as for cadmium content. This behavior is predicted by the model, as the velocity depends on the Kane matrix parameter, which is constant for all HgCdTe compounds, and is temperature independent.

The second part of this thesis, presented in Chapter 4.1, deals with HgTe/CdTe QW system. This system was the first in which the QSH insulating phase was observed experimentally. Since then it has been intensively studied by numerous groups all over the world. The observation of the QSHE is a great advance in the ability to segregate electronic currents characterized by an opposite spin. This effect paves the way to new applications, especially for spintronics and quantum computation. Moreover, 2D Dirac fermions arise at the point of a topological phase transition in this system.

So far, topological phase transitions in HgTe/CdTe QW have been widely studied as a function of the HgTe layer thickness. In this thesis a different approach was taken – the temperature was used to tune the band structure of investigated samples. Similarly as in the case of HgCdTe bulk samples, two samples were investigated. The first sample was characterized by a regular band order at the whole available temperature range. Moreover, the first sample was p-type, which allowed to observe three interband transitions, which provided information about the band gap evolution as the temperature increased.

The second sample was characterized by an inverted band structure at low temperature, and underwent a phase transition at the critical temperature $T_c = 90$ K accompanied by a change of band order to regular and an arise of Dirac fermions. In the case of the second sample, both intra- and interband transitions were observed originating from the zero-mode LLs. An anticrossing of those zero-mode LLs was observed at two temperatures (2 K and 30 K), which is a direct indication of an inverted band order. This anticrossing was attributed to the existence of BIA in the system. However, it can be also caused by electron-electron interactions.

A discussion was presented treating about the possibility to approximate the band structure using the Dirac Hamiltonian, which gives the analytical solutions of the band structure of a HgTe/CdTe QW. It was stated that the Dirac Hamiltonian is valid and can be used only in the vicinity of $k = 0$ and for low magnetic field, as its results are comparable with the numerical calculations using the 8-band Kane Hamiltonian, which was used to make the calculations for both samples. In the case of the Sample A, the agreement of the data with the calculations is excellent. However, for the case of the Sample B, there are visible discrepancies. It was speculated that they can be attributed to electron-electron interactions or the change of the structure of the sample due to cadmium diffusion into the barriers. The future experimental plans regarding HgTe QWs deal with studying phase transitions as a function of pressure.

The third part of this thesis, presented in Chapter 4.2, deals with strained HgTe films which were predicted to be 3D TIs. An application of strain to a HgTe film opens up an energy gap as a consequence of a lowered symmetry. The most widely studied 3D TIs are bismuth-based crystals, notably Bi₂Se₃ and Bi₂Te₃. However, they are characterized by a low crystal quality and a usually high electron concentration, which is reflected on transport properties. On the contrary, strained HgTe films are characterized by a high crystal quality, which assures a high carrier mobility and a negligible parallel bulk conductance. To preserve the crystal quality and the homogeneity of the strain the thickness of the films have to be of the order of few tens of nm. This means that they can be considered to be in an intermediate state between a QW and a bulk system. On one hand they resemble a 2D system because of the residual quantum confinement, which splits energy bands into subbands. On the other hand they resemble a 3D system because of the fact, that the wave functions of the surface states are well separated (for samples of thickness higher than 50 nm). Because of this, there are two valid descriptions of the band structure of these systems – one originates from the QW approach, the other from the bulk approach.

Strained HgTe films provide a special opportunity to study an evolution of the surface states as a function of the parameters of the film like the thickness and the cadmium content, and external parameters like temperature and potentially pressure. The study of the surface states might help to understand their origin and unique properties – spin polarization, robustness against disorder, effective mass of carriers, etc. These systems hold a great potential for the studies of fundamental science, including but not limited to superconducting proximity effects and the long sought Majorana fermions, which discovery and understanding might be a prominent step in a direction of spintronics and quantum computing.

Three strained HgTe films characterized by different thicknesses (50 nm, 25 nm, and 15 nm) were investigated. Various thicknesses allow to study how the band structure is influenced by the residual quantum confinement and how it changes with respect to the interaction of the surface states. So far, only the results obtained on the 50 nm sample were interpreted, because the remaining LLs calculations are still in progress. As the band structure is split into subbands due to the quantum confinement, and each of the subbands split into separate LLs, the band structure is very complicated. Because of this, the transmission spectra are very rich in absorption lines. Interestingly, some transitions were identified as intraband transitions between the surface states and interband transitions between the surface states and the bulk states. We could therefore clearly observe the surface states of HgTe-based 3D TIs by magneto-transmission spectroscopy.

The future experimental plans regarding HgTe films deal with studying the evolution of the surface states and phase transitions as a function of cadmium content and/or temperature. This will allow to understand thoroughly the properties and the origin of those surface states.

Soon after the realization of a topological insulating phase in HgTe/CdTe QW, a similar phase was proposed and observed in a different system – a InAs/GaSb QW. In this system, the inverted phase does not appear due to the spin-orbit coupling, but is created in a different way – by a particular band alignment, where the valence band of GaSb lies higher in energy than the conduction band of InAs. This effect act as a band inversion mechanism. The bulk band gap is assured by the hybridization gap created by the electron and hole level in the QW. Up to the very recently the only studied InAs/GaSb systems were two-layered heterostructures. This has some drawback – the presence of SIA, or the position of Dirac point at $k \neq 0$.

Our recent proposal was to restore the symmetry in the system by using three-layered structures. Moreover, in three-layered systems levels of the same energy lie in two QW, the hybridization effect is stronger, which increases an energy gap. If an additional strain is applied, the energy gap might become even higher than the thermal energy at the room temperature. A short overview and the preliminary experimental results are presented in Appendix A. These compounds hold vast possibilities for realization of physics of topological phases, and their manufacturing is easier from technological point of view than in the case of HgCdTe systems.

Appendix A

InAs/GaSb Quantum Wells

The first system, in which QSH phase was experimentally observed, is HgTe/CdTe QW. It allows to investigate and understand the physics of topological insulators and phase transitions and is still a subject of great interest of scientists. However, despite the remarkable progress of development of the MCT growth method, there still are plenty of technological challenges, preventing from the wide use of HgTe/CdTe QW in device and industry applications. The first most important problem is the difficulty of processing of mercury-based compounds. Because Hg is highly volatile and quickly diffuses in temperatures above 80 °C [82], it excludes the use of standard processing technologies. The second important problem is the general use of Hg and Cd elements, which are highly toxic.

An InAs/GaSb QW is a system based on III-V semiconductor groups, which can be used as an alternative to HgCdTe-based systems. The growth and processing of III-V semiconductors is well known as well and their toxicity is relatively low compared to HgCdTe. InAs/GaSb QW also exhibit a band inversion and QSH phase, however, the mechanism behind it differs from the one, responsible for band inversion in HgTe/CdTe QW. Topological insulator state has been already predicted theoretically [20] and observed experimentally [42] in InAs/GaSb. This chapter contains a short review of the properties of InAs/GaSb systems with preliminary experimental results obtained by our team. Broader review can be found for example in the work of Kroemer [125].

A.1 General Properties

There is a group of well lattice matched materials, so called 6.1 Å family, which consists of compounds such as InAs, GaSb, and AlSb. The name origins from a common lattice constant value, which is similar for all compounds and equals approximately 6.1 Å at the room temperature. InAs, GaSb, and AlSb crystallize in the zincblende structure. The similarity of the lattice constant allows growing lattice-matched heterostructures, without strain or other lattice-mismatch defects, like dislocations etc. The exact values of the lattice constants are 6.0584 Å for InAs, 6.0959 Å for GaSb, and 6.1355 Å for AlSb at 300 K [121].

Both InAs and GaSb are direct-gap semiconductor, with the exact value of energy gap measured at the Γ point is $E_g^{InAs} = 415 - 0.276T^2/(T - 83)$ for InAs [122], and $E_g^{GaSb} = 813 - 0.108T^2/(T - 10.3)$ for GaSb [123]. AlSb has an indirect gap — the gap measured at the X point equals to $E_g^{AlSb} = 1696 - 0.390T^2/(T + 140)$ [124]. The values of energy gaps at 300 K are equal to 350 meV for InAs, 727 meV for GaSb, and 1616 meV for AlSb. This wide range of gaps allows to create high energy electron confinement in quantum wells due to the high energy gap in AlSb barriers, which translates to deep

quantum well with barriers as high as 1350 meV. The values of energy gap and lattice constants of 6.1 Å family are presented on Figure A.1.

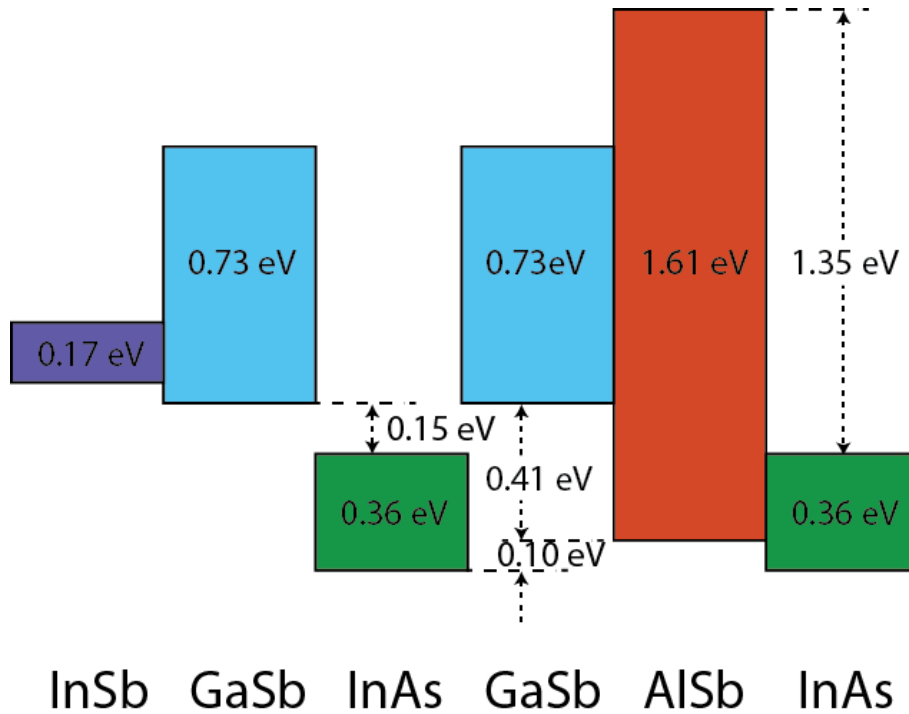


Figure A.1: *Band lineups in the 6.1 Å family of semiconductors. The colored areas represent the energy gaps. All energies are in eV.*

A.1.1 Carrier Concentration

Because of an extraordinary depth of quantum well, there are multiple sources of electrons, which can influence the carrier density in the quantum well. Consequently, even not-intentionally doped structures have relatively high carrier concentration, of the order of magnitude of $1 \cdot 10^{12} \text{ cm}^{-2}$ [126]. This particularly high concentration is mainly caused by three sources – conventional shallow bulk donors, surface states, and deep donors at or near the interfaces.

- **Conventional shallow donors and modulation doping**

Because of high barriers a modulation doping technique can be applied in those systems. It means that the donors are placed in the barrier instead of in the quantum well, and supplied electrons tunnel into the well leaving the ionized impurities away from the active part of the quantum well, and consequently reducing scattering and hence enhancing carrier mobility in comparison with bulk-doped quantum well. This method is widely used in structures, where both high concentration and mobility matters [125].

- **Surface states**

The states on the surface also take part in populating the quantum well. Electrons in the layers, placed outside barriers, can tunnel inside the well. The effect exists as a consequence of the extreme depth of the quantum well itself and strongly depends on the energetic location of the surface states and the chemical nature of the surface coverage [125]. The top surface is usually made of either GaSb or InAs cap layers, which prevent against the oxidation of the

structure. The cap layer can exhibit very high density of states (of the order of 10^{12} cm^{-2}), at the energies 0.85 eV below the conduction band edge of the AlSb barrier [127]. As a consequence the electrons will flow into the well until the electric field in the barrier pulls the surface states down to the same energy as the Fermi level inside the well. The barrier thickness strongly influences the tunneling, hence can suppress this effect.

- **Interface donors and defects**

Another source of electrons, responsible for such a high concentration, even in low temperature limit, might be connected with interface donors and/or defects. A study of temperature dependence of the electron concentration suggested that there exist a donor level less than 50 meV above the bottom of the bulk conduction band of InAs, which implies a level below the bottom of the quantum well, and below the Fermi level in the well at the observed electron concentrations. But in this case only a small fraction of the donors will be ionized, calling for a donor concentration much higher than the observed electron concentrations, on the order of about $3 \cdot 10^{12} \text{ donors cm}^{-2}$ per well [125]. The nature of these donors is not clear. Kroemer proposed that they are not ordinary point defects, but are Tamm states at the InAs–AlSb interface [128], inherent to the band structure of that interface. Alternatively, Shen *et al.* [129] proposed that the donors are very deep bulk donor states associated with AlSb antisite defects, that is, Al atoms on Sb sites.

A.1.2 Carrier Mobility

One of the most interesting properties of InAs is the second highest electron mobility of all semiconductors (the first being InSb). This is a result of one of the smallest electron effective mass, only 0.023 of the free electron mass. This property makes this material very interesting, especially from a device perspective – high mobility allows to create faster electronics (eg. HEMTs). Also, high mobility improves transport properties – allows to observe quantum effects such as Shubnikov-de Haas oscillations or QHE.

There are multiple factors influencing the mobility of carriers in an InAs/GaSb quantum well. There is a strong dependence on the well width and on the electron sheet concentration, as well as on the quality of growth. Especially at low temperatures, where mobility is limited by impurity and interface scattering, the growth quality plays a very important role [130].

- **Quantum well width**

Both room-temperature and low-temperature mobilities are significantly reduced in narrow wells due to the dominance of interface roughness scattering. The mobility peaks for well widths around 125 Å, and then decays again, most probably due to the onset of scattering by misfit dislocations nucleated as the quantum well width exceeds the critical layer thickness imposed by the 1.3% lattice mismatch between InAs and AlSb [131]. As a result, the majority of studies have used a 15 nm InAs quantum well for transport studies of this systems [132].

- **Layers' interfaces**

There is an evidence, that the mobility can depend on the interfaces between separate layers themselves. Tuttle *et al.* [133] found that because both anion and cation change across an InAs–AlSb interface, it is possible to grow such wells with two different types of interfaces, one with an InSb-like bond configuration, the other AlAs-like. The electron mobility and concentration were found to depend very strongly on the manner in which the quantum wells' interfaces were grown,

indicating that high mobilities are seen only if the bottom interface is InSb-like. The AlAs type of interfaces can introduce a sheet of donor defects, which increase the scattering, hence lower the mobility [133]. Jenichen *et al.* examined the interfaces in InAs/AlSb superlattices via X-ray scattering, and claims that strong interface roughness and intermixing is definitely present at those sites [134].

- **Buffer type**

There were studies showing that not only the active part of QW influences the mobility and transport properties. Li *et al.* [132] showed by magneto-transport, Atomic Force Microscopy and X-Ray Diffraction that the electron mobility of AlSb/InAs/AlSb quantum well with GaSb buffer is higher than that with AlSb buffer though the surface and crystal qualities of AlSb buffer are better than GaSb buffer. The crystal quality can be increased by improving the growth process. Because of InAs relaxation on AlSb buffer, mismatch dislocations will appear in the InAs layer and the interfaces of InAs QW will get rough, which is suggested as the reason leading to the lower mobility of InAs quantum well grown on AlSb buffer than on GaSb buffer [132].

Thomas *et al.* [135] investigated this matter as well, and found that GaSb buffers provide atomically flat interfaces on the scale of the electron Fermi wavelength for the quantum wells. In contrast, AlSb buffers generate a very rough interface on the same scale. The low temperature mobility of their samples with GaSb buffer ($\mu = 240000 \text{ cm}^2/\text{Vs}$) was seven times greater than of the samples with the AlSb buffer ($\mu = 35000 \text{ cm}^2/\text{Vs}$), for concentration $n = 5.5 \cdot 10^{11} \text{ cm}^{-2}$. For the concentration of $n = 1.3 \cdot 10^{12} \text{ cm}^{-2}$ the difference was a bit smaller, but the mobilities were enormous $\mu = 944000 \text{ cm}^2/\text{Vs}$ and $\mu = 244000 \text{ cm}^2/\text{Vs}$ for GaSb and AlSb, respectively [130][135][136].

- **Electron population**

There are generally two ways to change the electron concentration of the sample – with and without altering the sample structure. The first method is doping, which was already mentioned. Doping with donors, provides additional carriers into the structure, which tunnel into the QW and increase its carrier density. On the other hand it introduces scattering centers, which gradually lower the concentration, even with a modulation doping technique [136].

The latter is based on gating technique or photoexcitation effects like persistent photoconductivity effect, which will be discussed later. Structure with a gate allow to continuously tune the carrier concentration in a relatively broad range. However there is a strong relation between electron concentration and mobility. Nguyen *et al.* investigated this dependence in gated InAs/AlSb quantum wells and found that the dependence is not monotonic – mobility increases as the first subband gets populated, then peaks, and has a minimum when the second subband is populated, then increases again [130].

A.2 Band Structure

The title of the most bizarre lineup of the 6.1 Å family belongs to the InAs/GaSb heterojunctions. It was found already back in 1977 by Sasaki *et al.* [137], that they exhibit a broken gap band ordering – at the interface, the bottom of the conduction band of InAs has lower energy states than the valence band states of GaSb, with a break gap of 150 meV. This discovery most likely attracted that much attention and interest in the entire 6.1 Å family. This particular band ordering was also predicted

theoretically – in the same year Frensley and Kroemer [138] claimed that there was a possibility of such a lineup to exist. Also, Harrison using LCAO theory [139] suggested a similar prediction. Quantum wells of InAs/GaSb sandwiched between layers of AlSb were named broken-gap quantum wells (BGQW) or composite quantum wells (CQW). The band structure of InAs/GaSb CQW is presented on Panel (a) of Figure A.2. The valence band of AlSb lies about 0.4 eV lower than the valence band of GaSb, while the conduction band of AlSb lies approximately 0.4 eV higher than the conduction band of InAs. As a consequence, AlSb can be used as a quantum well barrier in CQW systems.

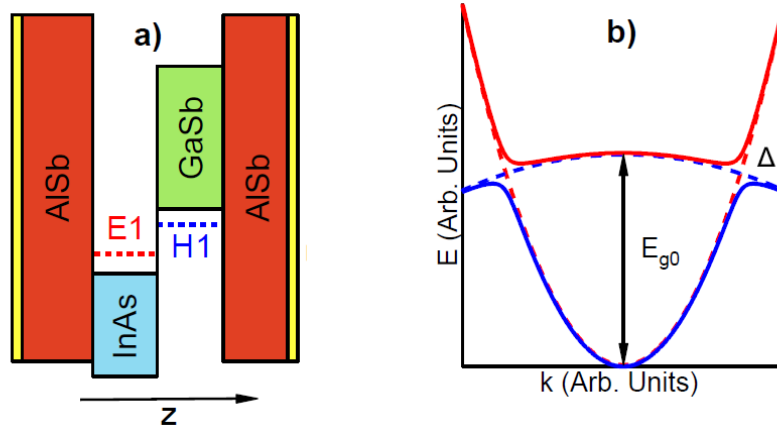


Figure A.2: **Panel (a)**: The structure and energy spectrum of an inverted CQW with $E_1 < H_1$. **Panel (b)**: The energy dispersion of uncoupled E_1 and H_1 bands (dashed) and coupled (full line). At the anticrossing point, where $n \propto p$, a hybridization gap Δ opens. The image comes from the Ph.D. of Knez [140].

The quantum well width governs two fundamentally different regimes of the system. Similarly to HgCdTe QW the energy position of levels in a QW depends strongly on QW width. However, in the case of InAs/GaSb CQW, where none of the compounds used has an inverted structure by itself, the relative position of E_1 in InAs well and H_1 in GaSb well decides whether the CQW is in an inverted regime or not. For thin layers E_1 lies higher in energy than H_1 and the structure is in the normal state. On the other hand, for sufficiently thick layers the band order is reversed. In the past, the inverted regime was considered as a semimetallic [141].

Since the transition between an inverted regime and a normal regime has to be smooth and continuous, there must be a point, where the $E_1 = H_1$, so the momentum and carrier energy in the two wells are close to be equal. In this state the system is strongly coupled, and both the electron states and the hole states are mixed. This mixing leads to hybridization of the bands or, simply speaking, to lifting of degeneracy of the levels. As a consequence, in analogy to bonding and antibonding states, a relatively small (of the order of a few of meV) hybridization gap appears. Thus, the semimetallic band dispersion relation presented on Panel (b) of Figure A.2 (dashed) becomes nonmonotonic (full line), with a mini-gap Δ . Because of this, a InAs/GaSb CQW in an inverted regime is not a semimetal, but has a gap [33]. The presence of the gap means that the bulk of the sample is resistive, as long as the Fermi energy lies within the gap, which is the case in a theoretical intrinsic case. The existence of the gap was discovered experimentally by Yang *et al.* [34] and Lakrimi *et al.* [142]. The presence of the hybridization gap makes this system different from HgTe/CdTe QW. This is a consequence of inversion asymmetry present in InAs/GaSb CQW – the QW is not symmetrical in the growth

direction, which is not the case for HgTe/CdTe systems.

A.2.1 Magnetic Field Tunability

Magnetic field can be used to induce a electron and hole recombination in GaSb/InAs QW in inverted regime. There is a set of LLs, which behavior is similar to the zero-mode LLs of HgTe/CdTe QW. Energies of these levels increase for electrons and decrease for holes as the magnetic field gets stronger. Works of Lo [143] and Smith [144] show that it is possible, by applying external magnetic field, to bring the hole Landau level and the electron Landau level to the same value of energy, thus effectively crossing them and force electrons to recombine with holes, which leads to semiconductor-to-semimetal phase transition.

A.2.2 Electric Field Tunability

The relative position of the bands can be altered also with electric field. Naveh *et al.* found that by applying small electric fields in a growth direction of an AlSb/InAs/GaSb/AlSb QW, any value can be achieved for such parameters as the energy gaps, effective masses, and carrier types and densities in the material, which is a consequence of a strong electron-hole coupling in this system [145].

The electron and hole levels in this system, when subjected to an external electrical field usually by a metallic gate on the top (and/or the bottom) of the structure, shift in opposite directions, approaching each other and eventually crossing. In the intrinsic case, thus when $n_H = n_E$, Fermi energy lies somewhere between the first electron level (E_1) and the first hole level (H_1), and with increasing electric field H_1 crosses it first, removing the holes from the system. The E_1 follows it at higher voltages applied between the gate and the channel, depleting completely the region of carriers. It gives a possibility to control the concentrations of carriers by relatively small electric field and to induce a semimetal-to-semiconductor phase transition [146]. This process is explained in Figure A.3, which presents self-consistent effective bond-orbital results for the band structure under various applied fields. For large negative fields $E_v - E_c < 0$, the two bands do not overlap (a), and the regular electron and hole dispersion are obtained. The energy gap in this case is entirely determined by the magnitude of the electric field [145]. If the value of the field is increased (towards positive values), the regime of the positive overlap is reached, and the bands start to interact (b). If the field is further increased, due to the overlapping of the bands, the band structure takes form as previously described (c,d).

However, to control both the band structure and the Fermi level position, there is a need to use a two gate configuration. A top gate and a back gate are used to tune the concentration of electrons and holes. The two gate configuration is required because of the screening of top gate induced electric field by electrons in InAs layer. Also, a very important issue is resolved in this way — electron and hole densities can be tuned almost independently, with respect to the total charge in the system. This idea was used by Cooper *et al.* [147] to study a coupling of electrons and holes in InAs/GaSb/AlSb systems as a function of temperature and concentration. The two gate configuration was used as a concept in a theoretical work of Liu *et al.*, in which the idea of a topological insulator based on a InAs/GaSb/AlSb QW was introduced [20].

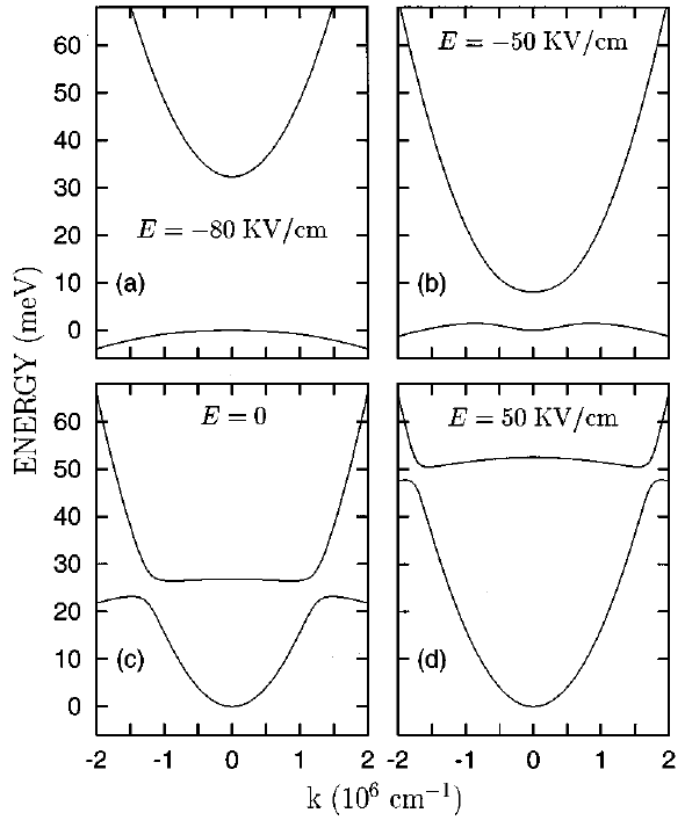


Figure A.3: The in-plane band structure of the AlSb/InAs/GaSb/AlSb heterostructure under various external electric fields E . **Panel (a)**: Regular band structure. **Panel (b)**: Bands start to interact. **Panels (c,d)**: Inverted band structure. The image comes from the work of Naveh et al. [145].

A.3 Trilayer Quantum Well

Since the prediction of QSH effect in InAs/GaSb CQW most of the investigation considered only two layered (InAs layer and GaSb) systems. This introduced an inversion asymmetry into the structures, which does not exist in the case of HgTe/CdTe QW (which is symmetrical). As a consequence, the crossing of E_1 and H_1 subbands did not occur at the Γ point of the Brillouin zone [149] (A.2), which had further implications on the shape of Landau levels.

In order to eliminate the problem of asymmetry in a growth direction, Krishtopenko [148] proposed to attach an additional layer of InAs or GaSb to the structure, which restores the inversion symmetry in the system and brings the crossing of the E_1 and H_1 subbands at the Γ point, as in the case of HgTe/CdTe QW. The layer order and the band structure for InAs-designed (with an additional InAs layer) and GaSb-designed (with an additional GaSb layer) quantum wells are presented on Figure A.4.

This new class of structures, based on InAs/GaSb, which differ from the broken-gap QWs by the band-gap inversion at the Γ point. As hybridization between electron-like and heavy-hole-like subbands vanishes at $\mathbf{k} = 0$, the crossing of E_1 and H_1 subbands at the Γ point results in the gapless state with 2D massless Dirac Fermions. The dispersion relation is presented in Figure A.5.

These materials have zincblende lattice structure and direct energy gaps in the vicinity of Γ point, thus the system can be well described by 8-band Kane model [75], like in the case of a BGQW [20].

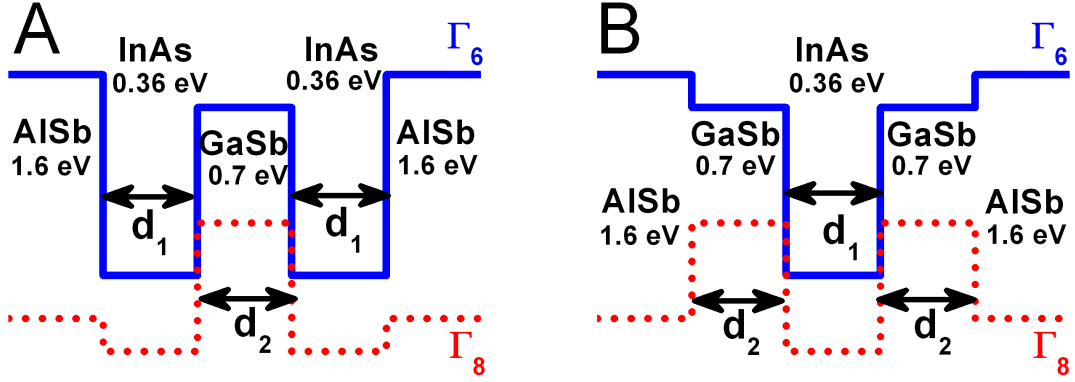


Figure A.4: The energy structure of InAs/GaSb-based systems, with values of energy gaps corresponding to each layer. The conduction band is plotted as a solid blue line, while the valence band is plotted as a dotted red line. **Panel (a)**: InAs-designed system, **Panel (b)**: GaSb-designed system.

However, trilayer structure can be considered as a double QW with a middle barrier. In the case of InAs-designed QW, a GaSb layer in the middle plays a role of a tunnel barrier separating two QW for electrons. On the other hand, GaSb-designed QW has a barrier of InAs in the middle, separating two QW for holes, being a single QW for electron itself at the same time. The energy levels in the wells are sensitive to the QW width, like in the case of QW mentioned before. Since the relative position of E_1 and H_1 subbands decide whether the whole structure is inverted or not, it means that there is a possibility to drive the system from inverted regime to normal, simply by changing the QW width. The bands structure calculations are still ongoing work during the writing of this thesis.

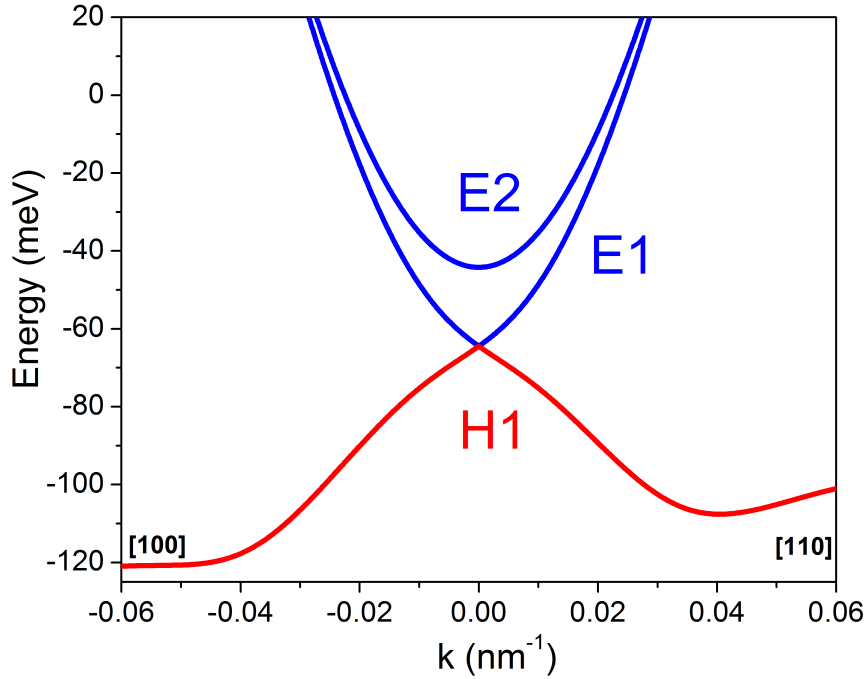


Figure A.5: Dispersion relation of an InAs/GaSb/InAs QW. Due to preserved symmetry, the band crossing takes place at $k = 0$. The E_1 and E_2 bands are plotted in blue, while the H_1 band is plotted in red.

A.4 Experiment

A.4.1 Samples

The InAs/GaSb/InAs QWs were grown using the MBE technique by Eric Tournié's group in Institute d'Electronique et des Systèmes in Montpellier. They consist of two main parts, highlighted in Figure A.6 by dashed rectangles.

- The top region represents an active part of the QW – InAs/GaSb/InAs layers sandwiched between AlSb barriers. The thickness of each layer was carefully chosen to obtain desired band structure, considering an effect of strain caused by a metamorphic buffer underneath.
- The bottom region is the metamorphic buffer [150] which consists of one layer of GaSb on top of a layer of AlSb, repeated 10 times. This structure allowed to accommodate the growth of InAs, GaSb, and InAs layers on GaAs substrates.

The whole structure was designed to exhibit high carrier concentration, according to the characteristics given in the overview – the interfaces are InSb-like, the QW width was chosen to preserve the desired band structure, while minimizing the scattering effects. Moreover, a thick buffer layer is embedded into the structure, which preserves the high mobility as well. The carrier concentration was kept as low as possible, which optimizes the mobility and is critical for the purposes of spectroscopy.

		Sample A	Sample B
	GaSb Cap Layer	6 nm	6 nm
Quantum well	AlSb	50 nm	50 nm
	InAs	12.6 nm	10.1 nm
	GaSb	2.7 nm	3.7 nm
	InAs	12.6 nm	10.1 nm
	AlSb	50 nm	50 nm
	Metamorphic buffer	GaSb	} x10 2.5 nm
	AlSb	2.5 nm	
	GaSb	2000 nm	1600 nm
	AlSb	100 nm	100 nm
	GaAs buffer	100 nm	100 nm
	GaAs substrate	200 nm	200 nm

Figure A.6: Layer scheme of three investigated InAs/GaSb/InAs quantum wells. The active region of quantum well was marked by dashed rectangle. Below the quantum well a metamorphic buffer was placed, consisting of 2.5 nm layers of GaSb and AlSb (repeated 10 times), which allowed to control the strain in the structure. The layers thicknesses, corresponding to Samples A, B, and C, are presented on the right.

A.4.2 Experimental Details

The magneto-spectroscopy study of InAs/GaSb provides information about the energy structure of this system, especially related to the hybridization and strain-induced band gap. All experiments were performed at $T = 2$ K, in magnetic fields from 0 T to 16 T. The radiation source was a globar lamp coupled to a Fourier spectrometer. The spectral range was from around 10 meV to around 100 meV, with 0.5 meV resolution. The infrared transmittance spectra were measured by a Fourier spectrometer with a Globar lamp as a source of radiation. The system was coupled to a liquid helium cryostat. The transmission spectra were obtained by dividing the spectra taken at given magnetic field by the spectra obtained at zero magnetic field. On each spectra there is a completely opaque region due to the presence of reststrahlen bands, existing between 32 and 38 meV corresponding to a phonon absorption of a GaAs substrate. Because of that, the energy regions corresponding to these bands were covered by grey areas on the spectra.

A.4.3 Results

Sample A

The results of LL calculations for Sample A are presented in Figure A.7. The sample is gapless. Three bands (E1, E2, and H1) are present. Two intraband transitions are visible, marked in Figure A.7 by small Greek letters (α_1 , β_1) and solid arrows.

The experimental points and the results of calculated transitions are presented in Figure A.8.

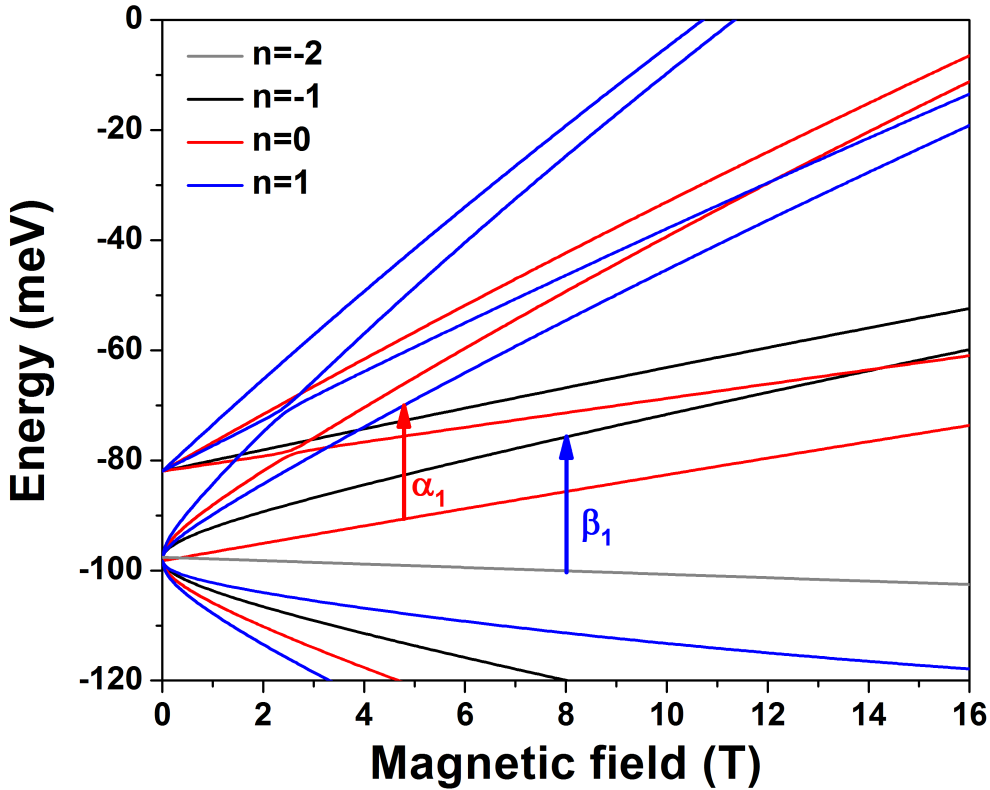


Figure A.7: Landau level graph of Sample A as a function of magnetic field at $T = 2$ K. Vertical arrows with a corresponding Greek letter represent observed transitions between Landau levels in this system. Solid arrows (α and β) are interband transitions.

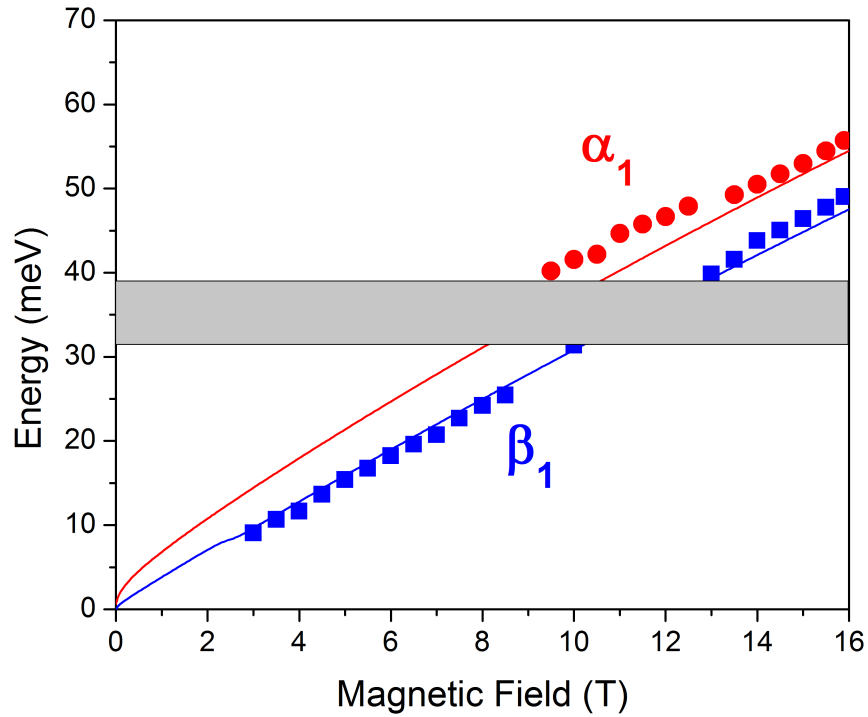


Figure A.8: Points corresponding to the minima of transmission for Sample A at $T = 2$ K with curves showing the calculated transitions as a function of magnetic field.

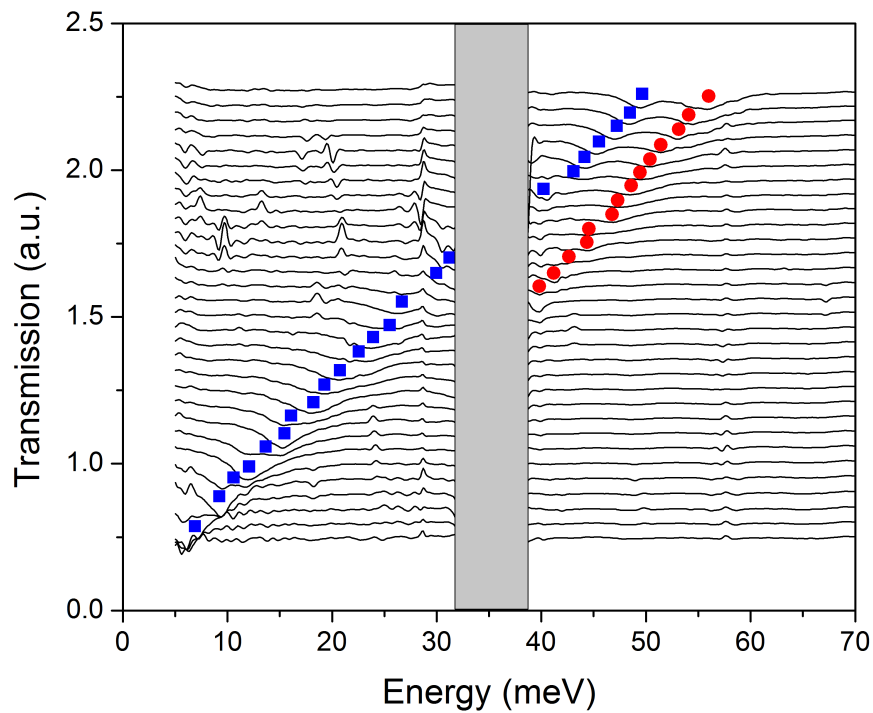


Figure A.9: Points corresponding to the minima of transmission for Sample A at $T = 2$ K with curves showing the calculated transitions as a function of magnetic field.

Sample B

The results of LL calculations for Sample B are presented in Figure A.10. The sample is gapless as well. Three bands (E1, E2, and H1) are present. Three intraband transitions are visible and possibly one interband, marked in Figure A.7 by small Greek letters (α_1 , β_1 , α_2 , and β_2) and solid arrows. The experimental points and the results of calculated transitions are presented in Figure A.11. There are only three points corresponding to the interband transition (β_2), as it appears at $B \approx 15$ T, as is presented in the inset of Figure A.11. Moreover, the transition α_2 is very faint – it is almost invisible in the waterfall plot in Figure A.12, however, it can be traced on the colormap presented in the inset of Figure A.11.

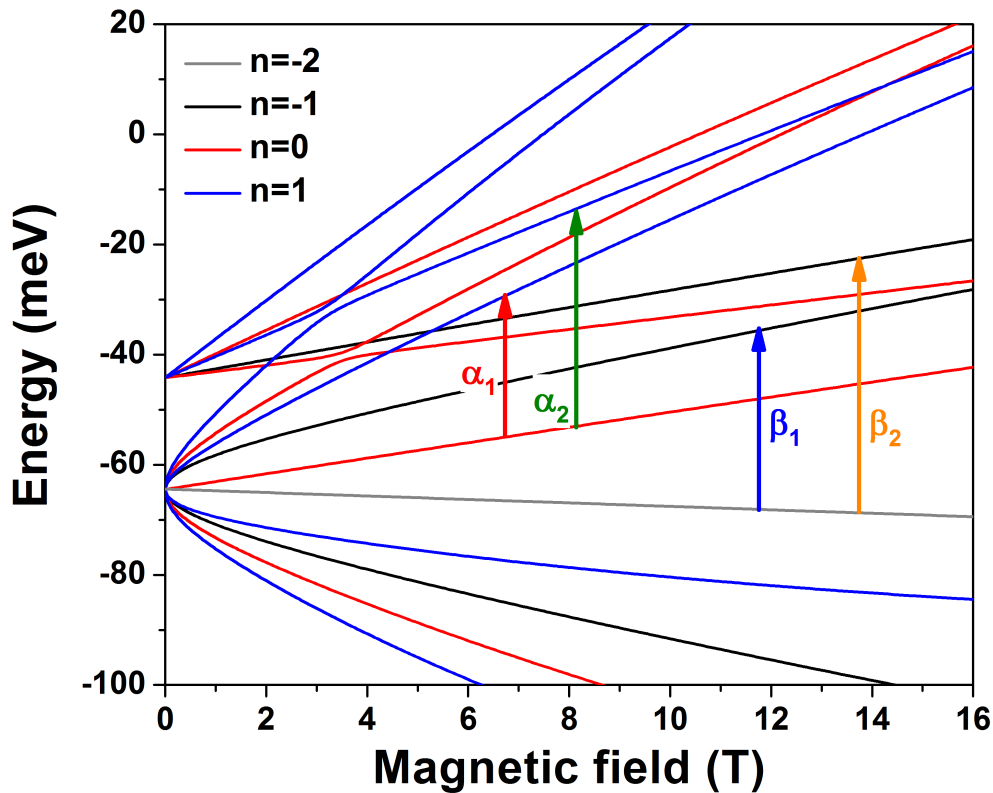


Figure A.10: Landau level graph of Sample B as a function of magnetic field at $T = 2$ K. Vertical arrows with a corresponding Greek letter represent observed transitions between Landau levels in this system. Solid arrows (α and β) are interband transitions.

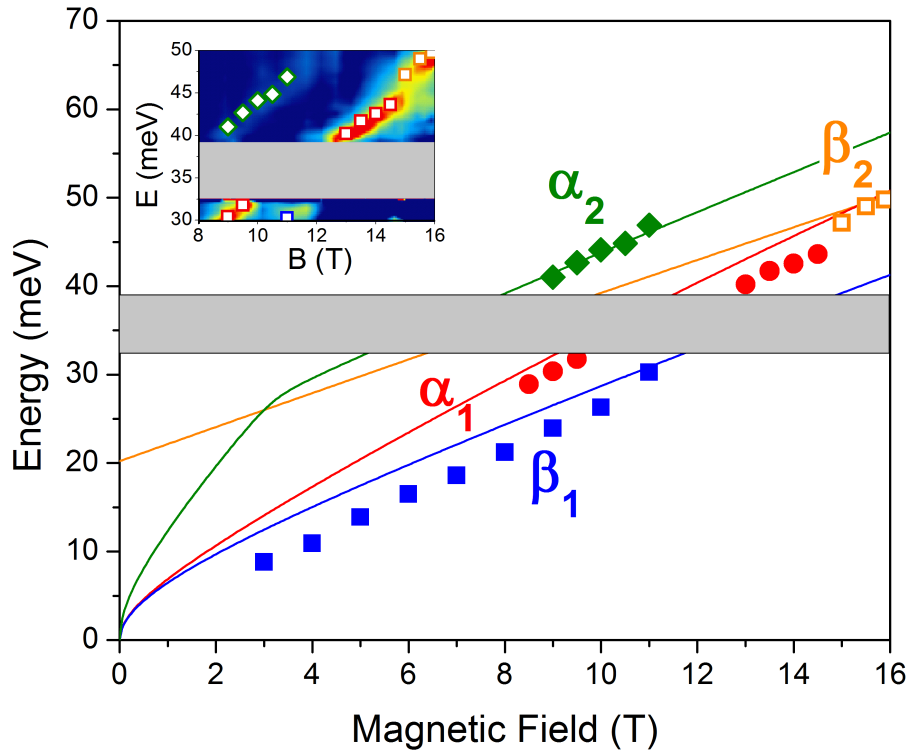


Figure A.11: Points corresponding to the minima of transmission for Sample B at $T = 2$ K with curves showing the calculated transitions as a function of magnetic field. Inset contains the part of colormap with marked experimental points, presenting the end of transition α_1 (red points) and the beginning of transition β_2 (orange points).

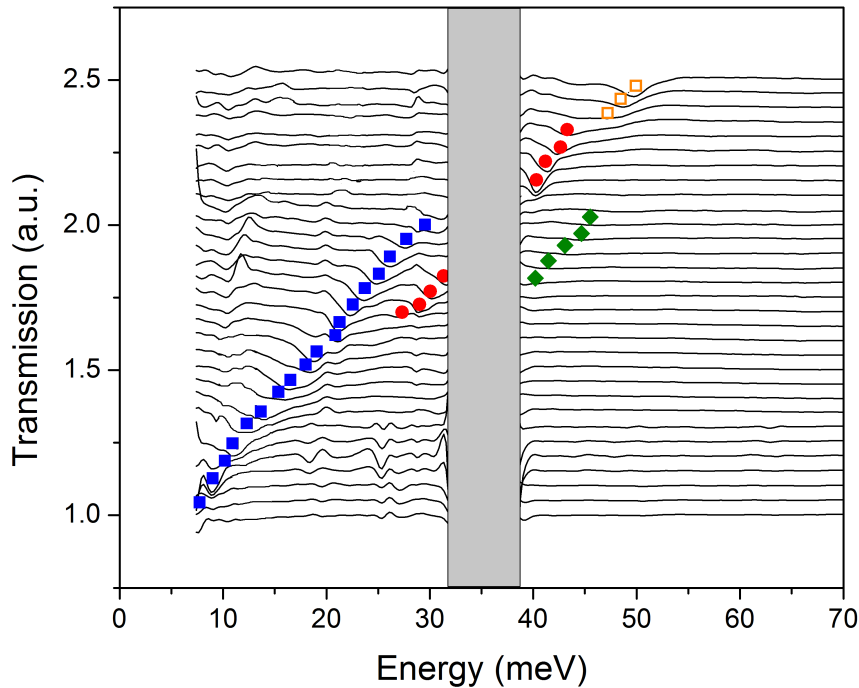


Figure A.12: Points corresponding to the minima of transmission for Sample A at $T = 2$ K with curves showing the calculated transitions as a function of magnetic field.

A.5 Summary

This Chapter presented an overview of a different system, after HgTe/CdTe QW, which is a 2D topological insulator. The differences between those systems were explained, most notably the different origin of an inverted band ordering, which does not result from SOC as in the case of HgCdTe, but from an extraordinary band line-up present in InAs/GaSb systems. Widely known two-layered systems InAs/GaSb were described as well as the new tri-layered systems InAs/GaSb/InAs (GaSb/InAs/GaSb) were introduced.

The preliminary experimental magneto-spectroscopy results were shown, which indicate the fingerprint of the massless Dirac Fermions being present in a InAs/GaSb/InAs system. However, more experiments have to be performed to draw any definitive conclusions, preferably with samples with a broader range parameters (thicknesses of layers, strain, etc) and at higher magnetic fields. The new samples will be grown shortly and hopefully they will allow us to understand the physics of TIs and phase transitions. Moreover, the preliminary calculations show a very weak dependence of the band structure of InAs/GaSb systems on temperature, which may allow to preserve the relativistic graphene-like band structure up to higher temperatures.

Appendix B

HgCdTe Bulk

This appendix contains the remaining results of magneto-transport and magneto-spectroscopy measurements on bulk HgCdTe samples, not shown in Chapter 3.

B.1 Magneto-transport Measurements

To estimate the properties of the samples, like carrier concentration, the transport measurements were performed at magnetic field as a function of temperature. Samples were contacted with indium balls in a Van der Pauw configuration and placed in perpendicular quantized magnetic field (the Faraday configuration).

B.1.1 Sample A

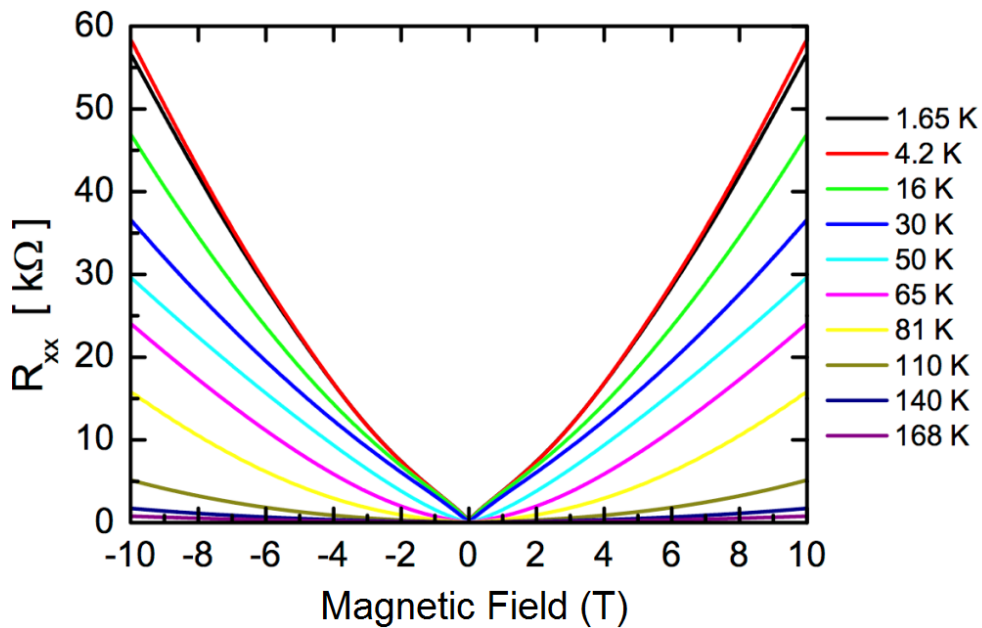


Figure B.1: *Longitudinal resistance R_{xx} of Sample A as a function of magnetic field at different temperatures.*

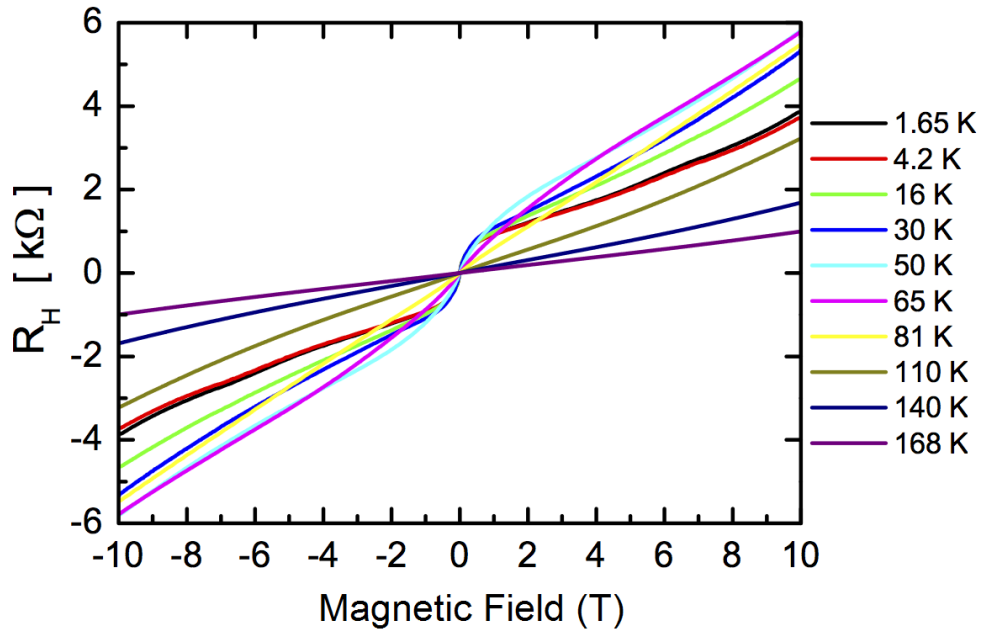


Figure B.2: *Hall resistance R_H of Sample A as a function of magnetic field at different temperatures. The values of the carrier concentration were extracted from low field measurements.*

B.1.2 Sample B

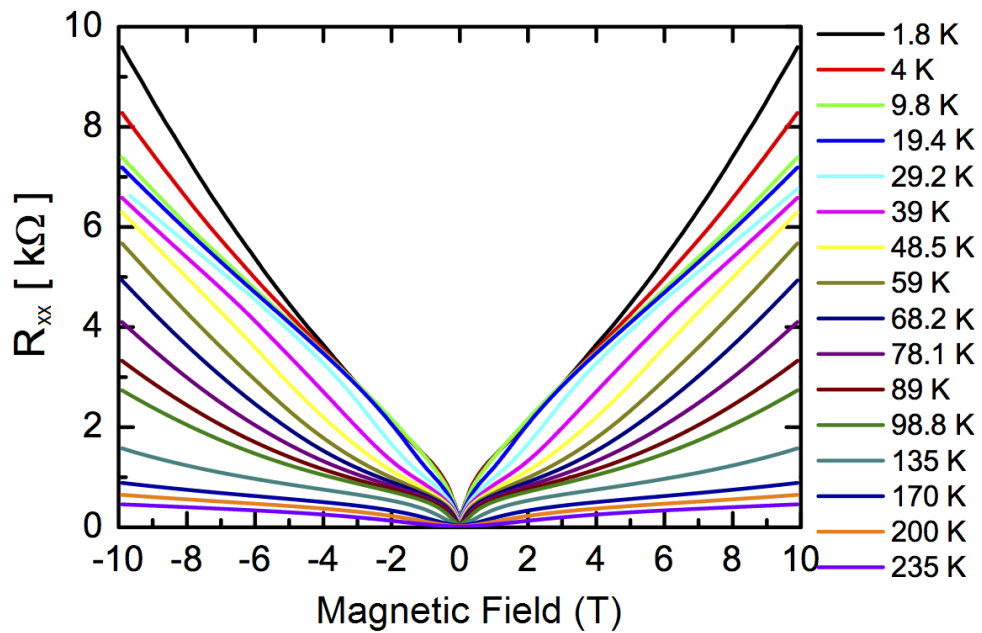


Figure B.3: *Longitudinal resistance R_{xx} of Sample B as a function of magnetic field at different temperatures.*

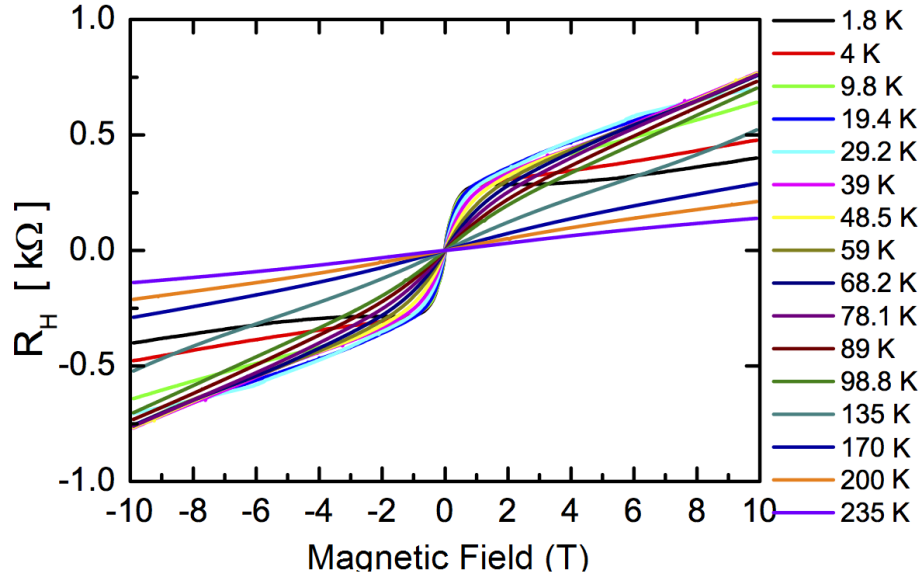


Figure B.4: Hall resistance R_H of Sample B as a function of magnetic field at different temperatures. The values of the carrier concentration were extracted from low field measurements.

B.2 Magneto-spectroscopy Measurements

Magneto-spectroscopy measurements were performed at magnetic fields up to 16 T and in energy range $80 - 800 \text{ cm}^{-1}$ ($\approx 10 - 100 \text{ meV}$) with a 4 cm^{-1} resolution. The infrared transmittance spectra were measured by a Fourier spectrometer with a Globar lamp as a source of radiation. The system was coupled to a liquid helium cryostat. The transmission spectra were obtained by dividing the spectra taken at given magnetic field by the spectra obtained at zero magnetic field.

In order to interpret the experimental results, a set of temperature-dependent band structure and LL structure calculations based on the 8-band Kane Hamiltonian were performed.

On each spectra there is a completely opaque region due to the presence of reststrahlen bands, existing between 16 and 21 meV and 30 and 37 meV corresponding to a phonon absorption of HgCdTe layers and a GaAs substrate, respectively. Because of that, the energy regions corresponding to these bands were covered by grey areas on the spectra.

B.2.1 Sample A

Temperature 20 K

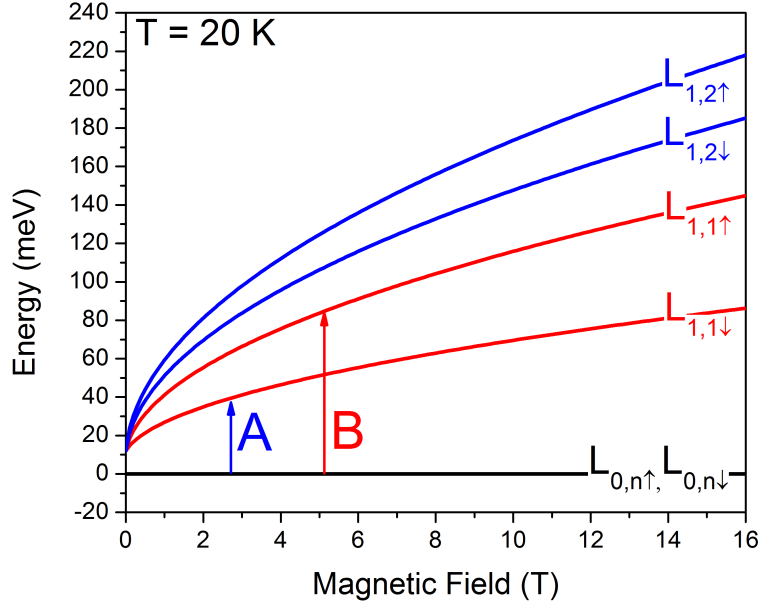


Figure B.5: Landau level graph of Sample A as a function of magnetic field at $T = 20$ K. Colored lines represent Landau levels, characterized by a different value of ε , n , and σ , as described in indices of L on the right side of the graph. The electron band Landau levels (with $\varepsilon = 1$) have a near- \sqrt{B} behavior. The heavy-hole Landau level, plotted in black, is fully degenerated. The vertical arrows with a corresponding capital letter represent observed transitions between Landau levels in this system. Solid arrows (A and B) are interband transitions.

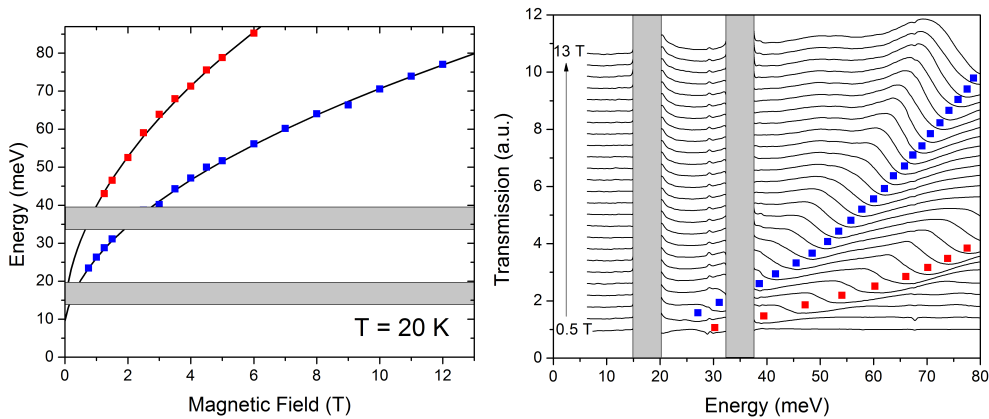


Figure B.6: **Left panel:** Points corresponding to the minima of the transmission of Sample A at $T = 1.8$ K with fits showing the expected transition evolution as a function of magnetic field. **Right panel:** Transmission spectra plotted at magnetic fields in range from 0 to 13 T, with symbols corresponding to the transitions from left panel. Symbols represent interband transitions.

Temperature 100 K

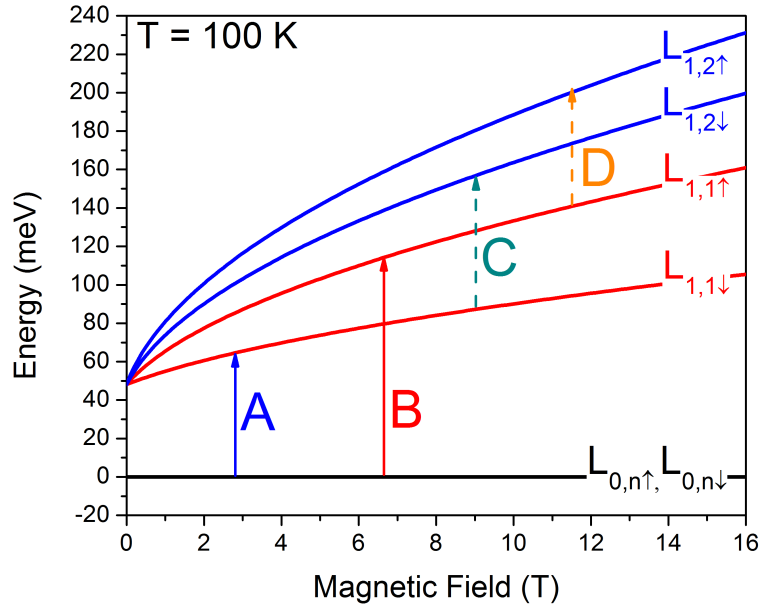


Figure B.7: Landau level graph of Sample A as a function of magnetic field at $T = 100$ K. Colored lines represent Landau levels, characterized by a different value of ϵ , n , and σ , as described in indices of L on the right side of the graph. The electron band Landau levels (with $\epsilon = 1$) have a near- \sqrt{B} behavior. The heavy-hole Landau level, plotted in black, is fully degenerated. The vertical arrows with a corresponding capital letter represent observed transitions between Landau levels in this system. Solid arrows (A and B) are interband transitions, while dashed arrows (C and D) are intraband transitions.

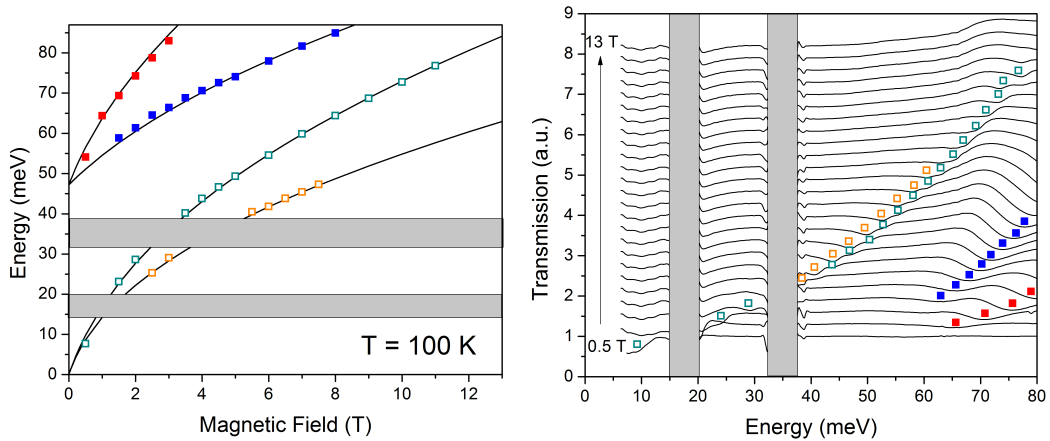


Figure B.8: **Left panel:** Points corresponding to the minima of transmission of Sample A at $T = 100$ K with fits showing the expected transition evolution as a function of magnetic field. **Right panel:** Transmission spectra plotted at magnetic fields in range from 0 to 13 T, with symbols corresponding to the transitions from left panel. Symbols represent interband transitions.

B.2.2 Sample B

Temperature 20 K

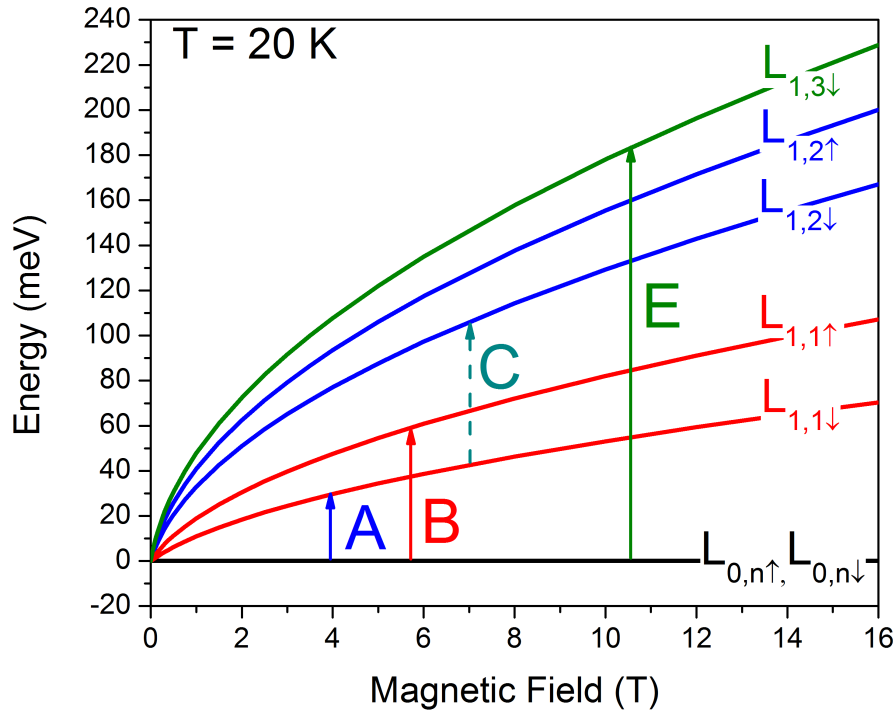


Figure B.9: Landau level graph of Sample B as a function of magnetic field at $T = 20$ K. Colored lines represent Landau levels, characterized by a different value of ε , n , and σ , as described in indices of L on the right side of the graph. The electron band Landau levels (with $\varepsilon = 1$) have a near- \sqrt{B} behavior. The heavy-hole Landau level, plotted in black, is fully degenerated. The vertical arrows with a corresponding capital letter represent observed transitions between Landau levels in this system. Solid arrows (A, B, and E) are interband transitions, while dashed arrow (C) is an intraband transition.

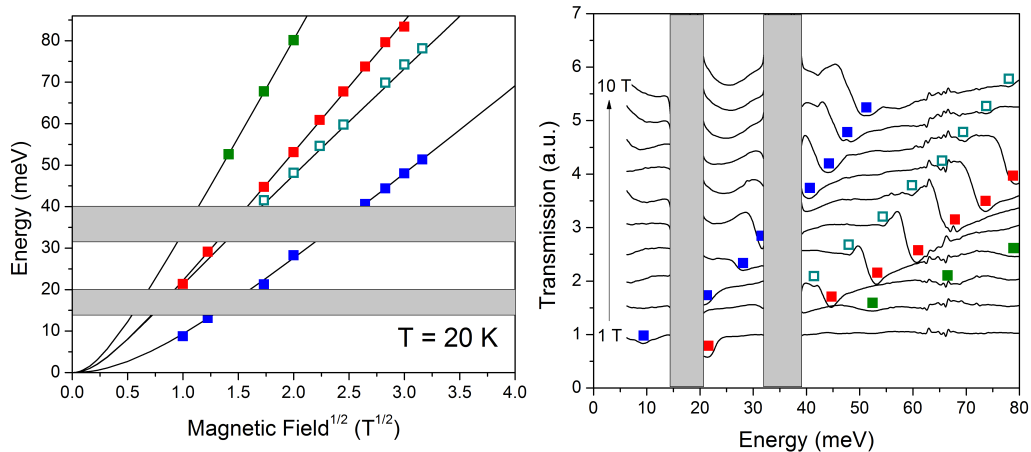


Figure B.10: **Left panel:** Points corresponding to the minima of the transmission of Sample B at $T = 20$ K with fits showing the expected transition evolution as a function of magnetic field. **Right panel:** Transmission spectra plotted at magnetic fields in range from 0 to 10 T, with symbols corresponding to the transitions from left panel. Open (full) symbols represent intraband (interband) transitions.

Temperature 57 K

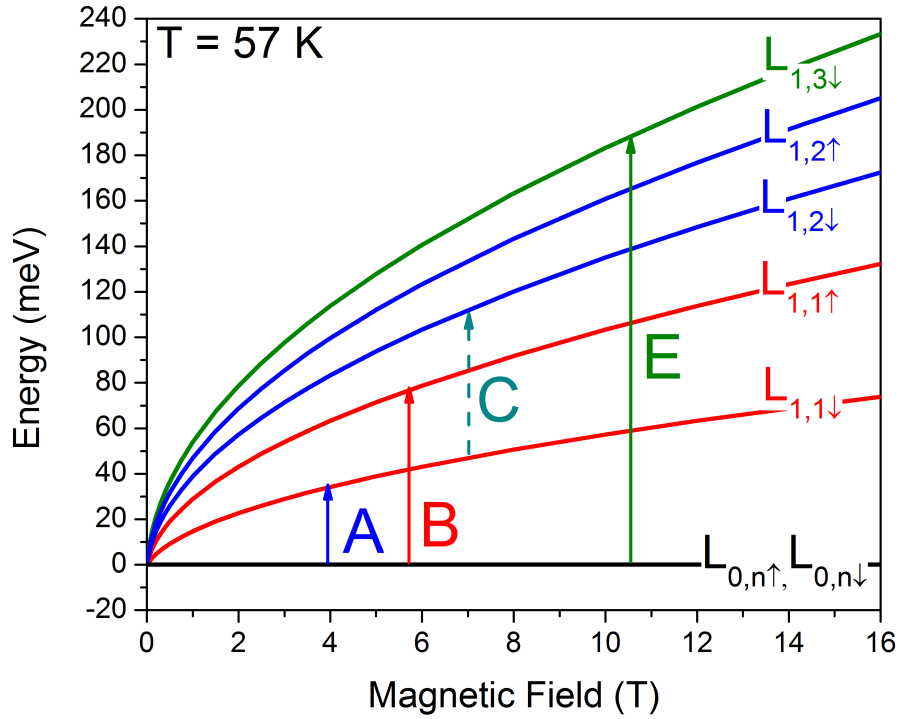


Figure B.11: Landau level graph of Sample B as a function of magnetic field at $T = 57$ K. Colored lines represent Landau levels, characterized by a different value of ϵ , n , and σ , as described in indices of L on the right side of the graph. The electron band Landau levels (with $\epsilon = 1$) have a near- \sqrt{B} behavior. The heavy-hole Landau level, plotted in black, is fully degenerated. The vertical arrows with a corresponding capital letter represent observed transitions between Landau levels in this system. Solid arrows (A, B, and E) are interband transitions, while a dashed arrow (C) is an intraband transition.

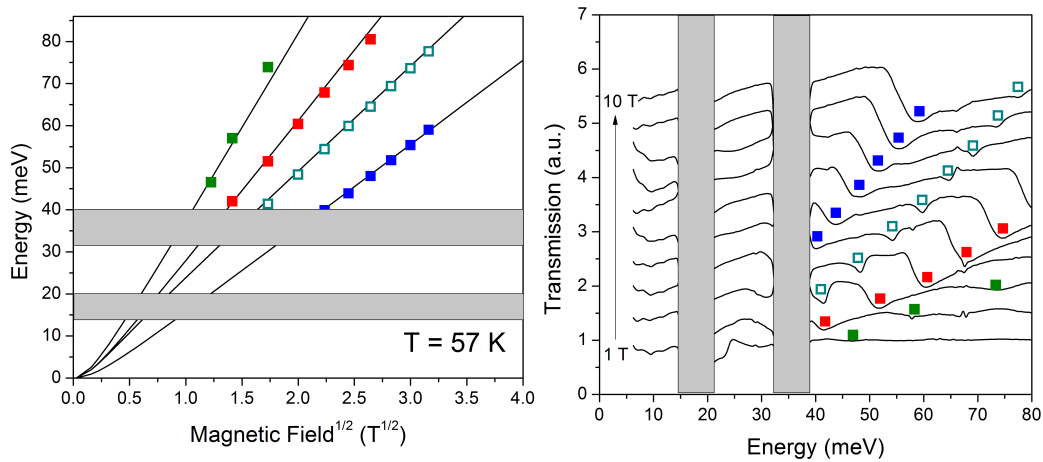


Figure B.12: **Left panel:** Points corresponding to the minima of the transmission for Sample B at $T = 57$ K with fits showing the expected transition evolution as a function of magnetic field. **Right panel:** Transmission spectra plotted at magnetic fields in range from 0 to 10 T, with symbols corresponding to the transitions from left panel. Open (full) symbols represent intraband (interband) transitions.

Temperature 87 K

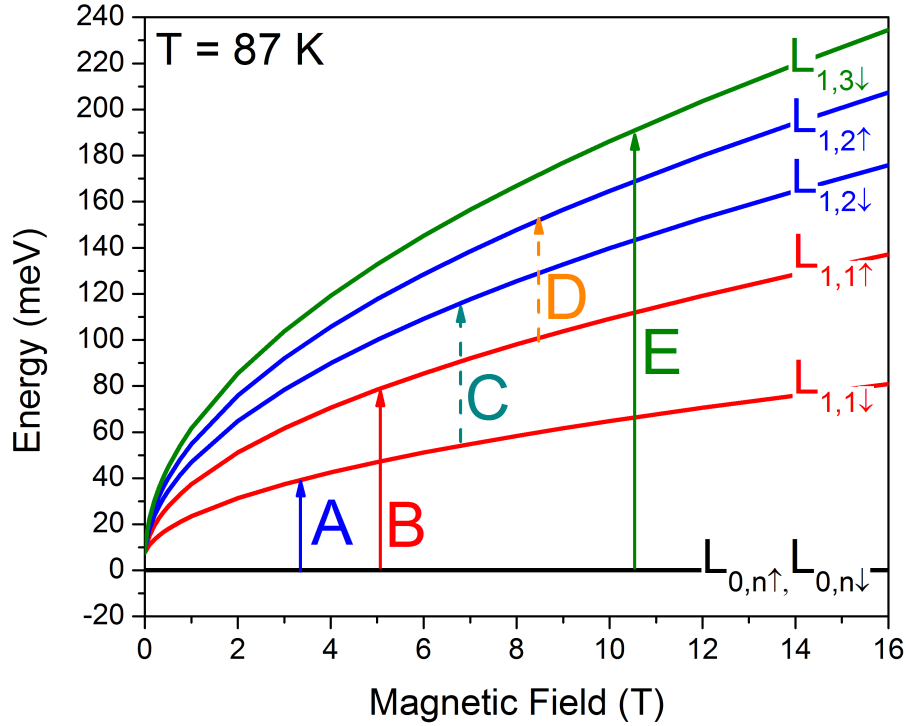


Figure B.13: Landau level graph of Sample B as a function of magnetic field at $T = 87$ K. Colored lines represent Landau levels, characterized by a different value of ε , n , and σ , as described in indices of L on the right side of the graph. The electron band Landau levels (with $\varepsilon = 1$) have a near- \sqrt{B} behavior. The heavy-hole Landau level, plotted in black, is fully degenerated. The vertical arrows with a corresponding capital letter represent observed transitions between Landau levels in this system. Solid arrows (A, B, and E) are interband transitions, while dashed arrows (C and D) are intraband transition.

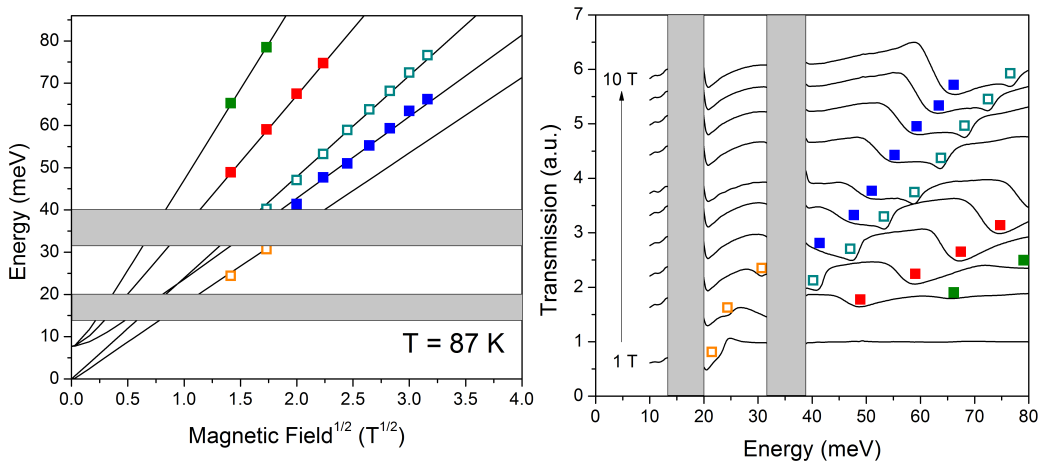


Figure B.14: **Left panel:** Points corresponding to the minima of the transmission of Sample B at $T = 87$ K with fits showing the expected transition evolution as a function of magnetic field. **Right panel:** Transmission spectra plotted at magnetic fields in range from 0 to 10 T, with symbols corresponding to the transitions from left panel. Open (full) symbols represent intraband (interband) transitions.

Appendix C

HgTe Quantum Wells

C.1 Hamiltonians

The complete effective Hamiltonian describing HgTe QW near the critical thickness in magnetic field, as described by Bernevig, Hughes, and Zhang [17], is determined by four states $|E_1, \frac{1}{2}\rangle$, $|H_1, \frac{3}{2}\rangle$, $|E_1, -\frac{1}{2}\rangle$, $|H_1, -\frac{3}{2}\rangle$. With these states acting as a basis, the Hamiltonian of the system in applied magnetic field B_\perp in z -direction takes form:

$$\hat{H} = H_{eff} + H_{Zeeman} + H_{SIA} + H_{BIA}, \quad (\text{C.1})$$

where H_{eff} is given in Equation 4.1 in Chapter 4.1, and the Zeeman Hamiltonian H_{Zeeman} can be written as:

$$H_{Zeeman} = \frac{\mu_B B_\perp}{2} \begin{pmatrix} g_E & 0 & 0 & 0 \\ 0 & g_H & 0 & 0 \\ 0 & 0 & -g_E & 0 \\ 0 & 0 & 0 & -g_H \end{pmatrix}, \quad (\text{C.2})$$

where $\mu_B = \frac{e\hbar}{2m_0}$ and g_E (g_H) is the effective g-factor for E1 (H1) bands.

In HgTe QWs the inversion symmetry is broken, therefore SIA and BIA terms have to be considered

$$H_{SIA} = \begin{pmatrix} 0 & 0 & i\xi_e k_- & -i\chi k_-^2 \\ 0 & 0 & i\chi k_-^2 & -i\xi_h k_-^3 \\ -i\xi_e k_+ & i\chi k_+^2 & 0 & 0 \\ -i\chi k_+^2 & -i\xi_h k_+^3 & 0 & 0 \end{pmatrix}, \quad (\text{C.3})$$

Since the zinc-blende crystal structure of HgTe does not preserve the inversion symmetry, an usually neglected in calculations BIA term has to be included. Moreover, an inclusion of BIA allows to explain an anticrossing of zero-mode Landau levels. The Hamiltonian of BIA takes form of:

$$H_{BIA} = \begin{pmatrix} 0 & 0 & 0 & -\Delta_0 \\ 0 & 0 & \Delta_0 & 0 \\ 0 & \Delta_0 & 0 & 0 \\ -\Delta_0 & 0 & 0 & 0 \end{pmatrix}, \quad (\text{C.4})$$

C.2 Experimental Results

This Appendix presents results of magneto-spectroscopy performed on HgTe/CdTe QWs characterized by thicknesses close to the critical. Those results supplementary to those in the Chapter 4.1. Magneto-spectroscopy measurements were performed at magnetic fields up to 16 T and in energy range 80 - 800 cm^{-1} ($\approx 10 - 100$ meV) with a 4 cm^{-1} resolution. The infrared transmittance spectra were measured by a Fourier spectrometer with a Globar lamp as a source of radiation. The system was coupled to a liquid helium cryostat. The transmission spectra were obtained by dividing the spectra taken at given magnetic field by the spectra obtained at zero magnetic field.

In order to interpret the experimental results, a set of temperature-dependent band structure and LL structure calculations based on the 8-band Kane Hamiltonian were performed. The calculations took into account a tensile strain in the layers resulting from the mismatch of lattice constants of CdTe buffer, $\text{Cd}_x\text{Hg}_{1-x}\text{Te}$ barriers, and HgTe QW. The energies of LLs were obtained using an axial approximation, while the calculations of dispersion relations held also non-axial terms.

On each spectra there is a completely opaque region due to the presence of reststrahlen bands, existing between 16 and 21 meV and 30 and 37 meV corresponding to a phonon absorption of HgTe/HgCdTe layers and a GaAs substrate, respectively. Because of that, the energy regions corresponding to these bands were covered by grey areas on the spectra.

C.2.1 Sample A

Temperature 15 K

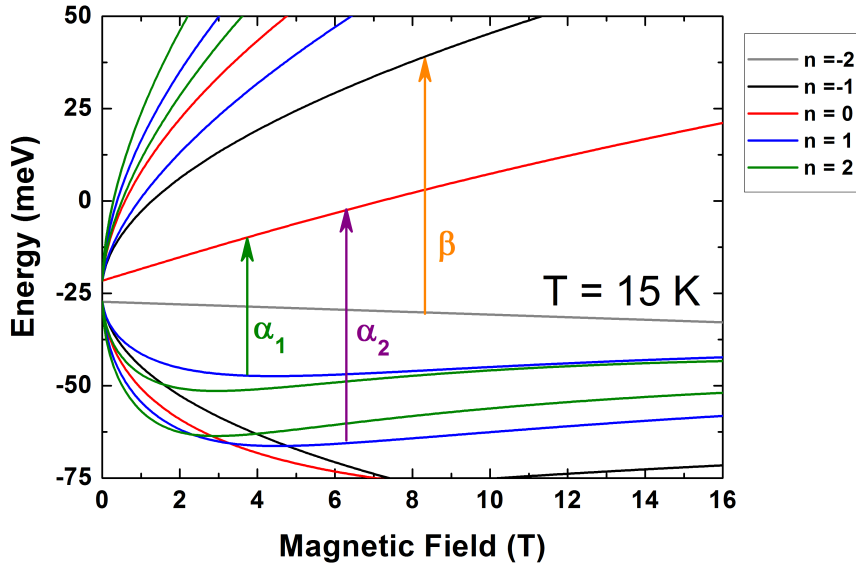


Figure C.1: Landau level graph of Sample A as a function of magnetic field at $T = 15$ K. Colored lines represent Landau levels, characterized by a different value of n , as described as indices of L on the right side of the graph. The Landau levels with $n = -2$ and $n = 0$ are zero-mode Landau levels. The energy of those levels at zero magnetic field is an indication of the band gap. The vertical arrows with corresponding Greek letters represent observed transitions between Landau levels in this system. Solid arrows α_1 , α_2 , and β indicate interband transitions.

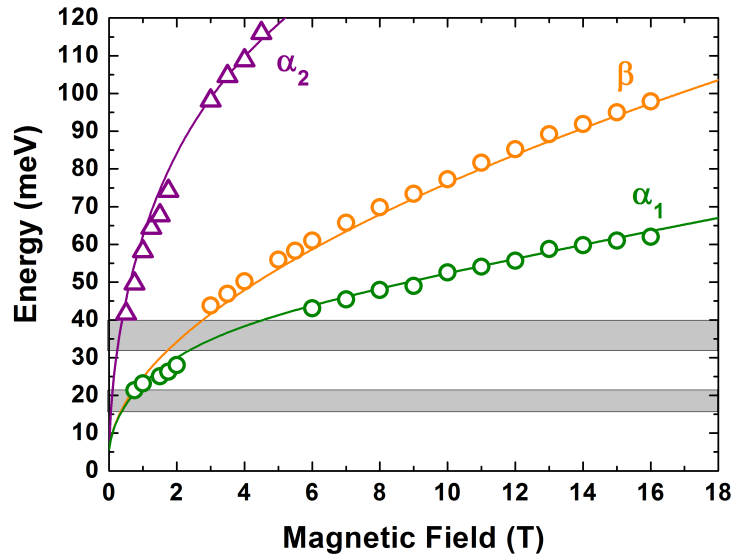


Figure C.2: Points corresponding to the minima of the transmission of Sample A at $T = 2$ K with theoretical predictions of transitions as a function of magnetic field.

Temperature 50 K

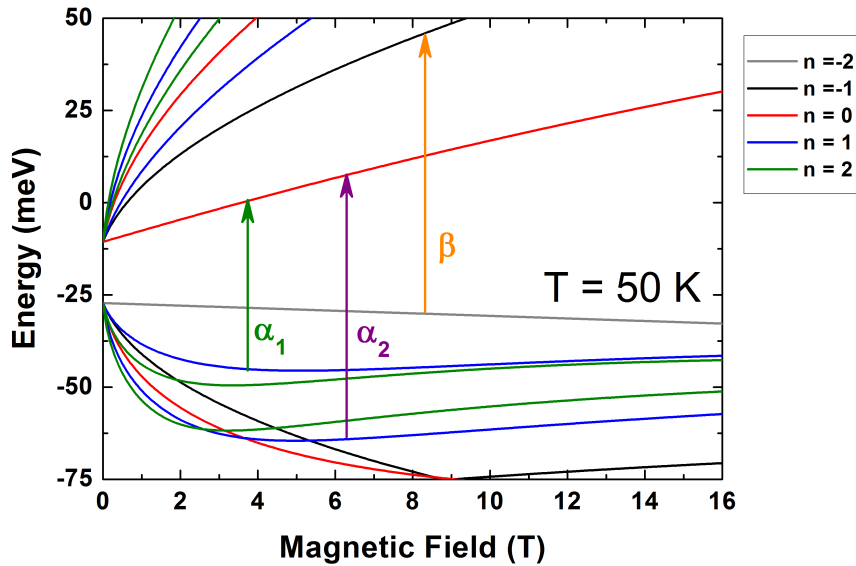


Figure C.3: Landau level graph of Sample A as a function of magnetic field at $T = 50$ K. Colored lines represent Landau levels, characterized by a different value of n , as described as indices of L on the right side of the graph. The Landau levels with $n = -2$ and $n = 0$ are zero-mode Landau levels. The energy of those levels at zero magnetic field is an indication of the band gap. The vertical arrows with corresponding Greek letters represent observed transitions between Landau levels in this system. Solid arrows α_1 , α_2 , and β indicate interband transitions.

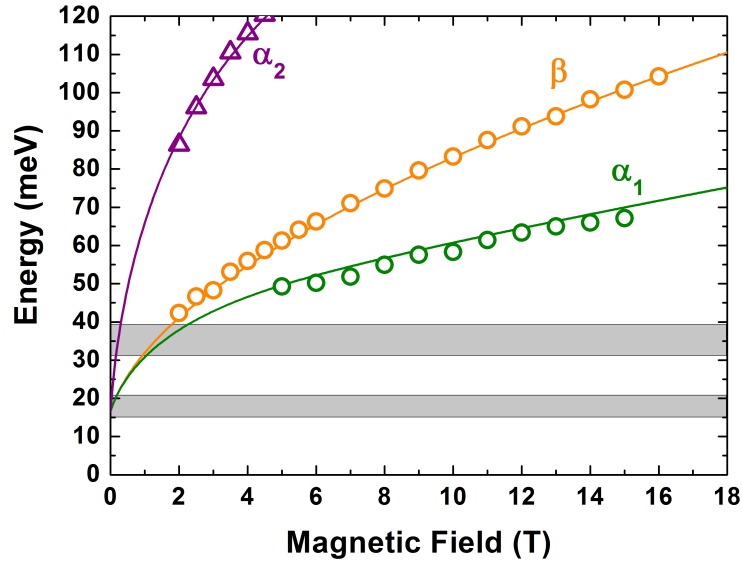


Figure C.4: Points corresponding to the minima of the transmission of Sample A at $T = 50$ K with theoretical predictions of transitions as a function of magnetic field.

C.2.2 Sample B

Temperature 30 K

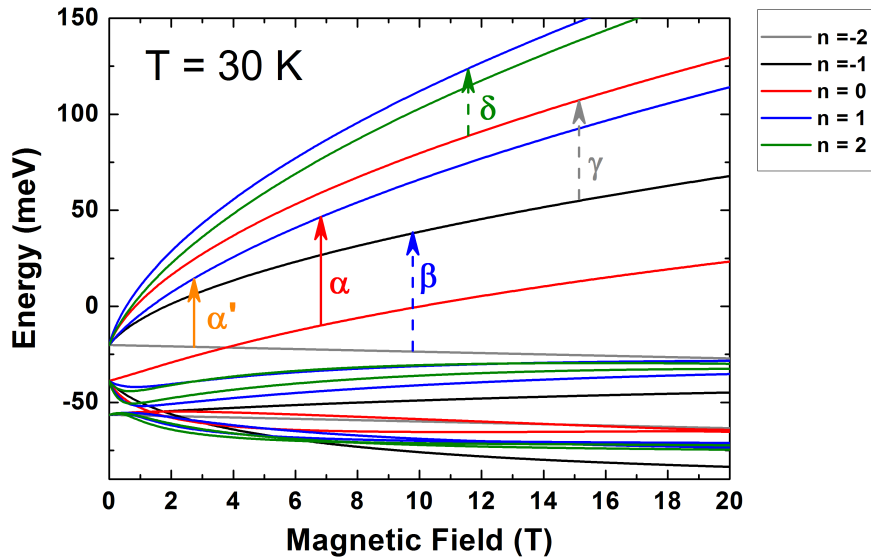


Figure C.5: Landau level graph of Sample B as a function of magnetic field at $T = 30$ K. Colored lines represent Landau levels, characterized by a different value of n , as described as indices of L on the right side of the graph. The Landau levels with $n = -2$ and $n = 0$ are zero-mode Landau levels. The energy of those levels at zero magnetic field is an indication of the band gap. Their crossing indicates the point of field induced semiconductor-metal-semiconductor phase transition, and assures that the sample is in the inverted band order phase. The vertical arrows with corresponding Greek letters represent observed transitions between Landau levels in this system. The solid arrows indicates interband transitions α and α' , while dashed arrows indicate intraband transitions β , γ , and δ .

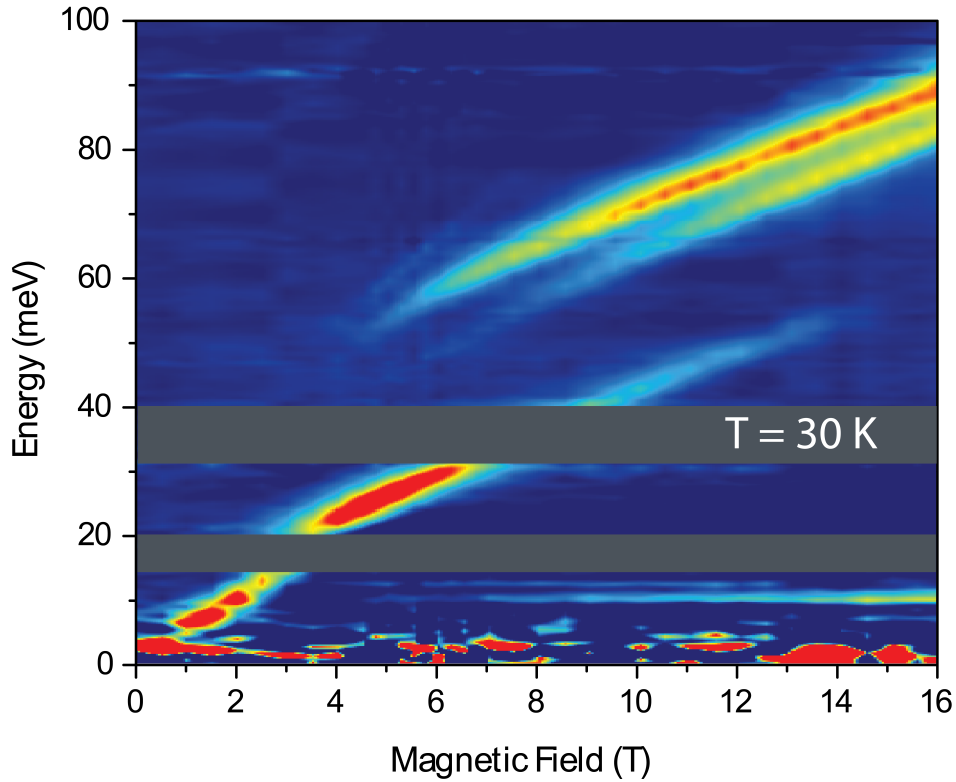


Figure C.6: False color map of transmission of Sample B as a function of energy and magnetic field at $T = 30$ K. Blue color represents areas where transmission is equal to 1, while lightblue/yellow/red colors indicate where absorption takes place. An anticrossing of transitions originating from the zero-mode Landau levels is visible close to $B_c = 5$ T.

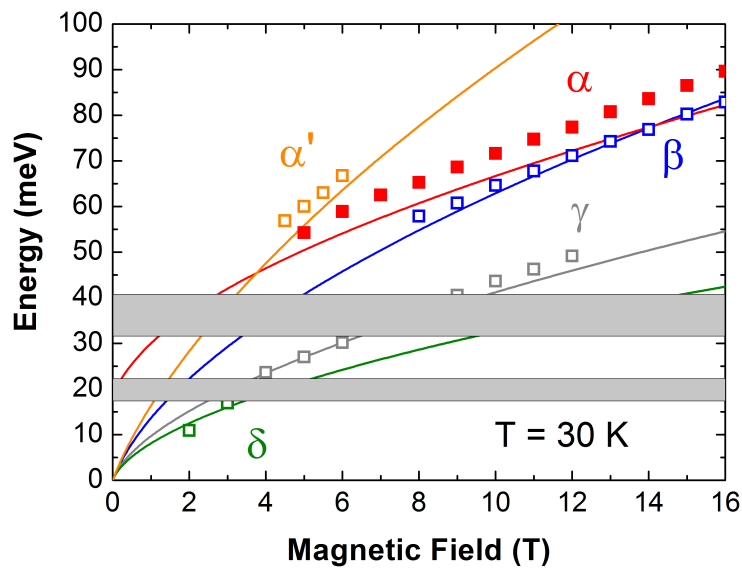


Figure C.7: Points corresponding to the minima of the transmission of Sample B at $T = 30$ K with theoretical predictions of transitions as a function of magnetic field. Full symbols represent interband transitions, while open symbols represent intraband transitions.

Temperature 70 K

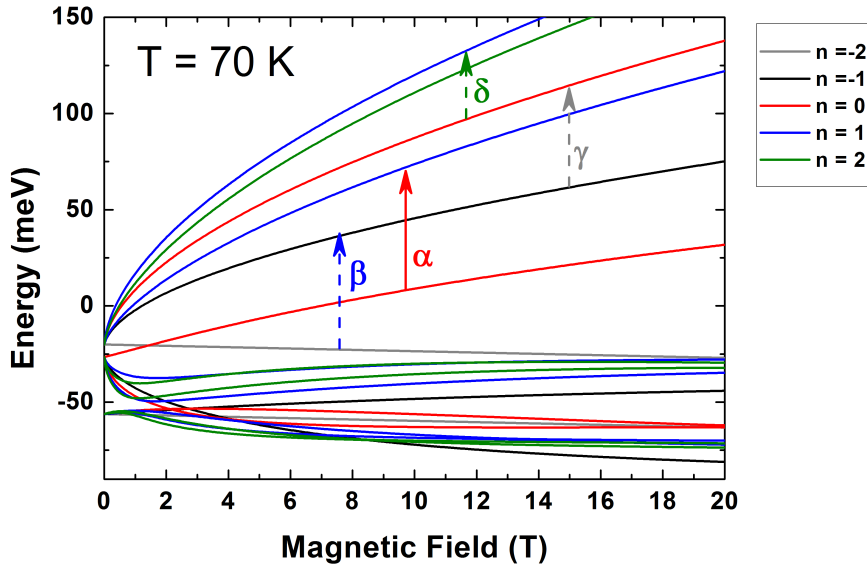


Figure C.8: Landau level graph of Sample B as a function of magnetic field at $T = 70$ K. Colored lines represent Landau levels, characterized by a different value of n , as described as indices of L on the right side of the graph. The Landau levels with $n = -2$ and $n = 0$ are zero-mode Landau levels. The energy of those levels at zero magnetic field is an indication of the band gap. Their crossing indicates the point of field induced semiconductor-metal-semiconductor phase transition, and assures that the sample is in the inverted band order phase. The vertical arrows with corresponding Greek letters represent observed transitions between Landau levels in this system. A solid arrow indicates an interband transition α , while dashed arrows indicate intraband transitions β , γ , and δ .

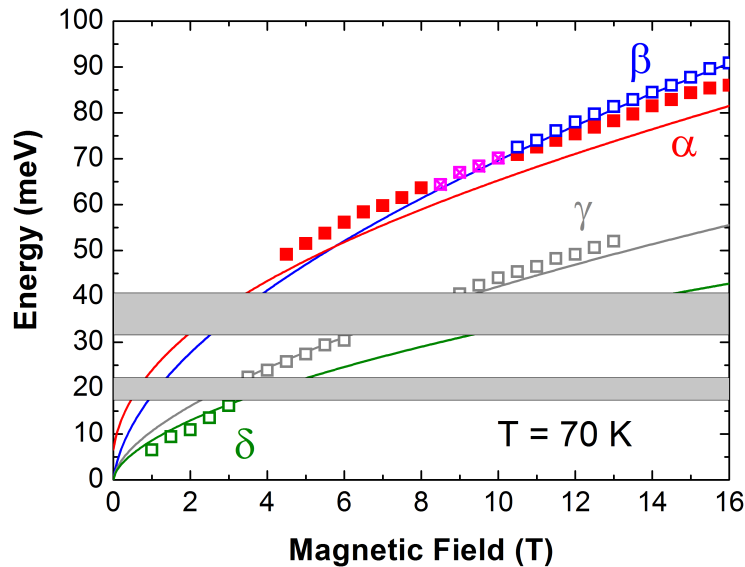


Figure C.9: Points corresponding to the minima of the transmission of Sample B at $T = 70$ K with theoretical predictions of transitions as a function of magnetic field. Full symbols represent interband transitions, while open symbols represent intraband transitions. Magenta symbols represent experimental data where the transitions α and β are indistinguishable.

Temperature 80 K

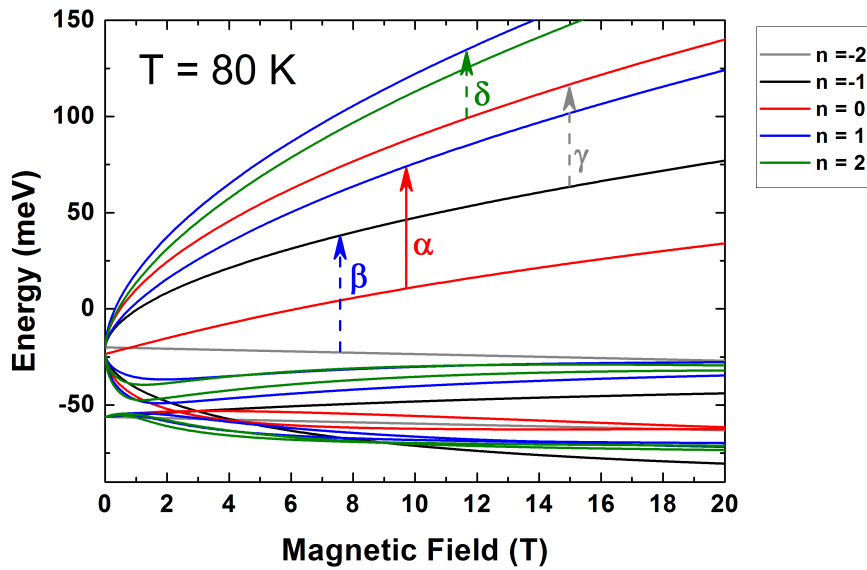


Figure C.10: Landau level graph of Sample B as a function of magnetic field at $T = 80$ K. Colored lines represent Landau levels, characterized by a different value of n , as described as indices of L on the right side of the graph. The Landau levels with $n = -2$ and $n = 0$ are zero-mode Landau levels. The energy of those levels at zero magnetic field is an indication of the band gap. Their crossing indicates the point of field induced semiconductor-metal-semiconductor phase transition, and assures that the sample is in the inverted band order phase. The vertical arrows with corresponding Greek letters represent observed transitions between Landau levels in this system. A solid arrow indicates an interband transition α , while dashed arrows indicate intraband transitions β , γ , and δ .

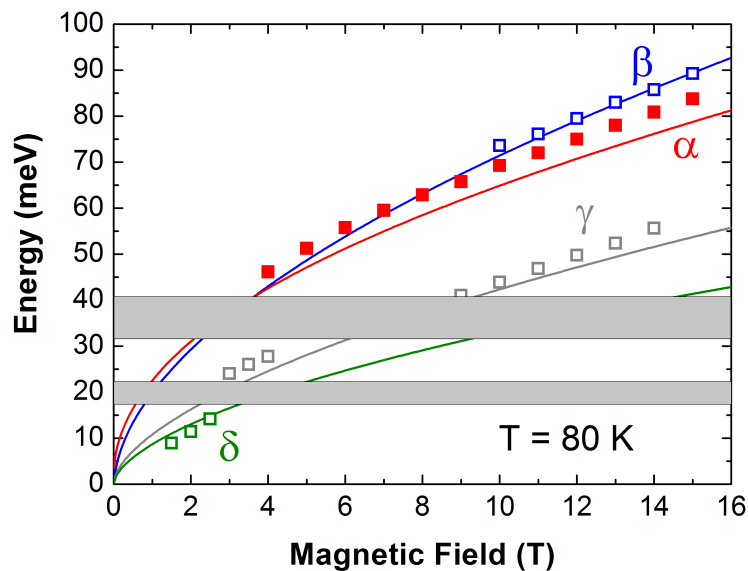


Figure C.11: Points corresponding to the minima of the transmission of Sample B at $T = 80$ K with theoretical predictions of transitions as a function of magnetic field. Full symbols represent interband transitions, while open symbols represent intraband transitions.

Temperature 100 K

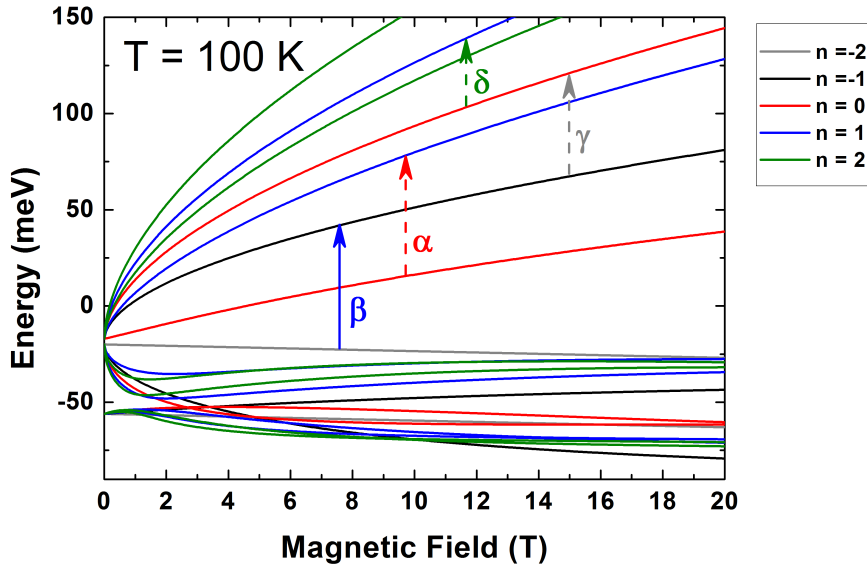


Figure C.12: Landau level graph of Sample B as a function of magnetic field at $T = 100$ K. Colored lines represent Landau levels, characterized by a different value of n , as described as indices of L on the right side of the graph. The Landau levels with $n = -2$ and $n = 0$ are zero-mode Landau levels. The energy of those levels at zero magnetic field is an indication of the band gap. Their crossing indicates the point of field induced semiconductor-metal-semiconductor phase transition, and assures that the sample is in the inverted band order phase. The vertical arrows with corresponding Greek letters represent observed transitions between Landau levels in this system. A solid arrow indicates an interband transition β , while dashed arrows indicate intraband transitions α , γ , and δ .

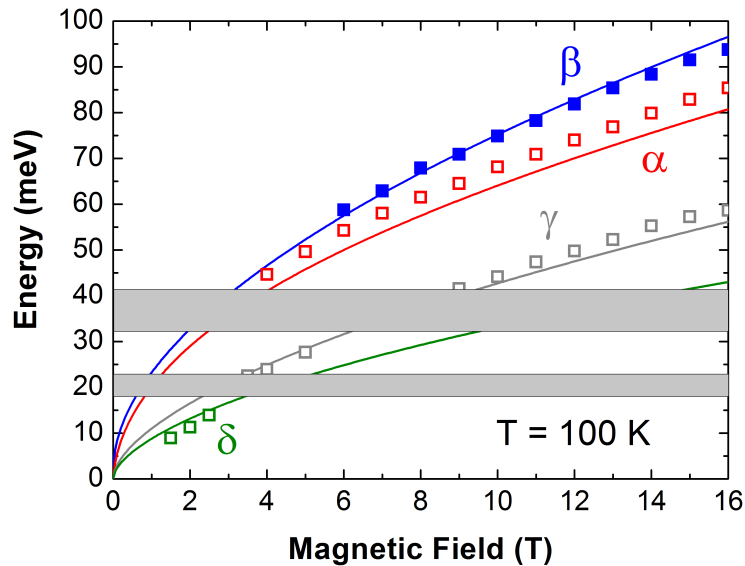


Figure C.13: Points corresponding to the minima of the transmission of Sample B at $T = 100$ K with theoretical predictions of transitions as a function of magnetic field. Full symbols represent interband transitions, while open symbols represent intraband transitions.

Bibliography

- [1] P. W. Anderson. *Basic Notions of Condensed Matter Physics* (Westview Press), (1997).
- [2] L. D. Landau and E. M. Lifshitz. *Statistical Physics* (Pergamon Press, Oxford), (1980).
- [3] B. D. Josephson. Possible new effects in superconductive tunneling. *Phys. Lett.* **1**, pp. 251–253 (1962).
- [4] K. v. Klitzing, G. Dorda, and M. Pepper. New Method for High-Accuracy Determination of the Fine-Structure Constant Based on Quantized Hall Resistance. *Phys. Rev. Lett.* **45**, 494 (1980).
- [5] D. C. Tsui, H. L. Stormer, and A. C. Gossard. Two-Dimensional Magnetotransport in the Extreme Quantum Limit. *Phys. Rev. Lett.* **48**, 1559 (1982).
- [6] R. B. Laughlin. Quantized Hall conductivity in two dimensions. *Phys. Rev. B* **23**, 5632 (1981).
- [7] D. J. Thouless, M. Kohmoto, M. P. Nightingale, and M. den Nijs. Quantized Hall Conductance in a Two-Dimensional Periodic Potential. *Phys. Rev. Lett.* **49**, 405 (1982).
- [8] M. V. Berry. Quantal Phase Factors Accompanying Adiabatic Changes. *Proceedings of the Royal Society A.* **392**, 1802, pp. 45-57 (1984).
- [9] V. L. Berezinski. Destruction of Long-range Order in One-dimensional and Two-dimensional Systems Having a Continuous Symmetry Group I. Classical Systems. *Zh. Eksp. Teor. Fiz* **59**, pp. 907-920 (1970) [*Sov. Phys.-JETP* **32**, 493 (1971)].
- [10] V. L. Berezinski. Destruction of Long-range Order in One-dimensional and Two-dimensional Systems Possessing a Continuous Symmetry Group II. Classical Systems. *Zh. Eksp. Teor. Fiz* **61**, pp. 1144-1156 (1971) [*Sov. Phys.-JETP* **34**, 610 (1972)].
- [11] J. M. Kosterlitz and D. J. Thouless. Ordering, metastability and phase transitions in two-dimensional systems. *Journal of Physics C: Solid State Physics* **6**, pp. 1181-1203 (1973).
- [12] C. L. Kane and E. J. Mele. \mathbb{Z}_2 Topological Order and the Quantum Spin Hall Effect. *Phys. Rev. Lett.* **95**, 146802 (2005).
- [13] C. L. Kane and E. J. Mele. Quantum Spin Hall Effect in Graphene. *Phys. Rev. Lett.* **95**, 226801 (2005).
- [14] M. König *et al.* Quantum Spin Hall Insulator State in HgTe Quantum Wells. *Science* **318**, 5851, pp. 766-770 (2007).
- [15] Y. Yao, F. Ye, X.-L. Qi, S.-C. Zhang, and Z. Fang. Spin-orbit gap of graphene: First-principles calculations. *Phys. Rev. B* **75**, 041401(R) (2007).

- [16] H. Min, J. E. Hill, N. A. Sinitsyn, B. R. Sahu, L. Kleinman, and A. H. MacDonald. Intrinsic and Rashba spin-orbit interactions in graphene sheets. *Phys. Rev. B* **74**, 165310 (2006).
- [17] B. A. Bernevig, T. L. Hughes, and S.-C. Zhang. Quantum Spin Hall Effect and Topological Phase Transition in HgTe Quantum Wells. *Science* **314**, 5806, pp. 1757-1761 (2006).
- [18] B. A. Bernevig and S.-C. Zhang. Quantum Spin Hall Effect. *Phys. Rev. Lett.* **96**, 106802 (2006).
- [19] M. Büttiker. Absence of backscattering in the quantum Hall effect in multiprobe conductors. *Phys. Rev. B* **38**, 9375 (1988).
- [20] C. Liu, T. L. Hughes, X.-L. Qi, K. Wang, and S.-C. Zhang. Quantum Spin Hall Effect in Inverted Type-II Semiconductors. *Phys. Rev. Lett.* **100**, 236601 (2008).
- [21] Y. Xia *et al.* Observation of a large-gap topological-insulator class with a single Dirac cone on the surface. *Nature Physics* **5**, pp.398-402 (2009).
- [22] L. Fu, C. L. Kane, and E. J. Mele. Topological Insulators in Three Dimensions. *Phys. Rev. Lett.* **98**, 106803 (2007).
- [23] D. Hsieh *et al.* A topological Dirac insulator in a quantum spin Hall phase. *Nature* **452**, pp. 970-974 (2008).
- [24] H. Zhang *et al.* Topological insulators in Bi₂Se₃, Bi₂Te₃ and Sb₂Te₃ with a single Dirac cone on the surface. *Nature Physics* **5**, pp. 438-442 (2009).
- [25] Y. L. Chen *et al.* Experimental Realization of a Three-Dimensional Topological Insulator Bi₂Te₃. *Science* **325**, 5937 pp. 178-181 (2009).
- [26] M. Brahlek *et al.* Transport properties of topological insulators: Band bending, bulk metal-to-insulator transition, and weak anti-localization. *Solid State Communications* **215**, pp. 54-62 (2014).
- [27] C. Brüne *et al.* Quantum Hall Effect from the Topological Surface States of Strained Bulk HgTe. *Phys. Rev. Lett.* **106**, 126803 (2011).
- [28] L. Fu and C. L. Kane. Topological insulators with inversion symmetry. *Phys. Rev. B* **76**, 045302 (2007).
- [29] B. A. Bernevig and T. L. Hughes. *Topological insulators and topological superconductors*. Princeton University Press, 1st edition (2013).
- [30] W. Zawadzki. *Intraband magneto-optics in InSb-type semiconductors*. Narrow Gap Semiconductors Physics and Applications. *Lecture Notes in Physics* **133**, Springer, Berlin, Heidelberg (1980).
- [31] B. I. Halperin. Quantized Hall conductance, current-carrying edge states, and the existence of extended states in a two-dimensional disordered potential. *Phys. Rev. B* **25**, 2185 (1982).
- [32] S. Murakami, N. Nagaosa, and S.-C. Zhang. Spin-Hall Insulator. *Phys. Rev. Lett.* **93**, 156804 (2006).
- [33] M. Altarelli. Electronic structure and semiconductor-semimetal transition in InAs-GaSb superlattices. *Phys. Rev. B* **28**, 842 (1983).

- [34] M. J. Yang, C. H. Yang, B. R. Bennett, and B. V. Shanabrook. Evidence of a Hybridization Gap in "Semimetallic" InAs/GaSb Systems. *Phys. Rev. Lett.* **78**, 4613 (1997).
- [35] A. Roth *et al.* Nonlocal Transport in the Quantum Spin Hall State. *Science* **17**, 5938, pp. 294-297 (2009).
- [36] M. Büttiker. Edge-State Physics Without Magnetic Fields. *Science* **325**, 5938, pp. 278-279 (2009).
- [37] C. Brüne *et al.* Spin polarization of the quantum spin Hall edge states. *Nature Physics* **8**, pp. 485-490 (2012).
- [38] E. M. Hankiewicz, L. W. Molenkamp, T. Jungwirth, and J. Sinova. Manifestation of the spin Hall effect through charge-transport in the mesoscopic regime. *Phys. Rev. B* **70**, 241301(R) (2004).
- [39] S. O. Valenzuela and M. Tinkham. Direct electronic measurement of the spin Hall effect. *Nature* **442**, pp. 176-179 (2006).
- [40] I. Knez, R. R. Du, and G. Sullivan. Finite conductivity in mesoscopic Hall bars of inverted InAs/GaSb quantum wells. *Phys. Rev. B* **81** 201301(R) (2010).
- [41] Y. Naveh and B. Laikhtman. Magnetotransport of coupled electron-holes. *Europhys. Lett.* **55**, pp. 545-551 (2001).
- [42] I. Knez, R. R. Du, and G. Sullivan. Evidence for Helical Edge Modes in Inverted InAs/GaSb Quantum Wells. *Phys. Rev. Lett.* **107** 136603 (2011).
- [43] B. Zhou, H.-Z. Lu, R.-L. Chu, S.-Q. Shen, and Q. Niu. Finite Size Effects on Helical Edge States in a Quantum Spin-Hall System. *Phys. Rev. Lett.* **101** 246807 (2008).
- [44] K. Suzuki, Y. Harada, K. Onomitsu, and K. Muraki. Edge channel transport in the InAs/GaSb topological insulating phase. *Phys. Rev. B* **87** 235311 (2013).
- [45] L. Du, I. Knez, G. Sullivan, and R.-R. Du. Robust Helical Edge Transport in Gated InAs/GaSb Bilayers. *Phys. Rev. Lett.* **114**, 096802 (2015).
- [46] I. Knez *et al.* Observation of Edge Transport in the Disordered Regime of Topologically Insulating InAs/GaSb Quantum Wells. *Phys. Rev. Lett.* **112**, 026602 (2014).
- [47] C. Charpentier *et al.* Suppression of bulk conductivity in InAs/GaSb broken gap composite quantum wells. *Appl. Phys. Lett.* **103**, 112102 (2013).
- [48] M. E. Huber *et al.* Gradiometric micro-SQUID susceptometer for scanning measurements of mesoscopic samples. *Rev. Sci. Instrum.* **79**, 053704 (2008).
- [49] K. C. Nowack *et al.* Imaging currents in HgTe quantum wells in the quantum spin Hall regime. *Nature Materials* **12**, pp. 787-791 (2013).
- [50] E. M. Spanton *et al.* Images of Edge Current in InAs/GaSb Quantum Wells. *Phys. Rev. Lett.* **113**, 026804 (2014).
- [51] D. L. Smith and C. Mailhot. Proposal for strained type II superlattice infrared detectors. *J. Appl. Phys.* **62**, pp. 2545-2548 (1987).

- [52] L. Du *et al.* Strain-Engineering of InAs/GaInSb Topological Insulator Towards Majorana Platform. *arXiv:1608.06588* (2016).
- [53] T. Akiho *et al.* Engineering quantum spin Hall insulators by strained-layer heterostructures. *arXiv:1608.06751* (2016).
- [54] B. A. Volkov and O. A. Pankratov. Two-dimensional massless electrons in an inverted contact. *Zh. Eksp. Teor. Fiz.* **42**, No. 4, pp. 145-148 (1985).
- [55] X. Dai, T. L. Hughes, X.-L. Qi, Z. Fang, and S.-C. Zhang. Helical edge and surface states in HgTe quantum wells and bulk insulators. *Phys. Rev. B* **77**, 125319 (2008).
- [56] O. Crauste *et al.* Topological surface states of strained Mercury-Telluride probed by ARPES. *arXiv:1307.2008 [cond-mat.mes-hall]* (2013).
- [57] A. Pfeuffer-Jeschke. Ph.D. thesis. *Bandstruktur und Landau-Niveaus quecksilberhaltiger II-IV-Heterostrukturen*, Universität Würzburg (2000).
- [58] P. Leubner, L. Lunczer, C. Brüne, H. Buhmann, and L. W. Molenkamp. Strain Engineering of the Band Gap of HgTe Quantum Wells Using Superlattice Virtual Substrates. *Phys. Rev. Lett.* **117**, 086403 (2016).
- [59] S.-Y. Xu, *et al.* Observation of a topological crystalline insulator phase and topological phase transition in $\text{Pb}_{1-x}\text{Sn}_x\text{Te}$. *Nature Communications* **3**, 1192 (2012).
- [60] B. A. Assaf *et al.* Magneto-optical determination of a topological index. *arXiv:1608.08912 [cond-mat.mes-hall]* (2016).
- [61] T. Phuphachong *et al.* Direct Landau level Spectroscopy in $\text{Pb}_{1-x}\text{Sn}_x\text{Se}$ and $\text{Pb}_{1-x}\text{Sn}_x\text{Te}$ across the Topological Phase Transition: A Review. *Crystals* **2017**, 7(1), 29.
- [62] S. Wiedmann *et al.* Temperature-driven transition from a semiconductor to a topological insulator. *Phys. Rev. B* **91**, 205311 (2015).
- [63] M. S. Dresselhaus. *Solid State Physics Part II: Optical Properties of Solids*.
- [64] J. M. Martínez-Duart, R. J. Martín-Palma, and F. Agulló-Rueda. *Nanotechnology for microelectronics and optoelectronics*. ISBN-13: 978 0080 445533. Elsevier (2006).
- [65] S. Bellucci and P. Onorato. Landau levels and edge states in a cylindrical two-dimensional electron gas: A semiclassical approach. *Phys. Rev. B* **82**, 205305 (2010).
- [66] W. D. Lawson, S. Nielson, E. H. Putley, and A. S Young. Preparation and properties of HgTe and mixed crystals of HgTe-CdTe. *J. Phys. Chem. Solids* **9** 325-329 (1959).
- [67] J. L. Schmit and E. L. Stelzer. Temperature and Alloy Compositional Dependences of the Energy Gap of $\text{Hg}_{1-x}\text{Cd}_x\text{Te}$. *J. Appl. Phys.* **40**, 4865 (1969).
- [68] M. W. Scott. Energy Gap in $\text{Hg}_{1-x}\text{Cd}_x\text{Te}$ by Optical Absorption. *J. Appl. Phys.* **40**, 4077 (1969).
- [69] S. H. Groves, T. C. Harman, and C. R. Pidgeon. Interband Magnetoreflexion of $\text{Hg}_{1-x}\text{Cd}_x\text{Te}$. *Solid State Commun.* **9**, 451 (1971).

- [70] W. D. Saur. Long Wavelength Mercury-Cadmium Telluride Photoconductive Infrared Detectors. *Infrared Phys.* **8**, 255 (1968).
- [71] R. S. Kim and S. Narita. Far-Infrared Interband Magnetoabsorption and Band Structure of $\text{Hg}_{1-x}\text{Cd}_x\text{Te}$ Alloys. *Phys. Stat. Sol. B* **73**, 741 (1976).
- [72] Y. Guldner, C. Rigaux, A. Mycielski, and Y. Couder. Magneto-optical Investigation of $\text{Hg}_{1-x}\text{Cd}_x\text{Te}$ Mixed Crystals. *Phys. Stat. Sol. (b)* **81**, 615 (1977).
- [73] Y. Guldner, C. Rigaux, A. Mycielski, and Y. Couder. Magneto-optical Investigation of $\text{Hg}_{1-x}\text{Cd}_x\text{Te}$ Mixed Crystals. *Phys. Stat. Sol. (b)* **82**, 149 (1977).
- [74] C. Rigaux. *Interband magneto-optics in narrow gap semiconductors*. In: W. Zawadzki (eds.) *Narrow Gap Semiconductors Physics and Applications. Lecture Notes in Physics* **133**, Springer, Berlin, Heidelberg (1980).
- [75] E. O. Kane. Band structure of indium antimonide. *J. Phys. Chem. Solids* **1**, pp. 249-261 (1957).
- [76] M. Orlita, *et al.* Observation of three-dimensional massless Kane fermions in a zinc-blende crystal. *Nature Physics* **10**, pp. 233-238 (2014).
- [77] J. D. Malcolm and E. J. Nicol. Magneto-optics of massless Kane fermions: Role of the flat band and unusual Berry phase, *Phys. Rev. B* **92** 035118 (2015).
- [78] M. H. Weiler. *Semiconductors and Semimetals*. Vol. 16, pp. 119–191, Elsevier (1981).
- [79] P. Capper and J. W. Garland. *Mercury Cadmium Telluride: Growth, Properties and Applications*. Wiley Series in Materials for Electronic and Optoelectronic Applications (2010).
- [80] S. S. Krishtopenko *et al.* Pressure- and temperature-driven phase transitions in HgTe quantum wells. *Phys. Rev. B* **94**, 245402 (2016).
- [81] F. Teppe *et al.* Temperature-driven massless Kane fermions in HgCdTe crystals. *Nature Communications* **7**, 12576 (2016).
- [82] V. Daumer *et al.* Quasiballistic transport in HgTe quantum-well nanostructures. *Appl. Phys. Lett.* **83**, 1376-1378 (2003).
- [83] J. P. Laurenti, J. Camassel, and A. Bouhemadou. Temperature dependence of the fundamental absorption edge of mercury cadmium telluride. *J. Appl. Phys.* **67**, 6454 (1990).
- [84] E. G. Novik *et al.* Band structure of semimagnetic $\text{Hg}_{1-y}\text{Mn}_y\text{Te}$ quantum wells. *Phys. Rev. B* **72** 035321 (2005).
- [85] A. Akrap *et al.* Magneto-Optical Signature of Massless Kane Electrons in Cd_3As_2 . *Phys. Rev. Lett.* **117**, 136401 (2016).
- [86] Z. K. Liu, *et al.* A stable three-dimensional topological Dirac semimetal Cd_3As_2 . *Nature Materials* **13**, pp. 677-681 (2014).
- [87] I. Roseman. Effet Shubnikov de Haas dans Cd_3As_2 : Forme de la surface de Fermi et modele non parabolique de la bande de conduction. *J. Phys. Chem. Solids* **30**, 1385 (1969).

- [88] J. Bodnar. in Proc. III Conf. Narrow-Gap Semiconductors, Warsaw, edited by J. Raulszkiewicz, M. Górski, and E. Kaczmarek (Elsevier, 1977) p. 311.
- [89] S. Borisenko *et al.* Experimental Realization of a Three-Dimensional Dirac Semimetal. *Phys. Rev. Lett.* **113**, 027603 (2014).
- [90] M. Neupane *et al.* Observation of a three-dimensional topological Dirac semimetal phase in high-mobility Cd₃As₂. *Nature Communication* **5**, 3786 (2014).
- [91] E.O. Kane *Band structure of narrow gap semiconductors*. In: Zawadzki W. (eds) Narrow Gap Semiconductors Physics and Applications. *Lecture Notes in Physics* **133**, Springer, Berlin, Heidelberg (1980).
- [92] Z. Jiang *et al.* Infrared spectroscopy of Landau levels of graphene. *Phys. Rev. Lett.* **98**, 197403 (2007).
- [93] Y. Chang *et al.* Narrow gap HgCdTe absorption behavior near the band edge including non-parabolicity and the Urbach tail. *Appl. Phys. Lett.* **89**, 062109 (2006).
- [94] A. B. Kuzmenko *et al.* Universal optical conductance of graphite. *Phys. Rev. Lett.* **100**, 117401 (2008).
- [95] D. V. Kozlov *et al.* Mercury vacancies as divalent acceptors in Hg_yTe_{1-x}/Cd_xHg_{1-x}Te structures with quantum wells. *Semiconductors* **50**, pp.1662-1668 (2016).
- [96] E. M. Sheregii, J. Cebulski, A. Marcelli, and M. Piccinini. Temperature dependence discontinuity of the phonon mode frequencies caused by a zero-gap state in HgCdTe alloys. *Phys. Rev. Lett.* **102**, 045504 (2009).
- [97] J. D. Malcolm and E. J. Nicol. Magneto-optics of general pseudospin-s two-dimensional Dirac-Weyl fermions. *Phys. Rev. B* **90**, 035405 (2014).
- [98] M. König, *et al.* The Quantum Spin Hall Effect: Theory and Experiment. *J. Phys. Soc. Jpn* **77**, 031007 (2008).
- [99] B. Büttner *et al.* Single valley Dirac fermions in zero-gap HgTe quantum wells. *Nature Physics* **7**, pp. 418-422 (2011).
- [100] N. Castro *et al.* The electronic properties of graphene. *Reviews of Modern Physics* **81**, 109 (2009).
- [101] M. Orlita *et al.* Fine structure of "zero-mode" Landau levels in HgTe/CdTe quantum wells. *Phys. Rev. B* **83**, 115307 (2011).
- [102] M. Zholudev *et al.* Magnetospectroscopy of two-dimensional HgTe-based topological insulators around the critical thickness. *Phys. Rev. B* **86**, 205420 (2012).
- [103] M. Schultz *et al.* Crossing of conduction- and valence-subband Landau levels in an inverted HgTe/CdTe quantum well. *Phys. Rev. B* **57**, 14772 (1998).
- [104] S. Dvoretzky *et al.* Growth of HgTe Quantum Wells for IR to THz Detectors. *J. Electron. Mater.* **39**, 918 (2010).

- [105] M. S. Zholudev *et al.* Anticrossing of Landau levels in HgTe/CdHgTe (013) quantum wells with an inverted band structure. *Jetp Lett.* **100**, 790 (2015).
- [106] A. V. Ikonnikov *et al.* Temperature-dependent magnetospectroscopy of HgTe quantum wells. *Phys. Rev. B* **94**, 155412 (2016).
- [107] J. Ludwig *et al.* Cyclotron resonance of single-valley Dirac fermions in nearly gapless HgTe quantum wells. *Phys. Rev. B* **89**, 241406 (2014).
- [108] M. Dyakonov and A. Khaetskii. Surface states in a gapless semiconductor. *JETP Lett.* **33**, 110 (1981).
- [109] Y.-C. Chang, J. N. Schulman, G. Bastard, Y. Guldner, and M. Voos. Effects of quasi-interface states in HgTe-CdTe superlattices. *Phys. Rev. B* **31**, 2557(R) (1985).
- [110] X.-L. Qi, T. L. Hughes, and S.-C. Zhang. Topological field theory of time-reversal invariant insulators. *Phys. Rev. B* **78**, 195424 (2008).
- [111] J. B. Oostinga *et al.* Josephson Supercurrent through the Topological Surface States of Strained Bulk HgTe. *Phys. Rev. X* **3**, 021007 (2013).
- [112] L. Fu and C. L. Kane. Superconducting Proximity Effect and Majorana Fermions at the Surface of a Topological Insulator. *Phys. Rev. Lett.* **100**, 096407 (2008).
- [113] K.-M. Dantscher *et al.* Cyclotron-resonance-assisted photocurrents in surface states of a three-dimensional topological insulator base on a strained high-mobility HgTe film. *Phys. Rev. B* **92**, 165314 (2015).
- [114] Y. Baum *et al.* Self-consistent k-p calculations for gated thin layers of three-dimensional topological insulators. *Phys. Rev. B* **89**, 245136 (2014).
- [115] R.-L. Chu, J. Shi, and S.-Q. Shen. Surface edge state and half-quantized Hall conductance in topological insulators. *Phys. Rev. B* **84**, 085312 (2011).
- [116] C. Thomas. Ph.D. thesis. *Strained HgTe/CdTe topological insulators, towards spintronic applications*. Université Grenoble Alpes (2016).
- [117] A. M. Shuvaev, G. V. Astakhov, A. Pimenov, C. Brüne, H. Buhmann, and L. W. Molenkamp. Giant Magneto-Optical Faraday Effect in HgTe Thin Films in the Terahertz Spectral Range. *Phys. Rev. Lett.* **106**, 107404 (2011).
- [118] A. M. Shuvaev, G. V. Astakhov, C. Brüne, H. Buhmann, L. W. Molenkamp, and A. Pimenov. Terahertz quantum Hall effect of Dirac fermions in a topological insulator. *Phys. Rev. B* **87**, 121104(R) (2013).
- [119] J. N. Hancock *et al.* Surface State Charge Dynamics of a High-Mobility Three-Dimensional Topological Insulator. *Phys. Rev. Lett.* **107**, 136803 (2011).
- [120] A. M. Shuvaev, G. V. Astakhov, C. Brüne, H. Buhmann, L. W. Molenkamp, and A. Pimenov. Terahertz magneto-optical spectroscopy in HgTe thin films. *Semicond. Sci. Technol.* **27**, 124004 (2012).

- [121] S. M. Sze, *Physics of Semiconductor Devices*. John Wiley and Sons, New York, second edition (1981).
- [122] Z. M. Fang *et al.* Photoluminescence of InSb, InAs, and InAsSb grown by organometallic vapor phase epitaxy. *J. Appl. Phys.* **67**, 7034 (1990).
- [123] M. Wu and C. Chen. Photoluminescence of high quality GaSb grown from Ga and Sb rich solutions by liquidphase epitaxy. *J. Appl. Phys.* **72**, 4275 (1992).
- [124] I. Vurgaftman, J. R. Meyer, and L. R. Ram-Mohan. Band parameters for III–V compound semiconductors and their alloys. *J. Appl. Phys.* **89**, 5815 (2001).
- [125] H. Kroemer. The 6.1 Å family (InAs, GaSb, AlSb) and its heterostructures: a selective review. *Physica E* **20**, pp. 196-203 (2004).
- [126] G. Tuttle, H. Kroemer, and J. H. English. Electron concentrations and mobilities in AlSb/InAs/AlSb quantum wells. *J. Appl. Phys.* **65**, 5239 (1989).
- [127] C. Ngyuen, B. Brar, H. Kroemer, and J. H. English. Surface donor contribution to electron sheet concentrations in not-intentionally doped InAs-AlSb quantum wells. *Appl. Phys.Lett.* **60**, 1854 (1992).
- [128] H. Kroemer, C. Ngyuen, and B. Brar. Are there Tamm-state donors at the InAs–AlSb quantum well interface. *J. Vac. Sci. Technol. B* **10**, 1769 (1992).
- [129] J. Shen, H. Goronkin, J. D. Dow, and S. Y. Ren. Tamm states and donors at InAs/AlSb interfaces. *J. Appl. Phys.* **77**, 1576 (1995).
- [130] C. Nguyen *et al.* Growth of InAs-AlSb Quantum Wells Having Both High Mobilities and High Concentrations. *Journal of Electronic Materials* **22**, 255-258 (1993).
- [131] C. R. Bolognesi, H. Kroemer, and J. H. English. Well width dependence of electron transport in molecular-beam epitaxially grown InAs/AlSb quantum wells. *J. Vac. Sci. Technol. B* **10**, 877 (1992).
- [132] Z. H. Li, *et al.* Buffer influence on AlSb/InAs/AlSb quantum wells. *Journal of Crystal Growth* **301–302**, pp. 181–184 (2007).
- [133] G. Tuttle, H. Kroemer, and J. H. English. Effects of interface layer sequencing on the transport properties of InAs/AlSb quantum wells: Evidence for antisite donors at the InAs/AlSb interface. *J. Appl. Phys.* **67**, 3032 (1990).
- [134] B. Jenichen, S. A. Stepanov, B. Brar, and H. Kroemer. Interface roughness of InAs/AlSb superlattices investigated by X-ray scattering. *J. Appl. Phys.* **79**, 120 (1996).
- [135] M. Thomas, H.-R. Blank, K. C. Wong, and H. Kroemer. Buffer-dependent mobility and morphology of InAs/(Al,Ga)Sb quantum wells. *Journal of Crystal Growth* **175/176**, pp. 849-897 (1997).
- [136] C. Ngyuen, K. Ensslin, and H. Kroemer. Magneto-transport in InAs/AlSb quantum wells with large electron concentration modulation. *Surface Science* **267**, pp. 549-552 (2007).

- [137] H. Sasaki *et al.* $\text{In}_{1-x}\text{Ga}_x\text{As-GaSb}_{1-y}\text{As}_y$ heterojunctions by molecular beam epitaxy. *Appl. Phys. Lett.* **31**, 211 (1977).
- [138] W. R. Frensley and H. Kroemer. Theory of the energy-band lineup at an abrupt semiconductor heterojunction. *Phys. Rev. B* **16**, 2642 (1977).
- [139] W. A. Harrison. Elementary theory of heterojunctions. *J. Vac. Sci. Technol.* **14**, 1016 (1977).
- [140] I. Knez. Ph.D. thesis. *Transport Properties of Topological Phases in Broken Gap InAs/GaSb Based Quantum Wells*. Rice University (2012).
- [141] L. L. Chang and L. Esaki. Electronic properties of InAs-GaSb superlattices. *Surf. Sci.* **98**, 70 (1980).
- [142] M. Lakrimi *et al.* Minigaps and Novel Giant Negative Magnetoresistance in InAs/GaSb Semimetallic Superlattices. *Phys. Rev. Lett.* **79**, 3034 (1997).
- [143] I. Lo, W. C. Mitchel, and J.-P. Cheng. Magnetic-field-induced free electron and hole recombination in semimetallic $\text{Al}_x\text{Ga}_{1-x}\text{Sb/InAs}$ quantum wells. *Phys. Rev. B* **48**, 9118 (1993).
- [144] T. P. Smith, H. Munekata, L. L. Chang, F. F. Fang, and L. Esaki. Magnetic-Field-Induced Transitions in InAs/ $\text{Ga}_{1-x}\text{Al}_x\text{Sb}$ Heterostructures. *Surface Science* **196**, pp. 687-693 (1988).
- [145] Y. Naveh and B. Laikhtman. Band-structure tailoring by electric field in a weakly coupled electron-hole system. *Appl. Phys. Lett.* **66**, 1980 (1995).
- [146] E. E. Mendez, L. L. Chang, and L. Esaki. Two-Dimensional Quantum States in Multi-Heterostructures of Three Constituents. *Surface Science* **13**, pp. 474-478 (1982).
- [147] L. J. Cooper *et al.* Resistance resonance induced by electron-hole hybridization in a strongly coupled InAs/GaSb/AlSb heterostructure. *Phys. Rev. B* **57**, 11915 (1998).
- [148] S. S. Krishtopenko *et al.* Cyclotron resonance of dirac fermions in InAs/GaSb/InAs quantum wells. *Semiconductors* 51:38 (2017).
- [149] S. Murakami *et al.* Tuning phase transition between quantum spin Hall and ordinary insulating phases. *Phys. Rev. B* **76**, 205304 (2007).
- [150] Yu. G. Sadofyev, A. Ramamoorthy, B. Naser, J. P. Bird, S. R. Jonson, and Y.-H. Zhang. Large g -factor enhancement in high-mobility InAs/AlSb quantum wells. *Appl. Phys. Lett.* **81**, 1833 (2002).